



Lawther, Susan E. M. (2012) *The effects of fluid flow through faults in granite gneiss exhumed from seismogenic depths*. PhD thesis.

<https://theses.gla.ac.uk/3374/>

Copyright and moral rights for this work are retained by the author

A copy can be downloaded for personal non-commercial research or study, without prior permission or charge

This work cannot be reproduced or quoted extensively from without first obtaining permission in writing from the author

The content must not be changed in any way or sold commercially in any format or medium without the formal permission of the author

When referring to this work, full bibliographic details including the author, title, awarding institution and date of the thesis must be given

Enlighten: Theses

<https://theses.gla.ac.uk/>
research-enlighten@glasgow.ac.uk

The Effects Of Fluid Flow Through Faults In Granite Gneiss Exhumed From Seismogenic Depths

Susan Lawther

B.Sc. (Hons) University Of Glasgow

Thesis submitted for Degree of Doctor of Philosophy

School of Geographical & Earth Sciences

College of Science & Engineering

University of Glasgow

October 2011
Susan Lawther 2011©

Dedication

For Mum.

You might not have been here to see me through my PhD, but one thing is for sure, I could not have coped with all the ups and downs of the past four years without the wisdom and knowledge that you imparted to me during your life. You were an amazing mother and role model and I hope I have done you proud.

Abstract

Fault zones are ubiquitous structures throughout the Earth's crust and as a fault evolves it can significantly influence the rheological and hydrological properties of the crust. Fluid flow through fault zones is typically associated with fault-fluid-rock interactions and these interactions can affect the mineralogy, strength and evolution of a fault zone. In this study, field mapping is combined with petro-physical and stable isotopic analyses of the fault rock to evaluate the fault-fluid-rock interactions that occur within different fault zones, and the effects of these reactions on fault zone and fault population evolution.

At Passo Moro in the NW Italian Alps, there are three sets of joints cross-cutting the granite gneiss and numerous faults have formed by reactivation of pre-existing joints. The distribution of faults at Passo Moro is ultimately controlled by the variability of joint density within the host rock and the pre-existing joint distribution also affects the likelihood of whether a fault will grow into a mature fault zone or not. Where the joint density is high, strain is unable to accumulate to significant levels to enable joint reactivation into faults, whereas where joint density is low, fault zones are isolated and thus there are no structures nearby to facilitate fault linkage.

At Passo Moro the fault population has evolved in a similar way as that described by Martel (1990) whereby small faults link to form simple faults which connect to form compound fault zones. The Virgin Fault and Spaghetti Fault would be considered as small fault zones and The Ciao Ciao Fault is equivalent to a compound fault zone. All three fault zones have different fault architectures and the small faults have been affected by different fluid-rock reactions compared to the larger fault. The small faults have experienced fault zone strengthening by K-feldspar precipitation, whereas the large fault has been weakened by muscovite precipitation.

The different reactions between the fault zones are primarily controlled by the water-rock ratio which in turn is governed by permeability and the volume of fluid that infiltrates the fault zone. The Virgin Fault is considered as a rock-dominated system (K-feldspar-rich) whereas The Ciao Ciao fault is a fluid-

dominated system (muscovite-rich). However, stable isotopes from both fault zones record a low water-rock ratio signifying rock-dominated conditions. Therefore the mineralogy of the fault rock is not solely controlled by the permeability defined water-rock ratio. The fluid dominated conditions promoting muscovitization in the Ciao Ciao Fault were probably enabled by an open fluid system and large volumes of fluid flowing through the fault during its lifetime. Stable isotopes indicate that water-rock ratios got lower with time in the Virgin Fault implying a limited open system, whereas muscovitization and stable water-rock ratios in the Ciao Ciao Fault point towards open system behaviour. In the Ciao Ciao Fault quartz precipitation *only* occurs in the foliated cataclasite within the fault core. Quartz precipitation is typically associated with closed system behaviour and suggests that the foliated cataclasite periodically ceased to be open to fluids and hence experienced cycles of higher and lower permeability.

Stable isotopes show that the Virgin Fault records mineral precipitation from a metamorphic-like fluid, but after fault deactivation, the fault periodically transmitted progressively more meteoric-like fluids via a micro-fracture network. The Ciao Ciao Fault records mineral precipitation from a more meteoric-like fluid compared to the Virgin Fault, and flow through micro-fracture networks is dominated by an essentially meteoric fluid. The Ciao Ciao Fault therefore does not preserve evidence of fluids from its early history.

This study indicates that the geochemical reactions that occur within a fault are controlled in part by the evolutionary stage of the fault, the fault rock permeability and the volume of fluids that pass through the fault. These results have been used to propose models for how the hydraulic properties and strength of a fault (population) evolve with time. The models produced from this study help advance our understanding of the processes that occur during the timescale of the seismic cycle, and how a population of faults will evolve in terms of mineralogy, strength and fluid flow. Such information will be of use to those involved in mineralization and mining studies, the storage of nuclear waste in crystalline rock, and earthquake prediction studies.

Table of Contents

Dedication	2
Abstract	3
Table of Contents.....	5
List of Figures	9
List of Tables	13
List of Tables	13
List of Equations	14
List of Equations	14
Acknowledgements	15
Acknowledgements	15
1 Introduction.....	18
1.1 Faults and fluid flow.....	18
1.1.1 Background	20
1.1.2 What are the gaps in our knowledge.....	22
1.1.3 How can we study seismogenic faults.....	23
1.1.4 Thesis aims and objectives	23
1.1.5 Thesis structure.....	24
2 Geological Setting/history.....	26
2.1 Introduction	26
2.2 The Alps.....	27
2.2.1 Western Alps	29
2.3 Previous studies of Monte Rosa nappe	31
2.3.1 Lithology of Monte Rosa and Passo Moro	33
2.3.2 Why study at Passo Moro?	36
3 Field mapping.....	37
3.1 Introduction	37
3.2 Mapping of Passo Moro - Techniques	38
3.3 Host rock.....	39
3.3.1 Logging	40
3.3.2 Host rock descriptions	42
3.3.2.1 Granite gneiss	42
3.3.2.2 Metasedimentary rocks	43
3.3.2.3 Amphibolite	44
3.3.2.4 Host Rock interpretation	44
3.4 Structures.....	45
3.4.1 Cross-cutting relationships.....	47
3.4.2 Joint Descriptions	47
3.4.2.1 Data recording transects.....	49
3.4.2.2 Joint relationships at Passo Moro	52
3.4.3 Interpretation.....	54
3.4.3.1 Mechanical boundaries overview	54
3.4.3.2 Host rock effects on joint development	55
3.4.3.2.1 Metasedimentary unit - 010 joint density.....	55
3.4.3.2.2 Granite gneiss - 010° joint density.....	56
3.4.3.3 Joints - Effects of pre-existing structures	57
3.4.3.3.1 Average joint density.....	58
3.4.4 Conclusions	59
4 Fault architecture.....	61
4.1 Introduction	61

4.2	Techniques	62
4.3	The studied fault zones	63
4.4	Virgin Fault	65
4.4.1	Overview	65
4.4.2	Host rock & pre-existing structures	67
4.4.3	Principal slip surface.....	67
4.4.4	Fault core.....	68
4.4.5	Damage zone	70
4.5	Spaghetti Fault	74
4.5.1	Host rock and pre-existing structures.....	75
4.5.2	Principal slip surface.....	78
4.5.3	Damage zone	79
4.6	Ciao Ciao fault	81
4.6.1	Host rock and pre-existing structures.....	82
4.6.2	Principal slip surfaces	82
4.6.3	Fault core.....	84
4.6.4	Damage zone	85
4.7	Discussion.....	86
4.7.1	Fault architecture	87
4.7.1.1	Virgin Fault	87
4.7.1.2	Spaghetti Fault	88
4.7.1.3	The Ciao Ciao Fault.....	90
4.7.2	Architectural differences	91
4.7.2.1	The effect of joint distribution on fault evolution	92
4.7.3	What the fault rocks tell us about faulting conditions in the fault zones	96
5	Microstructural analysis of faults	98
5.1	Introduction	98
5.2	Methodology.....	98
5.3	Host rock.....	100
5.3.1	Interpretation - Host rock.....	101
5.4	Virgin fault (VF)	103
5.4.1	Grain size and mineralogy	103
5.4.2	Micro-structures and textures in the VF	106
5.4.2.1	Outer Damage zone - minor bleaching	106
5.4.2.2	Inner Damage zone - intense bleaching	108
5.4.2.3	Fault core	112
5.4.2.3.1	Narrow fault core band	112
5.4.2.3.2	Thick fault core band	115
5.5	Virgin Fault Interpretation.....	117
5.5.1	Outer Damage Zone	117
5.5.1.1	Inner Damage Zone	120
5.5.1.2	Fault core - Narrow core.....	123
5.5.1.3	Fault core - Thick core.....	124
5.5.1.3.1	Comparison of the narrow and thick core	126
5.5.1.4	Virgin Fault Summary	127
5.6	Ciao Ciao fault (CCF)	128
5.6.1	Grain size and mineralogy	129
5.6.2	Micro-structures and -textures	131
5.6.2.1	Damage zone	131
5.6.2.2	Breccia.....	132
5.6.2.3	Cataclasite	134
5.6.2.4	Foliated cataclasite	135

5.7	Interpretation - Mineralogy and micro-structures	137
5.7.1	Damage zone	137
5.7.2	Breccia	138
5.7.3	Cataclasite	139
5.7.4	Foliated cataclasite	139
5.7.5	Summary CCF	141
5.8	Comparing the microstructural evolution of the Virgin and Ciao Ciao	
Faults	142
5.8.1	Grain size reduction	143
5.8.2	Reactions	144
5.8.3	Microstructural differences in cataclasite.....	146
5.9	Summary	147
6	Fluid inclusions and isotope studies.....	148
6.1	Introduction	148
6.2	Methods	150
6.2.1	Sample preparation	150
6.2.2	Analytical techniques	152
6.2.2.1	Stable isotope quality control	153
6.2.2.2	Chips or powders.....	155
6.3	Fluid inclusion study	156
6.3.1	Introduction	156
6.3.2	Previous work	156
6.3.3	Samples	157
6.3.4	Petrography	157
6.3.5	Heating and cooling results.....	159
6.3.6	Interpretation.....	161
6.3.6.1	Trapping temperatures	161
6.3.6.2	Interpretation of results	162
6.3.7	Summary	163
6.4	Stable Isotope Data	163
6.4.1	Host Rock Results.....	163
6.4.1.1	Frey's results	163
6.4.1.2	Host rock - this study.....	164
6.4.2	Fault rock results.....	167
6.4.2.1	Oxygen Isotope Compositions	167
6.4.2.2	Co-existing minerals.....	168
6.4.2.2.1	Fractionation plots	168
6.4.2.3	Equilibrium fluid plots	169
6.4.2.3.1	Virgin Fault.....	170
6.4.2.3.2	Ciao Ciao Fault	172
6.4.2.4	Structural Variations	173
6.4.2.4.1	Virgin Fault - Variation in fault rock type.....	173
6.4.2.4.2	Virgin Fault - Variation along strike.....	176
6.4.2.4.3	Ciao Ciao Fault - Variation in fault rock type	178
6.4.2.4.4	Variation along strike of the CCF.....	179
6.4.2.5	Hydrogen isotope compositions.....	181
6.4.2.5.1	The Virgin Fault	181
6.4.2.5.2	The Ciao Ciao Fault.....	183
6.4.2.5.3	Fault and fluid variations.....	183
6.4.2.6	Water-rock ratio modelling	184
6.4.2.6.1	Water-rock ratios	188
6.4.2.6.2	Fluid source.....	190
6.4.3	Discussion.....	191

6.4.3.1	Fluid flow through faults	191
6.4.3.1.1	What stable isotopes tell us.....	191
6.4.4	Conclusions	194
7	Discussion.....	196
7.1	Fault growth and fluid flow.....	196
7.1.1	Evolution of fault populations.....	196
7.1.2	Hydraulic properties of fault zones/populations.....	198
7.1.3	Fault growth and fluid flow at Passo Moro	199
7.1.4	A model for fluid flow associated with faults that grow by linkage of pre-existing joints	201
7.2	Effects of core development on fault strength.....	203
7.2.1	Mechanical deformation processes	204
7.2.2	Chemical processes	205
7.2.3	Fault core evolution at Passo Moro.....	207
7.2.4	Implications for fault strength during evolution	209
7.2.4.1	Fault core evolution in the CCF and implications for the strength of mature faults.....	211
7.2.4.2	A model for evolution of fault strength with time and during evolution	212
8	Conclusions and further work	214
8.1	Further work	217
Appendices.....		220
Appendix 1		220
Appendix 2		221
Appendix 3		222
Appendix 4		227
List of references		231

List of Figures

Figure 1-1: Conceptual model of a fault zone	19
Figure 1-2: Schematic diagram indicating fluid related processes that occur during the earthquake cycle.	20
Figure 2-1: Location map of the field area.	27
Figure 2-3: Schematic transect through the W. Alps.....	29
Figure 2-4: Typical P-T for subduction related metamorphism in Western and Eastern Alps. Modified from Bousquet et al., (2008).	29
Figure 2-5: P-T path for UHP rock in Zermatt-Sass ophiolites, which are stratigraphically above Monte Rosa.	30
Figure 2-6: Axial traces of major postnappe folds and sites of auriferous gold veins in Monte Rosa region.	31
Figure 2-7: Principal brittle lineaments (black lines) within the Monte Rosa Nappe.	33
Figure 2-8: The geology of Monte Rosa.....	34
Figure 2-9: A) General P-T-t path for Monte Rosa, area. Inset shown in C. Modified from Ring (1995). B) Location and age of gold deposits in the W. Alps. Modified from Pettke et al (1999). Units as in Figure 2-1. C) P-T-t path for Monte Rosa. Modified from Ring (1995) and additional data from Pettke et al (1999) and references therein.	35
Figure 3-1a) 1:2500 topographic map of Passo Moro b) Geology map of area highlighted in (a).....	39
Figure 3-2: Graphic log across Passo Moro.	41
Figure 3-3: Pie chart of host rock mineralogy and a representative photo of the creamy granite gneiss.	43
Figure 3-4: Stripy granite gneiss with increased proportions of mica.	45
Figure 3-5: Variations observed within the granite gneiss.	46
Figure 3-6a: Equal area stereonet and b) 1% contour diagram - contour interval = 2% per 1% area) for all fractures recorded at Passo Moro. n= 234.	48
Figure 3-7: Effect of a fault zone on 040° joint density.	49
Figure 3-8a-c: Histograms showing joint density along the 220° transects at Passo Moro.....	50
Figure 3-9: Joint density along NNE-SSW transects.	51
Figure 3-11: Average joint density for the 010° joints within the different lithological units. Average values are plotted with the standard errors and standard deviation stated.	55
Figure 3-12: Comparison between the 010° joint density and the density of later formed cross-joints within each rock unit.	59
Figure 4-1: Three published fault architectural descriptions.....	62
Figure 4-2: a) Example of area mapped by 40x40cm square and b) digitised version. Digitization highlights fractures (dark grey), fracture fill (green fractures = chlorite fill), core rock (peach), yellow/orange = quartz, and areas of no exposure (brown).	63
Figure 4-3a-c: Equal area stereonets showing poles to fault planes for the VF, SF and CCF. Mean fault plane shown as great circle and 95% confidence ellipse shown for each data set.	64
Figure 4-4: Map of the Virgin Fault.	66
Figure 4-5: Principal slip surface within the VF.	68
Figure 4-6: Jogs along the PSS of the VF.....	68
Figure 4-7: Core material from section 5 of the VF.....	69

Figure 4-8: Slice cut through the core material from section 3 in the VF.	69
Figure 4-9: Fracture counting transects across the VF in sections 1 to 5.	72
Figure 4-10: Veining and bleaching along strike of the VF.	73
Figure 4-11: Pale green epidote masses in section 3 of the VF.	74
Figure 4-12: Aerial photo of the area encompassing the Spaghetti Fault.	76
Figure 4-13: Map of the Spaghetti Fault.	77
Figure 4-14: Equal area stereonet of poles to plane for all PSS measurements within the SF.	79
Figure 4-15: Characteristic features of the Spaghetti Fault.	80
Figure 4-16: Mud pool along the Spaghetti Fault.	81
Figure 4-17: Ciao Ciao Fault map.	83
Figure 4-18: Transition from host rock to foliated cataclasite within the CCF. ...	84
Figure 4-19: Clay-like material at the boundary between the host rock and breccia.	85
Figure 4-20: Fracture density changes away from the PSS in the CCF at locality 5.	85
Figure 4-21: Central fractured zone of the CCF.	86
Figure 4-22: Schematic representation of the VF.	88
Figure 4-23: Schematic representation of the fault architecture for faults composed of multiple strands.	90
Figure 4-24: Fault growth model for growth and linkage from pre-existing fractures by Martel (1990).	93
Figure 5-1: Cross polarised image of the host rock showing the characteristic features such as foliation and augen.	101
Figure 5-2: Microstructures within the host rock.	101
Figure 5-3: Grain size variation across strike of the Virgin Fault for quartz and feldspar. (feldspar = albite & K-feldspar).	104
Figure 5-4: Mineral proportions for the different fault components across strike of the Virgin Fault.	105
Figure 5-5: Variation in mineral proportions across strike of the Virgin Fault for the main rock forming minerals.	105
Figure 5-6: Outer damage zone rock from the VF.	106
Figure 5-7: Microstructures that occur within the outer damage zone of the VF	107
Figure 5-8: SEM-BSE images of the K-feldspar-albite relationship in the outer damage zone of the VF.	108
Figure 5-9: Co-existing quartz and epidote veins within the inner damage zone of the VF. (xpl, sample VF6)	109
Figure 5-10: SEM-CL image of a K-feldspar augen with granoblastic K-feldspar around the edge of an augen.	110
Figure 5-11: Microstructures within the inner damage zone of the VF	111
Figure 5-12: xpl image of the narrow core from the VF.	113
Figure 5-13: Microstructures within the narrow core from the VF.	113
Figure 5-14: Microstructures in the narrow core material of the VF.	114
Figure 5-15: Raman spectrum from an original K-feldspar crystal and a non- luminescent K-feldspar microvein that cut the original crystal.	114
Figure 5-16: xpl image of cataclasite from the thick core within the VF.	116
Figure 5-17: Characteristic features of the cataclasite within the VF.	116
Figure 5-18: xpl image of a large quartz fragment within the cataclasite in the VF.	117
Figure 5-19: Evolution model for the fault core within the VF.	127
Figure 5-20: Grain size variation across strike for the main matrix minerals in the CCF.	129

Figure 5-21: Across strike variations of the minerals within the Ciao Ciao Fault.	130
Figure 5-22: Across strike variations of the main minerals in the Ciao Ciao Fault.	130
Figure 5-23: Damage zone rock from the CCF.	132
Figure 5-24: xpl image of the boundary between the breccia and cataclasite within the CCF.	133
Figure 5-25: Microstructures within the breccia from the CCF.....	133
Figure 5-26: Amorphous material at the boundary between the breccia and cataclasite	134
Figure 5-27: xpl image of the foliated cataclasite within the CCF.	136
Figure 5-28: xpl images of the quartz microstructures in foliated cataclasite.	136
Figure 5-29: Schematic representation of the different components of the Ciao Ciao Fault.	142
Figure 5-30: Flow chart showing the various feedbacks that occur in response to deformation.	144
Figure 6-1: Polished block prepared for micro-drilling with associated images of drill sites.	151
Figure 6-2: Drilling of polished blocks.	151
Figure 6-3: $\delta^{18}\text{O}$ Vs Yield percentage for all samples. Samples with a yield less than 60% are considered unreliable. Line shows cut-off point and all samples to the left will be disregarded in subsequent analyses and interpretations.....	154
Figure 6-4: Yield v δD for samples from both fault zones. Line at $0.025\mu\text{mol}/\text{mg}$ indicates cut off point for sample analyses. Anything less than $0.025\mu\text{mol}/\text{mg}$ may give results not entirely related to the circulating fluid.	155
Figure 6-5: Typical size of fluid inclusions within the VF	159
Figure 6-6: Fluid inclusions within the CCF fault rock.	159
Figure 6-7: Frequency plot of homogenization temperatures at Passo Moro ...	161
Figure 6-8: $\delta^{18}\text{O}$ values of fault rock minerals from the Virgin and Ciao Ciao Faults.	168
Figure 6-9: $\delta^{18}\text{O}_{\text{Quartz}}$ Vs $\delta^{18}\text{O}_{\text{K-feldspar}}$ for the host gneisses (from Frey et al., 1976) and fault rock samples from the VF and CCF.....	169
Figure 6-10: Equilibrium fluid diagram for co-existing minerals from VF3 in section 3 of the VF.	170
Figure 6-11: Equilibrium fluid diagram for co-existing minerals from VF03 in section 3 of the VF.	172
Figure 6-12: Equilibrium fluid plot for co-existing minerals from CC4 in the CCF.	173
Figure 6-13: $\delta^{18}\text{O}_{\text{Quartz}}$ and calculated temperatures across strike of the VF based on $\delta^{18}\text{O}_{\text{Fluid}}$ being $+1\text{‰}$	174
Figure 6-14: Fluid equilibrium diagram for quartz samples across strike of Section 3.	174
Figure 6-15: Calculated water-rock ratio curve.	176
Figure 6-16: Fluid-equilibrium plot for chlorite and K-feldspar in the damage zone and fault core at section 4 of the VF.	178
Figure 6-17: Equilibrium fluid diagram for across strike variations of Quartz on the CCF.	179
Figure 6-18: Fluid equilibrium diagram comparing the fractionation pattern for quartz and K-feldspar between the foliated cataclasite and the fractured central block in the CCF.....	180
Figure 6-19: Hydrogen results for both fault zones at Passo Moro.....	181

Figure 6-20: $\delta^{18}\text{O}_{\text{Fluid}} / \delta\text{D}_{\text{Fluid}}$ plot plus modelled fluid evolution profiles for three possible meteoric derived fluids.	186
Figure 6-21: $\delta^{18}\text{O}_{\text{Fluid}} / \delta\text{D}_{\text{Fluid}}$ plot with modified data from the VF and CCF. ..	187
Figure 6-22: $\delta^{18}\text{O}_{\text{Fluid}} / \delta\text{D}_{\text{Fluid}}$ plot with modelled fluid evolution curves and associated water-rock ratios.	190
Figure 7-1: A conceptual model for fault population and fluid evolution.	203
Figure 7-2: The effect of fracturing on permeability within a fault zone.	205
Figure 7-3: Fluid activity diagram showing mineral stability of muscovite and feldspar.	207
Figure 7-4: Illustration of the steps that occur during core formation within the VF and CCF.	208
Figure 7-5: Mohr diagrams showing changes that occur as a result of fluid-rock reactions.	210
Figure 7-6: Fault core strength changes during fault growth and fault population evolution.	213

List of Tables

Table 3-1: Host rock samples collected and grid references for their localities.	42
Table 4-1: Properties of the VF and San Gabriel Fault.	87
Table 5-1: List of all fault rock samples analysed from the VF and their location within the fault zone.....	99
Table 5-2: List of all fault rock samples analysed from the CCF and their location within the fault zone.....	100
Table 6-1: Comparison of results between powdered and chipped samples. ...	155
Table 6-2: Samples and fluid inclusion description.	158
Table 6-3: Heating/freezing data from fluid inclusions which were large enough to collect data from.	160
Table 6-4: Stable isotope results from Frey et al (1976).	164
Table 6-5: Oxygen and hydrogen stable isotope data for all samples at Passo Moro.	167
Table 6-6: $\delta^{18}\text{O}$ values from outer damage zone and fault core in section 3 (S3) & 4 (S4) of the Virgin Fault.	177

List of Equations

Equation 1: Garnet + oxygen + water = chlorite & epidote + Quartz (Brown, 1969)	102
Equation 2: K-feldspar + Na ⁺ = Albite + K ⁺ (Wintsch et al., 1995)	102
Equation 3: Biotite + H ⁺ = Chlorite + K ⁺ + Mg ²⁺ + Quartz (Parry & Downey, 1982)	118
Equation 4: Biotite + Muscovite + Water = Chlorite + Quartz + KOH (McNamara, 1966)	118
Equation 5: Biotite + K-feldspar + Water = Chlorite + Quartz + KOH (McNamara, 1966)	118
Equation 6: Muscovite + Quartz = K-feldspar (Wintsch et al., 1995)	122
Equation 7: K-feldspar = Sericite (muscovite) + quartz (Wintsch et al., 1995)	138
Equation 8: Albite = Sericite (muscovite) + quartz (Wintsch et al., 1995)	138
Equation 9	149
Equation 10	184
Equation 11: K-feldspar = Sericite (muscovite) + quartz	206
Equation 12: Albite = Sericite (muscovite) + quartz	206
Equation 13	227

Acknowledgements

This PhD studentship and the stable isotope work were possible due to funding from the National Environmental Research Council, and so to NERC - thank you.

There is such a long list of people who have helped me in some shape or form through what feels like the most eventful four years of my life! Firstly, a huge thank you to my supervisors Tim Dempster, Zoe Shipton and Cristina Persano. You patiently put up with me and my special ways and for the ladies - you bought me chocolate/cake which always helps at those moments when nothing else can. Tim - I think your office was just too close at times and so you probably got hassled more than the others, so thank you for keeping my head out of the clouds and my feet on the right track. Also, Brian Bell - you may not have been a supervisor but you gave me so much good advice and travel tips over the many field trips and wee chats. I appreciated it so much and it was always good to have someone outside the project to chat to - cheers.

Throughout my PhD there has been so much preparation for trips, analytical work and general stuff! The team of technicians at the University of Glasgow have been phenomenal and have done so much for me. Kenny, Peter, Gary, Robert and John - to you all, a MASSIVE thank you - I really could not have done this without you all. For my time at SUERC I am so grateful to Adrian and Craig for taking me on and guiding me through the dark world of isotopes. Also the rest of the team Alison, Terry and Chris - thank you for all the help while I broke things and tried to blow the place up. On fieldtrips I also had some pretty amazing field assistants - Sara, you definitely became a great friend but more importantly you colour coded my structure data and that still makes me laugh every time I look at it. Ross - you had to get your wisdom teeth out while in Italy but when you made it up to the top it was worth it!

Now for those who kept me sane - Clare - what a star you have been. You have been there through it all, good and bad, happy or sad. You always had the right things to say and knew just when I needed a hug. I really couldn't have survived without you. Laura/Jatpa, a legend in your own right! You always make me laugh and are always free for a cheeky pint when we really should be working -

ah well we got there in the end. German Steph, you have fed me, give me tea, put up with my whining and been an amazing friend, especially through this last year. Kate and Davie - you gave me somewhere to live, answered my random questions and fed me wine! I really could not have finished this without you guys.

The office and greg fellows - Heidi, Joanne, Heiko, Rachael, Nick, Fiona, Rebecca, Ram, Yannick, Euan, Mahmood. You guys have been around for so much, provided copious amounts of general banter, X-factor banter, cakes, cocktails, and in general - lots of craic! Thanks for making my time so pleasurable. Also, thanks to all the faffers for their input throughout the years.

My friends and family at home - I still think you have no idea about what I have been doing over the past four years, but you have supported me through thick and thin and for that I am eternally grateful. Dad, you loved me - what more could I ask for. Andrew and David - brothers will be brothers! Christine, Leanna and Alison - you are my family and you have done more for me than you could ever imagine.

Declaration

The material presented in this thesis is the result of four years independent research carried out at the School of Geographical and Earth Sciences and the Scottish Universities Environmental Research Centre. The research was supervised by Dr Tim Dempster, Prof. Zoe Shipton and Dr Cristina Persano. This thesis represents my own research and any published or unpublished work by other authors has been given full acknowledgement in the text.

Susan Lawther

1 Introduction

1.1 Faults and fluid flow

Fault zones are 4-D systems: complex 3-D zones that evolve through time (Shipton and Cowie, 2001) in terms of their architecture, mineralogy, deformation mechanisms and fluid content. Fault rocks are some of the only evidence we have to aid in reconstructing tectonic evolution (Passchier and Trouw, 2005), and hence it is essential to have a detailed account of the fault rock types and cross-cutting relationships within a fault zone. We are unable to monitor fault evolution directly. By comparing faults within similar lithology and geological context but with different displacement magnitudes; we can assess how a fault evolves since we can assume that a small fault represents the early stages of growth of a larger fault (Micarelli et al., 2006).

Over the years many studies have been carried out to advance our knowledge on how fault zones deform and grow. Faults are usually described in terms of their properties such as rock type, architectural style, growth mechanism, and fault rock permeability; with numerous conceptual models produced to aid our understanding of how a fault evolves (Caine et al., 1996; Di Toro and Pennacchioni, 2005; Evans and Chester, 1995; Martel, 1990; Wibberley, 1999). Studies show that fault zones are complex structures controlled by numerous inter-related intrinsic and extrinsic properties (e.g. (Caine et al., 1996); Figure 1-1) that can directly impact fault evolution (Di Toro and Pennacchioni, 2005; Kirkpatrick and Shipton, 2009; Wintsch, 1975; Wintsch et al., 1995). More recently studies on fluid-rock interactions have come to prominence (Person et al., 2007). Fluid-rock interactions can alter the rates of chemical and mechanical processes which influence deformation mechanisms and rock rheology (Janecke and Evans, 1988). Consequently fluid-rock interactions are of great importance with respect to fault zone evolution and the seismic cycle.

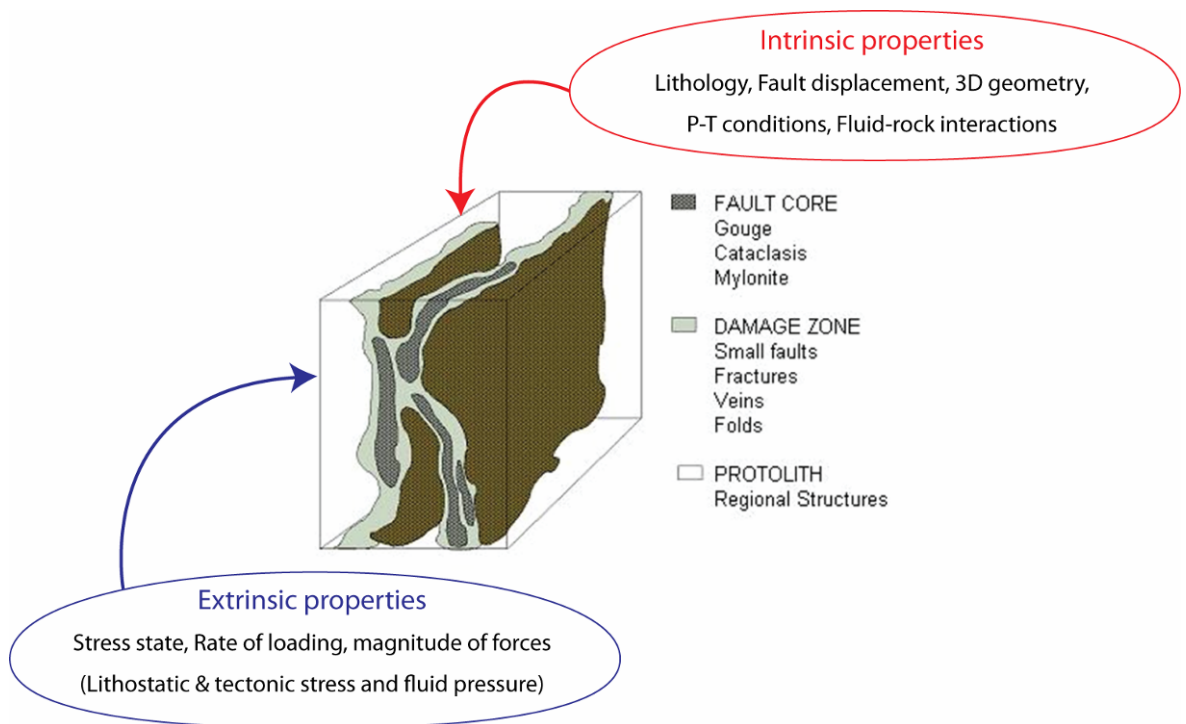


Figure 1-1: Conceptual model of a fault zone
Model shows the different fault components and the intrinsic and extrinsic controls. Image modified from Caine et al. (1996).

Within fault zones fluids can catalyse reactions, cause hydrolytic weakening, change the chemistry or temperature of the host rock, and be thermally pressurised. All of these factors have knock on effects to how a fault will subsequently deform and evolve.

The earthquake cycle can last anywhere from hundreds to thousands of years and is typically discussed in terms of the pre-, syn-, and post-earthquake processes (e.g. Figure 1-2). It is known that earthquakes can trigger fluid flow events because fracturing and dilation opens the rocks to episodic flow (e.g. (Bauer et al., 2000; Sibson et al., 1988)). The fluid-rock reactions that occur as a result of deformation can change with time (Wibberley, 1999; Wintsch et al., 1995). However, some of the most important reactions are those which affect the inter-seismic permeability and strength of a fault zone, thus controlling the recurrence time of earthquakes (Person et al., 2007). How reactions are coupled with deformation in fault zones is not well understood and so more detailed studies on fluid-rock geochemical interactions within a variety of fault zones are required.

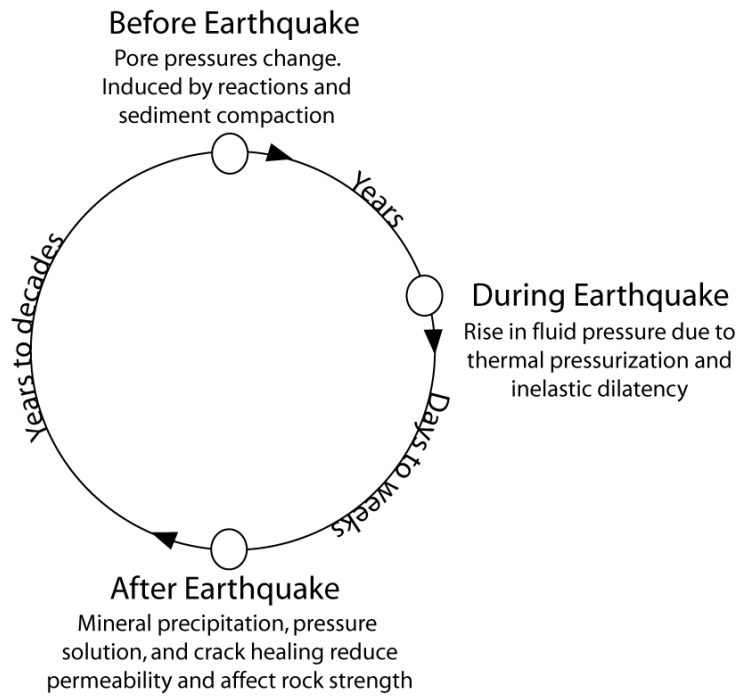


Figure 1-2: Schematic diagram indicating fluid related processes that occur during the earthquake cycle.

Modified from Pearson et al., (2007).

1.1.1 Background

Fault zones are typically described as being sites of increased fluid flow with respect to the surrounding rock (Bergbauer and Martel, 1999; Caine et al., 1996; Evans et al., 1997; Maréchal and Perrochet, 2001). Only a small proportion of faults act as the primary conduits for fluid flow through the crust (Evans, 2005); however hydrothermal alteration is common within most fault zones regardless of rock type and evolutionary stage (Brogi, 2008; Chester et al., 1993; Di Toro and Pennacchioni, 2005; Faulkner et al., 2008; J.D.Kirkpatrick, 2008; Kirkpatrick, 2008; O'Hara, 2007).

Fluid flow is primarily controlled by the permeability of the fault rocks which is variable in space and depends on the stage of faulting with respect to the earthquake cycle (Caine et al., 1996; Evans et al., 1997); Figure 1-2). The onset of a seismic rupture can change the permeability of a fault zone (Rojstaczer and Wolf, 1992) resetting its hydraulic properties. This means that any post-seismic flow will be controlled by the new permeability structure (Pearson et al., 2007). After an earthquake the presence of fluids in the fault zone controls what reactions occur and consequently the rheology of the fault zone.

A fluid-rock system can be classified as either fluid- or rock-dominated depending on the volume of fluids present in the rock. This changes the relative proportions of elements available for reaction and consequently can affect which minerals will precipitate and the reaction history (Wintsch et al., 1995). The volume of fluid that passes through a fault zone is partly controlled by the porosity and permeability of the rock and whether the system is open or closed to fluids. Open systems allow fluids to be flushed through the rock enabling continual refreshment of the fluid. This may prevent supersaturation of the fluid, enabling reactions to continue. For a closed system the reverse is true; the supersaturation of the fluids can result in mineral precipitation, sealing of the fault and cessation of the reactions.

Fluids are the primary vehicle for transporting dissolved chemical components. For reactions to occur within a fault zone requires chemical disequilibrium between the mineral assemblage and fluid. The fluid-rock reactions are strongly affected by the local conditions with the primary controls being temperature, pressure, and the physical and/or chemical conditions of the host rock and the fluids (Bucher and Frey, 2002). Elevated temperatures tend to increase the rate of reactions, whereas decreased temperatures result in slow reactions, which typically do not go to completion. Reaction rates will also be influenced by changes in grain size which affect the surface area available for fluid-rock reactions. Deformation decreases the grain size, which, in turn, increases the surface area available, thus promoting reaction (Fitz Gerald and Stünitz, 1993; Wibberley, 1999). Depending on the nature of the reactions; porosity can be created or destroyed, permeability increased or decreased, fault rocks weakened or strengthened; all these characteristics, in turn, affect seismic processes (Janssen et al., 1998; Kirkpatrick and Shipton, 2009; Mittempergher et al., 2009; Wibberley and Shimamoto, 2005; Wintsch et al., 1995). Ultimately fluid-rock reactions influence fault rock strength, which is one of the main controls on strain localization (Boulton et al., 2009; Janecke and Evans, 1988; Lockner et al., 2011). Hence, fluid-rock reactions will also influence how a fault will evolve in terms of its architecture (Di Toro and Pennacchioni, 2005; Faulkner et al., 2008).

1.1.2 What are the gaps in our knowledge

Relatively little is known about the hydraulic properties of fault zones within crystalline basement rocks. The majority of information comes from the shallow crust (e.g. The SAFOD Project¹) and indirect methods such as petrological studies (O'Hara, 2007; Wibberley, 1999; Wintsch et al., 1995), stable isotope analyses (Morrison and Anderson, 1998; Mulch et al., 2004), and studies of ore deposits (Sibson et al., 1988). On the whole, our understanding of fluid-rock geochemical reactions in seismogenic faults is in its infancy (Person M et al., 2007). The seismogenic zone is where earthquakes nucleate and is thought to extend from the earth's surface down to ~15km or the transition from frictional to quasi-plastic behaviour in quartzo-feldspathic crust (Sibson, 1982, 1984). Within the seismogenic zone larger earthquakes (Magnitude > 5.5) tend to nucleate towards the base of the seismogenic zone (Sibson, 1982). Thus, information about what processes occur at the base of the seismogenic zone are critical to understanding the nucleation of large earthquakes.

With respect to fluid-rock interactions at seismogenic depths there are four main areas of interest:

- 1) What are the sources of fluids and how do fluids migrate?
- 2) What are the fluid volumes and fluxes?
- 3) What is the nature of chemical and mechanical interactions between the fluids and the host rocks and what reactions have the most influence on fault strength?
- 4) How fluid flow processes change before, during and after earthquakes?

Such information would be of use for studies in the mineralization and mining industry, for the storage of nuclear waste in crystalline rock, and for earthquake rupture prediction.

¹ SAFOD project is the San Andreas Fault Observatory at Depth where they have drilled into the active fault zone at approximately 3km depth.

1.1.3 How can we study seismogenic faults

Our ability to examine faults at seismogenic depths is limited to seismic investigations. Seismic surveys are currently unable to provide detailed information on fault structure, fault rock type or fluid-rock interactions and thus exhumed faults represent the best means of carrying out research on seismogenic faults. Seismogenic fault zones will typically behave in a cyclic manner whereby there will be multiple deformation and fluid-flow events during the lifetime of a fault zone (Goddard and Evans, 1995; Logan and Decker, 1994). If a fault has been exhumed from depth and was active during exhumation, this means that much of the evidence of fluid-rock interactions at depth may have been destroyed. However it is possible that the microstructure of the rock and its mineral assemblages still record the fluid interaction that occurred at depth. Detailed microstructural analyses can establish a chronology of the deformation and of the fluid-rock interactions that occurred and therefore is a unique tool to unravel the reactions occurring at seismogenic depths.

Stable isotopes are an extremely powerful tool, which can be used to fingerprint the source of fluid, evaluate the equilibrium character of a mineral assemblage and model the evolution of fluid-rock ratios. Advances in technology now enable *insitu* sampling of fault zone minerals with only 1mg required to carry out oxygen isotopic analyses. By determining the isotopic composition of mineral assemblages formed during fluid-rock interactions at depth, the phases of deformation can be examined and related to the fault and fluid evolution.

1.1.4 Thesis aims and objectives

The main aim of this study is to understand the nature of fluid-rock interaction at seismogenic depths in order to provide insight on the effects of fluids on faults.

My objectives are:

1. Provide a detailed description of a previously unmapped set of fault zones that have been exhumed from the seismogenic zone.

2. Carry out detailed micro-structural analyses of the fault zones to decipher their microstructural evolution in terms of deformation and fluid flow.
3. Carry out fluid inclusion and stable isotope analysis (oxygen and hydrogen) of the host and fault rocks and relate these analyses to the microstructural and fluid flow evolution.

The results of this study will be used to attempt to answer the following questions:

- A. What temperature were the fluids in the fault zone?
- B. What is the sources and volume of fluids in the fault zones?
- C. What reactions were occurring and does fault architecture and fault size affect the reactions?
- D. How do the products of fluid-rock interactions (mineral dissolution/precipitation) affect fault zone evolution?

The study area for this research project is Monte Rosa, N.Italy within the western Italian Alps. The main reason Monte Rosa was chosen is due to there being approximately 100% rock exposure in the field area and the field is easily accessible by cable car and/or foot. Good rock exposure enables detailed mapping of the geology and of the along and across strike architecture of fault zones of different sizes to be carried out. Results can then be used to assess the relationship between architectural changes, fluid-rock interactions, and variations in the host rock. Also, the ability to map faults of different sizes within one area means that conclusions can be drawn on how small faults evolve into larger one and whether the fluid-rock interactions that occurred were alike and were with the same fluids.

1.1.5 Thesis structure

This study focuses on three fault zones in granite gneiss that have been exhumed from seismogenic depths. Within this thesis chapter 2 will describe the

geological setting and history of the field area; chapter 3 will describe the geology of the field area. Chapter 4 will describe the macro-scale architecture of the three fault zones (The Virgin, Spaghetti and Ciao Ciao Faults) and chapter 5 the microstructural characteristics of the faults. Chapter 6 discusses the fluid inclusions and stable isotopic results and the evolution of the fluids within the fault. Chapter 7 discusses fluid-rock interactions at seismogenic depths. A new model to help understand the effects of fluid-rock interactions on fault zone evolution will be proposed and tested on published fault zone descriptions. Chapter 8 summarises the conclusions and suggested further work that could be undertaken.

2 Geological Setting/history

2.1 Introduction

The Alps have been studied for over two centuries; they are the mountain range where the nappe theory was conceived and they have often been defined ‘an outstanding natural laboratory’ to study the formation and evolution of mountain belts (Bousquet et al., 2008)(see (Dal-Piaz, 2001; Trumpy, 2001) for historical reviews). Monte Rosa or ‘The Queen of the Alps’ (King, 1858) is part of a fossilised subduction zone, which contains some of the worlds most rapidly exhumed high pressure to ultra-high pressure rocks (Lapen et al., 2007).

The field area chosen for this study is Passo Moro within the Monte Rosa nappe of the Western Alps, Northern Italy (Figure 2-1a-b). The study area (Passo Moro) was primarily chosen because of excellent exposure due to recent de-glaciation, which enables detailed observations along and across strike of fault zones, with no soil or vegetation cover. Passo Moro is 3 km north of Macugnaga (Figure 2-1c), a small village within the Anzasca Valley. Passo Moro is situated at the saddle between the Joderhorn and Monte Moro and is at an elevation of 2870 m. The area is accessible by cable car or on foot following the Monte Rosa Trail.

During the Alpine Orogeny the Monte Rosa nappe was subducted to >30-40 km depth whereby the rocks experienced high-pressure eclogite facies metamorphism and this event has been dated at ~42 Ma (Lapen et al, 2007). Subsequently the Monte Rosa nappe was rapidly exhumed and by approximately 33 Ma it is thought to have been at a depth of ~11-15 km (Berger and Bousquet, 2008). Since then the area has been exhumed and during exhumation all deformation is thought to have been concentrated within fault zones (Hurford et al., 1991; Wagner et al., 1977). After subduction and exhumation the Monte Rosa nappe has experienced no subsequent regional metamorphic events; thus any hydrothermal alteration within the fault zones will be a consequence of fluid flow and fluid-rock reactions during faulting and exhumation. This makes the Western Alps an ideal location to study the effects of fluid flow and fluid-rock reactions on fault evolution and the seismic cycle.

The purpose of this chapter is to provide the geological context for the structural analyses. An overview of the formation and exhumation of the Alpine mountain belt and in particular, the W. Alps is therefore given. This will be followed by an overview of previous studies within the Monte Rosa area and a description of the lithologies in the Passo Moro area.

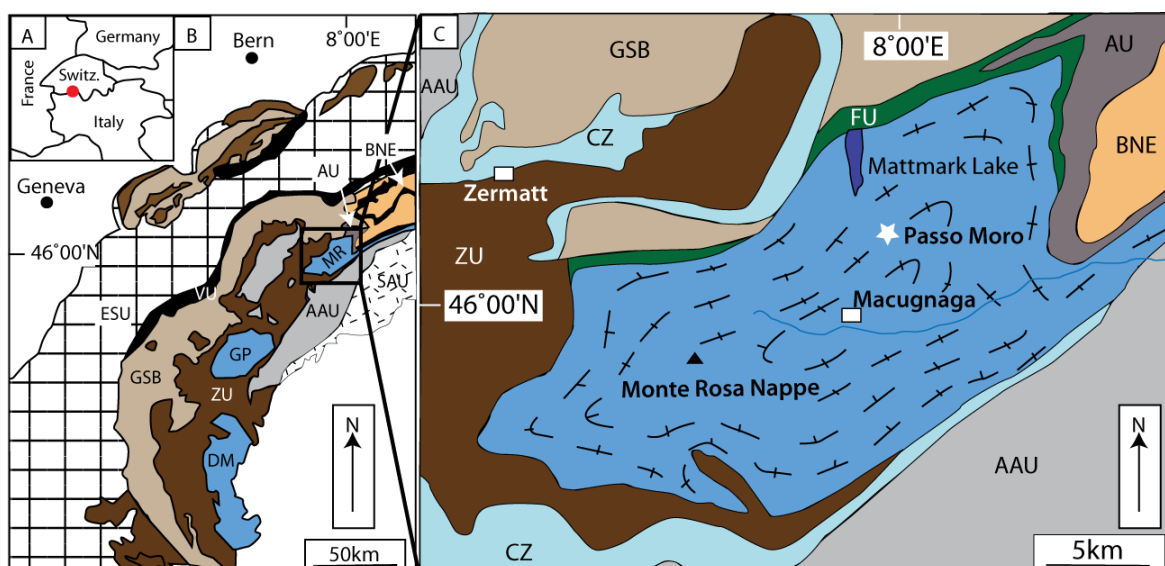


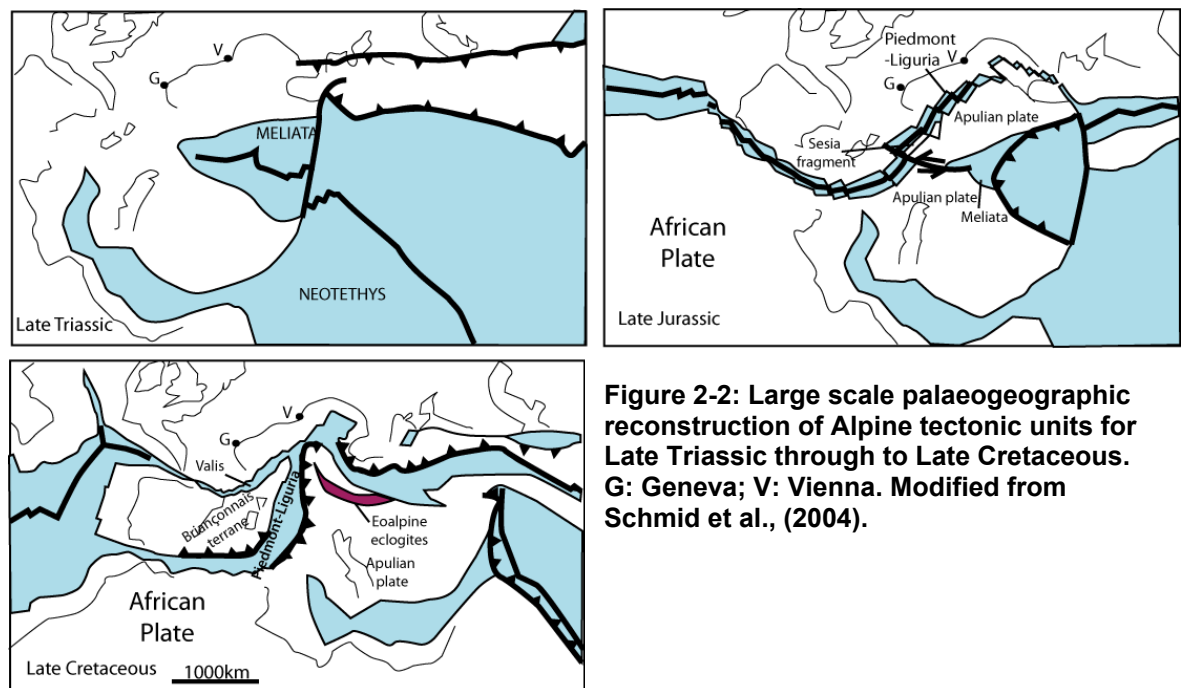
Figure 2-1: Location map of the field area.

A) Location of field area within central Europe. B) Simplified geological map of Western Alps and Monte Rosa nappe (C). Main tectonic units are: European units: European shelf (ESU), Basement nappes from European continental margin (BNE). Valais basin units: Valais unit (VU), Antrona unit (AU). Ligurian basin units: Combin Unit (CZ), Zermatt unit (ZU). Briançonnais units: Grand St. Bernard (GSB), Furgg Unit (FU), Internal crystalline massifs - Monte Rosa (MR), Gran Paradiso (GP), Dora Maria (DM). Adriatic continental margin units: Austro-alpine units (AAU), Souther Alps unit (SAU). Strike and dip lines on Monte Rosa indicate the changing orientation of the foliation within the nappe. Field area is marked by white star in (C). Modified after Ring & Merle, (1992) and Le Bayon et al., (2006).

2.2 The Alps

The Alpine mountain belt extends from Nice to Vienna stretching across SE France, N. Italy, Switzerland, Austria, N. Slovenia and parts of S. Germany; with the molasse basin of S. Germany and the Po plain in Italy being the northern and southern extents of the mountain belt respectively (Maxelon and Mancktelow, 2005). The main trend of the central and eastern Alps is WSW - ENE. However, at the boundary between the central and western Alps the mountains form an arc before merging into the NNW - SSE striking Apennines of the Italian peninsula (Maxelon and Mancktelow, 2005).

The Alps formed as a result of continental collision between Africa and Eurasia. The area in between the plates was occupied by the Tethys Ocean which was subducted during collision, thus the Alpine chain is composed of slices of sedimentary and continental crust scraped off both margins, as well as fragments of oceanic crust (Coward and Dietrich, 1989). The African plate started to rotate and move towards Europe from the Triassic in response to the break up of Pangea and the opening of the Atlantic Ocean (Figure 2-2). It is thought that several small oceans in the Tethys/Mediterranean region were formed and subducted during this period (Schmid et al., 2004). However, the southwest dipping subduction zone adjacent to the African (Austro-alpine) plate (Figure 2-2) is thought to be the most mature subduction zone (Coward and Dietrich, 1989) and was the site where the majority of oceanic crust was destroyed.



Oceanic subduction was followed by continental collision, which resulted in the formation of several continental and oceanic nappes (Figure 2-3), marked by blueschist to eclogite facies metamorphism during the Cretaceous and Eocene (Dal-Piaz et al., 2003). The occurrence of high pressure-low temperature metamorphism in ophiolites, which is related to subduction while high temperature-medium pressure metamorphism is associated with continental collision (Berger and Bousquet, 2008). The Western Alps lacks the high temperature overprint (high pressure only) related to collision i.e. there is a

single metamorphic peak (Figure 2-4). However, in the Central and Eastern Alps significant collision of continents did occur and so these areas do display the expected P-T signature of an evolved subduction zone which culminated in continental collision i.e. two metamorphic events (Figure 2-4).

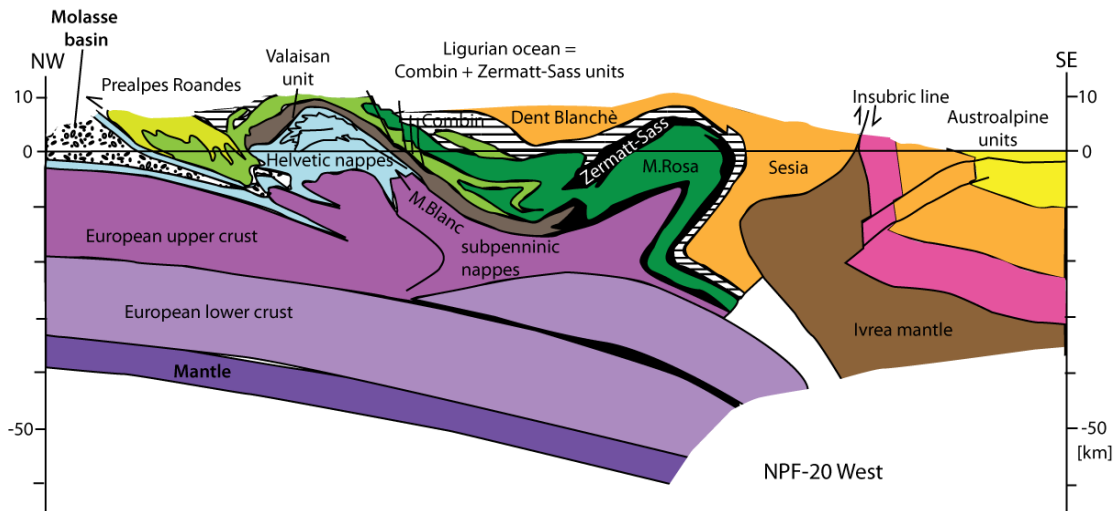


Figure 2-3: Schematic transect through the W. Alps. Transect modified from Schmid et al., (2004) and Schmid & Kissling (2000). Transects are based on seismic information (seismic profile NPF-20 west) from Transalps Working Group (2003).

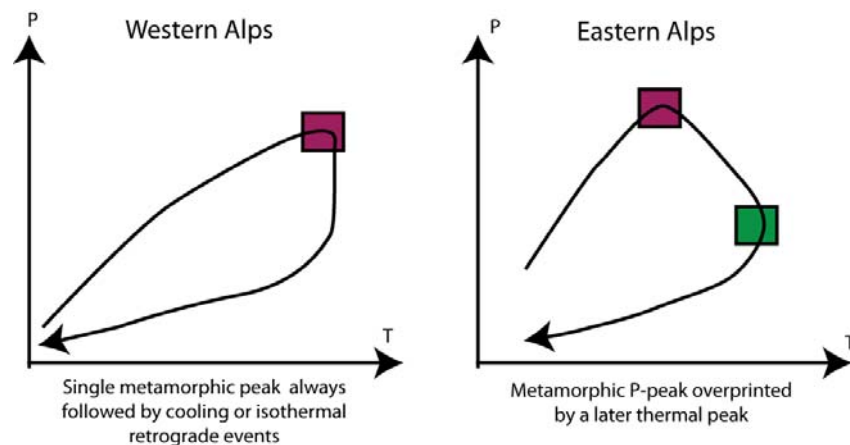


Figure 2-4: Typical P-T for subduction related metamorphism in Western and Eastern Alps. Modified from Bousquet et al., (2008).

2.2.1 Western Alps

The Western Alps are separated from the Central and Eastern Alps by the Simplon-Centovalli line (Beauregard, 1952; Steck, 2008). In general the Western Alps have a geologically simple structure whereby the internal high pressure metamorphic zone was thrust over an external low grade greenschist facies domain (Bousquet et al., 2008). In the Western Alps only a small accretionary

wedge was formed (Ceriani and Schmid, 2004) and this is partly the reason why the subduction zone did not develop into the high temperature regime, as the thermal overprint is primarily related to the amount of crust involved in subduction and collision processes (Bousquet et al., 1997; Goffé et al., 2003). Such a metamorphic signature as seen in the W. Alps is characteristic of subduction followed by exhumation along a cool decompression path (Bousquet et al., 2008). The Western Alps therefore represents a frozen subduction zone which was subsequently exhumed (Bousquet et al., 2008). The main Alpine event peaked in this region at 38 Ma (Amato et al., 1999; Bocquet et al., 1974) and grades from greenschist facies in the SW to amphibolite facies in the NE (Dal-Piaz et al., 1972). P-T paths have been calculated for different lithologies and localities throughout the W. Alps and regardless of location all confirm that subduction related metamorphism was followed by rapid decompression (Amato et al., 1999) (Figure 2-5).

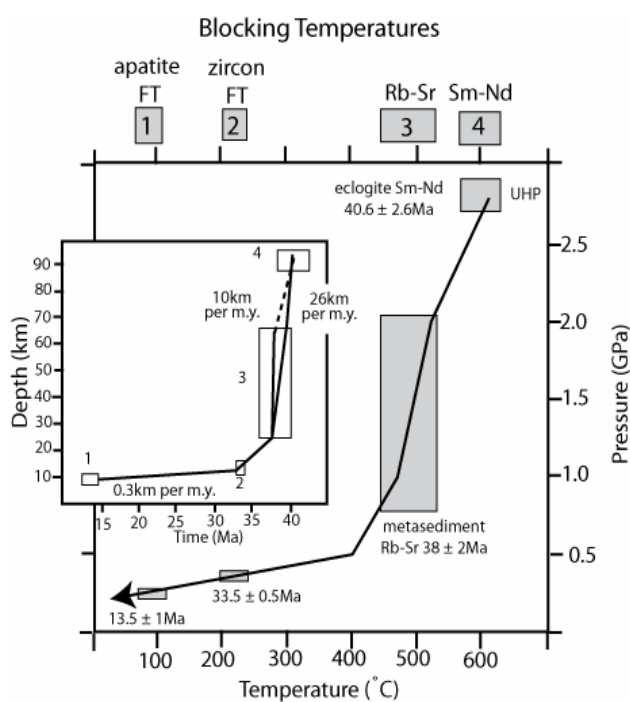


Figure 2-5: P-T path for UHP rock in Zermatt-Saas ophiolites, which are stratigraphically above Monte Rosa. Rectangles indicate geochronological constraints using data from 1) apatite fission track (FT) ages, 2) zircon FT ages, 3) Rb-Sr isochron ages (white mica) and U-Pb sphene ages, 4) Sm-Nd isochron ages (garnet). Grey bars above the diagram show average closure temperatures for the different isotope systems. Inset shows corresponding depth-time curve. Boxes denote uncertainty in depth and age. The preferred model has initial exhumation rate of 26km/m.y., based on inference that all phengite analysed in (3) recrystallised under greenschist-facies conditions. However, if phengite only partially records the HP event, an exhumation rate of 10km/m.y. is calculated. Modified from Amato et al (1999) and see Amato et al (1999) for explanation and discussion of exhumation rates.

Decompression and exhumation processes in the W. Alps were associated with regional scale faulting and folding. Four different ductile deformation phases have been recognised and are: D1 - nappe formation; D2 - early isoclinal folding; D3 - early back folding; and D4 - late backfolding (Figure 2-6) (Milnes et al., 1981). It is thought that formation of the Vanzone antiform (late backfolding)

was closely associated with the onset of brittle deformation and the formation of gold bearing veins along the axial plane of the antiform (Curti, 1987; Lattanzi et al., 1989) (Figure 2-6). Precipitation of the gold veins has been dated at 31 Ma in the southwest of Monte Rosa and at 10 Ma in the NW (gold lodes dated by $^{40}\text{Ar}/^{39}\text{Ar}$ analyses of mica (Pettke et al., 1999) (Pettke et al., 2000)). The variable ages have been interpreted as the gold veins forming in retrograde conditions at shallow depths, while rocks at deeper levels were experiencing prograde metamorphism (Pettke et al., 2000). Apatite Fission Track (AFT) analyses record when a rock cooled below 120° and differences in AFT data throughout the Western Alps reveal discontinuous and differential uplift (Hurford et al., 1991). Hence variation in ages of gold formation is likely due to differential uplift between the areas. Differences in AFT ages typically occur across the major fault zones in the area and so these faults subdivide Monte Rosa into individual uplifting blocks (Hurford et al., 1991).

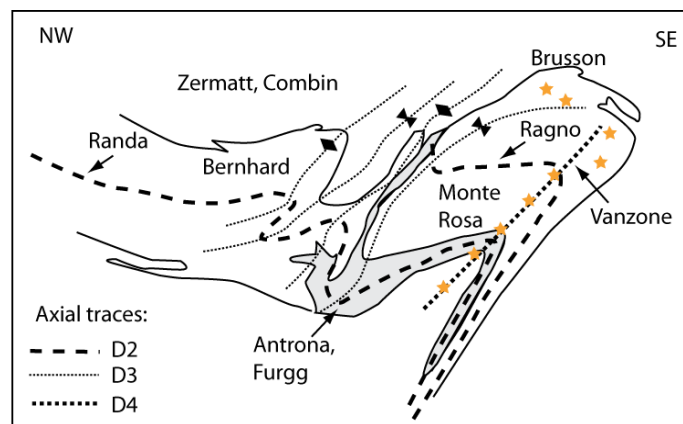


Figure 2-6: Axial traces of major postnappe folds and sites of auriferous gold veins in Monte Rosa region.

Gold veins = gold stars; modified from Froitzheim (2001) and Pettke et al., (2000).

2.3 Previous studies of Monte Rosa nappe

The Monte Rosa nappe has been studied for over two centuries with some of the original investigations carried out by De Saussure from 1779-96. The main pioneer in understanding the geology of Monte Rosa was Peter Bearth. He started his work there in 1934 and in 1952 produced a memoir 'The geology and petrography of Monte Rosa', which represents an important advance in our knowledge of Alpine and pre-Alpine history of Monte Rosa (Dal-Piaz, 2001). Since then numerous studies have been carried out on the Monte Rosa nappe including

petrographic, geochronological, thermochronological, and isotopic studies. The majority of studies have focused on constraining the timing and modes of nappe stacking and the tectono-thermal evolution (e.g. (Bousquet et al., 2008; Chopin and Monié, 1984; Dal-Piaz, 2001; Frey et al., 1976; Froitzheim, 2001) but more recently there has been a greater interest in the late collisional tectonics (Bistacchi et al., 2000; Mancktelow, 1992; Ring and Merle, 1992). Studies of faulting are typically restricted to the main boundary faults (e.g. Simplon and Insubric line) or the Aosta-Ranzola fault system and only limited amounts of work have been carried out on the faults with the individual tectonic blocks; however these faults are critical in unravelling the post-nappe evolution of the NW Alps (Bistacchi et al., 2001).

The main lineaments within the W.Alps have been mapped via remote sensing (Bistacchi et al., 2001; Bistacchi et al., 2000) and indicate two dominant trends: NE-SW and NW-SE (Figure 2-7). 75% of the lineaments are high angle faults and fractures which have been active from the Miocene to present, the remaining 25% of lineaments have not been confirmed in the field (Bistacchi et al., 2000). Apart from work by Bistacchi et al. (2001), the only detailed studies on brittle deformation within the Monte Rosa nappe are associated with the Monte Rosa Gold District and related structures (Pettke and Diamond, 1997; Pettke et al., 1999; Yardley et al., 1993).

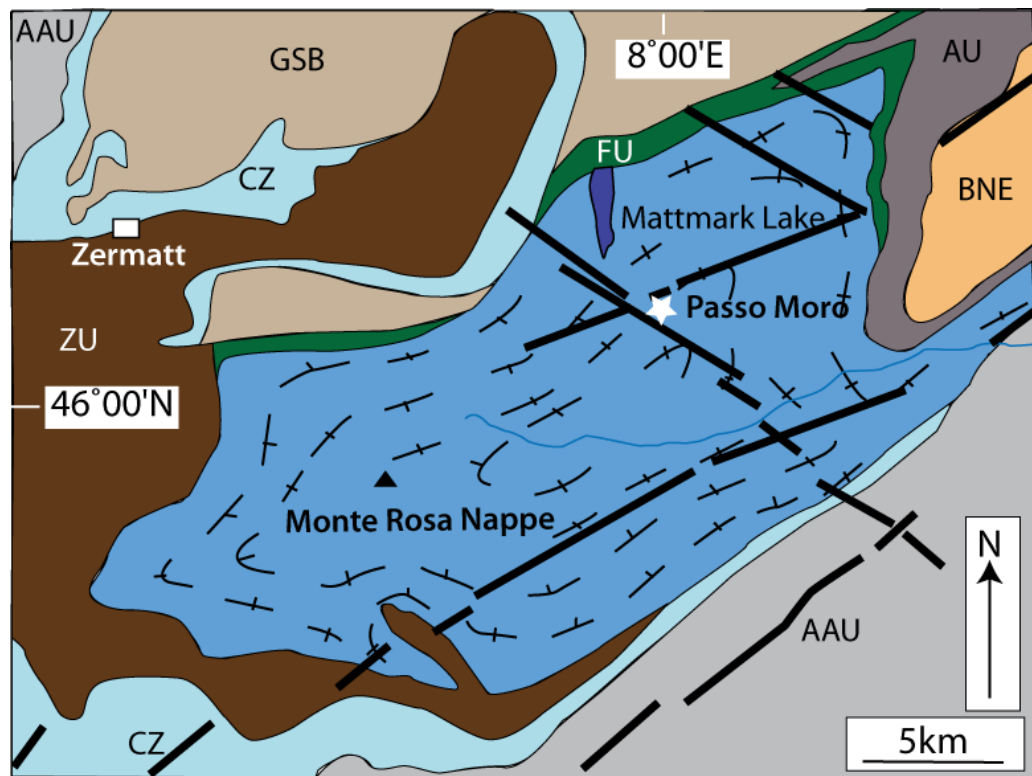


Figure 2-7: Principal brittle lineaments (black lines) within the Monte Rosa Nappe. The Ciao Ciao Fault which is analysed in this study is represented by the NW-SE lineament directly below the white star. Modified from Ring & Merle (1992), Bistacchi et al., (2000) and Le Bayon et al., (2006). Units as in Figure 2-1.

2.3.1 Lithology of Monte Rosa and Passo Moro

The Monte Rosa granite can be sub-divided into two granites: G1 & G2, which were intruded at 310 Ma and 260 Ma respectively (Frey et al., 1976). Subsequent gneissification of G1 is thought to have been contemporaneous with or soon after intrusion of G2 (Frey et al., 1976). The distribution of the granites at Monte Rosa were mapped by Bearth (1952) (Figure 2-8) and were split into three parts: Monte Rosa granite gneiss (G1); Stelli zone (strongly tectonised granite); and the Macugnaga augengneiss (G2).

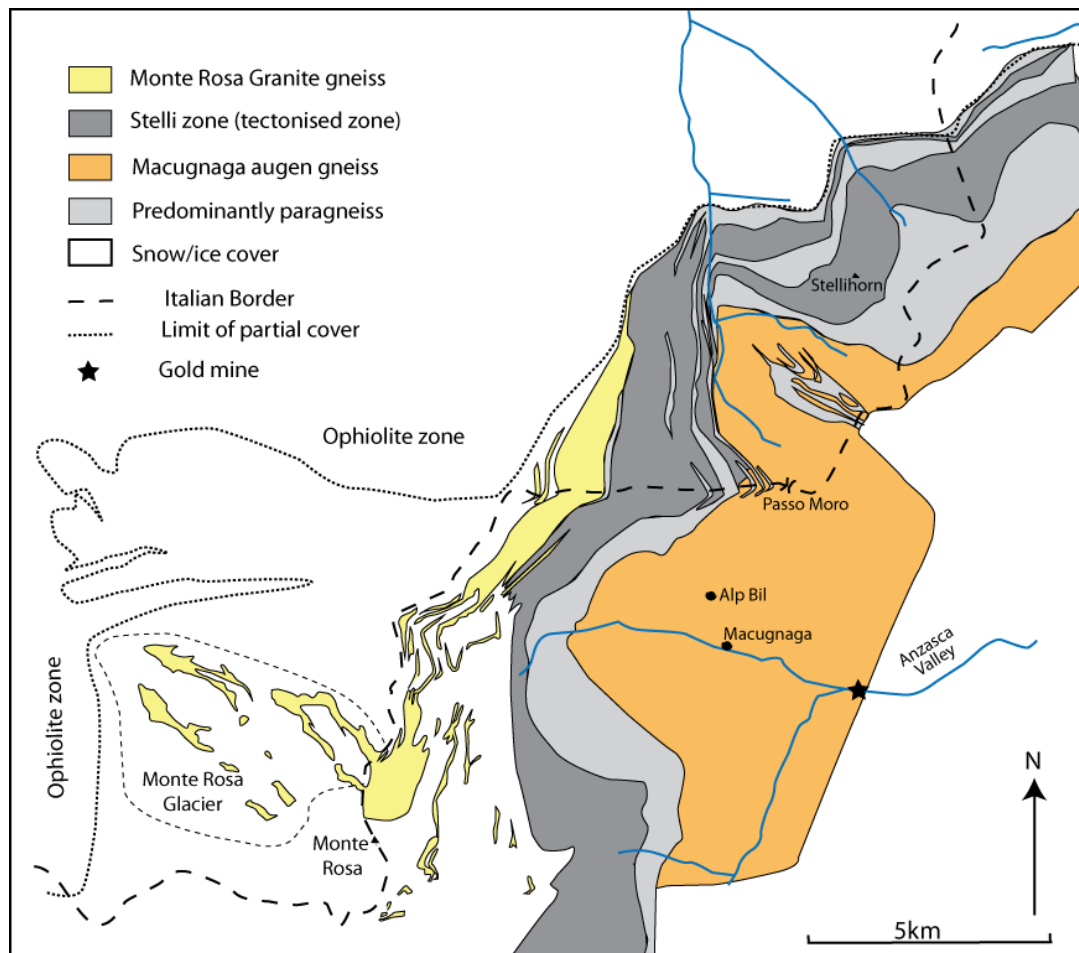


Figure 2-8: The geology of Monte Rosa.
 Modified from Bearth (1952).

The Macugnaga augengneiss occurs on both sides of the Anzasca Valley with Macugnaga valley being the central point of the granite mass (Figure 2-8). Although at first Bearth described the Macugnaga augengneiss as very homogenous, he soon realised it was neither genetically or compositionally homogenous. The dominant rock type is a coarse, two mica gneiss with up to centimetre K-feldspar augen, but there are also numerous bands parallel to the gneissic foliation that significantly differ in grain size, texture and composition. In some areas there are transitions into garnet-muscovite-biotite gneiss and these are often adjacent to a laminated augengneiss. The Monte Rosa granite gneiss is also cut by syn-genetic fractures that are filled with a K-feldspar-mica-biotite pegmatite which probably precipitated during the fracturing event (Bearth.P., 1952).

Several studies on the Monte Rosa granite provide age determinations for the granite emplacement, the Alpine deformation, metamorphism and exhumation (e.g. Frey et al., 1976). As with the rest of the W. Alps the results indicate an

eclogite facies high pressure event followed by decompression and a lower pressure greenschist facies event (Figure 2-9a). The earliest phase of faulting was associated with hydrothermal activity and was synchronous with formation of the Monte Rosa Gold lodes (Curti, 1987; Lattanzi et al., 1989). The precipitation of these gold lodes started in the south of the Monte Rosa nappe at approximately 33 Ma and migrated northwards with the Pestarena gold in the Anzasca Valley being dated at 29 Ma (Pettke et al., 1999) (Figure 2-9b). The gold veins are believed to have formed at 240-350 °C and ~5-12 km depth (Pettke et al., 1999). By combining the results from the gold veins with zircon and apatite fission track ages, a P-T-t path can be constrained for the low temperature evolution of the Passo Moro area (Figure 2-9c). Given that the gold veins formed in the Anzasca Valley during the earliest phase of faulting, this data pins the maximum age of faulting at Passo Moro to 29 Ma and at 5-12km depth.

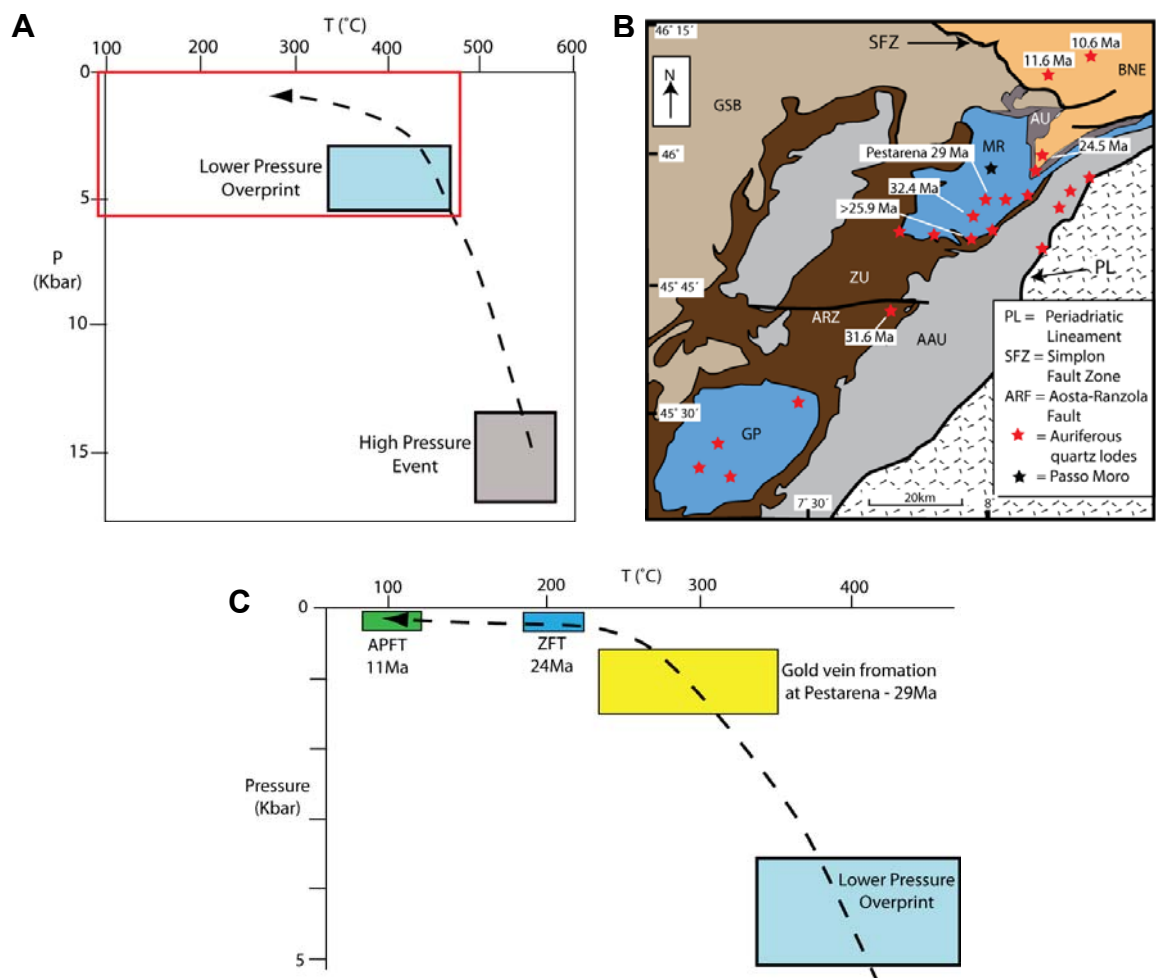


Figure 2-9: A) General P-T-t path for Monte Rosa, area. Inset shown in C. Modified from Ring (1995). B) Location and age of gold deposits in the W. Alps. Modified from Pettke et al (1999). Units as in Figure 2-1. C) P-T-t path for Monte Rosa. Modified from Ring (1995) and additional data from Pettke et al (1999) and references therein.

2.3.2 Why study at *Passo Moro*?

This chapter has outlined the geology and the history of the Monte Rosa nappe and has shown that the metamorphic evolution of Monte Rosa is well constrained. Brittle-ductile deformation in Monte Rosa nappe begun ~33 Ma (Lattanzi et al., 1989; Pettke et al., 2000) and ZFT data show that at this time the temperature was ~225°C and the rocks were at depths of ~11-15 km (Hurford et al., 1992). The seismogenic zone is considered to extend down to depths of ~15 km depth (Sibson, 1977) and therefore faults at *Passo Moro* could have been active from the base of the seismogenic zone. AFT shows that Monte Rosa was at 3-6km 10 Ma ago (Wagner et al., 1977; Hurford et al., 1991) and therefore between 33-10 Ma the rocks (and faults) of *Passo Moro* would have passed through the seismogenic zone.

The rocks at *Passo Moro* have not experienced any regional metamorphic events since exhumation and so any fluid-rock alteration within the fault zones will be related purely to the conditions experienced during exhumation and faulting. This makes *Passo Moro* an ideal place to study fluid-rock interactions in fault zones exhumed from seismogenic depths as we can be sure that the fluids recorded were related to one semi-continuous regional event.

At *Passo Moro* three newly identified faults have been selected to study the effects of fluid-rock interactions on fault evolution and the three chosen faults are: The Virgin Fault, The Spaghetti Fault and The Ciao Ciao Fault. The fault zones cut the same host rock but they vary in terms of fault length, accumulated displacement and fault architecture. Throughout *Passo Moro* there are a variety of different structures of which the most common are joints and faults. There are three main orientations of joints and one dominant set of faults. Host rock variability and pre-existing structures can influence fault development (Brogi, 2011; Gross et al., 1997; Lee and Kim, 2005; Wilkins and Gross, 2002), and hence it is essential to have a good understanding of the host rock prior to analysis and comparison of the fault architectures and histories.

3 Field mapping

3.1 Introduction

Field mapping provides a detailed record of the rock types, the pre-existing structures and their spatial distribution. Exhumed fault zones can be mapped along and across strike to gain information about fault architecture and the relationship between different fault rocks. The influence of host rock variability and pre-existing structures on faulting is well known (Gross et al., 1997; Wilkins & Gross, 2002; Lee & Kim, 2005; Brogi, 2011) and highlights the need for detailed mapping of the host lithology and structures in conjunction with fault mapping. Bearth (1952) states that the Macugnaga augen-gneiss is not compositionally uniform, so consequently a good understanding of the variation within the host rock is required prior to interpretation of the fault architecture.

Although Bearth (1952) did carry out a geological survey on the host rock of the Monte Rosa area, the majority of later studies have concentrated on the effects of the Alpine Orogeny on the Monte Rosa nappe and the P-T conditions which it experienced (Ellis et al., 1989; Frey et al., 1976; Froitzheim, 2001; Keller et al., 2004; Lapen et al., 2007; Ring and Merle, 1992). The brittle lineaments in the W. Alps have been mapped by Bistacchi et al (2000) and several were recognised within the Monte Rosa massif (including The Ciao Ciao Fault - this study) (Fig 2-7). Mapping was done by remote sensing but only structures greater than 400m in length could be recorded (Bistacchi et al., 2000). Therefore smaller scale structures or detailed information on fault architecture were not recorded yet both are critical in understanding the structural evolution of an area.

This chapter will provide a detailed description of the geology of Passo Moro, the structures present within the area and a chronological timeline for their formation. Field data will be used to establish the effects of host rock variability and pre-existing structures on the formation of later structures.

3.2 Mapping of Passo Moro - Techniques

Mapping of Passo Moro was carried out on a variety of scales. The main aims of the mapping were to: construct a base map of the area; map the lithologies and the lithological boundaries; identify any brittle structures which cross-cut the area and collect data about the structures e.g. spacing, cross-cutting relationships etc. This was done using three main techniques: GPS mapping, base mapping and multiple line transects. GPS data were recorded on a Garmin Trex GPS set to the CH 1903 co-ordinate system. Structural data were recorded using a compass-clinometer.

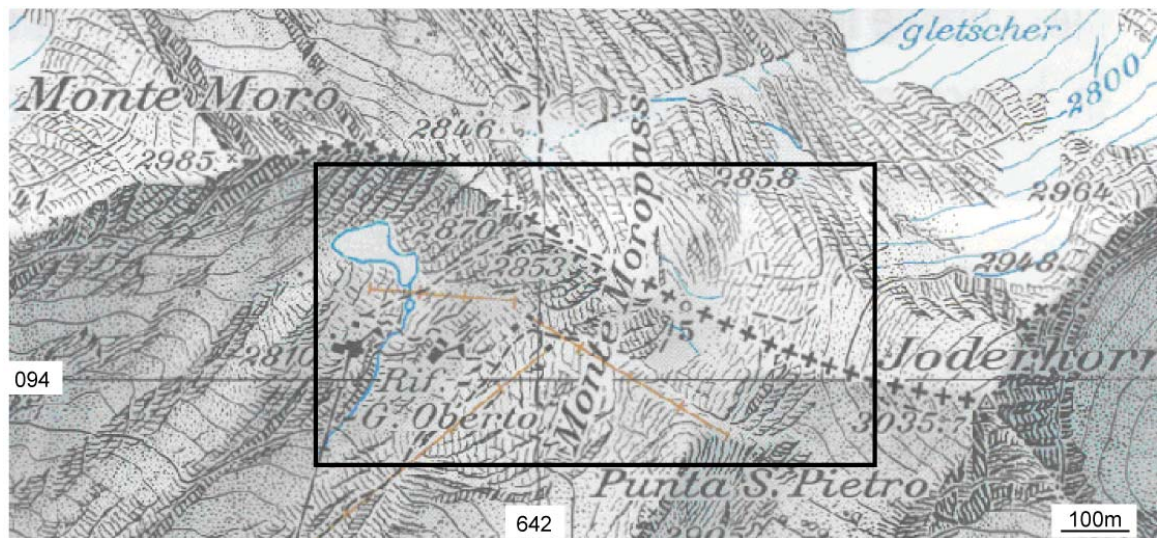
The mapping area was first assessed using a 1:25000 topographic map (Figure 3-1a). To create the base map key physical and geological features were given a GPS grid reference. These data were transferred onto graph paper at the appropriate scale and this provided the main framework for field location and geological mapping. Lithological boundaries were traced out by creating a GPS track. Individual points were recorded at 5-10 m intervals along the boundary and data transferred to the map (Figure 3-1b). To assess host rock variability across the area a graphic log was constructed perpendicular to the lithological boundaries (Line of section A-B in Figure 3-1b). Logging included outcrop descriptions, rock descriptions, augen content, foliation measurements and other structures. Joint data were collected on all joint orientations within the area.

Average grain size measurements were collected during logging. Grain size was measured for the main rock forming minerals (quartz and feldspar) and augen approximately every 10-20 m along the logged section. Average for each locality was based on 3 measurements of quartz, 3 of feldspar, and 3 augen (where they occur) from the exposure. Mineral proportions for the host rock were done by point counting and the average values presented are based on 5 host rock samples.

3.3 Host rock

Three main rock types were identified within the field area; granite gneiss, metasedimentary rocks and amphibolite (Figure 3-1b). The metasedimentary unit (MSU) sub-divides the area and based on the dip of the regional foliation (010/33W); the granite gneiss to the west of the MSU was classified as the Upper Gneiss (UG) and the gneiss to the east as the Lower Gneiss (LG) (Figure 3-1b).

a



b

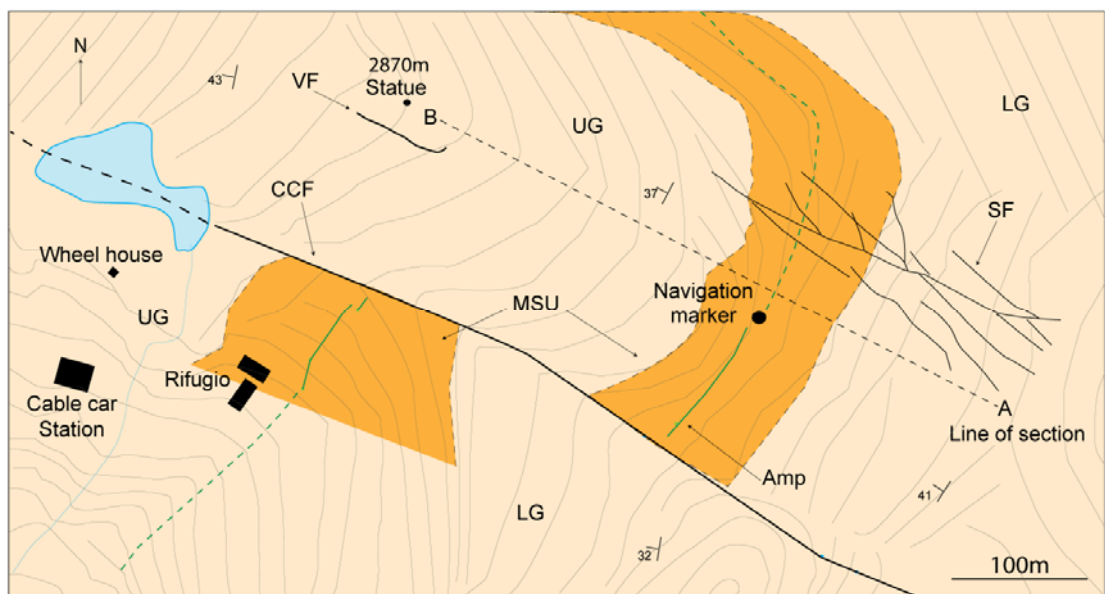


Figure 3-1a) 1:2500 topographic map of Passo Moro b) Geology map of area highlighted in (a). Section logged shown by line of section A-B. UG = Upper Gneiss, LG = Lower Gneiss, MSU = Metasedimentary unit, Amp = amphibolite, CCF = Ciao Ciao Fault, VF = Virgin Fault, SF = Spaghetti Faults. Strike and dip of foliation are shown for several locations.

The MSU is ~150 m thick and foliation strikes approximately NNE-SSW. Both the granite gneiss and metasedimentary rocks are foliated on a mm-cm scale (defined by muscovite and biotite) and joint planes often form parallel to foliation with an average orientation of 010/33W. The amphibolite occurs as sheets of which the largest is found within the MSU. It can be traced for approximately 150-200 m either side of the Ciao Ciao Fault (Figure 3-1b) before thinning and/or bifurcating and becoming more intermittent along strike. Several other amphibolite sheets occur throughout the area but are not mapable on the scale of the base map. Several folds are present throughout Passo Moro and affect all lithologies. Folds are typically open and upright with axial trace that trend either NW-SE or NE-SW.

3.3.1 Logging

A 500 m log across the field area was obtained from east to west along line A-B (Figure 3-1b). The logging was done perpendicular to bedding and parallel to the studied faults (Chapter 4) to enable a comparison to be made between host rock variability and fault architecture. The graphic log highlights changes in lithology, grain size, structures present, foliation changes and foliation parallel joint density (Figure 3-2).

The graphic log shows that the LG is from 0-120m, the MSU from 120-250 m and the UG from 250-500 m. This study has shown that the gneisses contain numerous amphibolite sheets, aplites- , and strongly sheared layers with amphibolite sheets being the most common. Aplite layers are restricted to the LG whereas amphibolite layers are more commonly found in the MSU and the UG. From approximately 430 m to the end of the logged section there are no lithological variations or intrusions - the granite gneiss is massive and homogenous. Due to the variability of the UG between 250-430 m it will hence forth be referred to as the Variable Upper Gneiss (VUG) and the homogenous gneiss from 430-500 m as the UG.

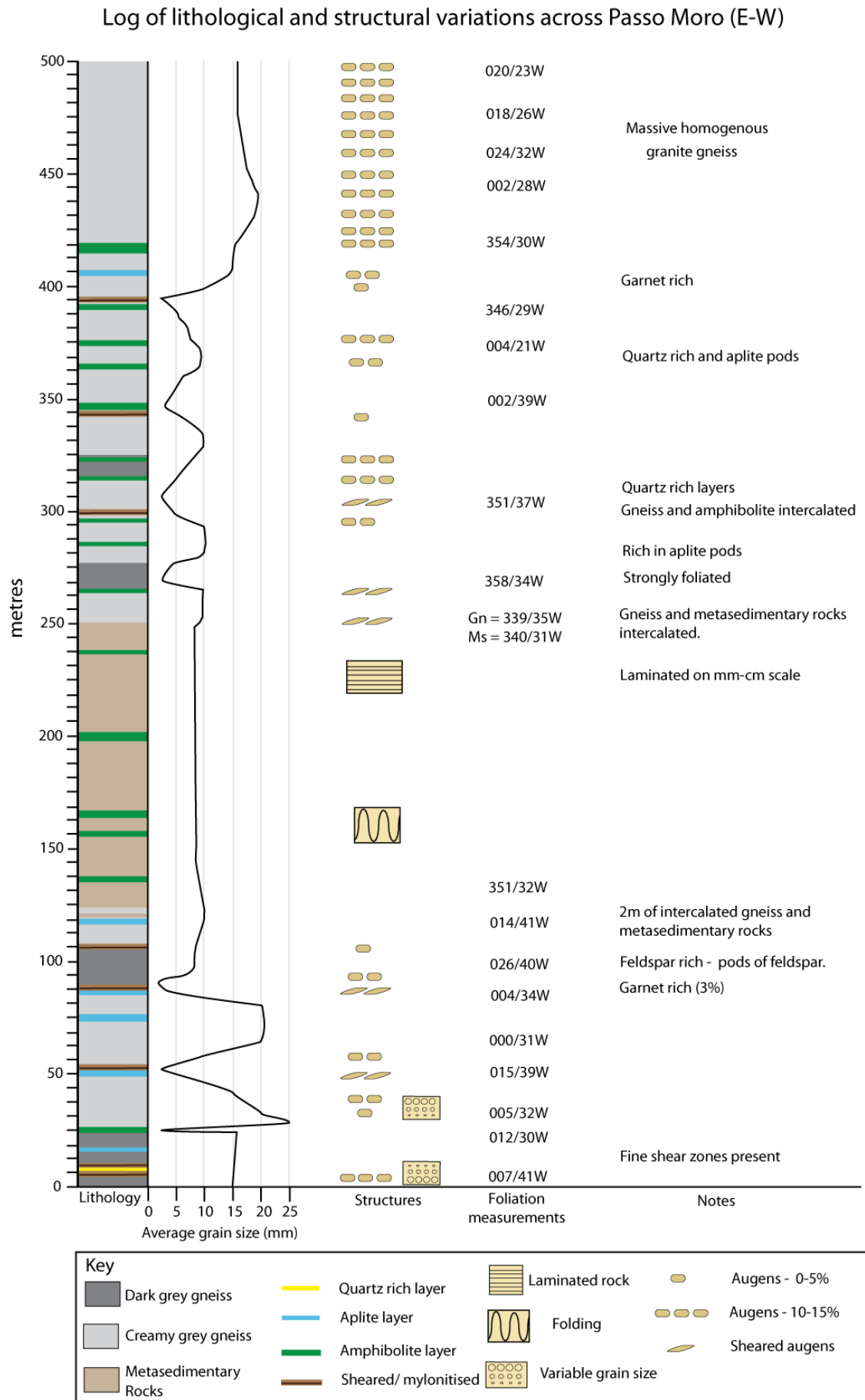


Figure 3-2: Graphic log across Passo Moro.
 Log was constructed along line of section A-B (Figure 3-1b) with A being the 0 m mark.

Throughout the logged section average grain size varies from 2-25 mm and variations in grain size tend to be sharp i.e. not a gradational change. Within the homogenous UG and the MSU the average grain size is 15 mm and 5 mm respectively and grain size is relatively consistent throughout both units. Within the VUG and the LG grain size is strongly variable (2-25 mm) between rocks. The smallest grain sizes recorded are often found at the boundaries between the gneisses and amphibolite sheets and within the sheared layers (Figure 3-2). The orientation of the foliation throughout the area varies from 346/29W to 026/40W with the mean being 010/33W.

3.3.2 Host rock descriptions

Several samples of the main host rock types were collected throughout the area (Table 3-1) and analysed in terms of their mineralogy, grain size and any other primary features.

Sample	Locality number	Rock type	Grid references (Grid - CH 1903)
Host 1	8	Granite gneiss – UG	642259, 094065
Host 2	9	Granite gneiss – UG	642117, 094174
Host 3	10	Granite gneiss – VUG	642099, 094185
Host 4	11	Granite gneiss – LG	641970, 094229
Host 5	12	Granite gneiss – LG	641934, 094196
Amp 1	13	Amphibolite - MSU	642224, 094099
MS 1	14	Metasedimentary rock – MSU	642171, 094134
Qtz-epi 1	15	Quartz-epidote vein – UG	641772, 094150
Qtz 1	16	Quartz vein – LG	642324, 094126

Table 3-1: Host rock samples collected and grid references for their localities. For precise locations see locality map in Appendix 1.

3.3.2.1 Granite gneiss

The granite gneiss at Passo Moro is typically creamy grey and composed of: 34% quartz; 26% plagioclase; 22% K-feldspar; 6.5% muscovite; 5.5% biotite; 2% garnet; 2% epidote; 1% chlorite; and <1% iron oxides² (Figure 3-3). Logging revealed obvious colour variations within the gneiss. A dark grey variety of granite gneiss is present at various localities throughout the area (Figure 3-2, Figure 3-5a). This

² Modal proportions calculated by point counting. Point counting was carried out on each host rock sample and for each sample n = ~800.

gneiss has a similar composition to the creamy gneiss but proportions of quartz are ~10-15% lower and micas (muscovite & biotite) correspondingly are more abundant. Average grain size of the granite gneiss varies throughout the area from 2-25 mm but the smallest grain size is repeatedly seen at lithological boundaries (Figure 3-2, Figure 3-5b).

The granite gneiss often contains K-feldspar augen which range from 1x1cm to 4x3cm, proportions vary from 0-15% and the augen can be sheared (Figure 3-2). There is no obvious pattern to the distribution of the augen however, the massive homogenous gneiss consistently has high proportions (~15%) and sheared augens occur at lithological boundaries (Figure 3-2). Throughout the gneiss there are also numerous small aplite intrusions (≤ 1 m thick) (Figure 3-5b). The boundary between the aplite and the gneiss is often associated with a finer grain size in the gneiss and foliation parallel joints usually occur at these boundaries (Figure 3-5d).

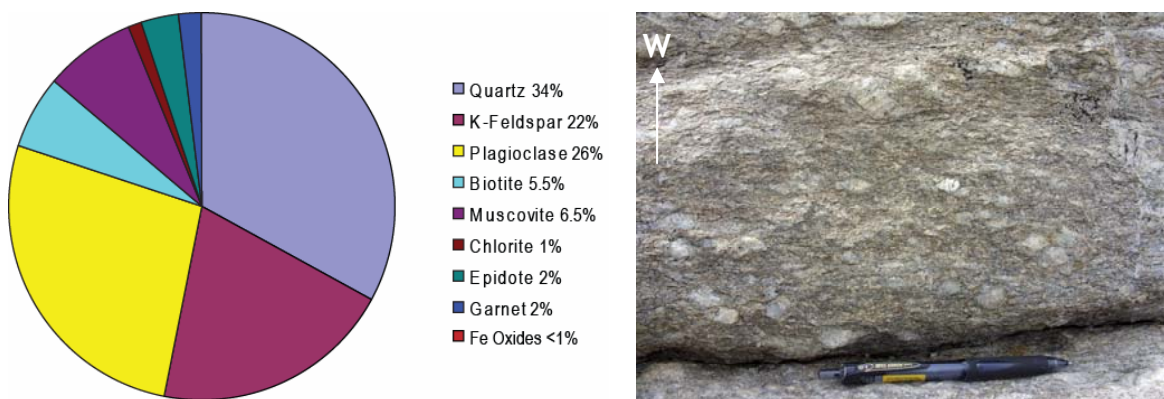


Figure 3-3: Pie chart of host rock mineralogy and a representative photo of the creamy granite gneiss. Locality 9.

3.3.2.2 Metasedimentary rocks

The metasedimentary rocks are creamy grey and composed of interbedded quartz and feldspar rich layers with micaceous layers (Figure 3-5c). The former are 2-15cm thick; medium grained (2-3mm); and typically composed of 50% quartz, 45% feldspar and 5% minor phases (muscovite, biotite, chlorite, iron oxides, apatite). The mica rich layers are typically 1-2 cm thick, medium grained (2-3 mm), and composed primarily of mica (muscovite & biotite) with only a small proportion of minor phases (quartz, albite, K-feldspar, chlorite, iron oxides, apatite). At locality 17 (230 m along the log) there are multiple

micaceous layers, the rock is finely laminated, and a crenulation cleavage is preserved (orientation of 001/62W and hinge trends 356°).

3.3.2.3 Amphibolite

The amphibolite is composed of: 70% amphibole; 10% albite; 10% quartz; 7% muscovite and 3% pyrite; and typically forms sheets sub-parallel to the regional foliation. The amphibolite is often shiny black, but several exposures are silvery brown. Each amphibolite sheet extends for approximately 200 m and on average is 1 m thick. Along strike the sheets undulate, bifurcate, thin out and terminate, and sheet thickness ranges from 5 cm to 8 m. The thickest amphibolite sheet (~8 m) is found at locality 18. At this locality the sheet intersects the Ciao Ciao fault. This sheet has been folded and this may in part explain the anomalously large thickness of the amphibolite sheet at this location.

3.3.2.4 Host Rock interpretation

Three dominant lithologies can be found at Passo Moro are: granite gneiss, metasedimentary rocks (quartzites & pelites) and amphibolite. Within the granite gneiss two varieties were distinguished - a creamy grey and a dark grey variety (Figure 3-2). Observations of the host rock suggest that the colour of the darker gneiss is in part due to higher proportions of micas (biotite and muscovite). Where mica proportions are high (>15%), mica rich layers are observed and make the gneiss look stripy (Figure 3-4).

Bearth (1952) and Frey et al (1976) both mention the variable composition of the Monte Rosa granite. In particular, the Macugnaga Augengneiss is primarily composed of a coarse grained, two mica gneiss with up to 4 cm long K-feldspar augen, but there are layers/zones parallel to foliation with variations in grain size, texture, composition and degree of lamination (Bearth, 1952). Bearth (1952) suggested that the compositional variation is likely to be related to the origin of the gneiss.

At Passo Moro the creamy grey and dark grey gneiss both contain K-feldspar augen. This indicates that both gneisses originated from a coarse grained granite. Based on the geology map from Bearth (1952) (Fig 2-8) the metasedimentary rocks within Passo Moro are what he classified as the

paragneiss. Therefore at Passo Moro there are two main types of granite gneiss: the granitic gneiss and the paragneiss.



Figure 3-4: Stripy granite gneiss with increased proportions of mica. Locality 19, photo taken looking west.

3.4 Structures

Joints and faults are present throughout the field area. Prior to collecting any of the joint or fault data (orientations, spacing, mineral coating etc) reconnaissance mapping was carried out to assess the main orientations of brittle structures and to consider the most appropriate technique for recording joint and fault data e.g. circular windows, scan lines, base mapping. Based on results from (Manda and Mabee, 2010), combined with the initial assessment of the field area; the multiple line transect method was selected as being the most suitable for data collection as it is the most time efficient and statistically valid method. This technique involved making two transects perpendicular to each other and every structure which intersected the transect line was recorded in terms of orientation, nature of mineral fill and distance along transect. One particular joint face was also mapped using the base mapping technique as this joint plane was intersected by all joint sets and provided clear and detailed information on their temporal relationships.

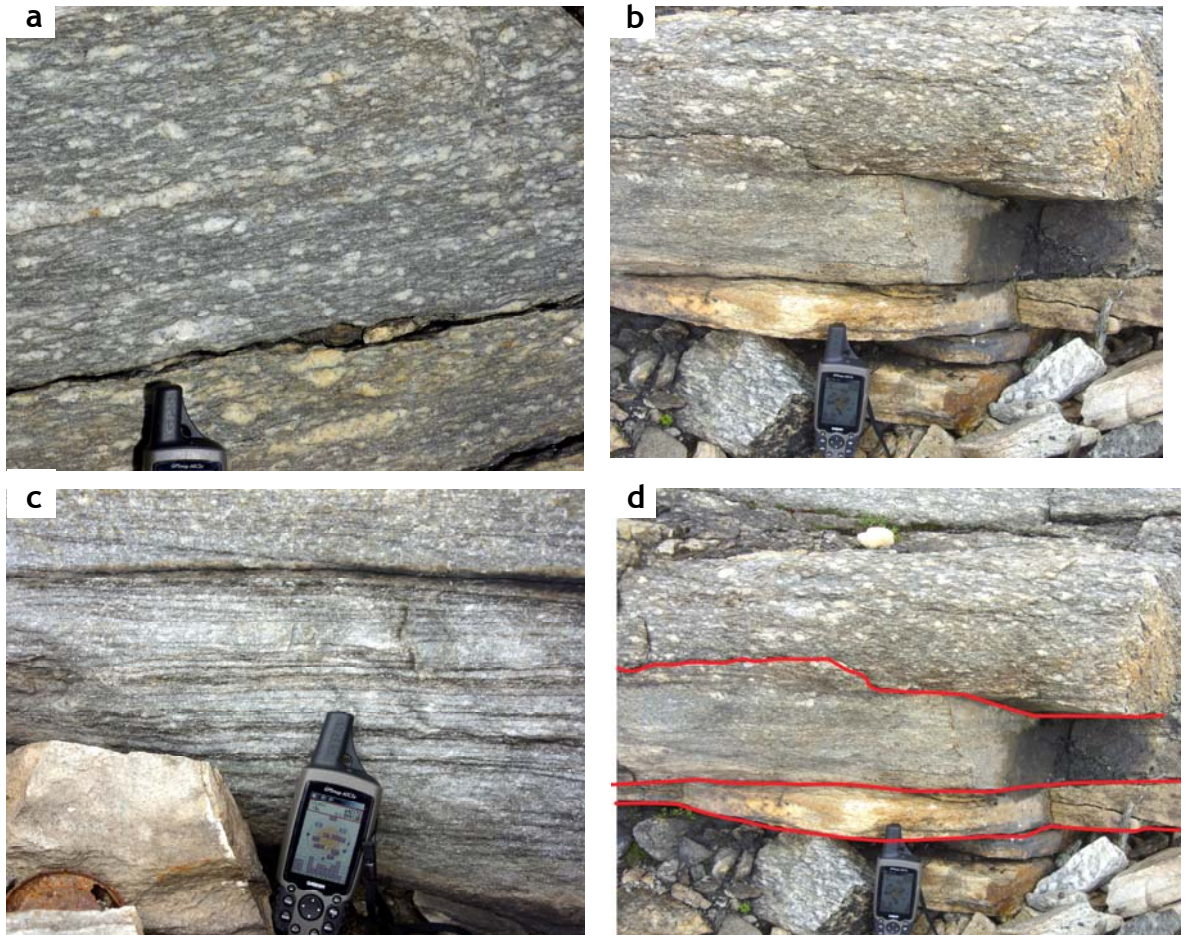


Figure 3-5: Variations observed within the granite gneiss.

a) Dark grey gneiss (locality 20) b) coarse gneiss grading into fine grained sheared gneiss (top to bottom) and the bottom pale layer is an aplite layer (locality 21) c) metasedimentary rocks, which are composed of intercalated quartzites and pelites (locality 22) d) As 4b but highlighting where the 010° joints formed. All photos taken looking west.

Transects were taken along 26 to 50 m stretches. The number of joints within a given stretch was counted and divided by the length of the transect they occupy to give the joint density. As well as the transect data, during the logging of the 500 m section joint density for the 010/33W joint set was recorded at each locality. Joint density was recorded for each metre and when combined with logging, it provides an overview of how this joint set varies throughout the entire field area (Figure 3-2).

The primary focus of this study was faults in granite gneiss and thus the detailed fault mapping was completed in the granite gneiss. It was therefore a priority to collect data from the gneiss with logging and joint data from the MSU only being needed for overview purposes.

3.4.1 Cross-cutting relationships

Joints are one of the most common brittle structures observed in nature (Hancock, 1985) and tend to form in response to the accumulation of elastic strain (Gross et al., 1997). To decipher the timing of brittle structures the cross-cutting relationships need to be assessed. Knowing the timing of each structure with respect to one another is critical as early joint formation can influence later fault development (Martel et al., 1988); and faults can also influence subsequent joint initiation and development (Rawnsley et al., 1992). Several different criteria can be utilised to establish timing of joint formation:

1. A younger joint will abut or cross-cut an older one (Hancock, 1985; Hodgson, 1961; Peacock, 2001) without being displaced.
2. Younger joints often curve as they approach older joints (Eyal et al., 2001; Peacock, 2001).
3. A younger fault may off-set an older joint/fault.
4. Joints formed synchronously with faults tend to increase in frequency towards faults (Peacock, 2001).

3.4.2 Joint Descriptions

Four dominant joint sets were recognised within the area and are oriented approximately 040/85; 090/90; 010/33W; and 146/74NE (Figure 3-6a). Joint properties which were assessed include: orientation; length; density; mineral fill; and reactivation. Orientations of the four joint sets are shown in Figure 3-6a and the contoured pole map (Figure 3-6b) highlights the different sets.

The 090/90 joints are several to tens of metres long and quartz filled. The width of the fill varies from 2-5cm and the quartz has subsequently been fractured. The orientations of fractures cutting the quartz veins are 040/87 and 139/78NE. Within the quartz vein these fractures are spaced approximately 2 cm apart. 090/90 joints are sparse throughout the area, with density typically being 0.2/m (Figure 3-8a).

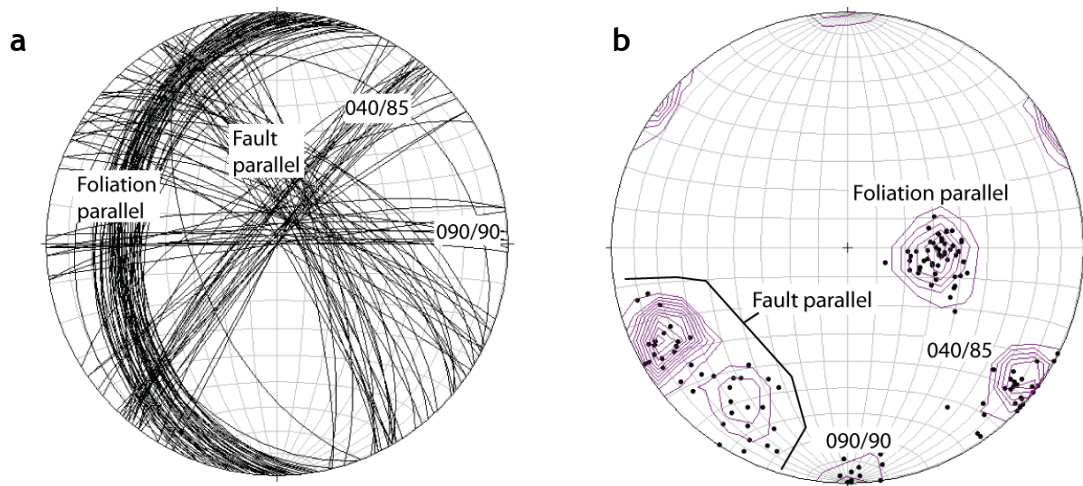


Figure 3-6a: Equal area stereonet and b) 1% contour diagram - contour interval = 2% per 1% area) for all fractures recorded at Passo Moro. n= 234.

The 010/33W joints are sub-parallel to the regional foliation and joint planes often coincide with lithological and textural contacts e.g. grain size changes Figure 3-5c & d. Joints are up to several metres long and primarily unmineralized but several joints are coated in a 1-2 mm thick layer of quartz. Joint density varies across the area from east to west with variations being associated with differences in lithology and the degree of heterogeneity throughout the granite gneiss (Figure 3-2). Within the UG joint density is low (2.1/m; standard deviation (σ) = 1.3), in the VUG density increases to 5.7/m (σ = 2.1), in the MSU density is 11.2/m (σ = 3.3), whereas in the LG joint density is 7.7/m (σ = 5). The standard deviation values for each unit indicate that joint density is more variable within the LG and MSU than in the VUG and the UG.

The 040/90 joints are 5 cms to tens of metres long and typically unmineralized. Mineralization of the joint surface is only observed at one locality (locality 25) where the joint is coated in up to 5mm of epidote. The average joint density for the 040/90 set is 0.6/m (Figure 3-8c). This varies throughout the area with the greatest increases in joint density (up to 5/m) being confined within fault zones (Figure 3-7).

The 146/74NE joints are approximately fault parallel (including splay faults) and the joints have a broad range in orientations (Figure 3-6a & b). The joint set can be subdivided into two sets (Figure 3-6b), which have mean values of 153° and 124°. The 153° set is the more tightly constrained of the two however; the mean orientation for the entire set is 146/74NE. The joints are centimetre to several

metres long and typically unmineralized. A number of these joints have been reactivated as faults and where this occurs the joint is: coated with quartz and/or chlorite and/or epidote; may preserve slickenlines ($\sim 11 \rightarrow 117^\circ$); and/or may offset other features. Average joint density is 2/m but this is variable along the 220° transect with density readings changing from 0/m up to 7/m over short distances (1-2 m) (Figure 3-8b). The histogram shows that increased densities coincide with the location of a fault zone (Figure 3-8b).

3.4.2.1 Data recording transects

NNE to SSW transects (26 m long) assessing joint density were collected in the UG, VUG and LG to assess the variation in average joint density (assessing all joint orientations intersected) throughout the area (Figure 3-9). The orientation of transect is important because it is within a single foliation plane.

Consequently it is representative of how the N-S joint density varies in association with changing $010/33W$ joint density (Figure 3-2). Joint density results for the NNE-SSW transects have been plotted against their location and the 010° joint density (Figure 3-9). Within the homogenous UG N-S joint density is 1.2/m ($\sigma = 0.96$); in the VUG it is 2.4/m ($\sigma = 1.0$), and in the LG it is 4/m ($\sigma = 2.4$). In general these results show that, as the amount of lithological variation in the granite gneiss increases, both the 010° joint density and the NNE-SSW joint density increases (Figure 3-9).

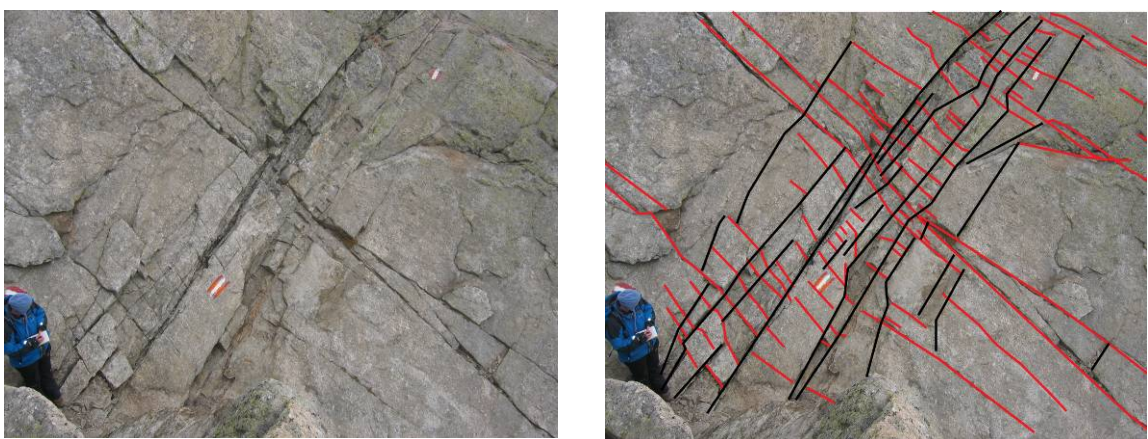


Figure 3-7: Effect of a fault zone on 040° joint density. Black lines are fault related fractures (146°) whereas red lines are the 040° joints. Note how the 040° fractures increase in density within the fault zone (highlighted by the black lines). Photo taken looking down onto a surface which is dipping towards the bottom right of the image. Length of fault from bottom left corner to top right is 11.3m. Locality 1.

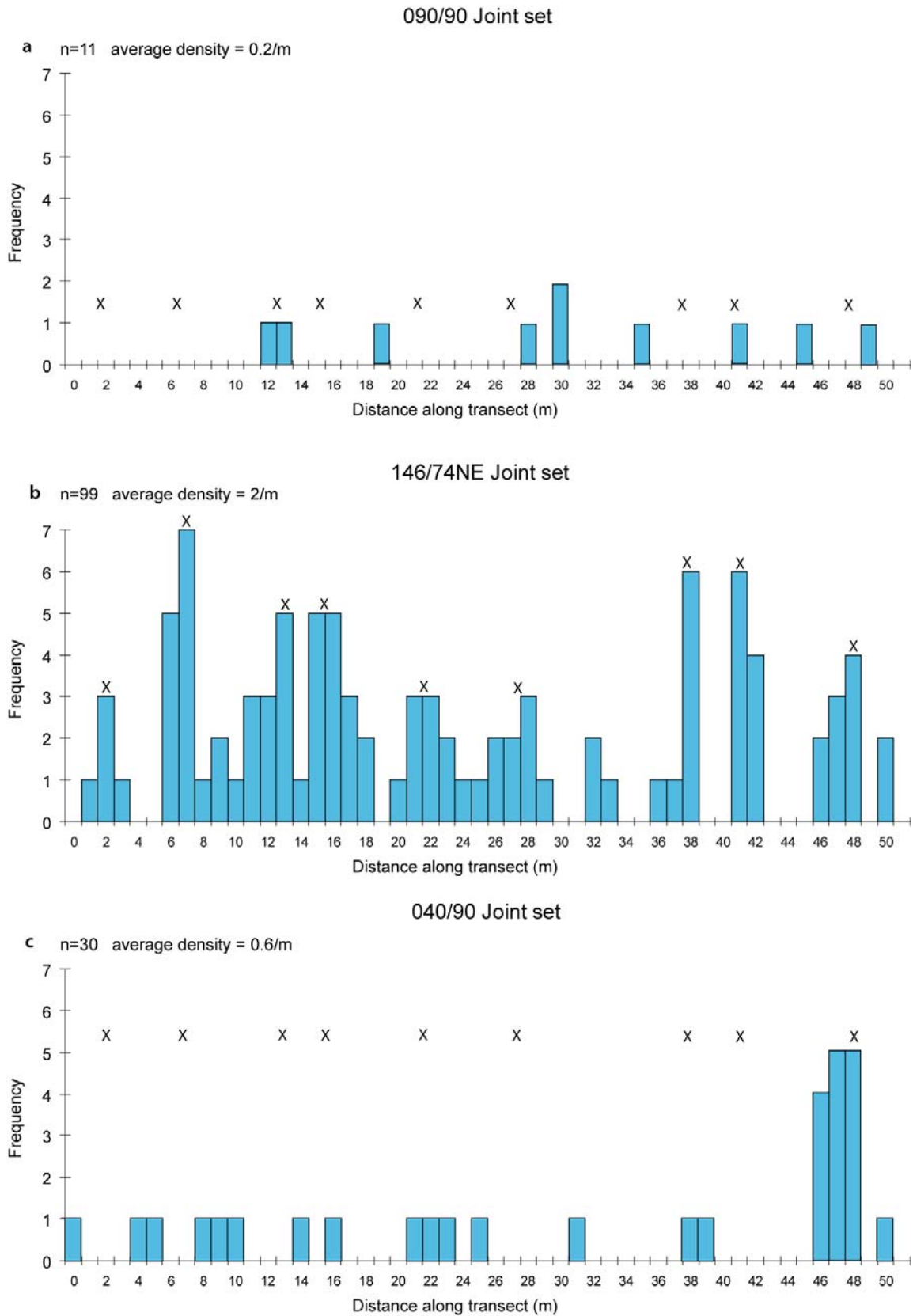


Figure 3-8a-c: Histograms showing joint density along the 220° transects at Passo Moro. X's on histograms mark the location of fault zones. Orientation of transects are approximately NE-SW with the 0m point being in the NE.

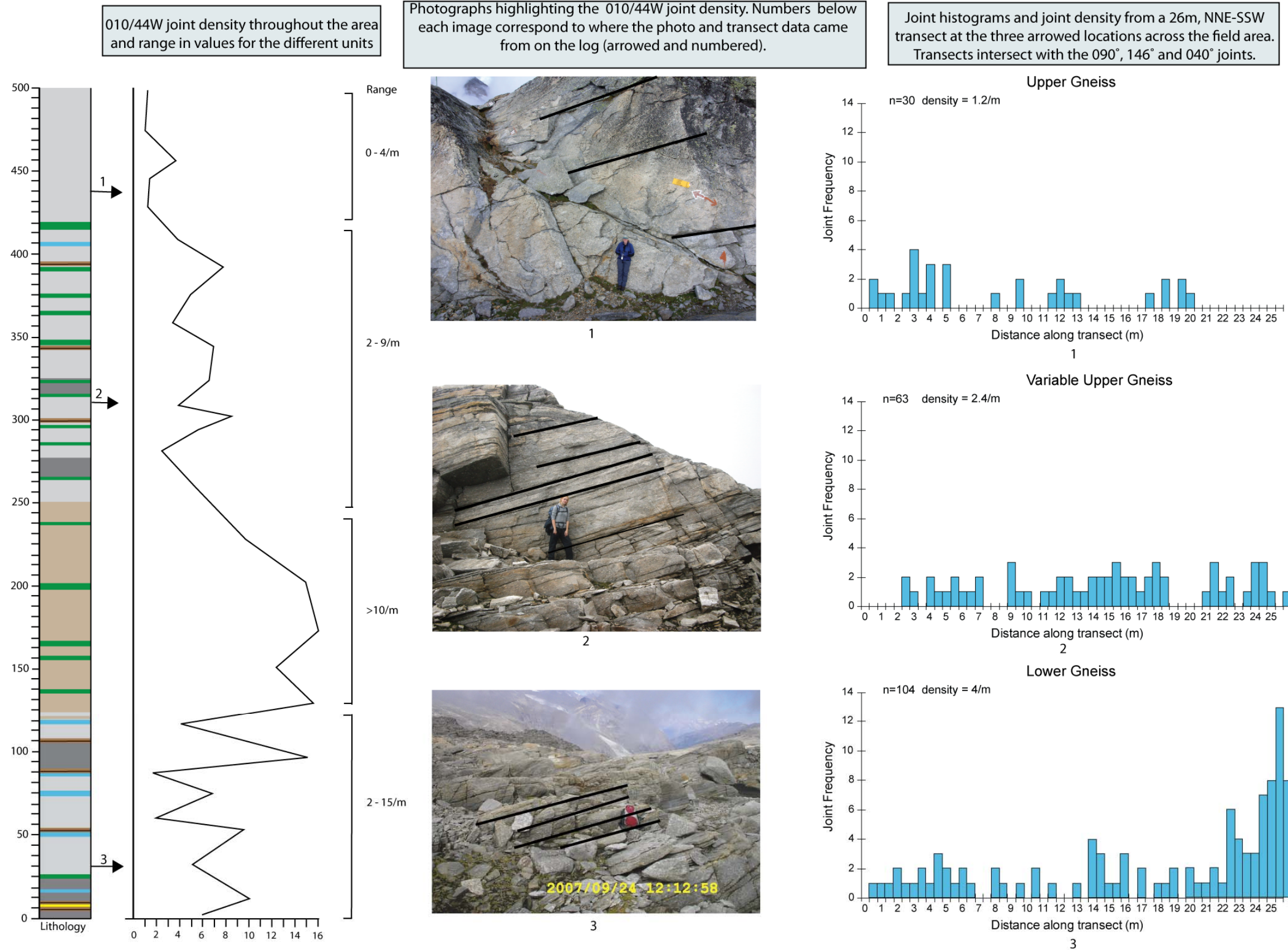


Figure 3-9: Joint density along NNE-SSW transects.
Arrowed locations relate to where the photographs and histogram data came from.

3.4.2.2 Joint relationships at Passo Moro

The 090°, 146° and 040° joints all cross-cut or abut against the 010° joints (Figure 3-10a). The 040° joints cross-cut, abut and curve towards the 146° joints (Figure 3-10b) implying that the 040° joints are younger. The 040° joint density also increases within fault zones which are sub-parallel to and bounded by the 146° joints (Figure 3-7). Martel (1997) states that the joint density of a newly forming joint set will be affected by pre-existing structures. This indicates that the 146° joints/faults were already there and that the 040° joint set formed later.

The 090° quartz filled joints have been offset by the 146° set (Figure 3-10c). Joints oriented 146° are mineralized with quartz and chlorite and preserve slickenlines (Figure 3-10d) indicating reactivation of some of the 146° joints as faults. The 090° quartz filled joints have also been fractured in two orientations (146° and 040°) (Figure 3-10e). For the quartz filled 090° joints to have preserved fracturing in a 146° and 040° orientation, means that both fracturing events must have occurred after precipitation of quartz in the 090° joints.

146° joint density varies across the area from NW-SE and NE-SW. In relation to the north to south transect, joint density increases towards the 146° fault zones (Figure 3-8b) and implies that the 146° joints and faults formed synchronously (Peacock, 2001).

The cross-cutting relationships between the joint sets enable the chronology of joint formation to be unravelled:

1. 010/33W (earliest)
2. 090/90
3. 146/74NE & faults
4. 040/90

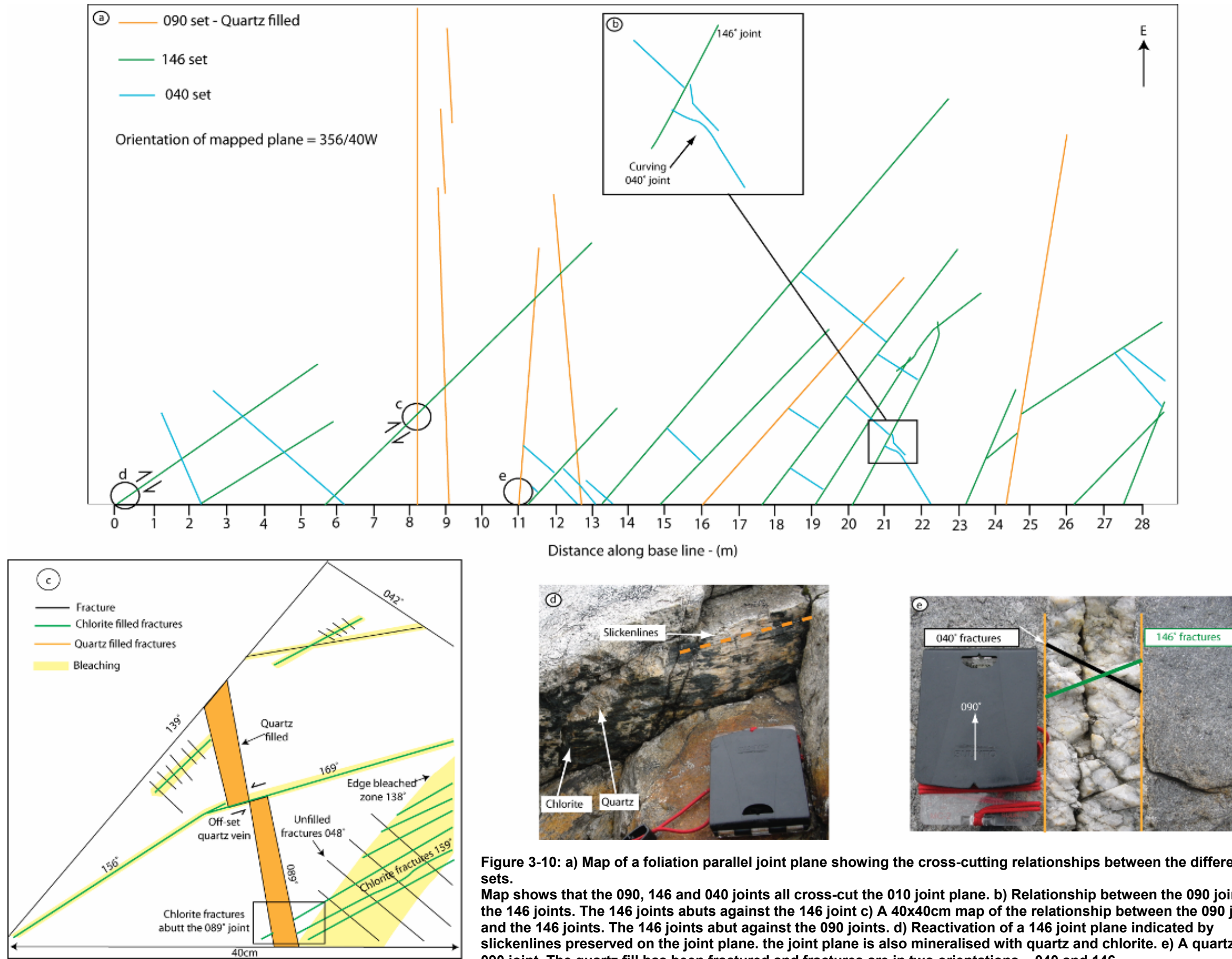


Figure 3-10: a) Map of a foliation parallel joint plane showing the cross-cutting relationships between the different joint sets. Map shows that the 090, 146 and 040 joints all cross-cut the 010 joint plane. b) Relationship between the 090 joints and the 146 joints. The 146 joints abuts against the 146 joint c) A 40x40cm map of the relationship between the 090 joints and the 146 joints. The 146 joints abut against the 090 joints. d) Reactivation of a 146 joint plane indicated by slickensides preserved on the joint plane. the joint plane is also mineralised with quartz and chlorite. e) A quartz filled 090 joint. The quartz fill has been fractured and fractures are in two orientations – 040 and 146.

3.4.3 Interpretation

Understanding the host rock is crucial to understanding how later structures evolve and the architectural development of the fault zones. Results have highlighted heterogeneities in the host rock lithologies and in the densities of the later formed brittle structures.

3.4.3.1 Mechanical boundaries overview

Studies in joint development typically discuss the relationships that occur in terms of mechanical boundaries, layers and units. To be able to link the observations of this study to others in literature it is therefore essential to outline what a mechanical boundary, layer and unit are, so my results can be compared to the published data sets.

Rock units are often described in terms of their mechanical boundaries, -layers or -units. A mechanical boundary is something that creates mechanical anisotropy within the rock e.g. bedding or joint planes (Gross and Eyal, 2007), a mechanical layer is the rock between two parallel mechanical boundaries (Gross, 1993; Ruf et al., 1998), and a mechanical unit is the thickness of rock that acts as a single unit (Wilkins & Gross, 2002 and references therein). The thickness of a mechanical unit will vary depending on the scale being mapped. At an outcrop scale, a mechanical layer and unit are essentially the same. However, on a regional scale, a mechanical unit might be considered as the entire sedimentary sequence between two major thrust planes.

Mechanical layers are usually described in terms of thickness (distance between two parallel mechanical layers) and this is usually either joint or lithology controlled (Gross et al., 1995; Ruf et al., 1998), i.e. the thickness of a mechanical layer is the distance between two bedding or joint planes. Within sedimentary rocks, bed thickness typically defines the thickness of the mechanical layer (Gross et al., 1995; Narr and Suppe, 1991; Ruf et al., 1998), but in a rock without any systematic discontinuities (e.g. granite) pre-existing joints act as mechanical boundaries for later cross-cutting joints (Dyer, 1988; Peacock, 2001; Ruf et al., 1998); thus defining the mechanical layer thickness. It has been widely observed that the distance between joints/mechanical

boundaries is roughly equivalent to mechanical layer thickness (Gross, 1993; Narr and Suppe, 1991); thus as mechanical layer thickness increases, spacing between cross-cutting joints also increases.

3.4.3.2 Host rock effects on joint development

The 010° joint set was first to form and it developed sub-parallel to the regional foliation (controlled by the micas). The 010° joint density will have only been affected by host rock properties as no joints previously existed. The 010° joint density varies across Passo Moro from east to west (Figure 3-11). The lowest density values are recorded within the homogenous UG and the highest are recorded in the MSU. Based on the assumption that the presence of mechanical boundaries, such as bedding promotes joint initiation (Tien et al., 2006), it would be expected that the unit with the highest proportion of original mechanical boundaries will have the highest joint density.

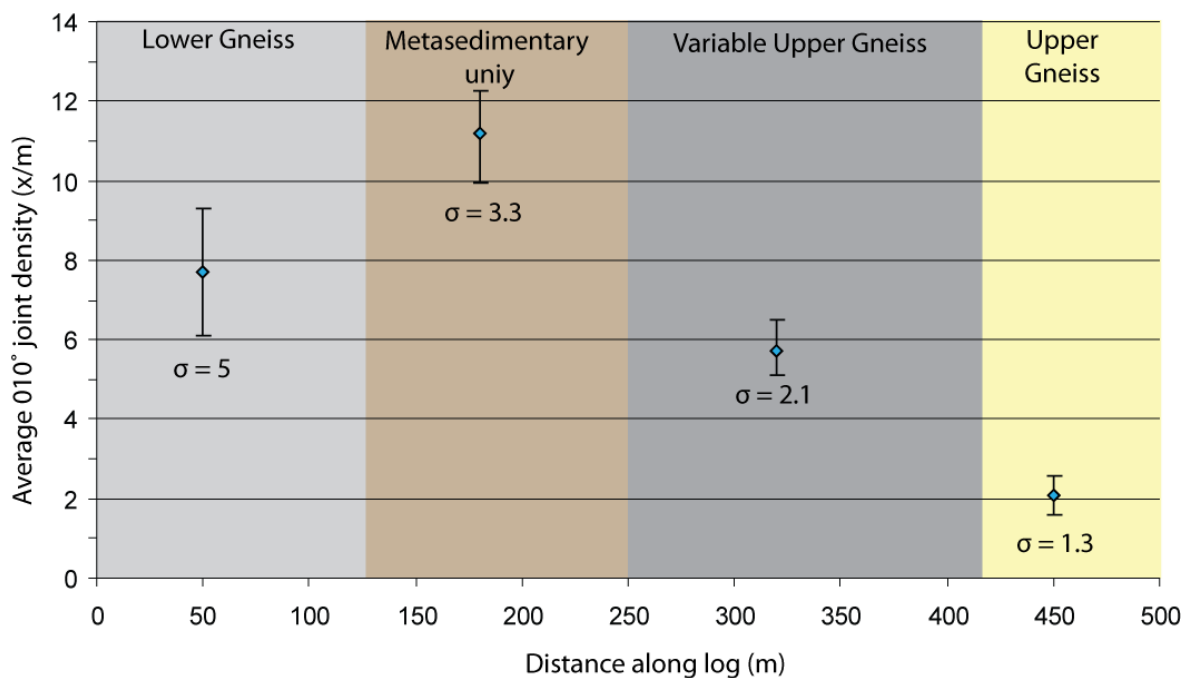


Figure 3-11: Average joint density for the 010° joints within the different lithological units. Average values are plotted with the standard errors and standard deviation stated.

3.4.3.2.1 Metasedimentary unit - 010° joint density

Within the MSU the most obvious natural boundaries are bedding planes. Bedding planes commonly act as strong mechanical discontinuities (Ruf et al., 1998) and so often coincide with joint planes (Gross, 1993). In the MSU bed thickness ranges from 2-15cm and within this area the 010° joint density has similar

spacing correlating to a joint density of approximately 11/m (Figure 3-11). A mechanical layer thickness of 9.1 cm (1m/11cm) is well within the range of bed thickness at Passo Moro, and so results imply that in the MSU bed thickness exerts a control over the density of the 010° joint set.

Within the MSU there are also several amphibolite sheets throughout. The lithological contacts between the metasedimentary rocks and intrusions are mechanical boundaries. The combination of bed thickness being ≤ 15 cm and multiple intrusions provides an abundance of natural mechanical boundaries and hence explains why joint density is high within this area.

3.4.3.2.2 Granite gneiss - 010° joint density

Crystalline rocks are typically considered as having no original systematic discontinuities (Casas et al., 2003; Fitz Gerald and Stünitz, 1993; Ruf et al., 1998), thus there are no obvious weaknesses or flaws on which joints may develop. However, the strength of a rock is controlled by: mineralogy; structural and textural features such as schistosity and discontinuities; proportion of weak minerals (phyllosilicates); and grain properties (e.g. size, shape & orientation) (Bürgi et al., 2001; Hartley, 1974; White, 1979). Gneiss does have a fabric and so this fabric is likely to influence the orientation of any later forming mechanical boundaries. Logging of the granite gneiss at Passo Moro also revealed numerous variations in terms of mineralogy and textures; thus these properties may have affected the overall strength of the granite gneiss and the joint location.

010° joint density varies throughout Passo Moro with the lowest readings in the UG and the highest readings within the VUG and the LG (Figure 3-11). Given that the VUG and LG contain the most lithological, mineralogical and textural variation it is likely that the fluctuations in joint density are related to the variations within the host rock.

The creamy and dark grey gneiss are interpreted as being of a granitic origin however the dark grey gneiss has higher proportions of mica. Within both gneisses the micas are aligned and this occurred due to gneissification of the host rock during nappe formation (Milnes et al., 1981). Since the proportion of mica-rich gneiss is higher within the VUG and LG, the foliation created by mineral alignment is more defined in these areas. Alignment of micas causes

mechanical anisotropy within the gneiss (Park et al., 2006), as the strength of the mica layers is less than that of the quartz and/or feldspar layers (Kronenberg et al., 1990; O'Hara, 2007; Shea and Kronenberg, 1992). A foliated rock is more likely to break parallel to the mica layers rather than across the planes or in any other orientation (Tien et al., 2006); thus foliation development within the granite gneiss would have promoted parallel joint formation (i.e. in the 010° orientation). The higher proportion of mica rich gneiss in the VUG and LG would provide more planes of weakness for joint initiation, which in turn would lead to increased joint density in these areas.

Logging of the gneiss revealed compositional and textural variations (e.g. grain size, augen content), and multiple intrusions (Figure 3-2). The mineralogical/textural transitions represent boundaries over which the strength and thus mechanical properties of the rock changes i.e. they represent mechanical boundaries (Chester and Logan, 1986). Throughout the gneiss the lithological and textural boundaries can therefore be interpreted as mechanical discontinuities, and so will be utilised as planes of weakness on which joints initiate.

The 010° average joint density varies from 2.1/m in the UG up to 7.7/m in the LG (Figure 3-11). Combined with the logging data this shows that as the number of lithological/textural contacts increase, the 010° joint density also increases. Hence, results indicate that the compositional, structural and textural variations all act as mechanical boundaries throughout the gneiss. Consequently variations in host rock properties influence the location of mechanical boundaries and how the rock will respond to subsequent deformation (Ruf et al., 1998; Peacock, 2001; Wilkins & Gross, 2002; Gross & Eyal, 2007).

3.4.3.3 Joints – Effects of pre-existing structures

After formation of the $010/33W$ joint set, another three joint sets and a fault set formed. It has been recorded in previous studies that the presence of pre-existing structures can affect those that form later, as pre-existing structures act as mechanical boundaries for later events. The relationship between mechanical layer thickness and spacing of cross joints indicates that as the mechanical layer thickness increases, the spacing of cross joints also increases.

This means that the joints which formed after the 010/33W joint set should produce predictable joint density patterns.

3.4.3.3.1 *Average joint density*

At Passo Moro the 010/33W joint density generally increases from west to east i.e. it is lowest in the UG and highest in the LG (Figure 3-11). As joint density increases the mechanical layer thickness decreases thus cross-joint density increases. Therefore cross-joint density would be expected to increase from west to east at Passo Moro.

NNE-SSW transects were obtained within the UG, VUG and LG. Transects are within the plane of a 010° joint and thus transects monitor the average joint density in relation to changing 010° joint density. The joint density along a NNE-SSW transect in the UG, VUG and LG are 1.2/m ($\sigma = 0.96$), 2.4/m ($\sigma = 1.0$) and 4/m ($\sigma = 2.4$) respectively demonstrating that density increases from west to east. When compared to location along the logged section and the 010° joint density (

Figure 3-9) the relationship between pre-existing joints and cross-joint density is clear (Figure 3-12). Observations of the UG show that 010° joint density is low and so the mechanical layer thickness is large (~2m). The cross-joint density in this area is 1.2/m which is relatively low and is the lowest cross-joint density in the area. When compared to the LG, Figure 3-12 shows that the 010° joint density is high, thus mechanical layer thickness is low (~20cm) and subsequently cross-joint density is high (4/m). This indicates that the pre-existing joints controlled the density of later forming joints.

The 040° joint density typically increases from west to east at Passo Moro. However, there are also localised increases in 040° joint densities within the 146° fault zones. This increase in 040° joint density is only recorded in transects within and/or along strike of a fault zone (Figure 3-7), as out-with the fault zones the 040° joint density is at background levels (average measured Figure 3-8c). Previous studies have shown that fault zones act as mechanical boundaries for later joint forming events and that different joint patterns within a fault may exist due to variations in mechanical properties within the fault (Peacock, 2000). The 040° joint density is therefore controlled not only by the pre-existing joints but also by the fault zones.

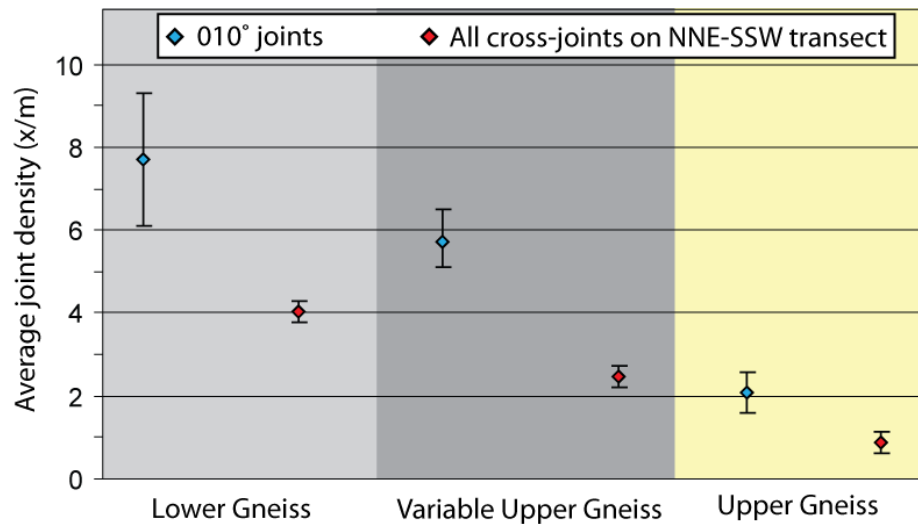


Figure 3-12: Comparison between the 010° joint density and the density of later formed cross-joints within each rock unit. Plot shows that as 010° joint density increases, the density of later formed cross-joints also increases. Standard error from the mean shown by the error bars.

The changes in joint density at Passo Moro are predicted based on the relationship that exists between mechanical layer thickness and cross joint spacing. Results from this study therefore agree with previous studies and indicate that pre-existing structures effect/control the distribution of latter structures. In this study those pre-existing structures are joints and faults and these were ultimately controlled by the host rock variations and foliation.

3.4.4 Conclusions

Field mapping at Passo Moro has provided a detailed description of the host rock and distribution of joints and faults within the field area. Host rock logging has shown that the three main rock types are present (granite gneiss, metasedimentary rocks and amphibolite), and that the host rock has variable grain size, texture, structure and contains of minor intrusions.

The granite gneiss has been divided into three units based upon location and internal variability: Upper Gneiss, Variable Upper Gneiss and Lower Gneiss. The Upper Gneiss is creamy grey, massive and homogenous. The Variable Upper Gneiss and Lower Gneiss is composed of a creamy grey and dark grey gneiss the dark grey gneiss containing a higher proportion of micas. Throughout the two units there are also multiple minor intrusions and variations in rock properties such as grain size and mineral alignment. The host rock properties have an

effect on the mechanical properties of the rock and consequently affect the density of the 010° joints.

The Metasedimentary Unit is comprised of interbedded quartzites and pelites with bed thickness ranging from 2-15cm. Within this unit the bedding planes have acted as the mechanical boundaries and thus the 010° joint density is lithology controlled.

The 010° joint density within all units at Passo Moro affected the distribution of later forming joints. Data from all units concur with the relationship between mechanical layer thickness and spacing of cross-joint spacing i.e. as mechanical layer thickness increases, cross-joint spacing also increases thus joint density decreases. Fault zones formed synchronously with the 146° joints and these structures also acted as mechanical boundaries for formation of the 040° joints.

In conclusion, within crystalline rocks lithological variations act as mechanical boundaries for the initiation of joints and influence joint density; early joints affect the distribution of later forming structures; and fault zones act as mechanical boundaries for later cross cutting joints. For all cross-cutting relationships the mechanical layer thickness-cross-joint spacing relationship was upheld.

4 Fault architecture

4.1 Introduction

Deformation within fault zones typically happens at depths where we are unable to directly observe the processes that occur, however exhumed fault zones are one of the few sources of information available for the reconstruction of tectonic evolution (Passchier & Trouw, 2005). Faults can have different appearances along strike, in different lithologies, and tectonic settings and therefore a description of its appearance or architecture enables comparisons to be made between faults. Also, by studying faults of different size and displacement and analysing the fault architecture, fault rocks and associated microstructures it is possible to assess the conditions of faulting and fault evolution.

Fault zones are generally composed of three main components: a principal slip surface (PSS); a fault core; and a damage zone (Figure 4-1a) (Caine et al., 1996; Chester et al., 1993; Schulz and Evans, 1998; Shipton et al., 2006). The majority of slip and deformation is accommodated within the fault core (Caine et al., 1996; Shipton et al., 2006). Each fault component is characterised by a variety of fault rock types or structures (Caine et al., 1996) implying that the different fault components developed with varying deformation mechanisms and properties. Proportions of each fault component can vary between and within different fault zones leading to differences in architectural styles (Figure 4-1a-c). The fault zones shown in Figure 4-1 all cut through crystalline basement rock but have very different architectural styles indicating that there are other influential factors as well as lithology. Differences in architecture may be in response to a) depth of faulting, b) the protolith, c) the fault displacement, d) interaction with other faults and/or pre-existing structures, and e) fluid-rock reactions (Faulkner et al., 2008).

Faults at Passo Moro have been exhumed from seismogenic depths and primarily cut granite gneiss. By comparing how fault architecture differs between different faults with similar displacements, how pre-existing structures influence fault architecture can be assessed. Also, by comparing faults of different lengths

and displacements an assessment of how fluid-rock reactions differ with fault size is possible.

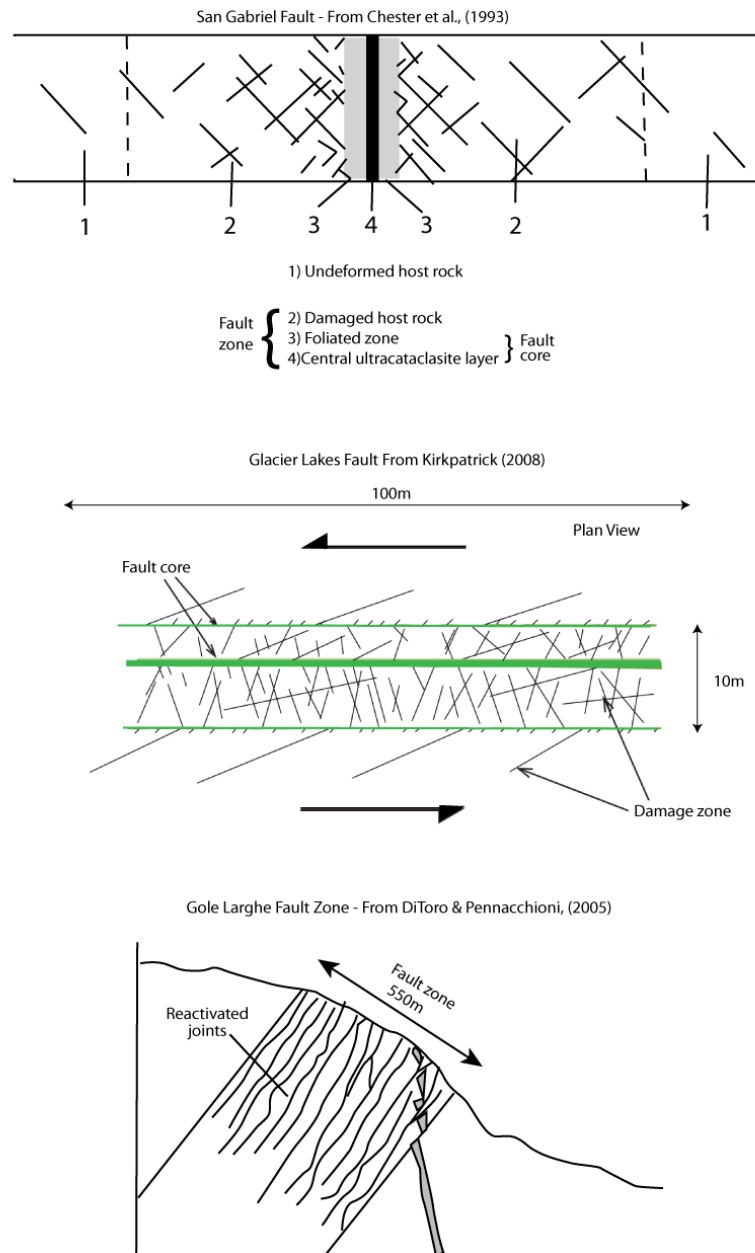


Figure 4-1: Three published fault architectural descriptions.

a) central fault core surrounded by a damage zone b) deformation is primarily contained between two bounding fault cores strands c) fault zone is composed of numerous sub-parallel fault strands.

4.2 Techniques

Various techniques were used for fault mapping depending on the size of the fault zone being mapped, the scale of the features and the desired level of detail required. The main techniques used were base line mapping, GPS mapping and detailed drawings of small areas (40x40 cm) (Figure 4-2). Orientation

measurements were recorded using a compass-clinometer. Measurements were taken using the right hand rule convention and all data reported will follow the same convention. Structural orientation data collected in the field have been analysed using Stereonet for Windows V1.2.

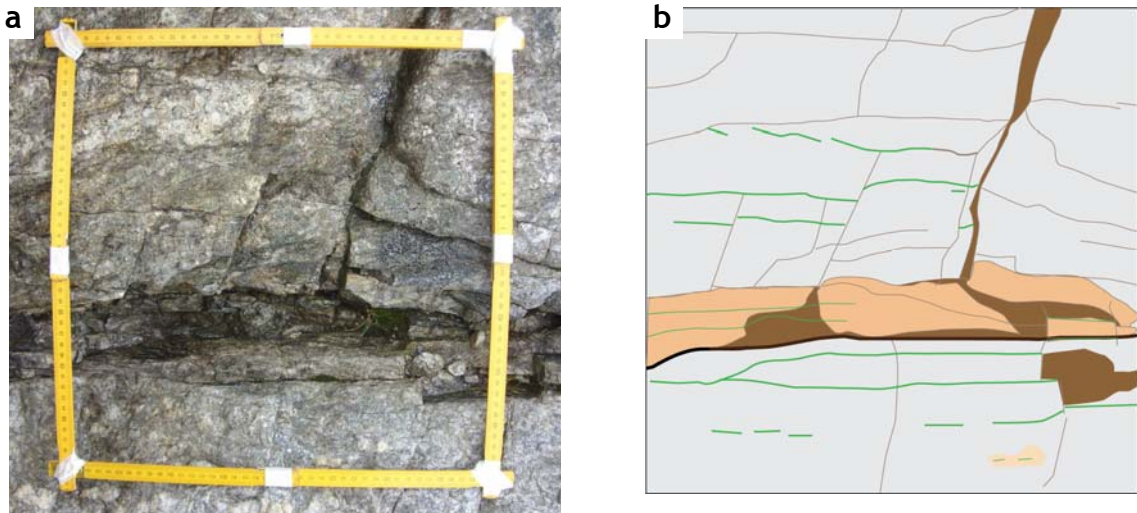


Figure 4-2: a) Example of area mapped by 40x40cm square and b) digitised version. Digitization highlights fractures (dark grey), fracture fill (green fractures = chlorite fill), core rock (peach), yellow/orange = quartz, and areas of no exposure (brown).

4.3 The studied fault zones

Multiple fault zones are exposed throughout the Passo Moro area, but this study focusses on three fault zones: The Spaghetti Faults (SF); The Virgin Fault (VF); and The Ciao Ciao Fault (CCF). All three faults have almost identical orientations but they differ in terms of architecture and/or displacement. The VF and SF have both accumulated similar amounts of displacement (5-20 cm) but have different lengths and very different architectural styles. The VF is similar to the San Gabriel Fault (Chester et al., 1993)(Figure 4-1a) while the SF resembles the Gole Larghe Fault (Di Toro and Pennacchioni, 2005) (Figure 4-1c). The CCF has accumulated ~250 m of displacement and so is a larger fault than the VF or SF. The architecture of the CCF is similar to the Glacier Lakes Fault (Kirkpatrick, 2008) (Figure 4-1b).

The architecture of all three fault zones will be described. The VF and SF will be compared to assess the effects of pre-existing structures on architecture. The VF and CCF will be compared to focus on conditions during faulting and the evolution of fluid-rock interactions.

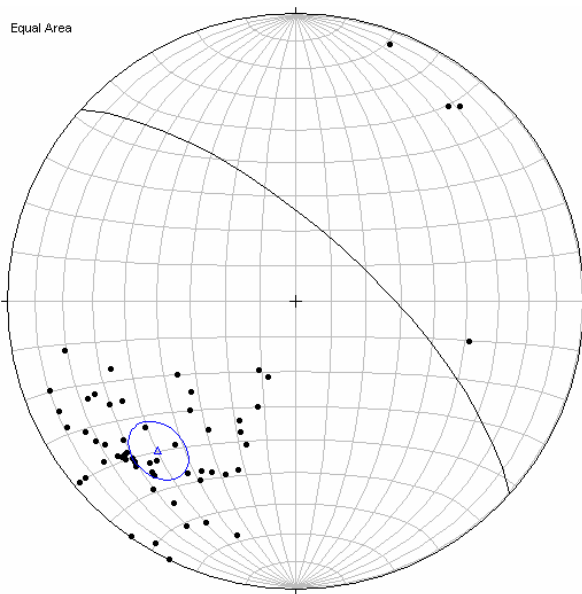
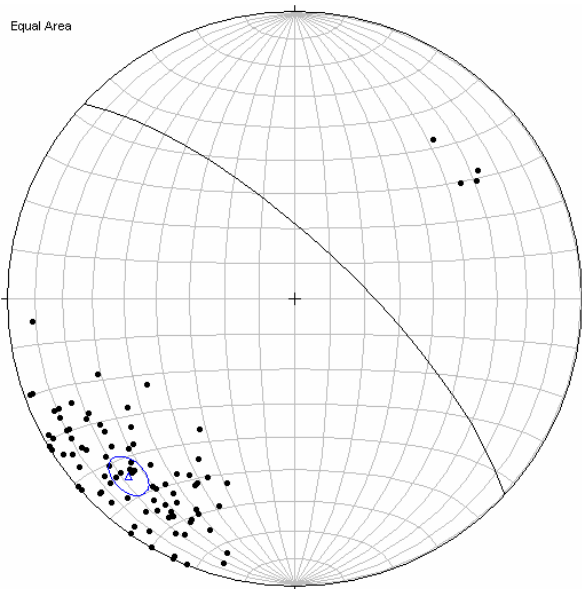
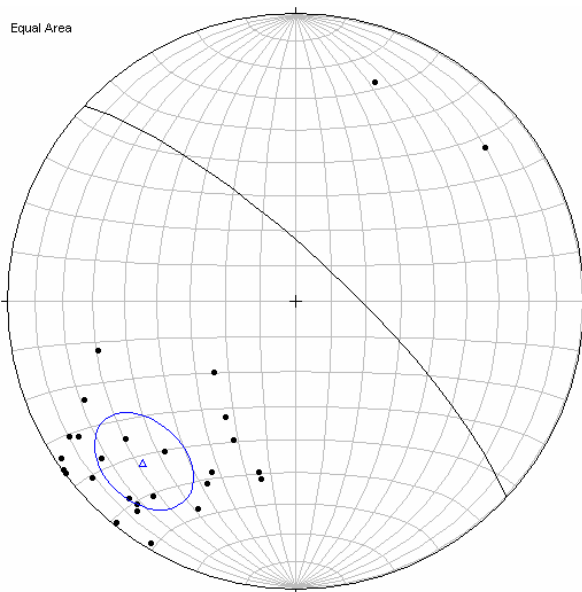


Figure 4-3a-c: Equal area stereonets showing poles to fault planes for the VF, SF and CCF. Mean fault plane shown as great circle and 95% confidence ellipse shown for each data set.

a) Virgin Fault – n = 60, mean fault plane orientation is 132/70N.



b) Spaghetti Faults – n = 94, mean fault plane orientation is 133/74N.



c) Ciao Ciao Fault – n = 28, mean fault plane orientation is 133/77N.

4.4 Virgin Fault

4.4.1 Overview

The Virgin Fault is located within the upper granite gneiss in the west of Passo Moro (Figure 3-1b). There is almost 100% exposure of the VF with only small areas which are not exposed. The VF is a 70 m long right-lateral strike slip fault, it has a mean strike and dip of 132/70N (Figure 4-3a), and has accumulated approximately 10 cm of offset (constrained from an offset aplite dyke). Due to the lack of inactivated process zones³, the VF probably grew from linkage of pre-existing joints e.g. Segall and Pollard (1983) & Pachell & Evans (2002). The VF is an isolated fault as there is no evidence of interaction with other fault zones.

The VF is composed of a central PSS and/or fault core surrounded by a damage zone. The fault core is commonly associated with alteration and mineral precipitation, whereas the damage zone is characterised by an increase in fracture density compared to host rock (Figure 3-7). The width of the fault zone is defined by the size of the fractured area either side of the fault core. In general fault width increases along strike from west to east but thins over a distance of 10 m towards the eastern tip (Figure 4-4).

The VF was sub-divided into five sections (Figure 4-4) with each section separated by either a vertical change in topography and/or an area of no exposure (Figure 4-4). The main problem encountered in observing the fault rocks was the amount of lichen cover in some areas.

³ A process zone is an area of increased fracturing that occurs at the tip of a fault as it propagates through the rock. As propagation continues a new process zone forms at the newly formed fault tip and consequently, a wake of inactive process zones form during growth.

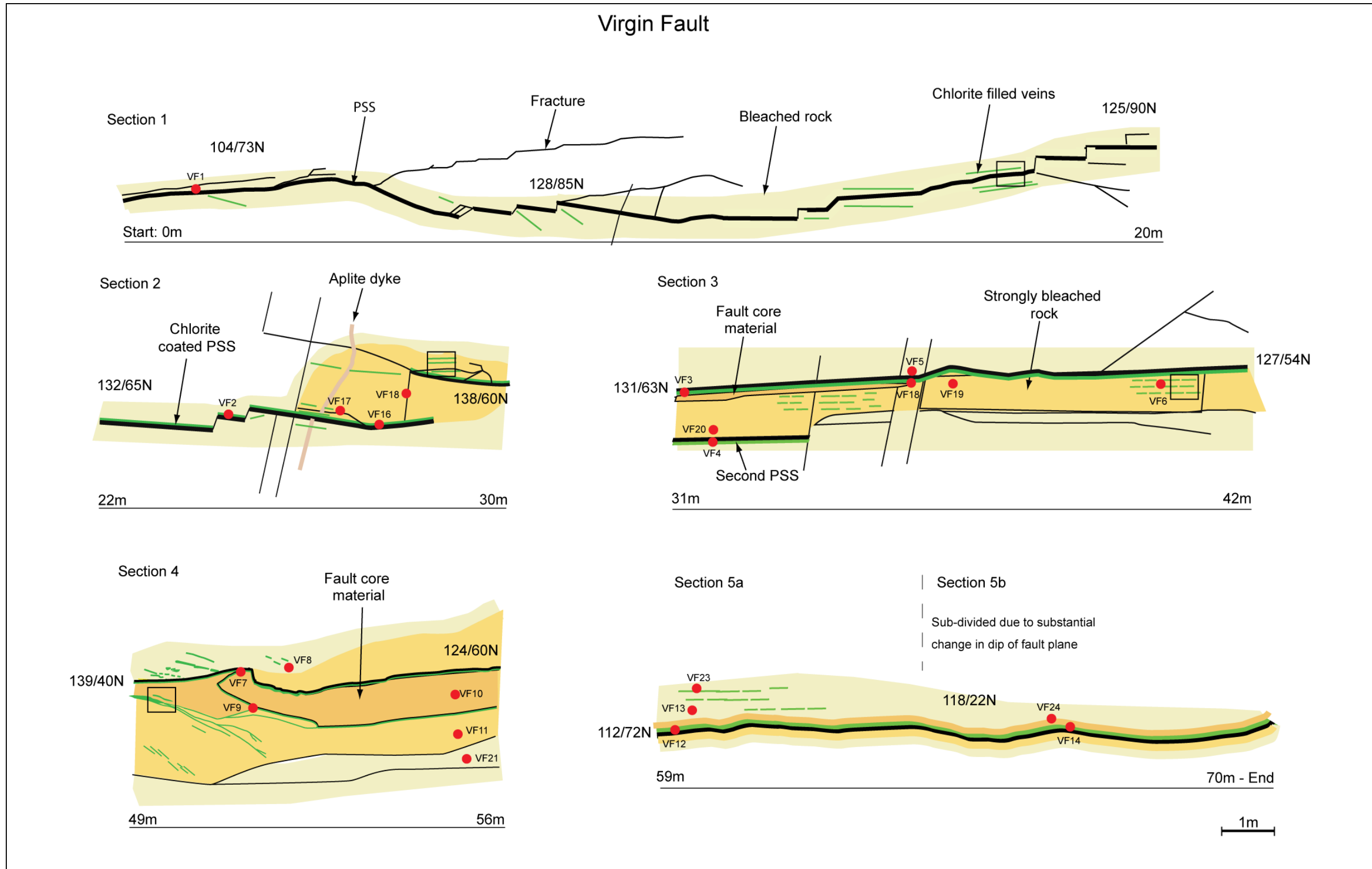


Figure 4-4: Map of the Virgin Fault. Differences in fault rock are highlighted. Chlorite veins and bleached areas are partly schematic. Chlorite veins represent length covered by veins but are not representative of the width or number of individual veins present. More detailed maps have been reproduced of the areas in boxes in Figure 4-10. Gaps in distance between sections due to the changes in topography and/or areas of debris or no exposure. Numbers and red spots = sample numbers and locations. Strike and dip values are from the fault plane adjacent to where the value is located on the map.

4.4.2 Host rock & pre-existing structures

The VF cuts through the upper granite gneiss which is in the west of the field area (Figure 3-1b). The host gneiss is massive and homogenous. There are three sets of joints which formed either pre- or syn-faulting. They are quartz-filled joints oriented 090/90, foliation parallel joints oriented 010/33W, and fault parallel joints oriented 146/74NE.

In the area around the VF, the average joint density (090, 146 & 040 joints) is 1.2/m (Figure 3.8). None of the 090 joints intersect the VF but the foliation parallel joints regularly intersect the fault and their density varies along the length of the fault. On average it is 0.5/m but in section 4 of the VF the density is ~4/m (450 m along the structural log in Figure 3.8).

4.4.3 Principal slip surface

The PSS is semi-continuous for the entire length of the Virgin fault with only a few localities where it is not easily identified (e.g. section 4 Figure 4-5a). The mean strike and dip of the PSS is 132/70N, however towards the eastern end of the fault the dip is as low as 22° (Figure 4-5b). Typically the PSS appears to be a single plane, however detailed examination reveals that the fault contains numerous sub-parallel slip surfaces (Figure 4-4). Multiple slip surfaces are commonly found in sections 1 & 2 (Figure 4-4). In these sections the slip surfaces are 0.5-5 m long. Slip surfaces curve slightly and adjacent slip surfaces are linked by a step/jog which is always in a northward direction (when observed from west to east) (Figure 4-6). The PSS is polished and may be mineralised with quartz and/or chlorite and/or epidote. Slickenlines and striations are frequently preserved on the PSS between sections 2-5 and predominantly record strike-slip motion (e.g. 2→103° and 24→133°). Slickenlines are defined by elongate crystals of quartz, chlorite or epidote. In section 3 of the fault there are two sub-parallel PSSs which at the lower level of exposure are not connected (Figure 4-4). The northern most PSS extends for the entire length of section 3 (11m) while the southern PSS only extends for 4m. The southern PSS at section 3 has a strike and dip of ~124/67N, is mineralised and preserves slickenlines which have an orientation of 47→127° which is more indicative of dip-slip motion.

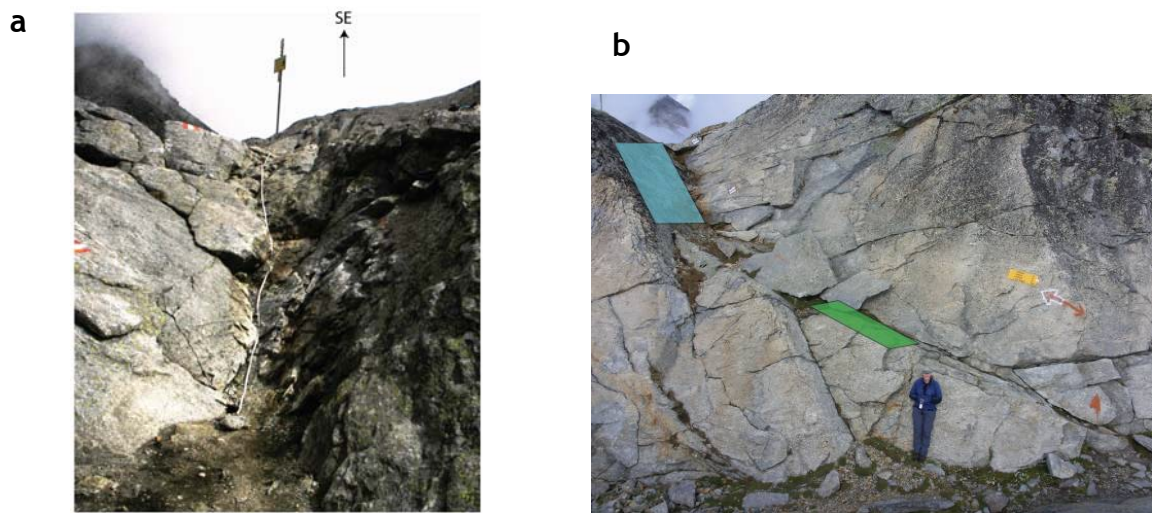


Figure 4-5: Principal slip surface within the VF.

a) Section 4 of the VF – note no well defined PSS, tape measure lies along approximate line of the PSS. grid ref: 641961, 094224 b) Change of dip of the PSS along section 5 of the VF. Blue plane shows dip on fault plane of $\sim 65^\circ\text{N}$ while green plane shows how dip has shallowed to 22°N . Photo taken looking west, grid ref: 641975, 094214.

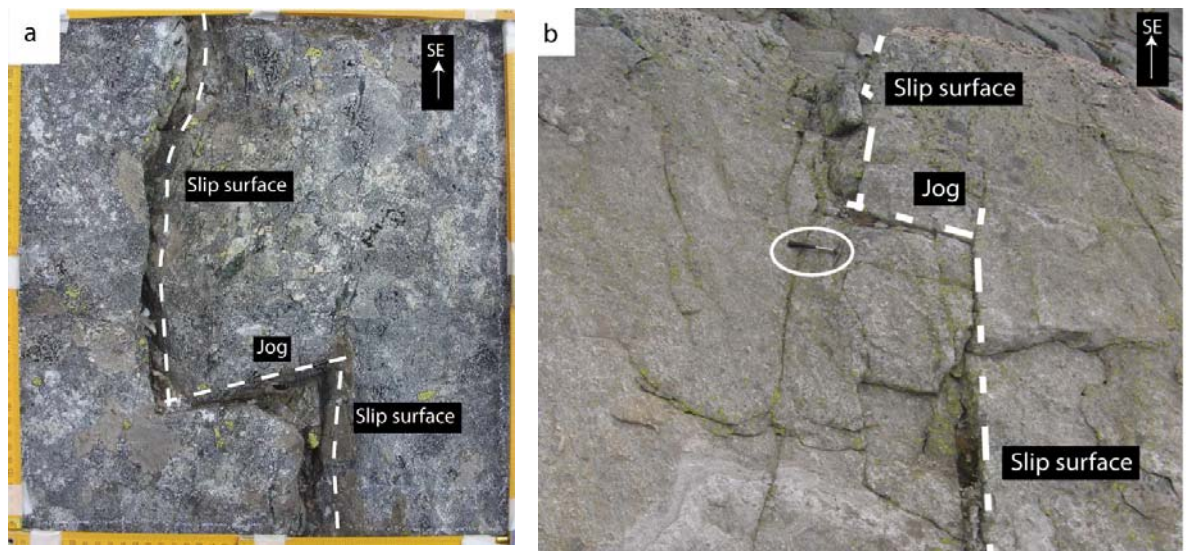


Figure 4-6: Jogs along the PSS of the VF.

a) 15cm jog in section 1. Square = 40x40cm, grid ref: 641925, 094236. b) 1.3 m jog in section 2, hammer for scale (circled), grid ref: 641928, 094222.

4.4.4 Fault core

The fault core of the VF is discontinuous along strike. Core material (breccia and cataclasite) is present from section 2 through to section 5 and it varies in thickness from 3 mm to 75 cm (Figure 4-4). The main fault core rocks are cataclasite and/or breccia (Figure 4-7) and they are typically composed of white (feldspar) and/or clear glassy (quartz) fragments in a dark green (chlorite) and/or light green (epidote) matrix. Where the core material is only a few

millimetres thick it is dark green, no fragments are observed and microscopic analysis is required to identify what the fault core components are.

In section 2 the core is up to 5 cm thick. The breccia is visible by eye but cataclasite is only distinguished by microscopic analysis. In sections 3-5 the fault core is greater than 5cm thick and the breccia and cataclasite can be distinguished apart. The cataclasite and breccia either coexist together with the bands of cataclasite cross-cutting the breccia (Figure 4-8) or the two rock types are separate units which are adjacent to each other (Figure 4-7).



Figure 4-7: Core material from section 5 of the VF. Cataclasite and breccia are easily distinguished apart. Sample VF14.

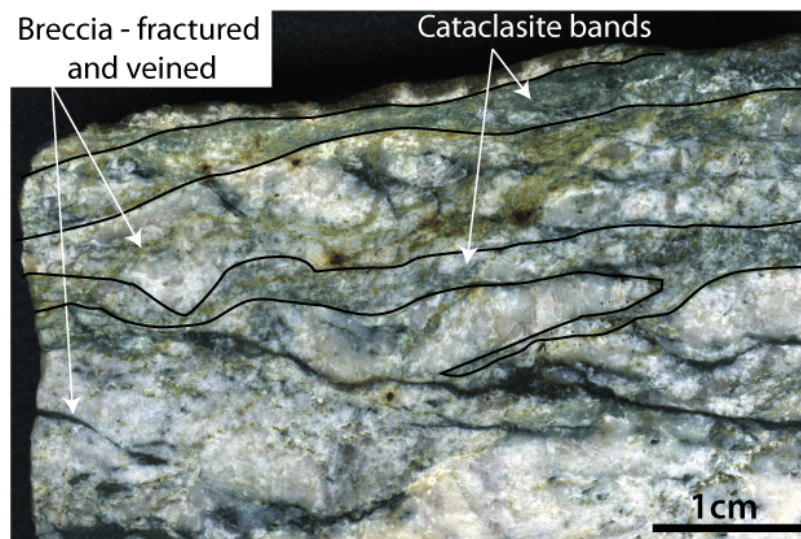


Figure 4-8: Slice cut through the core material from section 3 in the VF. The core material is composed of breccia with cross-cutting bands of cataclasite. Sample VF3.

4.4.5 Damage zone

The damage zone of the VF is characterised by veins, chemical alteration (or bleaching) and fracturing. These components can occur individually or in any combination. The most obvious feature of the damage zone are the fractures and it is the increased fracture density compared to host (0.5/m) that is used to demarcate the limits of the fault zone. The dominant fracture orientation is fault parallel (~132/70N), however the orientation does vary from approximately 117-151° and dip from 22-87°. 040/90 fractures also occur in the fault zone but the cross-cutting relationships indicate that they formed post-faulting (3.4.2.2).

Fault parallel fracture density is highest adjacent to the PSS but the width of the zone of increased fracturing varies along the length of the VF (Figure 4-9). The fault zone width increases from 0.4m in section 1 to 3.8 m in section 4 and decreases to 1.8 m in section 5 (Figure 4-9). In general the width of increased fracturing is asymmetric with respect to the PSS with the width of fracturing being greater on the northern side. In section 4 the distribution of the zone of increased fracturing is symmetrical about the PSS and in section 3 where there are two PSSs; increased fracturing occurs between the two slip surfaces (Figure 4-9).

Bleaching or whitening of the rock occurs in all sections of the VF (Figure 4-4). Bleaching has been subdivided into minor and intense bleaching. Minor bleaching causes a subtle change in colour (e.g. section 1 Figure 4-10) whereas intense bleaching produces bright white rocks (e.g. section 4 Figure 4-10). Minor bleaching occurs throughout the entire fault zone (Figure 4-4) and the width of the zone of minor bleaching mimics the fault zone width along strike. Intense bleaching of the fault rock occurs immediately adjacent to the PSS and/or core material in sections 2-5 (Figure 4-4 and section 4 Figure 4-10). The width of the zone of intensely bleached material is variable along the fault from approximately 0.4 m to 2 m (Figure 4-4). The widest zone of intensely bleached fault rock occurs where the fault zone is at it widest (Section 4 Figure 4-4). The transition from intensely bleached to minor bleaching is gradational and typically occurs over a distance of several centimetres.

Veins occur throughout the damage zone of the VF and are primarily chlorite- and/or epidote-filled, with the former being more common (Figure 4-4). At the outcrop scale veins and/or small masses of epidote (Figure 4-11) tend to be restricted to sections 2 and 3, however more epidote veins were observed in thin section from this part of the fault. Chlorite veins tend to be restricted to the intensely bleached rock and/or within approximately 50 cm of the PSS (Figure 4-4).

Chlorite veins range from 5 mm to 30 cm long and aperture varies from approximately 1-2 mm to 2.5 cm (Figure 4-10). Chlorite veins tend to be shorter, thinner and more isolated in section 1 but length, width and connectivity increase towards the east through to section 4 (Figure 4-10). In section 4, chlorite veins are common throughout but they are concentrated along the PSS and at the boundary between the fault core and damage zone rock (Figure 4-4 & Figure 4-10).

The orientation of the fault and the nature of the exposure at section 5 did not permit a thorough analysis of the chlorite veins in this section. Some chlorite veins occur at the north western part of section 5a (Figure 4-4) and the aperture and connectivity is similar to that observed in section 4 (Figure 4-10). However no chlorite veins were observed throughout the rest of the damage zone in section 5.

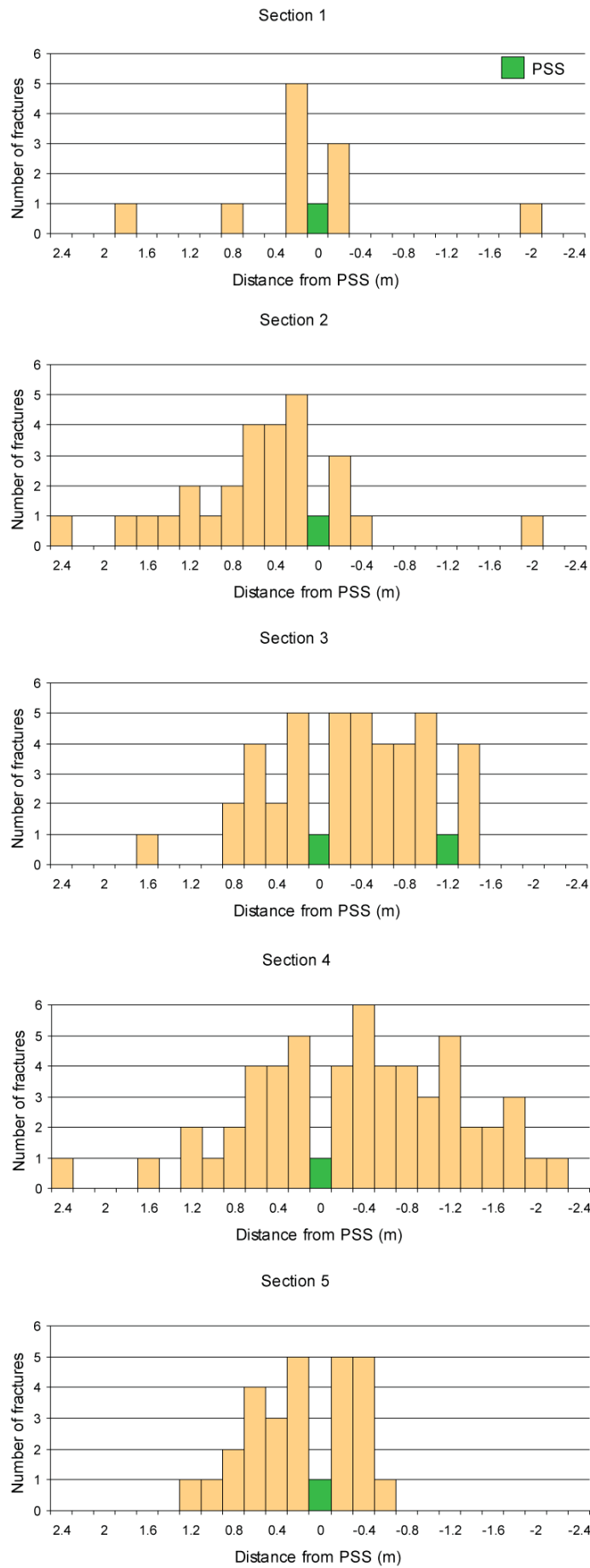


Figure 4-9: Fracture counting transects across the VF in sections 1 to 5. Transects were NE-SW and positive and negative numbers represent NE and SW of the PSS respectively.

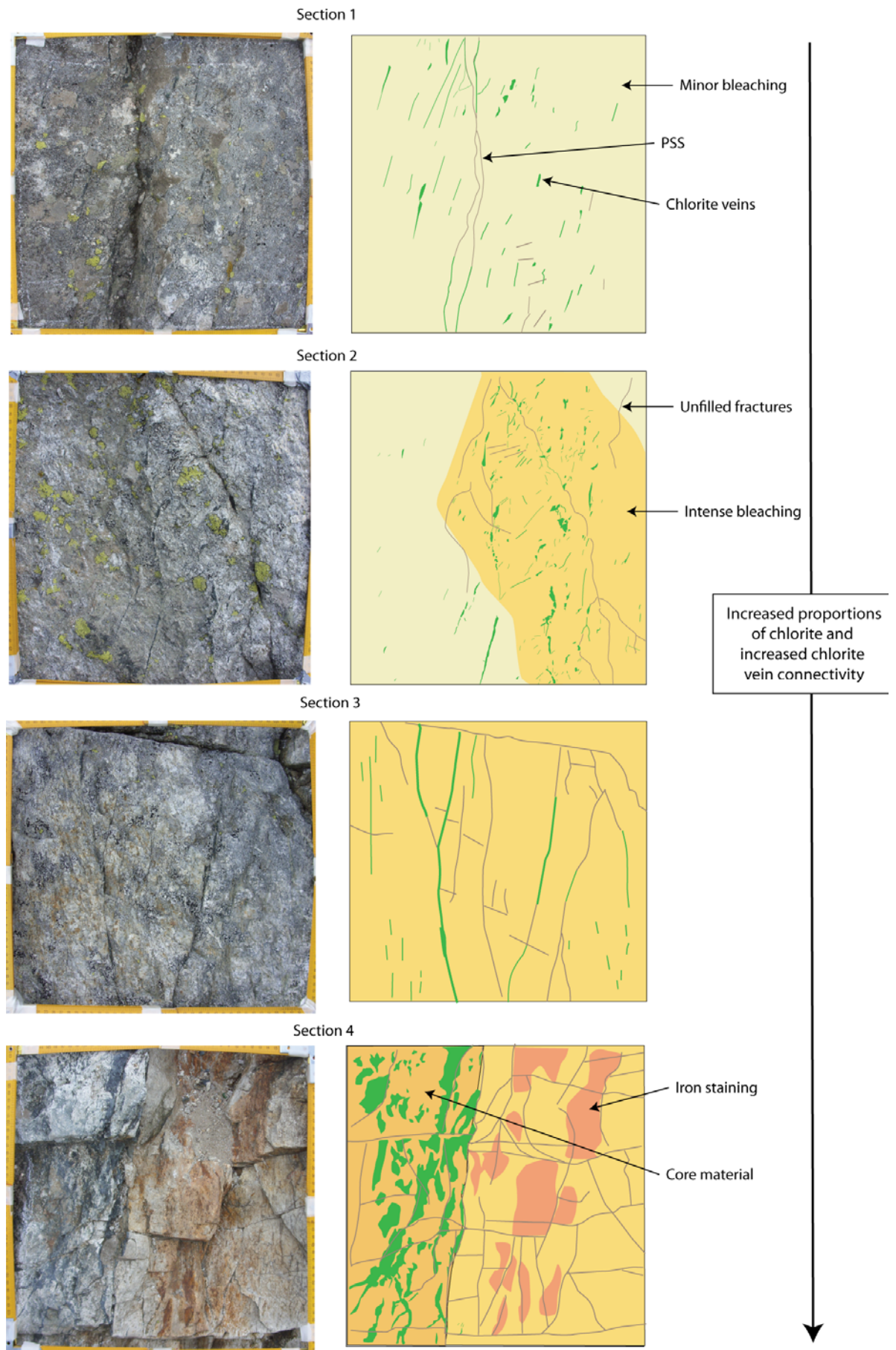


Figure 4-10: Veining and bleaching along strike of the VF. Each square is 40x40cm and the location of each square within the VF is shown in Figure 4-4.

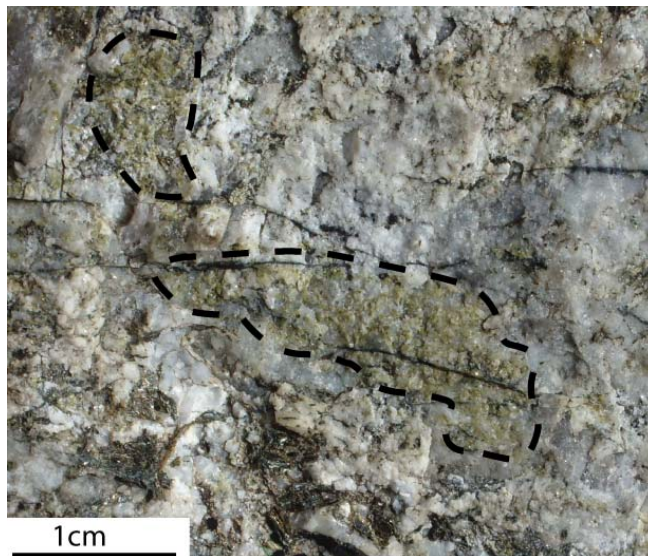


Figure 4-11: Pale green epidote masses in section 3 of the VF. Epidote masses highlighted by dashed line. Photo taken looking down onto the fault. Grid ref 641952, 094214.

4.5 Spaghetti Fault

The Spaghetti Fault is located in the eastern part of Passo Moro. The SF cuts through the lower granite gneiss, metasedimentary rocks and amphibolite (Fig 3-1b). The fault is composed of numerous sub-parallel fault strands (Figure 4-12) of which each strand has an average strike and dip of 133/74N (Figure 4-3b) and strand length varies between 50 to 200 m. Adjacent strands may be connected by or have splay faults that are 20-50 m long and are oriented 20-40° clockwise of the main strands (Figure 4-13). Fault strands are spaced approximately 10-15 m apart however within the metasedimentary rocks the spacing typically decreases to approximately 5-6 m. Due to increased weathering in the east of Passo Moro much of the fault zone is covered in rubble and/or snow (Figure 4-12) making it difficult to describe the faults in this area and assess the relationship between different fault strands.

The SF is a right lateral strike slip fault and each individual strand has accumulated approximately 5 cm of offset (constrained from an offset quartz vein). As with the VF, due to the lack of deactivated process zones it has been thought that the SF grew by linkage of pre-existing structures. The faults are composed of a PSS and a damage zone but fault core material is observed on any of the fault strands. In general a SF strand is marked by increased fracturing or an area of no exposure adjacent to the PSS.

The SF was mapped for 220 m along strike but it was estimated from aerial photos that the fault extended for approximately another 100 m (Figure 4-12). The following descriptions of the Spaghetti fault zone components will be for a typical fault strand within the SF and is applicable to all of the fault strands unless otherwise stated.

4.5.1 Host rock and pre-existing structures

The SF primarily cuts through granite gneiss including the lower granite gneiss, the metasedimentary rocks and the variable upper gneiss. The lower gneiss and upper variable gneiss are compositionally, mineralogically and texturally heterogeneous with variations in grain size, augen content and number of intrusions (Fig 3-2). Therefore the SF not only cuts through different rock types but the primary host rock (granite gneiss) is itself extremely variable.

Average joint density (090, 146 & 040 joints) in the rock that encompasses the SF varies from 2.4/m in the variable upper gneiss to 4/m in the lower gneiss (Fig 3-8). Along the fault the foliation parallel joint density is also extremely variable. In the lower gneiss it is 2-15/m; in the metasedimentary rock it is 10-25/m; and in the variable upper gneiss it is 2-9/m (Fig 3.8).

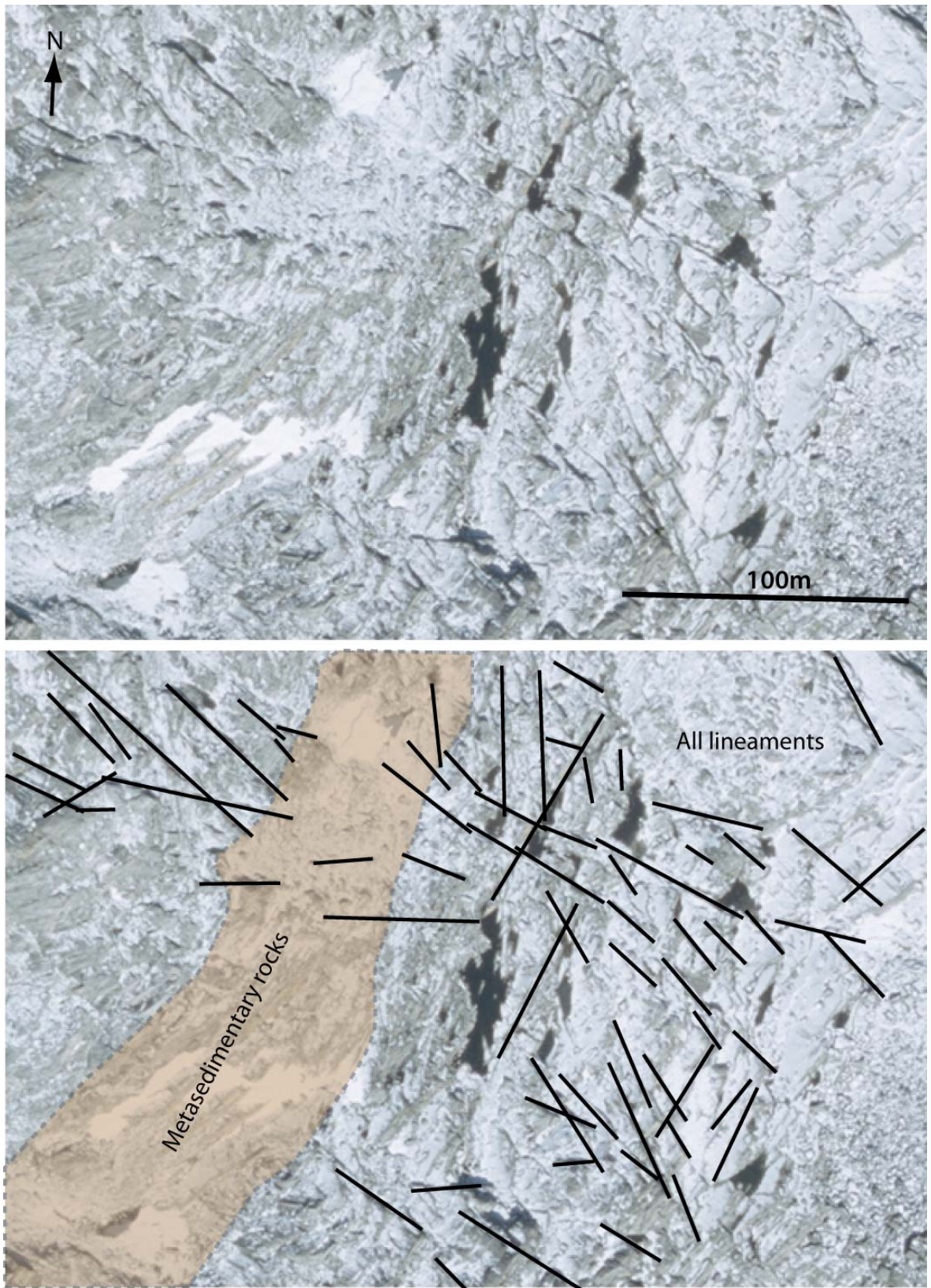


Figure 4-12: Aerial photo of the area encompassing the Spaghetti Fault. Lower image highlights where the metasedimentary rocks are located and lineaments that cross cut the area. Note that within the metasedimentary units very few structures can be picked out and due to the low lying nature of the ground snow tends to gather in this area. Lineaments include all structures in the area as well as the fault related lineaments. Source of airphoto – Toposhop, date taken: 14/09/05.

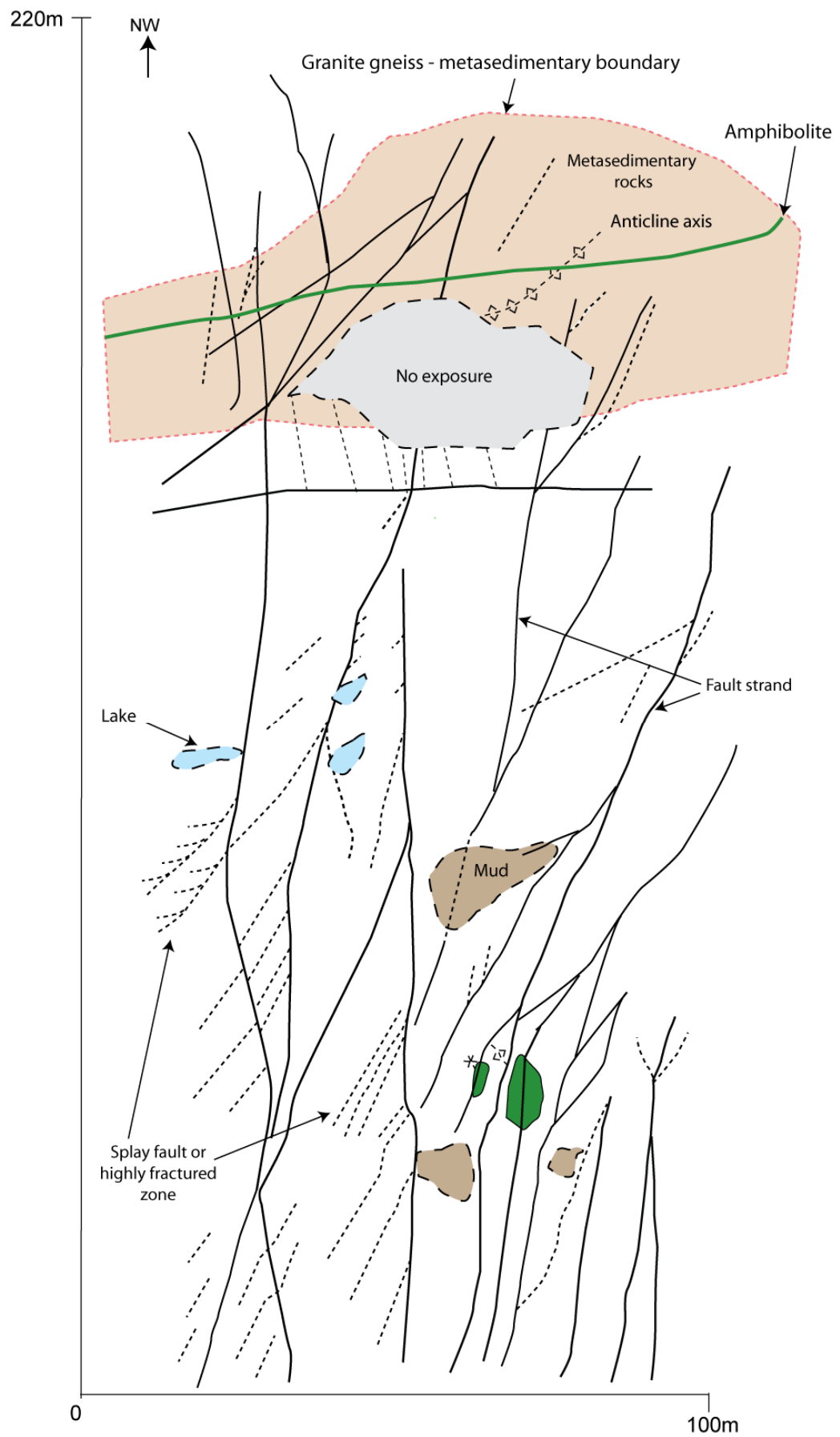


Figure 4-13: Map of the Spaghetti Fault.
 The main strands strike $\sim 133^\circ$ while the splay faults are oriented $\sim 150^\circ$.

4.5.2 Principal slip surface

The PSS is curvi-planar, and semi-continuous for the entire length of an individual strand of the SF. The PSS curves and undulates along strike and it is usually the most recognisable feature within the fault zone. This is due to the lack of rock exposed adjacent to the PSS and thus the PSS is often fully exposed (Figure 4-15a). The only place where the PSS is not observed is where rubble covers the entire fault zone. Due to the large number of faults and joints in the area it is difficult to assess whether fault jogs occur or whether the PSS is simply an adjacent structure.

The mean orientation of the PSS is 133/74N however, a 1% area contour plot shows three distinct groups of structures which have a strike and dip of approximately: 128/69N; 136/71N; and 147/82N (Figure 4-14). The mean fault orientation of the SF throughout the field area is approximately 133/70N (Figure 4-3) and the mean orientation of the fault parallel joints is 146/74N (Fig 3-8). Thus the main fault strands and fault parallel joints would correlate with the 136/71N and 147/82N slip surfaces respectively. The slip surfaces which are oriented 128/69N can not be correlated to the average fault or joint orientation and so are likely to be splay faults that are newly formed as a result of faulting processes.

The PSS is smooth and polished and is typically not mineralised, but at several locations small amounts of chlorite and/or quartz coat the PSS. Where the PSS is coated slickenlines and/or striations are usually preserved. Slickenlines are defined by elongate chlorite crystals and indicate dextral strike slip movement (e.g. 5→136° and 9→141°).

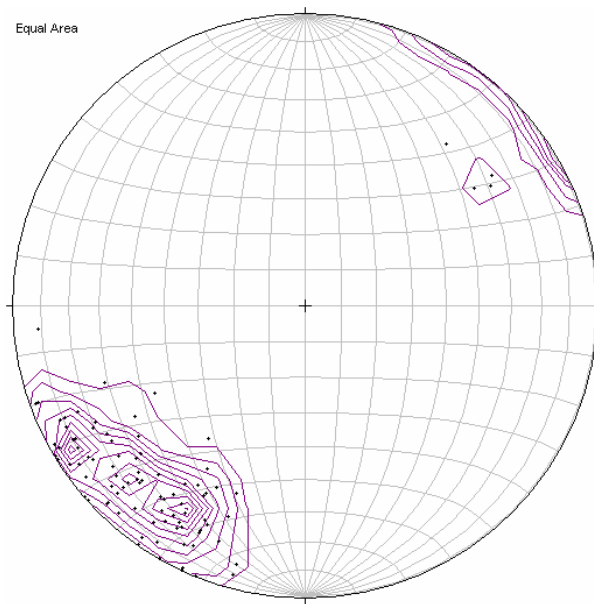


Figure 4-14: Equal area stereonet of poles to plane for all PSS measurements within the SF. Stereonet has been overlaid with a 1% area contour map. Results show three clusters of results. N=94

4.5.3 Damage zone

The damage zone in the SF is dominated by high fracture density with chlorite veins and bleaching rarely observed. The width of the zone of increased fracturing (perpendicular to the PSS) is typically ca. 1.5 m and is used as a proxy for fault width as little fault related deformation is observed outside this zone (Figure 4-15a). This appears to be reasonably consistent along strike except for where two faults intersect or a splay fault occurs; at these locations the fault width can be up to 8 m. However, for approximately 50% of the length of the SF the hanging wall has been removed by erosion (Figure 4-15b). This means that the estimate of an average fault width of 1.5m may not be typical of the whole fault.

Where the entire damage zone is observed, the damage is often preferentially concentrated on the hanging wall side of the fault zone (Figure 4-15a). The width of the zone of increased fracturing within the footwall is usually only 10-20 cm while in the hanging wall it is approximately 1-1.2 m wide. Increased fracturing in the hanging wall gneisses may in part explain why the hanging wall is often eroded out.



Figure 4-15: Characteristic features of the Spaghetti Fault.

a) The photo shows that the damage zone material has been eroded out adjacent to PSS on the hanging wall. Locality 2. Photo taken looking NW. b) Photo shows that the zone of increased fracturing is concentrated on the hanging wall side. Locality 3. Photo taken looking WNW.

An eroded out hanging wall is common along strike of the SF. These areas are typically either associated with closely spaced fault strands or a high density of foliation parallel joints (e.g. Figure 4-16). The fault zone is most eroded where the SF intersects the metasedimentary rocks. However, in the vicinity of this area the fault strands are spaced approximately 5-6 m apart and within the metasedimentary rocks the foliation parallel joint density is high (~10/m). Due to the nature of these areas it is difficult to assess whether the damage is a result of faulting or simply due to the host gneisses being highly fractured.

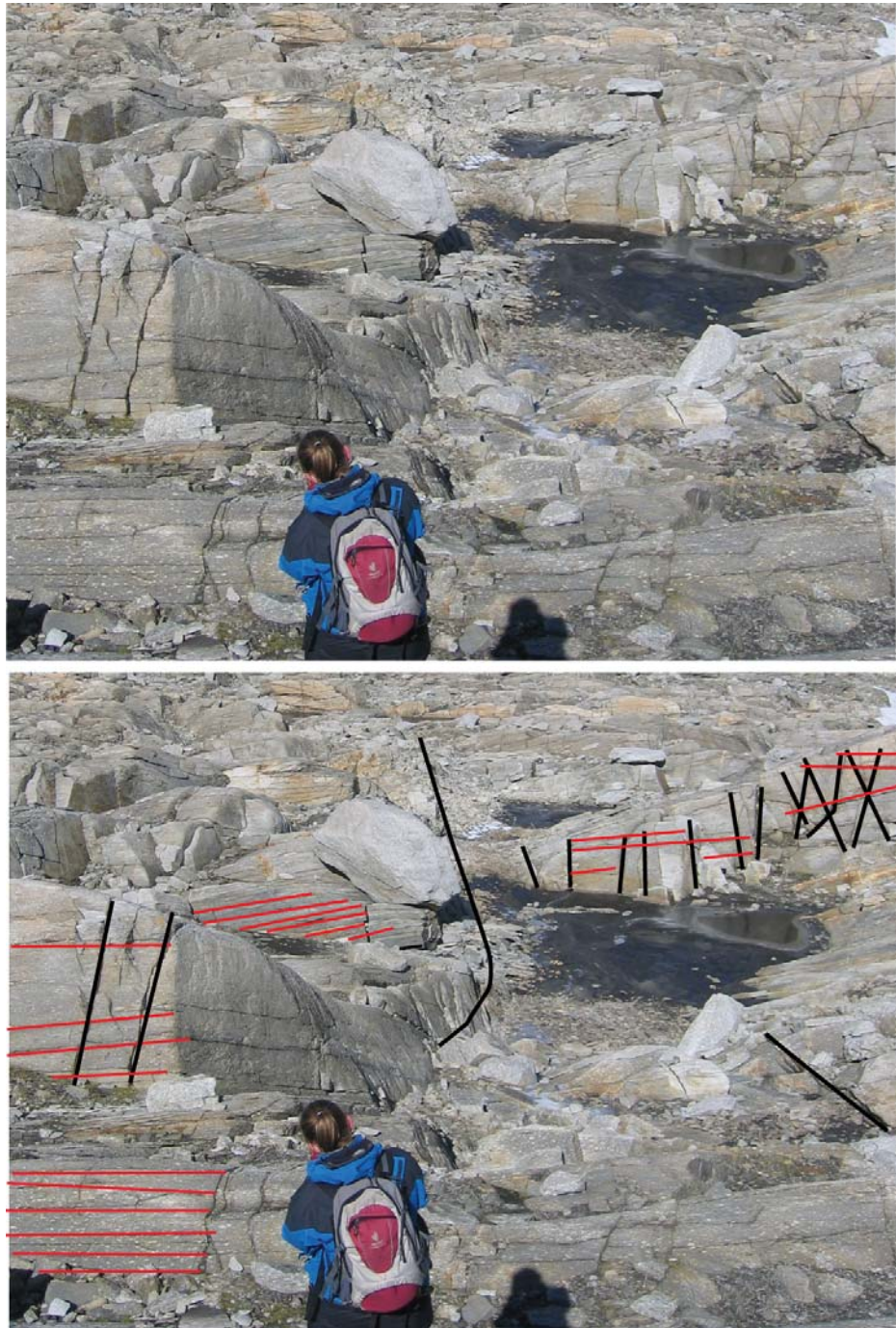


Figure 4-16: Mud pool along the Spaghetti Fault.

Mud pool coincides with the intersection of two or more fault strands and an area where the foliation parallel joint density is high. The faults (black lines) and foliation parallel joints (red lines) are highlighted in the lower image. Locality 4. Photo taken looking WNW.

4.6 Ciao Ciao fault

The CCF is the largest fault zone in the field area and it cuts through the upper and lower granite gneiss, metasedimentary rocks and amphibolite (Figure 3-1). The CCF is a dextral strike slip fault, it is oriented $\sim 133/77N$, and has accumulated a minimum of 250 m of offset (constrained by an offset amphibolite sheet) (Figure 4-17). The CCF was mapped for 800 m along strike but neither

fault tip was found. Based on remote sensing data from Bistacchi et al. (2000) and analysis of aerial photographs the estimated length of the CCF is 10 km (Figure 2-7).

The CCF is less well exposed than the VF and SF and there is apparently limited variability in the architecture along strike. The fault trace is typically expressed as a gully ~15-25 m wide, it is rubble or snow filled, although fault rocks are locally exposed (Figure 4-17). The gully is used as a proxy for fault zone width as deformation is limited beyond the gully walls. The fault zone is composed of a zone of highly fractured rock bounded by two sub-parallel approximately planar faults. The bounding faults are characterised by a PSS embedded within fault core material.

4.6.1 Host rock and pre-existing structures

The CCF has a NW-SE orientation and cuts through all of the different lithologies at Passo Moro (Figure 4-17). It intersects all of the pre-existing joint sets and also all of the zones of joint density variation.

4.6.2 Principal slip surfaces

The PSS's is exposed at several localities along strike of the CCF. Where it is exposed it is curvi-planar and the trace of the PSS undulates along strike. The best exposure of the PSS is at locality 5 where the transition from host rock to fault core is well exposed (Figure 4-18). At this location two slip surfaces can be identified: one between the damage zone and the breccia; and another between the breccia and the fault core. Both slip surfaces are sharp, planar and oriented 101/49N and 108/39N respectively. Where a portion of a slip surface is exposed it is often polished and chlorite coated.

Schematic cross section of northern most bounding fault - note how fault width varies along strike and also what fault components occur.

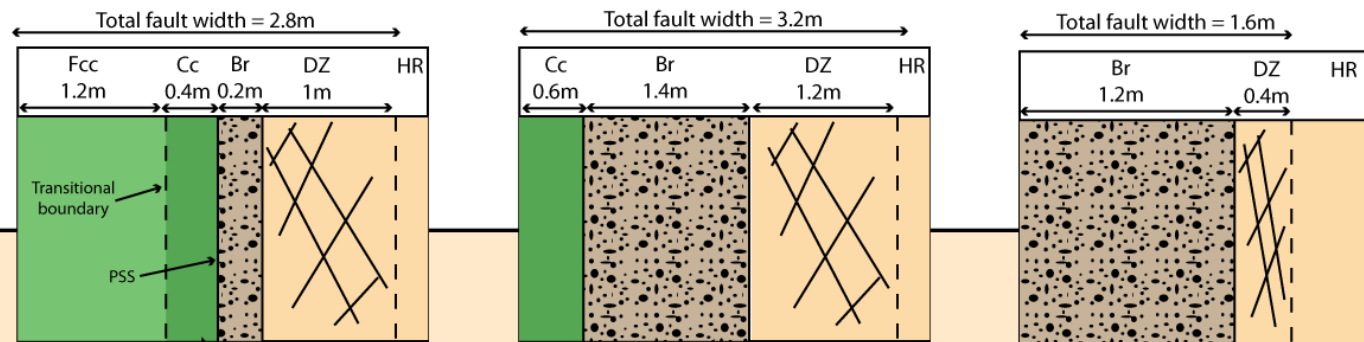
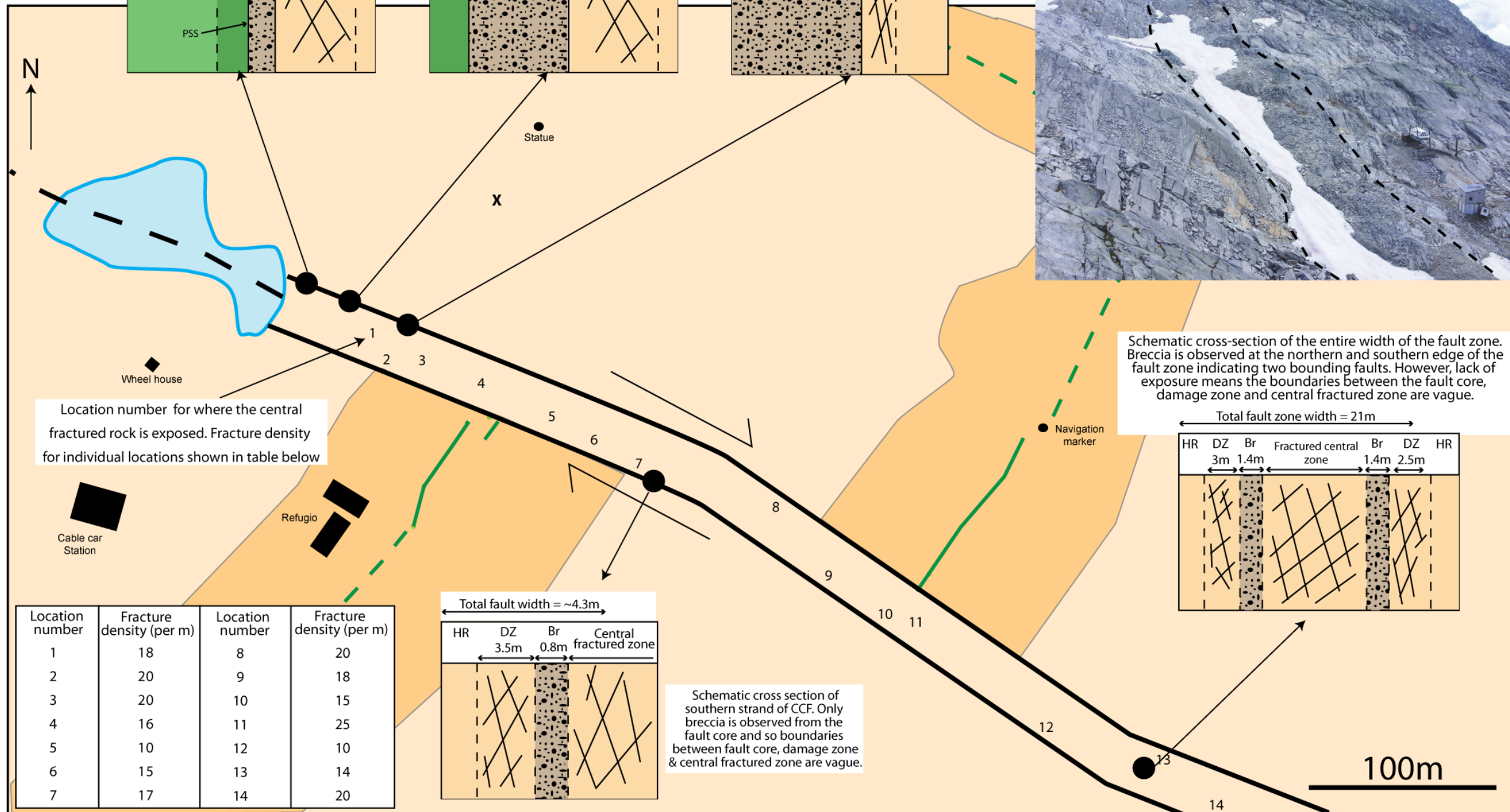


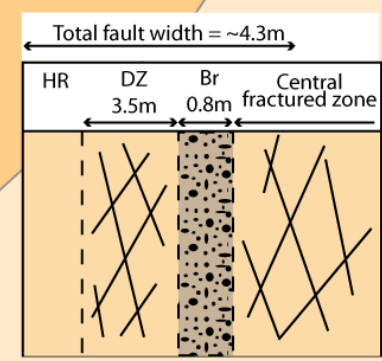
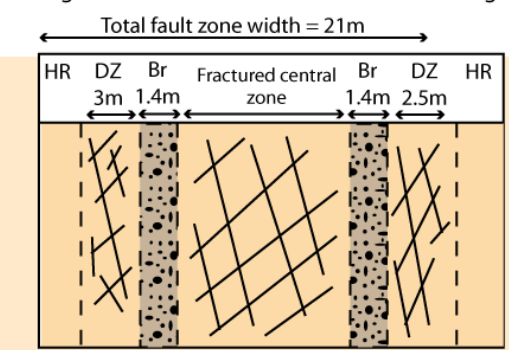
Photo taken from location X (this map) looking along the CCF towards the SE. Dashed lines mark the inferred location of the two boundary fault. End of fault in photo correlates to approximately location 12 on the CCF fault map.



Location number for where the central fractured rock is exposed. Fracture density for individual locations shown in table below

Location number	Fracture density (per m)	Location number	Fracture density (per m)
1	18	8	20
2	20	9	18
3	20	10	15
4	16	11	25
5	10	12	10
6	15	13	14
7	17	14	20

Schematic cross-section of the entire width of the fault zone. Breccia is observed at the northern and southern edge of the fault zone indicating two bounding faults. However, lack of exposure means the boundaries between the fault core, damage zone and central fractured zone are vague.



Schematic cross section of southern strand of CCF. Only breccia is observed from the fault core and so boundaries between fault core, damage zone & central fractured zone are vague.

Figure 4-17: Ciao Ciao Fault map.

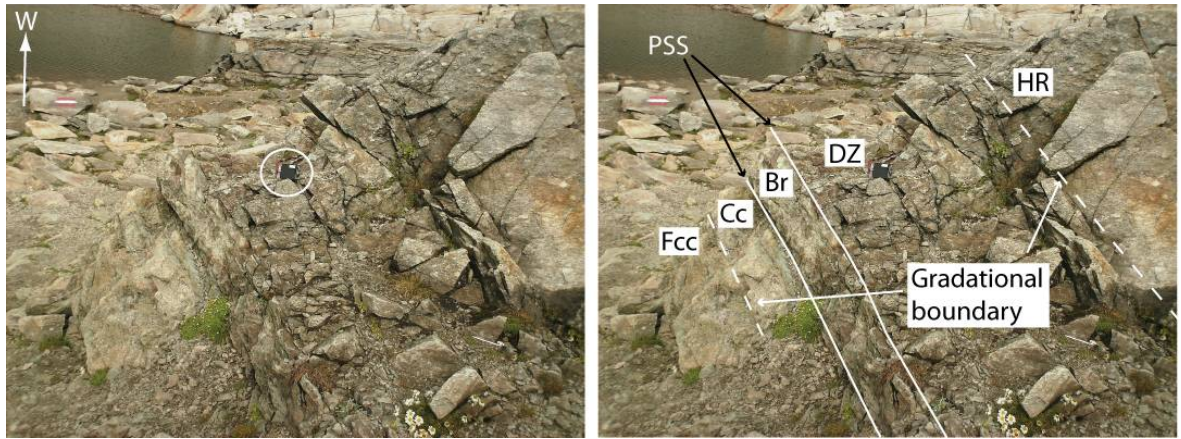


Figure 4-18: Transition from host rock to foliated cataclasite within the CCF. The principal slip surfaces (PSS) and boundaries between the different rock types are highlighted. Fault core is composed of foliated cataclasite (Fcc), cataclasite (Cc) and breccia (Br). Solid white lines indicate a sharp boundary while dashed lines indicate a more gradational boundary. DZ = damage zone, HR = host rock. Compass-clino for scale (circled). Locality 5.

4.6.3 Fault core

The FC is composed of breccia, cataclasite and foliated cataclasite (Figure 4-18). The breccia is pale green and composed of clasts which are 0.2-2 cm in diameter. The clasts are angular and there is no fabric within the rock. The boundary between the breccia and damage zone is not always defined by a slip surface. Where there is no slip surface the boundary is still sharp but is also lined by red-brown clay-like material (Figure 4-19). The cataclasite and foliated cataclasite are predominantly pale green with smears of red/brown clay-like material throughout. Foliated cataclasite and cataclasite are composed of angular and matrix supported fragments which are 1-10 mm in diameter. The matrix is pale green and fine grained. Within the foliated cataclasite the foliation is oriented 146/88N, with a spacing of 0.5 cm between foliation planes. Veins of K-feldspar also cross-cut the cataclasite and the foliated cataclasite and vary in length (2-8 cm) and width (0.1-2 cm).

Exposures of the core material are limited along the CCF (Figure 4-17). However, where they occur the proportions of the different core components are variable along strike and in some instances certain components are not present (Figure 4-17). On the northern bounding fault all of the different core components are present, whereas in the southern bounding fault only breccia is exposed.



Figure 4-19: Clay-like material at the boundary between the host rock and breccia. Locality 6.

4.6.4 Damage zone

The damage zone along the CCF is narrow (Figure 4-17). It typically varies from 1-5 m wide along strike on both the northern and southern boundaries and is characterised by a high density of fracturing and incipient alteration. No chlorite coated surfaces are present in the damage zones for the entire mapped length of the fault. Fracture density increases towards the fault core (Figure 4-20) but the boundary between the damage zone and fault core is sharp (Figure 4-18).

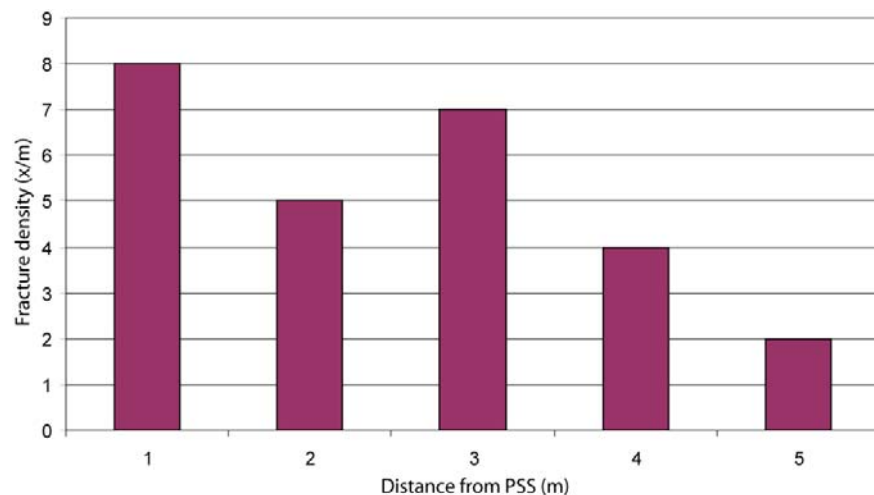


Figure 4-20: Fracture density changes away from the PSS in the CCF at locality 5.

Between the two bounding fault zones the central area is composed of highly fractured rock and is similar to damage zone material - fractured and effected by fluid-rock alteration. Several exposures in the central area occur along strike (Figure 4-17). The material is strongly fractured and the mean fracture

orientation is 138/76N, however a 1% contour map indicates two fracture populations: 149/84N and 130/74N. Throughout the central area, the fracture density for both fracture populations combined is approximately 20/m (Figure 4-17). Fractures oriented at 040/90 also cross-cut the central area and where the 138/76N and 040/90 fractures intersect the gneisses are friable (Figure 4-21). The material in the central zone is strongly bleached, fractures are chlorite coated and where slickenlines are preserved they indicate strike-slip motion ($9^{\circ} \rightarrow 143^{\circ}$).



Figure 4-21: Central fractured zone of the CCF. Fracture density is high within the central fractured zone and the rock is friable (arrowed). Photo taken looking NW at locality 7.

4.7 Discussion

Three fault zones have been described: the VF, SF and CCF. The fault zones are all dextral strike slip faults, they range in length from 70 m (VF) to ~10km (CCF), have accumulated several centimetres (SF & VF) to 250 m (CCF) of offset, and have very different architectural styles. Each fault will be discussed in terms of its architectural style, a schematic architectural model presented, and then the faults will be compared in terms of architectural differences (VF and SF) and faulting conditions (VF & CCF).

4.7.1 Fault architecture

4.7.1.1 Virgin Fault

The VF cuts the homogenous upper gneiss and the fault is composed of a central PSS, with or without a fault core, and a damage zone. Where present the fault core may be several millimetres thick or up to ~1 m thick (Figure 4-4). Core material includes breccia and cataclasite. There can be multiple strands of cataclasite cutting the breccia (Figure 4-8) but a cataclasite band is always adjacent to the PSS. The damage zone is characterised by fractures, veins and bleaching. All three damage zone components vary along strike but the damage zone is most intense in section 4 where the fault is at its widest (Figure 4-4).

Compared to published architectural models, the VF would be akin to the San Gabriel Fault (Figure 4-1a) as described by Chester et al. (1993). The basic morphology of the VF and San Gabriel Fault are very similar, with both having a central fault core surrounded by a damage zone. However, there are many differences between the two faults (Table 4-1). In terms of size, displacement and faulting conditions; the San Gabriel fault is more mature, has accumulated ~22 km more displacement, and faulting was at relatively shallow depths (2-5km) compared to the VF (seismogenic depths - 7-15 km). The fault core of the San Gabriel fault is composed of a central ultracataclasite surrounded by foliated cataclasite while the VF has a PSS whereas may be surrounded by a fault core of cataclasite and breccia. The damage zone of the San Gabriel Fault contains fractures and subsidiary faults and is tens of metres wide whereas in the VF the damage zone contains fractures, veins and bleached material and is decimetres up to 3.5 m wide. Hydrothermal minerals in the San Gabriel fault are dominated by zeolites and clays whereas the VF is dominated by quartz, K-feldspar, chlorite and epidote.

Property	Fault	Virgin Fault	San Gabriel Fault
Length		70m	140km
Displacement		~10cm	22km
Depth of faulting		7-15km	2-5km

Table 4-1: Properties of the VF and San Gabriel Fault.

The two fault zones are different in terms of size, displacement, depth of faulting and fluid-rock interactions. As a fault continues to deform it accumulates damage, and the fault rocks can evolve and grow with time e.g. damage zone rock is incorporated into fault core material (Billi et al., 2003). The differences in maturity of the VF and San Gabriel fault may explain the differences in the volumes of fault rock observed and types of fault rock. The architectural model proposed by Chester et al. (1993) (Figure 4-1a) may be suitable for mature faults cutting crystalline rock at shallow depths. The VF was exhumed from seismogenic depths (Figure 2-5), it has accumulated a small amount of displacement, it cuts a homogenous host rock in terms of lithology and pre-existing structures, and records no interaction with other faults. A schematic representation of the VF architecture is shown in Figure 4-22 and can be used as an analogue for small immature faults in homogenous rock at seismogenic depths.

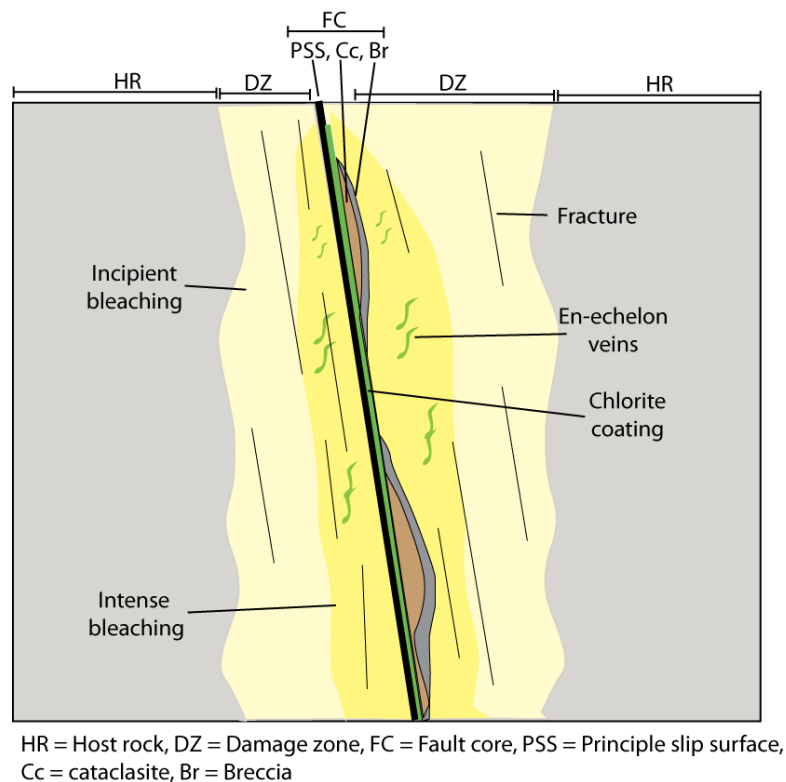


Figure 4-22: Schematic representation of the VF.

4.7.1.2 Spaghetti Fault

The SF cuts the lower gneiss, metasedimentary rocks and variable upper gneiss. The fault is comprised of numerous sub-parallel fault strands, where each

individual strand is composed of a PSS and damage zone with no obvious core material. The damage zone contains fractured rock and alteration is incipient. The average fault width is 1.5 m, however where faults intersect and/or where foliation parallel joint density is high, the fault width can be up to several metres.

The SF is very similar to the Gole Large Fault zone as described by DiToro & Pennacchioni (2005) (Figure 4-1c). Both faults cut crystalline basement, have been exhumed from seismogenic depths, and are composed of numerous sub-parallel fault strands. In both locations there is a large population of pre-existing fault parallel joints with density of 1.6/m around the Gole Larghe Fault and 4/m around the SF. The main differences between the faults are offset and fault rock types. The individual strands within the Gole Larghe Fault have accumulated decimetres to metres of offset and are primarily composed of a PSS and core rock (cataclasite and pseudotachylite). Strands of the SF each strand may have accumulated several centimetres of offset and are composed of a PSS and damage zone material (fractured rock).

The Gole Larghe Fault description does not include host rock or damage zone variations. The host rock of the SF is heterogeneous and there is a high density of foliation parallel joints (which are perpendicular to faults) as well as the fault parallel joints. The SF is composed mainly of damage zone material and where two faults intersect the damage zone is wider. A schematic representation of the SF architecture is presented in Figure 4-23 and highlights how fault spacing is closer in areas where the foliation parallel joint density is higher. The image also includes the damage zone width and how it varies in response to fault intersections.

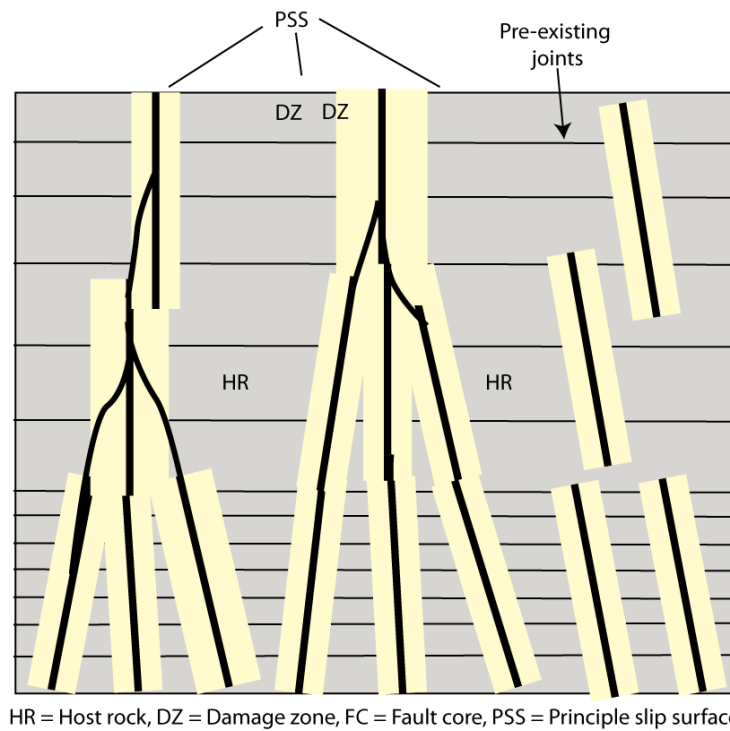


Figure 4-23: Schematic representation of the fault architecture for faults composed of multiple strands. Representation includes variations in density of pre-existing structures which are perpendicular to the fault.

4.7.1.3 The Ciao Ciao Fault

The CCF cuts through all of the lithologies at Passo Moro and therefore through units with a variety of different joint densities (Figure 3-8). The CCF has two bounding faults, a relatively narrow damage zone and a central fractured and bleached zone. The bounding faults are dominantly composed of core material which includes variable amounts of breccia, cataclasite and foliated cataclasite. The damage zones are on the outer edges of the bounding faults and are 1-5 m wide. The entire fault zone is 15-20 m wide and has limited variability along strike within the mapped section.

The CCF is similar in architecture to the Glacier Lakes Fault (Kirkpatrick, 2008) (Figure 4-1b). Both faults cut crystalline rock, they formed by linkage of pre-existing joints, were exhumed from seismogenic depths and are of similar width, length and offset. The main difference between the faults is that the Glacier Lakes Fault has a central fault core. Exposures are limited along the CCF and so although a central core was not observed it does not mean that there is not a core present. Due to the similarities between the two faults, the architecture described by Kirkpatrick (2008) could be representative of mature faults formed

by linkage of joints in crystalline rock exhumed from seismogenic depths. Due to this I have not created a new architectural model for the CCF.

4.7.2 Architectural differences

At Passo Moro the three mapped fault zones have very different architectural styles. The differences in architecture may be in response to the depth of faulting, the protolith, fault displacement, interaction with other faults and/or pre-existing structures, and fluid-rock reactions (Faulkner et al., 2008). Between the three fault zones, the VF and SF appear to be identical in terms of depth of faulting, protolith, fault displacement, and fluid-rock reactions. However, the two fault zones have extremely different architectures (Figure 4-22 & Figure 4-23). Given the similarities between the faults, formation of a similar architectural style might be expected. The only observable difference between the faulting conditions of the two faults is the host rock variability and the distribution of pre-existing structures. The VF cuts the upper granite gneiss which is massive and homogenous, has a low foliation parallel joint density, and a low fault parallel joint density. The SF cuts the lower gneiss, metasedimentary rocks and upper variable gneiss. The granite gneiss in this area is compositionally and texturally variable, the foliation parallel joint density is high, and the fault parallel joint density is also high.

Within the Gole Larghe Fault zone three different categories of faults were described and distinguished on the basis of fault spacing, fault thickness, and cumulative displacement (DiToro & Pennacchioni, 2005). The initial fault distribution was explained by the original arrangement of joints and differences in fault displacement and thickness were correlated to fault spacing. The faults that are widely spaced (10s of metres) have the most displacement (>10 m) and the thickest fault zone (10-100cm thick); whereas the faults that are closely spaced (2-5 m), have lower displacements (tens of centimetres to 10 m) and thinner fault zones (millimetres to a few decimetres).

Mapping revealed that the fault parallel joint density (which was determined by host rock variations and the 010/33W joint distribution - Figure 3-12) is ~4/m in the east of Passo Moro where the SF formed, while in the west of the area where the VF formed the fault parallel joint density is 0.5/m. Given the differences in

initial joint density, more faults might be expected to develop in the east of Passo Moro than the west. This appears to be reflected in the development of the SF.

With respect to the architecture of the faults, DiToro & Pennacchioni (2005) indicate that the faults that are spaced further apart are thicker and have accumulated more displacement. The VF is up to 3.5 m wide, has accumulated ~20 cm of displacement, and fault spacing is low within the upper gneiss (0.05 to 0.1/m), whereas an individual strand of the SF is ~1.5m wide, has accumulated ~5cm of displacement and fault spacing is high in the lower and variable upper gneiss (~0.2/m). These results concur with those of DiToro & Pennacchioni (2005) and indicate that the differences in fault architecture of these two fault zones is a result of the initial fault parallel joint spacing which subsequently determines the spacing of the later formed fault zones.

4.7.2.1 The effect of joint distribution on fault evolution

Differences in fault architecture between the VF and SF may be due to differences in the initial fault parallel joint distribution. Thus relatively minor initial differences in the host rock characteristics are able to generate very different fault architectures and consequently these systems evolve on different pathways. Whether either of these small faults could evolve into a larger fault such as the CCF, is a question that is considered below.

Within the Mount Abbot Quadrangle in the Sierra Nevada Segall & Pollard (1983) and Martel et al. (1988) describe a very similar fracture and fault distribution to that observed in both the Gole Larghe and Spaghetti Fault zones. It was concluded by Segall & Pollard (1983) that the nature and array of pre-existing fractures were very important in controlling the nucleation and growth of some faults. Martel et al. (1988) produced a model for the development of simple fault zones from a set of sub-parallel pre-existing fractures. The model describes how deformation becomes more localised with time and that some faults remain active after slip had ceased on many of the adjacent small faults. This is due to some faults of greater lengths (related to original fracture length) accommodating more slip (Pollard and Segall, 1987), which progressively reduces the shear stress on adjacent small faults (Pollard & Segall, 1987). Such stress

reduction results in a 'stress shadow' and faults within the stress shadow become inactive⁴ (Martel et al., 1988). Martel (1990) included the formation of larger 'compound fault zones' and the model highlights the relationship between the larger faults and adjacent smaller deactivated faults (Figure 4-24).

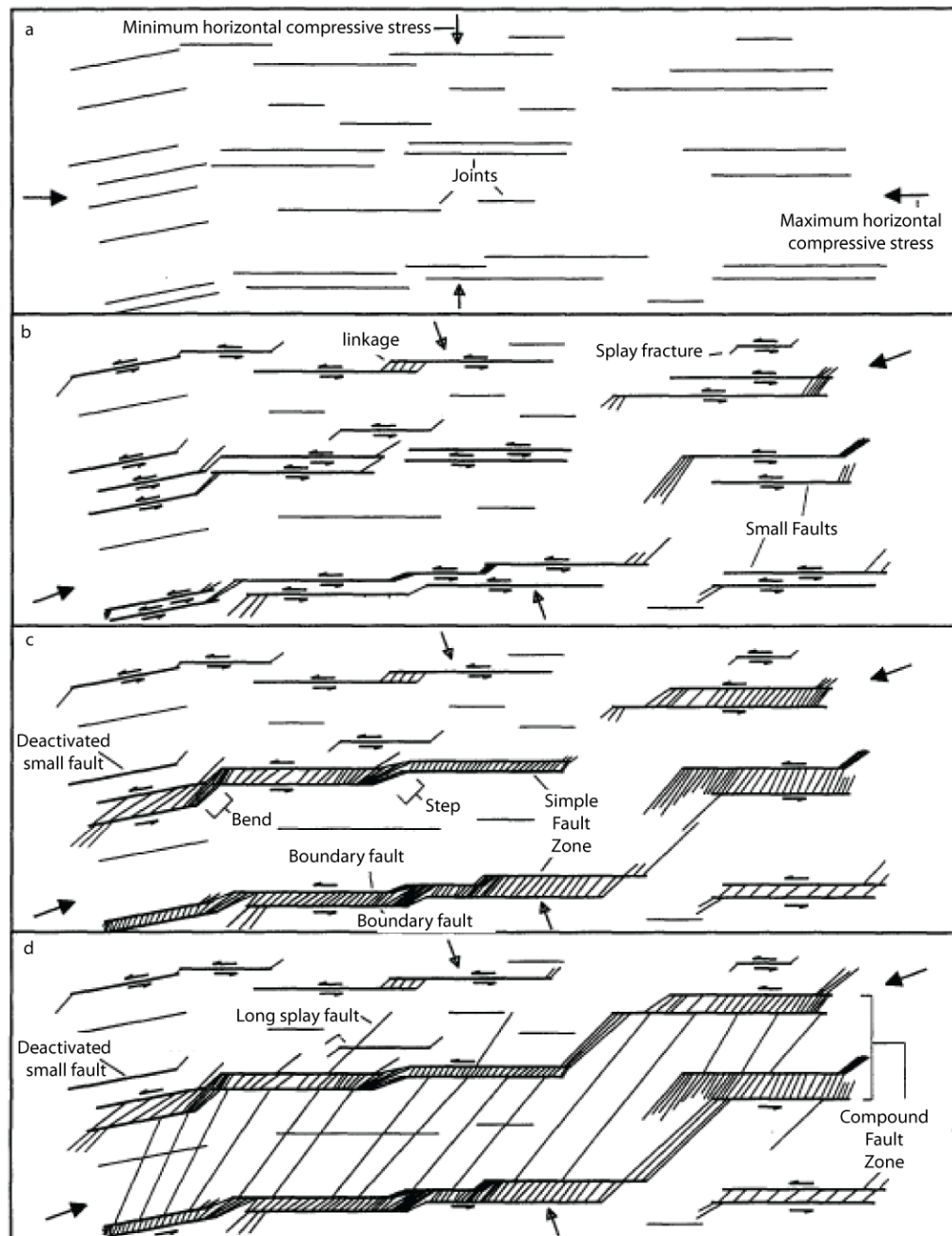


Figure 4-24: Fault growth model for growth and linkage from pre-existing fractures by Martel (1990).

a) opening of joints b) development of small left lateral faults c) development of simple fault zones d) formation of compound fault zones.

⁴ Deactivated/inactive means that the fault is no longer propagating, linking, or accumulating deformation, but it still can transmit fluids if the permeability permits.

The faults at Passo Moro have formed by reactivation and linkage of pre-existing structures similar to that observed at Mount Abbot Quadrangle. Given the similarity of the two field sites (Monte Rosa & Mount Abbot Quadrangle) and the faulting conditions (in both areas the faults cut crystalline basement rocks, were exhumed from seismogenic depths, and preserve similar hydrothermal mineral assemblages) it is likely that the VF and SF could have developed within a similar setting to that described by Martel (1990) (Figure 4-24). In general where faults have grown from pre-existing structures; there is a positive correlation between fault length, fault spacing and displacement (Di Toro and Pennacchioni, 2005; Segall and Pollard, 1983). A result of this, a fault population will evolve from having numerous small active faults to only a few large active faults, thus numerous small faults deactivate during fault population evolution (Cowie et al., 2000; Martel, 1990; Martel et al., 1988; Walsh et al., 2003).

Within the SF, the spacing of faults is low ($\sim 0.2/m$) and the cumulative displacement on an individual strand is low but trace length can be large (10-100 metres). A large trace length can be inherited or established early on by reactivation of pre-existing structures (Walsh et al., 2002). Length therefore would remain relatively constant during evolution with only displacement accumulating through time (Walsh et al., 2002). Based on studies of fault populations (e.g. Martel, 1990; Cowie et al., 2000; Walsh et al., 2002; Walsh et al., 2003), to uphold the length-spacing-displacement scaling relationship; only a few of the strands within the SF would have continued to grow into small, simple or compound fault zones. However, by taking into account the lack of core material observed within *all* strands of the SF; the observations compared with the fault descriptions in Martel et al. (1988) indicate that the strands within the SF only developed into 'small faults'. This means that the SF strands became inactive and thus, displacement could not accumulate so as to scale with fault length and spacing.

Within the upper gneiss (where the VF is located) fault spacing is high with faults being a minimum of 20m apart. 20cm of displacement has accumulated on the VF and the fault is 70m long. In Martel et al's (1988) descriptions a small fault is millimetres thick and has mylonitic fabrics whereas a simple fault zone is 1.5-3m wide and the boundary faults contain cataclastic fabrics. The change from mylonitic to cataclastic deformation was interpreted to be in response to an

increase in shear strain rate across widely spaced fault zones promoting brittle deformation (Martel et al., 1988; Patterson, 1978). Changes in temperature were ruled out as a possible cause for changing deformation mechanisms as all fractures contain the same mineral assemblage implying similar pressure-temperature conditions. Fault spacing and the presence of cataclastic rocks within the VF imply that it is similar to one of the boundary faults within a simple fault zone. However, simple faults can be up to 1km long and require the presence of two boundary faults (Martel et al., 1988). The VF is only 70m long and the only place where there could be evidence of two boundary faults is in section 3 where for 4m of the along strike length, two principal slip surfaces occur (Figure 4-4). Based on length and the lack of an additional boundary fault it would seem that the VF is more akin to a 'small fault'. The VF is essentially isolated in 2D and so the increased spacing of faults in this area would have resulted in an increase in the shear strain across the fault (Martel et al., 1988). This in turn would have promoted brittle deformation (Patterson, 1978) and the formation of cataclastic material.

The increased displacement within the VF compared to a SF strand does indicate that the VF is more evolved than the SF, however both faults can be classified as a 'small fault' in relation to Martel et al's (1988) and Martel's (1990) model.

Surrounding the SF the density of pre-existing fault parallel structures is so high that the en-echelon-like arrangement of joints becomes a major obstacle for shear reactivation (DiToro & Pennacchioni, 2005). This is because if the shear strain rate across an area remained constant, where there are multiple closely spaced faults the shear strain rate across an individual fault will be decreased (Martel et al., 1988), thus inhibiting shear reactivation. The opposite scenario is true for the area around the VF whereby the original fault parallel joint spacing is so low that after reactivation of a joint, there are no near-by joints to link onto. The fault would therefore have to grow by propagation instead of linkage, however if the shear resistance to slip increases significantly, this can cause the fault to curve and fault propagation to cease (Martel, 1999). The VF does curve at its eastern tip (Figure 4-5) and indicates that it may have deactivated as a result of an increase in the shear resistance to slip. Hence the VF and SF may be deactivated but for very different reasons.

As a result of the initial joint distribution neither the VF or SF could have evolved into something similar to the CCF. However, if an arrangement of pre-existing joints existed that was intermediate between the two joint distributions described; then it may be possible for fault linkage to continue and a situation as described by Martel (1990) to occur (Figure 4-24). Since the VF did begin to accumulate deformation and records evidence of cataclastic (high strain) deformation, of the two faults the VF is perhaps most similar to the nascent CCF.

4.7.3 What the fault rocks tell us about faulting conditions in the fault zones

The formation of fault rocks can be affected by properties such as friction, temperature, effective and differential stress, velocity mode of faulting, and type of faulting (thrust, normal etc) (Sibson, 1977). Also depending on the temperature and chemistry of a hydrothermal fluid, different mineral assemblages will be precipitated. By analysing what the different fault rocks, fabrics and mineral assemblages, the ambient conditions can be assessed. These can then compared for the different faults and used to assess if conditions changed during fault evolution.

Within both the VF and CCF, the fault zone is composed of one or more PSSs, a fault core and a damage zone. The core of the VF is composed of breccia and cataclasite whereas in the CCF the core also includes foliated cataclasite. The fault rocks within both fault zones are representative of brittle deformation and imply increased shear strain across the faults (Martel et al., 1988). However, each fault rock type forms in response to certain deformation mechanisms. Breccia forms primarily by fracturing, cataclasis involves fracturing and rotation, and formation of a foliated cataclasite typically involves mechanical and chemical breakdown, and syn-tectonic dissolution-precipitation in the presence of a fluid (O'Hara, 2007; Wibberley, 1999; Wintsch, 1978). The main difference between the two faults is the presence of foliated cataclasite in the CCF. This implies that in the CCF there has been an additional chemical reaction to enable the formation of the foliated cataclasite. The formation of foliated cataclasite tends to be a progressive process whereby repeated deformation and fluid flow

events are required to produce a penetrative foliation (Wibberley, 1999). Therefore, the foliated cataclasite also indicates more deformation and fluid flow events compared to the VF.

The hydrothermal minerals within the two faults are chlorite, quartz and K-feldspar, with the addition of epidote in the VF. Such mineral assemblages are often described as indicating propylitic alteration (with the exception of K-feldspar) (Hemley and Jones, 1964) and typically associated with temperatures in the region of 200-300°C (Di Toro and Pennacchioni, 2005; Mittempergher et al., 2009; Wintsch, 1975). Therefore both fault zones record similar hydrothermal conditions throughout their evolution.

The main difference between the two faults is the presence of foliated cataclasite within the CCF. This implies an additional reaction taking place, different active deformation mechanisms and more episodes of deformation and fluid flow. Mineralogy implies that the temperature conditions were essentially the same in the two faults and therefore other fault properties (such as permeability and fluid-rock ratios) must have been involved in creating the differences observed. Microstructural analyses will enable detailed characterization of the fault rocks and thus will provide insight into why the differences occur between the faults.

5 Microstructural analysis of faults

5.1 Introduction

Faults are extremely complex zones of deformation which can be mapped by different techniques and on a variety of scales ranging from the macro- to micro-scale. Each technique and scale provides a level of detail to add to the microstructural puzzle and by combining all the data we can begin to understand what processes occur and how they feedback into fault evolution.

Mineralogy within a fault can vary as a result of different fluid-rock processes including dissolution, precipitation and chemical reactions. All of these processes affect the proportions of minerals and the addition of fluid can enhance the rate at which these processes take place (Hemley & Jones, 1964). Mineral textures provide evidence about what minerals are reacting, dissolving or precipitating, and the deformation history. The degree to which the various mineral reactions have occurred coupled to the textural history provides information on temperatures, deformation mechanisms, composition and volume of fluids, and the relative timing of deformation phases. Results can be used to piece together the metamorphic history of the fault zone. Reaction products will have a range of effects on fault rheology but ultimately may result in either fault weakening or hardening, thus influencing fault mechanics and evolution.

This chapter will provide a microstructural description of the various fault components found within the VF and CCF. Particular focus will be given to evidence of fluid-rock interactions and reactions to enable better understanding of the role fluid plays within an evolving fault zone. The SF records only minor amounts of fluid-rock interactions and since the VF is more representative of a 'small fault' (Section 4.7.2.1); therefore the SF will not be described.

5.2 Methodology

Oriented samples of different fault rocks were collected at Passo Moro and re-oriented in Glasgow for polished section preparation. All thin sections were cut perpendicular to the fault plane and parallel to the slip direction. Analysis was

carried out using a light microscope in plane polarised light (ppl) and cross polarised light (xpl), a scanning electron microscope utilising back scattered electron (SEM-BSE), secondary-electron (SEM-SE) and cathodo-luminescence imaging (SEM-CL), and X-ray spot analysis with Edax software for mineral identification. The combination of techniques allows mm- μ m scale analysis to be carried out on the fault rocks. Mineral proportions were calculated for each fault rock sample by point counting and results are associated with an error of $\pm 3\%$. A list of the host rock samples analysed can be found in Table 3-1 and a list of all fault rock samples analysed is shown in Table 5-1 and Table 5-2.

Virgin Fault		
Location (See Map Fig 4-4)	Sample Number	Fault component
Section 1	VF 1	ODZ
Section 2	VF15	ODZ
	VF16	FC
	VF17	IDZ
	VF2	FC
Section 3	VF5	ODZ
	VF18	IDZ
	VF19	IDZ
	VF20	ODZ
	VF6	IDZ
	VF4	Core 2
	VF3	Core 1
Section 4	VF8	IDZ
	VF7	FC - cataclasite
	VF10	FC - Breccia
	VF21	ODZ
	VF11	IDZ
	VF9	FC - Breccia
Section 5		
5b	VF14	FC - cataclasite
5a	VF23	ODZ
5a	VF13	ODZ
5a	VF24	IDZ
5a	VF12	IDZ
FC = Fault core, ODZ = Outer Damage Zone, IDZ = Inner Damage Zone		

Table 5-1: List of all fault rock samples analysed from the VF and their location within the fault zone.

Ciao Ciao Fault		
Locality Number (see map in appendix 1)	Sample Number	Fault component
5	CC1	DZ
5	CC2	Breccia-cataclasite transition
5	CC3	F.Cata
5	CC6	FC - Breccia
24	CC7	Central fractured zone
25	CC4	Central fractured - Bleached

FC = Fault core, DZ = Damage zone F.Cata = Foliated cataclasite

Table 5-2: List of all fault rock samples analysed from the CCF and their location within the fault zone.

5.3 Host rock

The main host rock in the field area is granite gneiss and it is typically composed of 26% quartz; 41% Albite; 13% K-feldspar; 8% muscovite; 6% biotite; 1% garnet; 2% epidote; and 3% chlorite (Fig 3-3). The primary structure observed within the host rock is the NE-SW oriented foliation (Figure 5-1). The foliation is defined by biotite and muscovite, foliation planes are spaced 1-5 mm apart, and the rock in between the foliation planes is quartz and albite rich. Host rock crystals are typically large (up to 3 mm) and euhedral with straight grain boundaries. Quartz can have undulose extinction, fractures, and bulging recrystallization (BLG) (Figure 5-1). BLG is restricted to grain boundaries and may only affect part of the grain boundary (Figure 5-2). Primary and secondary fluid inclusions occur in quartz; primary inclusions are 20-30 μm and are isolated within the crystals; secondary inclusions occur as trails, are $\sim 20 \mu\text{m}$ and only a few trails are present in any of the host rock samples. Albite is the dominant feldspar within the matrix and is often inclusion rich, and inclusions are typically of muscovite and quartz. K-feldspar forms augen up to 4x3cm and the augen contain patches of euhedral albite (Figure 5-1). Subhedral K-feldspar occurs within the matrix and varies in size from 10-500 μm . Garnet is sparse but where present it is anhedral and is often closely associated or speckled with chlorite and epidote (Figure 5-2b). Red/brown biotite is present within the foliation planes and also randomly distributed throughout the gneiss.

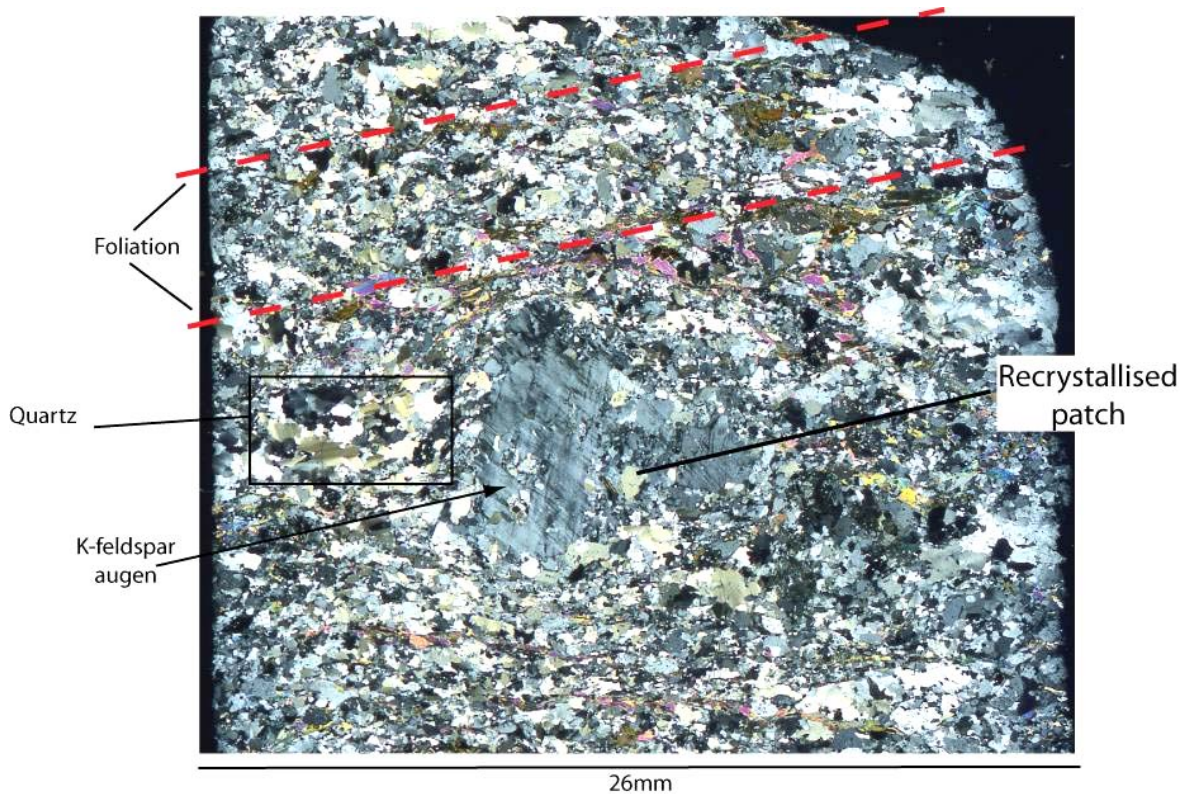


Figure 5-1: Cross polarised image of the host rock showing the characteristic features such as foliation and augen. Area in the box is enlarged in Fig 5-2 (Sample = Host 3, locality 10)

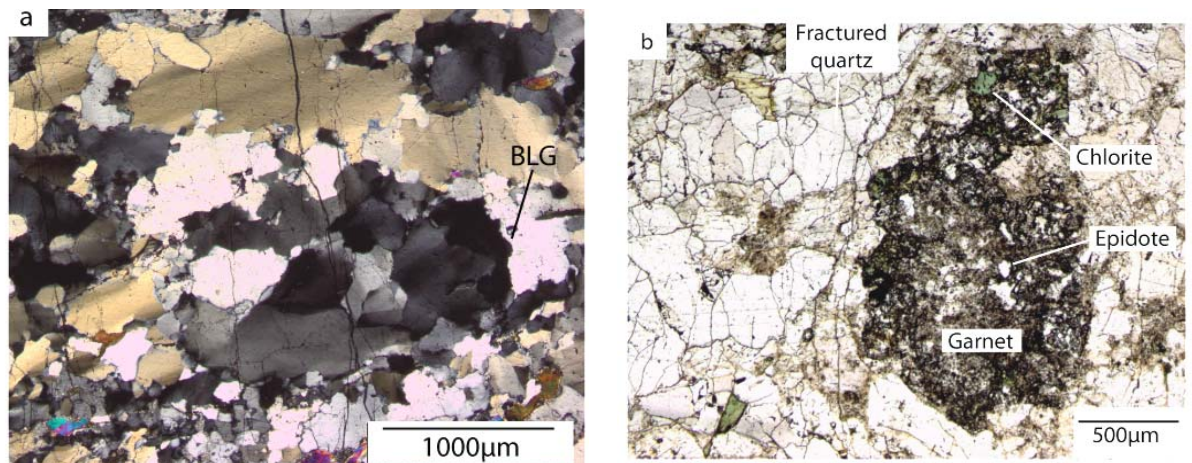


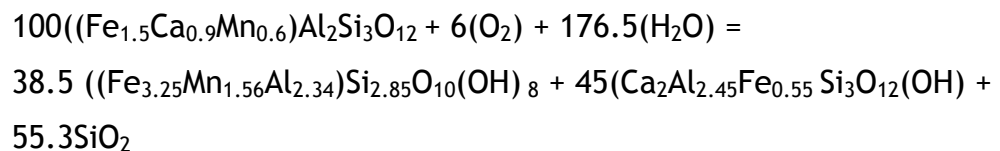
Figure 5-2: Microstructures within the host rock. a) Xpl image of quartz showing undulose extinction and bulging recrystallization (BLG) along grain boundaries in quartz (highlighted in Fig 5-1). b) ppl image of a garnet crystal associated with chlorite and epidote. Also note the fractures cutting quartz (sample = Host 1).

5.3.1 Interpretation - Host rock

The garnet has poor crystal habit, and contains numerous small epidote and chlorite inclusions (Figure 5-2b). Garnet can retrogress to epidote and chlorite

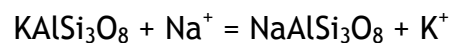
(Equation 1). The altered nature of the garnet and the presence of epidote and chlorite therefore imply that the garnet was probably retrogressing within the host. The reaction requires the input of water, however given that the garnet has not been completely replaced suggests that the reaction did not go to completion, and is probably due to a lack of reactant (fluid) available.

Equation 1: Garnet + oxygen + water = chlorite & epidote + Quartz (Brown, 1969)



The presence of the albite within the K-feldspar augen and the pristine nature of the albite crystals (Figure 5-1) indicate that the albite is newly formed. Therefore it is likely that the K-feldspar was being replaced by albite. This reaction can occur by direct replacement of one feldspar by another (Equation 2), and requires potassium to be removed from the K-feldspar most likely within a fluid and replaced by sodium.

Equation 2: K-feldspar + Na⁺ = Albite + K⁺ (Wintsch et al., 1995)



Undulose extinction is a form of intracrystalline deformation that occurs without fracturing and indicates that the crystal lattice is slightly bent (Passchier & Trouw, 2005). BLG is a form of dynamic recrystallization that occurs between 300-350°C (Stipp et al., 2002). It is a recovery mechanism which is an indicator of temperature and plastic (ductile) deformation within quartz. Below 300°C, quartz will deform by fracturing while above 350°C sub-grain rotation (SGR) becomes the dominant recovery mechanism (Stipp et al., 2002). BLG in the host rock is sparse and restricted to grain boundaries indicating that temperatures were approximately 300°C. The quartz is cross-cut by fractures and show that plastic deformation gave way to brittle deformation, indicating that temperatures decreased to less than 300°C (Stipp et al., 2002). Primary fluid inclusions are trapped during initial crystallization of a mineral (Shepherd et al., 1985). The secondary fluid inclusion trails form due to micro-fracturing and subsequent healing in the presence of a fluid.

The microstructures within the host gneisses indicate that plastic deformation was distributed throughout the rock, however due to the small amounts of BLG observed it signifies that deformation was negligible. Plastic deformation was followed by fracturing and fracture healing in the presence of a fluid and subsequently a later fracturing event. The fluids within the rock caused partial retrogression of garnet to epidote and chlorite, and replacement of K-feldspar by albite. The microstructures indicate plastic deformation overprinted by brittle deformation and hence, the rock records exhumation to lower temperatures and pressures.

5.4 Virgin fault (VF)

The VF is composed of multiple Principal slip surfaces (PSS), a damage zone and a fault core, composed of breccia and cataclasite (Figure 4-4). The maximum width of the VF is 3.5 m and to provide a detailed account of how the petrology varies across strike, the damage zone has been sub-divided into an inner and outer damage zone which represent the weakly and strongly bleached rocks. Fault rocks from all sections have been analysed and a summary of the mineralogy across section 3 of the VF is shown in Figure 5-4. Section 3 was chosen as it is approximately in the middle of the fault (along strike), all fault components are easily recognisable and easy to sample. The individual fault rock samples are considered to be representative of that particular fault rock type. The descriptions of microstructures are based on fault rock samples from the entire fault. Sample numbers are included with each image and sample locations are marked on the map of the VF (Figure 4-4) and on the sample map (Appendix 1) for samples from the CCF.

5.4.1 Grain size and mineralogy

Across strike of the Virgin Fault grain size measurements were recorded for quartz, K-feldspar and albite. Results show that the average grain size decreases from ~1200 μm in the host rock to ~100 μm in the fault core (Figure 5-3). Quartz and feldspar (albite & K-feldspar) have a similar grain size within the host rock and outer damage zone but within the inner damage zone, breccia and

cataclasite the quartz is approximately 150 μm larger than the feldspar (Figure 5-3).

Across strike from host rock to the fault core, the proportion of K-feldspar, chlorite and epidote are all higher in the fault core; proportions of albite, muscovite, biotite and garnet are all lower; and there is no change in the proportion of quartz (Figure 5-4). Biotite and garnet are the only minerals which occur in the host rock but are not present in the fault core. Across strike the most significant change in mineralogy usually occurs between the inner and outer damage zone. The largest change in mineral proportions is associated with K-feldspar, albite and muscovite abundance (Figure 5-5). The lower modal proportions of albite in the fault core relative to the host gneiss are balanced by higher volumes of K-feldspar. Muscovite proportions are lower in the inner damage zone and fault core compared to those in the host rock and the outer damage zone (Figure 5-5).

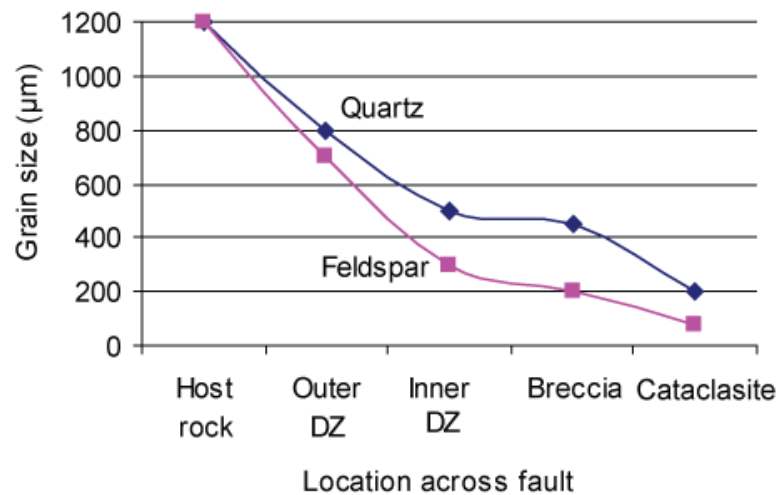


Figure 5-3: Grain size variation across strike of the Virgin Fault for quartz and feldspar. (feldspar = albite & K-feldspar).

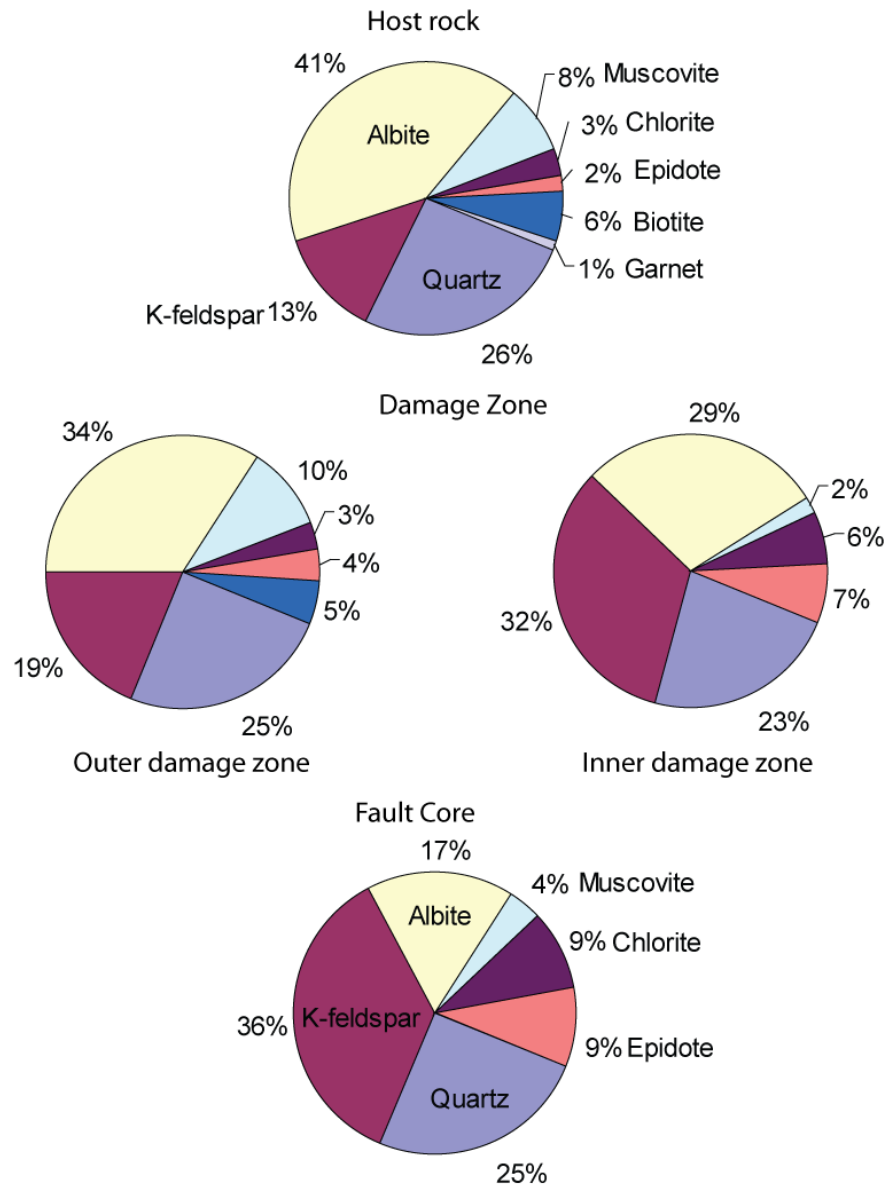


Figure 5-4: Mineral proportions for the different fault components across strike of the Virgin Fault.

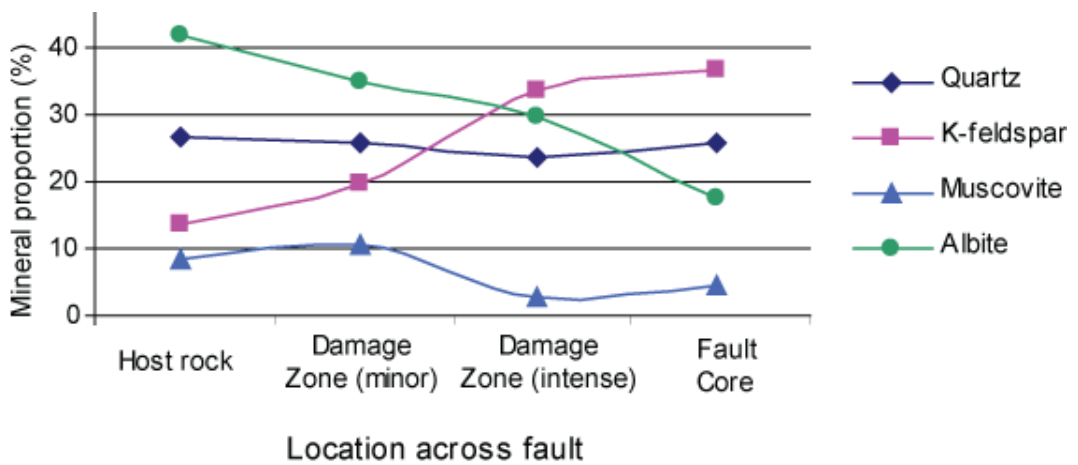


Figure 5-5: Variation in mineral proportions across strike of the Virgin Fault for the main rock forming minerals.

5.4.2 Micro-structures and textures in the VF

5.4.2.1 Outer Damage zone – minor bleaching

The outer damage zone retains many of the host rock characteristics such as a foliation (defined by muscovite), K-feldspar augen, and the dominant matrix minerals are quartz and albite. The foliation has the same orientation as in the host rock (NE-SW) and consists of alternating muscovite rich, and quartz and feldspar rich bands. However, close to the boundary between the inner and outer damage zone the foliation is not as well defined (Figure 5-6).

Quartz is rare in the matrix but occurs as microveins which crosscut the matrix (Figure 5-6). The microveins are oriented NW-SE, are typically spaced ~2 mm apart and are ~0.5 mm thick and ~2 mm long. All quartz is fractured (N-S), has undulose extinction, contains primary (isolated) and secondary (trails) fluid inclusions (Figure 5-7a), and BLG recrystallization is common on grain boundaries. Primary fluid inclusions in the matrix quartz are small (~10 μm) but in the microveins the primary inclusions are ~20-40 μm and the secondary inclusions are <20 μm (Figure 5-7a).

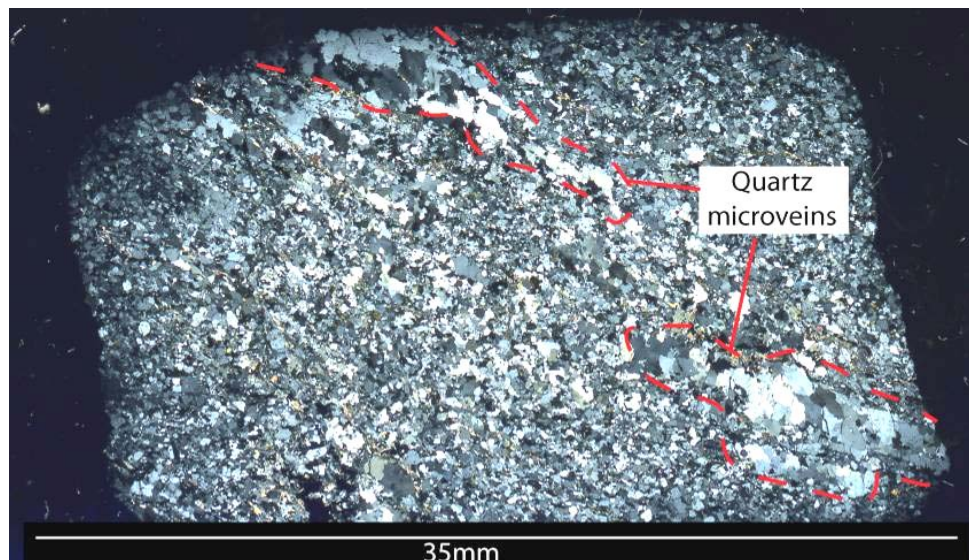


Figure 5-6: Outer damage zone rock from the VF.
Xpl image showing quartz microveins and no clearly defined foliation within the rock (Sample VF5)

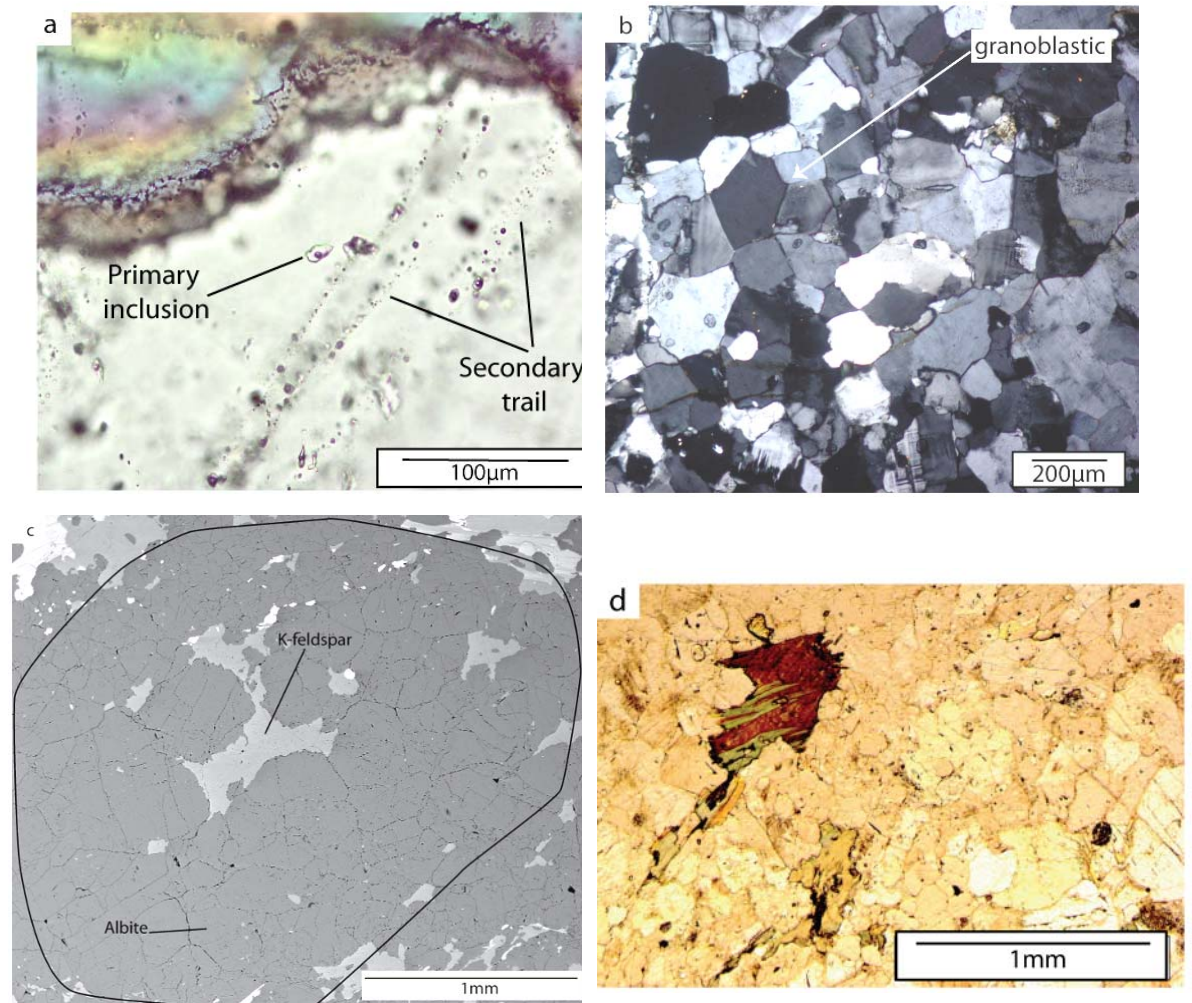


Figure 5-7: Microstructures that occur within the outer damage zone of the VF
a) Fluid inclusions in the quartz microveins. Sample VF5 (ppl) b) Granoblastic texture formed in a feldspar-rich area – triple grain boundary arrowed. Sample VF8 (xpl) c) SEM-BSE image of granoblastic texture in feldspars with albite being the dominant mineral and K-feldspar being interstitial. Sample VF8 d) Biotite partly replaced to chlorite. Sample VF1 (ppl).

Albite and K-feldspar typically retain general characteristics of those in the host gneiss but crystals are subhedral, grain boundaries are irregular and grain size is ca 500µm smaller than those in the host. Throughout the matrix of the fault rock there are circular patches (~500-1000 µm in diameter) of feldspar (K-feldspar and albite) that have a granoblastic texture and/or gently curving boundaries (Figure 5-7b). These areas are composed of albite with minor interstitial K-feldspar (Figure 5-7c). Albite also dominates the matrix feldspar (Figure 5-5) and K-feldspar occurs as irregular shapes which may enclose the albite crystals (Figure 5-8).

Red-brown biotite is distributed throughout the matrix and is partially retrogressed to chlorite (Figure 5-7d). Chlorite is randomly distributed

throughout the matrix. No garnet is observed within the outer damage zone and epidote is sparse and randomly dispersed throughout the matrix.

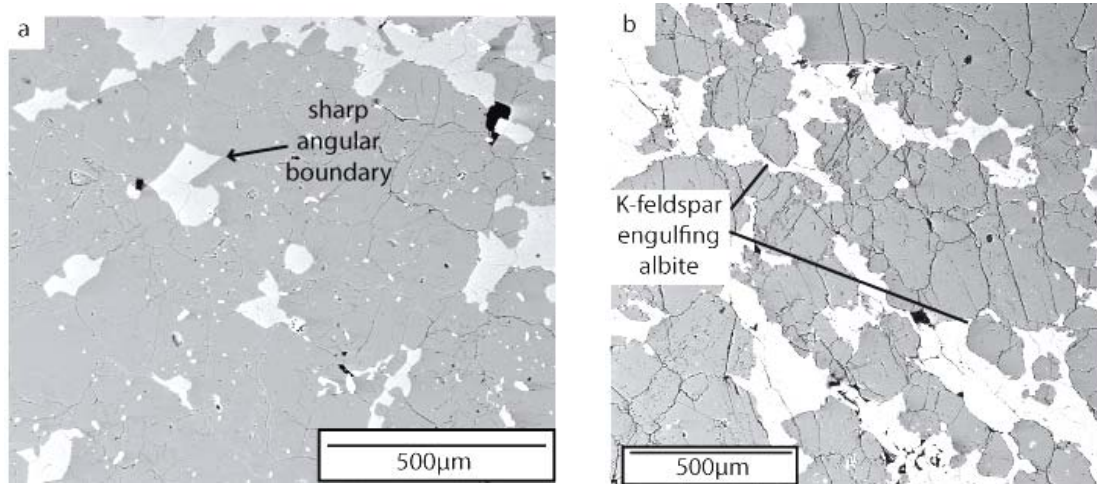


Figure 5-8: SEM-BSE images of the K-feldspar-albite relationship in the outer damage zone of the VF.

a) Albite matrix with anhedral K-feldspar crystals which have sharp angular boundaries (arrowed). b) Irregularly shaped K-feldspar crystals which in some areas completely encloses the albite crystal (arrowed). (both images are from sample VF5).

5.4.2.2 Inner Damage zone – intense bleaching

The inner damage zone is primarily composed of quartz and feldspar (Figure 5-4), there is no biotite within the matrix and there is no foliation. Quartz microveins and/or chlorite- and/or epidote veins crosscut the rock. Quartz microveins are up to 1.5 mm wide, 5mm long and oriented either NW-SE or E-W with the latter usually occurring closer to the boundary with fault core (Figure 5-9). Quartz crystals are fractured N-S, have undulose extinction and BLG recrystallization with BLG being more common than in the outer damage zone. Quartz microveins contain an abundance of fluid inclusions. Primary inclusions are ~40-70 µm while the secondary fluid inclusion trails tend to be small (~20 µm).

Chlorite and epidote veins are oriented E-W and NW-SE and so have the same orientation as the quartz microveins. Chlorite veins are up to 500 µm wide and can cross-cut the entire thin section indicating that the veins can be greater than 3 cm long. Chlorite is pale green in plane-polarised light but in cross polarised light it has brown/gold interference colours and is composed of small randomly oriented platelets (Figure 5-11a). Epidote veins are up to 2 mm wide and 3 cm long and usually occur along the edges of quartz microveins (Figure

5-9). The epidote veins oriented E-W are typically thicker than those oriented NW-SE (500 μm compared to 100 μm), and the former are located closer to the boundary between the inner damage zone and fault core.

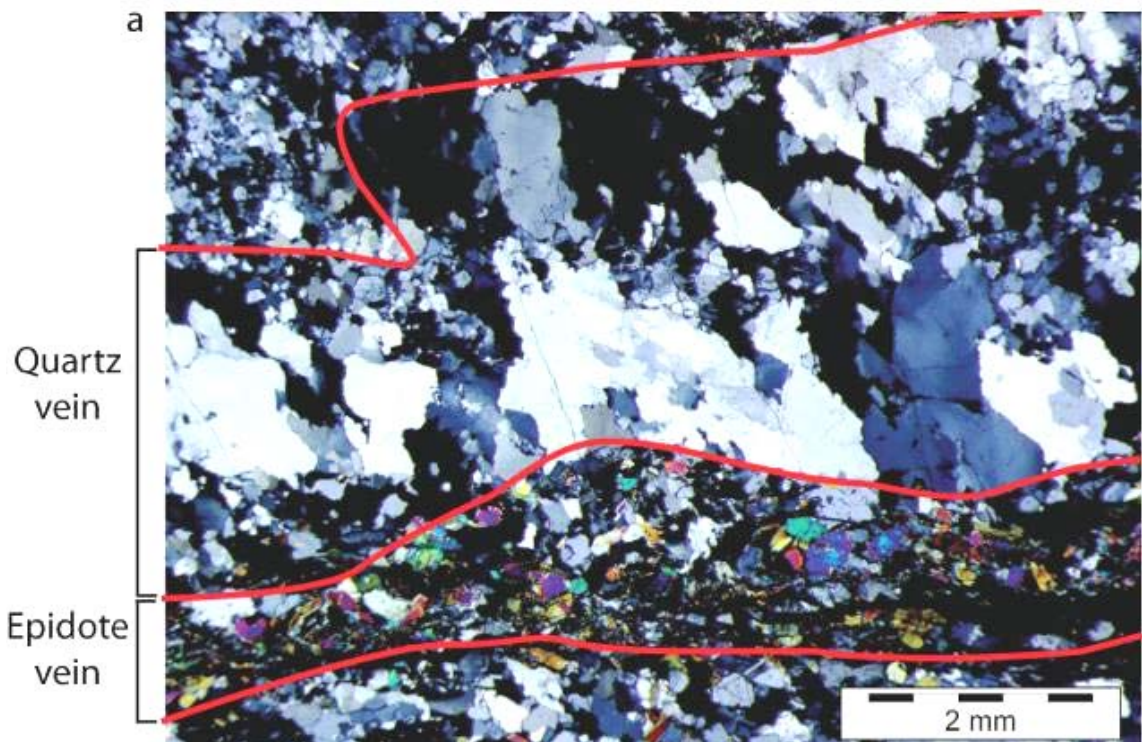


Figure 5-9: Co-existing quartz and epidote veins within the inner damage zone of the VF. (xpl, sample VF6)

Within the inner damage zone, the proportion of K-feldspar is higher than albite (Figure 5-4) and thus K-feldspar is the dominant matrix mineral. In general the feldspar textures are similar to those in the outer damage zone (granoblastic texture and subhedral crystal shape) except the grain size is smaller in inner damage zone (~50-400 μm) and the grain boundaries are lobate. K-feldspar augen are present but they are relatively small (1x1 mm) and their boundary is often surrounded by granoblastic K-feldspar (Figure 5-10). Isolated albite crystals may be completely surrounded by K-feldspar (Figure 5-11b). The albite crystals are inclusion rich and SEM-BSE imaging shows that they are fractured internally. K-feldspar has a range of morphologies including: smooth inclusion free; be turbid and pitted; inclusions of albite; and fractured internally (Figure 5-11c). Smooth K-feldspar is often granoblastic or may have sharp angular boundaries. The fractured K-feldspars tend to be subhedral.

In section 5a of the VF, the inner damage zone is different to that observed elsewhere. The matrix is composed almost entirely of albite (87%) with minor amounts of iron oxides distributed throughout (<1%). The remaining 12% is composed of quartz and chlorite and restricted to veins (Figure 5-11d). Individual veins contain both quartz and chlorite and the boundary between the two minerals is cusped (Figure 5-11e). The chlorite has blue/purple interference colours and the quartz is clean with no undulose extinction or BLG and only N-S fractures cutting through them (Figure 5-11e).

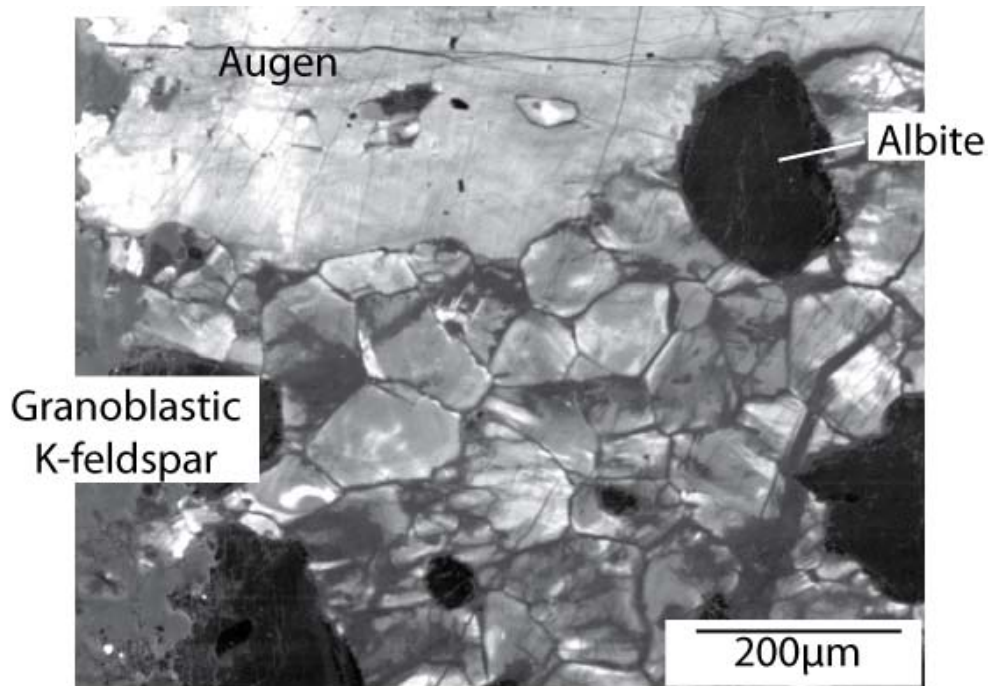


Figure 5-10: SEM-CL image of a K-feldspar augen with granoblastic K-feldspar around the edge of an augen. (Inner damage zone rock in the VF - Sample VF6)

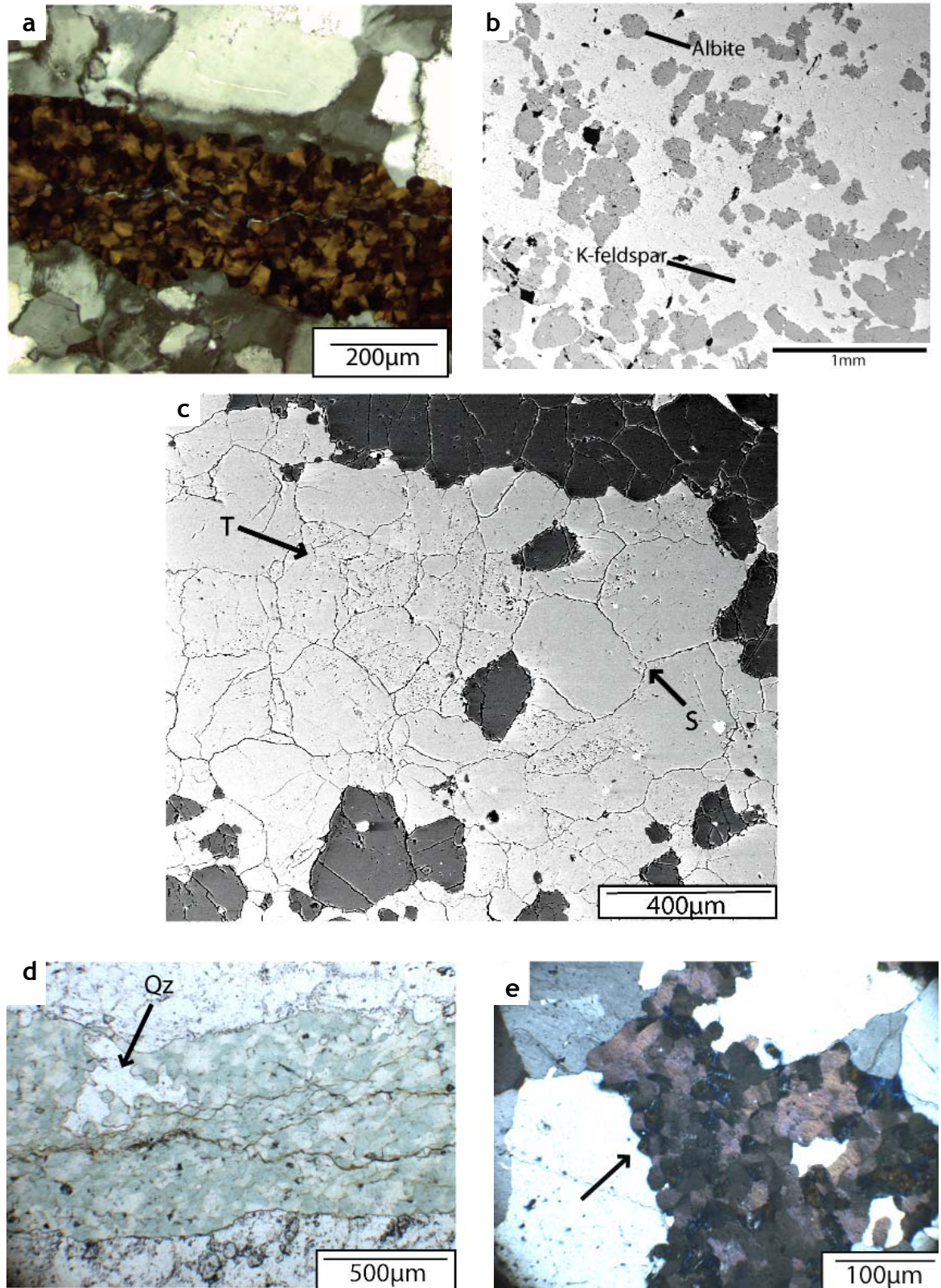


Figure 5-11: Microstructures within the inner damage zone of the VF
 a) xpl image of a chlorite vein composed of brown-gold platelets (Sample VF11) b) SEM-BSE image of albite and K-feldspar showing K-feldspar to be the dominant matrix mineral (Sample VF6) c) SEM-BSE image showing the textural variations of K-feldspar. Smooth and granoblastic (S) and turbid and pitted (T) – both textures are arrowed (Sample VF6) d) ppl image of a quartz (Qz) and chlorite vein in the inner damage zone at section 5a of the VF (Sample VF11) e) xpl image of the cusped quartz-chlorite boundary (arrowed) within the chlorite vein shown in Fig 5-11e.

5.4.2.3 Fault core

The fault core varies in thickness along strike from millimetres up to approximately 1m (Figure 4-4). In some samples breccia and cataclasite co-exist and are inter-related whereas in other samples the two rock types are separate. Microstructures vary between these different fault cores and so the thin core and thick core will be described separately. In general the composition of the inner damage zone and fault core is similar (quartz- and feldspar-rich) but in the fault core the proportion of K-feldspar is slightly larger. The main difference between the inner damage zone and fault core is the microstructure.

5.4.2.3.1 *Narrow fault core band*

Where the fault core is only millimetres to centimetres thick, the breccia and cataclasite co-exist (Figure 5-12). The dominant fault component is the breccia with cross-cutting bands of cataclasite of which the latter may completely enclose pods of breccia (Figure 5-12). The cataclasite is dark grey with golden/brown comminuted material disseminated throughout. Cataclasite is fine grained with all porphyroclasts being $\leq 50 \mu\text{m}$. The clasts are primarily composed of quartz, albite and epidote within a K-feldspar-rich fine grained matrix (Figure 5-13a).

Clast boundaries within the breccia are accentuated by an iron staining (Figure 5-13b). The breccia is composed of quartz, K-feldspar, albite and chlorite. The majority of the clasts are K-feldspar and may be up to 15x10mm (Figure 5-12). Albite crystals are $\leq 300 \mu\text{m}$ have lobate grain boundaries and are usually surrounded by K-feldspar with a granoblastic texture (Figure 5-14b). The K-feldspar clasts are strongly fractured and have been cut by microveins of K-feldspar that are dark grey in xpl and CL. The original K-feldspar crystal is light-dark grey in xpl and bright in CL (Figure 5-14a). Raman spectra of feldspars are a reflection of their structure, crystallinity and chemical composition (e.g. Freeman et al., 2008). The spectrums attained of the host and vein K-feldspar differ with some peaks being of different width or absent (e.g. peak 10 in group 1 and peak 584 in group 5) (Figure 5-15). Albite crystals are $\leq 300 \mu\text{m}$ have lobate grain boundaries and are usually surrounded by K-feldspar with a granoblastic texture.

Within the breccia, clasts of quartz are sub-rounded and vary from 20-1200 μm . The large fragments show multiple sub-grains and BLG is pervasive (Figure 5-14c). Smaller fragments appear to be almost completely recrystallised by BLG and these often occur adjacent to sheared out chlorite veins (Figure 5-14d). Chlorite veins cross-cut the breccia, they are oriented ~E-W (fault parallel), are 50-500 μm thick, they anastomose and bifurcate along strike, and the chlorite has brown-gold interference colours. Chlorite veins also cut the cataclasite and in section 2, there is a thin sliver of chlorite along the PSS and is chlorite has purple/blue interference colours.

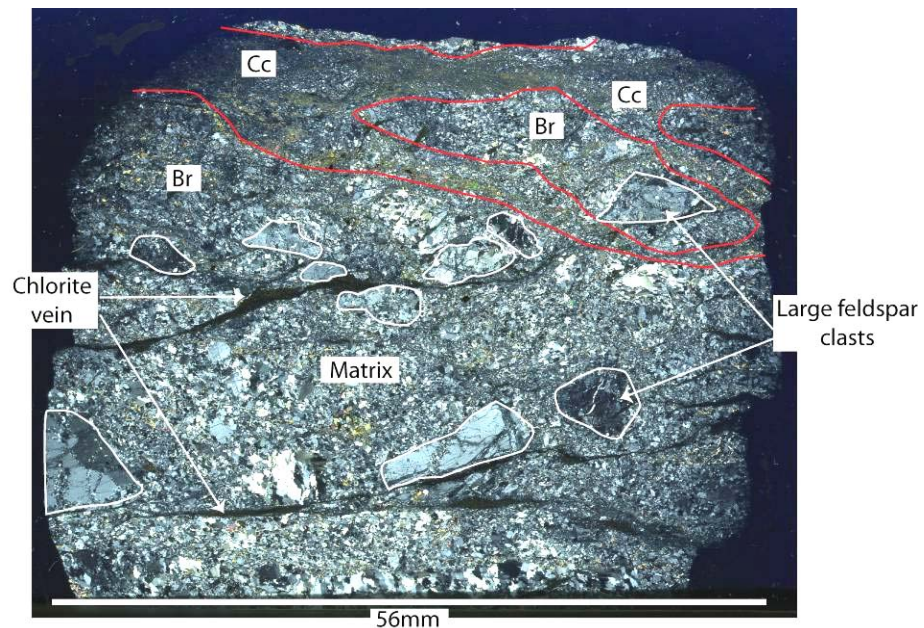


Figure 5-12: xpl image of the narrow core from the VF. Image shows chlorite veins and cataclasite bands (Cc) cross-cutting the breccia (br) (Sample = VF2)

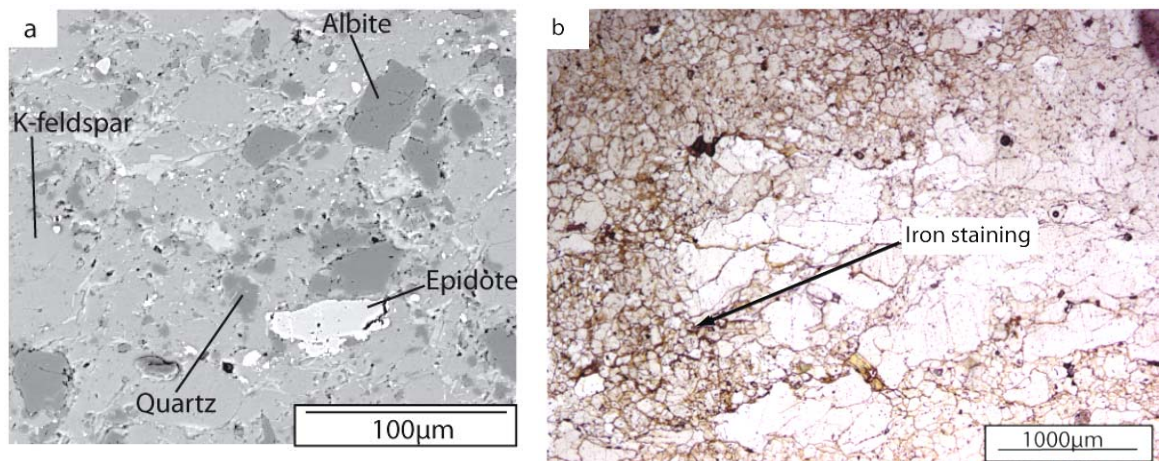


Figure 5-13: Microstructures within the narrow core from the VF
 a) SEM-BSE image of cataclasite. Cataclasite is composed of albite, K-feldspar, quartz and epidote within a K-feldspar cement (Sample VF2) b) ppl image of breccia with grain boundaries enhanced by iron staining (Sample = VF2).

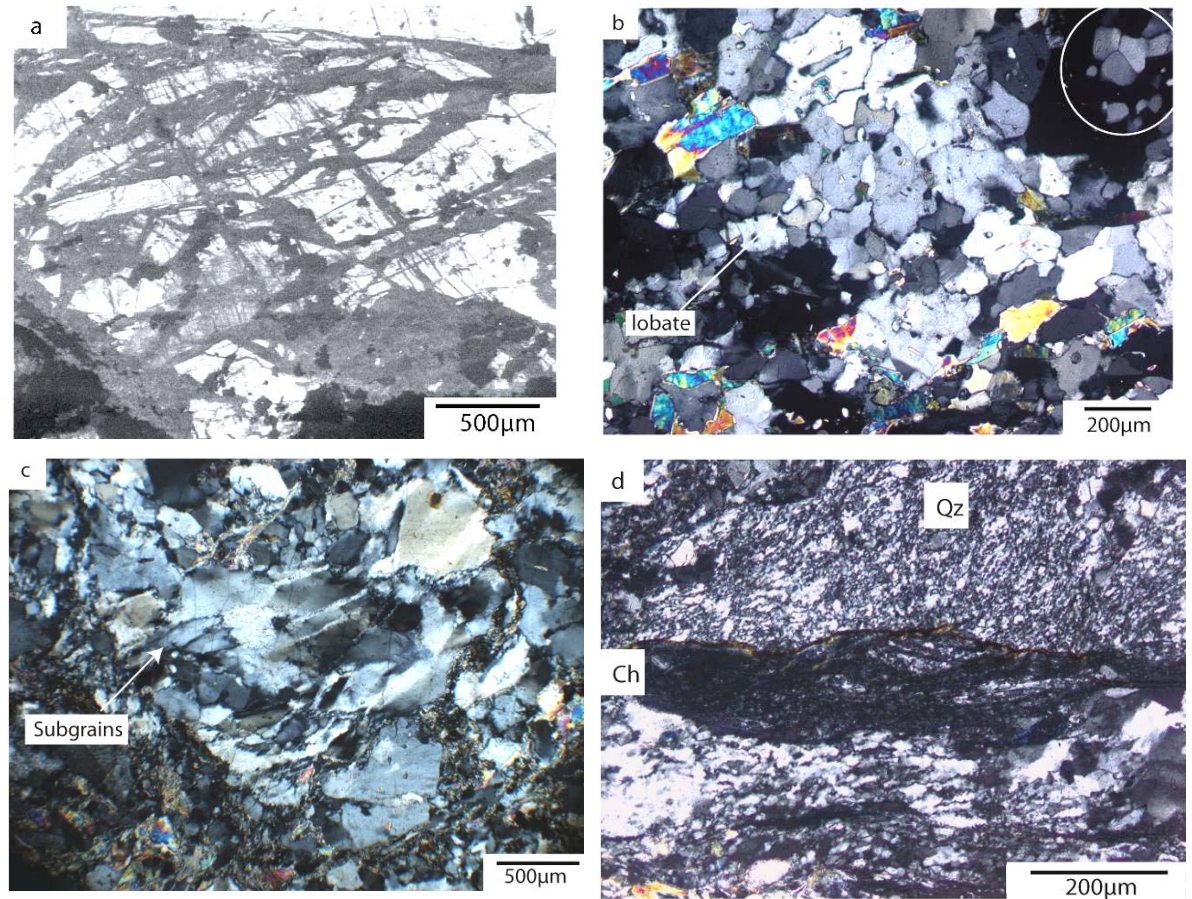


Figure 5-14: Microstructures in the narrow core material of the VF.

a) SEM-CL image of a K-feldspar crystal (white) that has been cross-cut by veins of non-luminescent K-feldspar b) xpl image of feldspars with lobate grain boundaries (arrowed) adjacent to granoblastic feldspar (circled) c) xpl image of quartz with undulose extinction, BLG, and sub-grains (arrowed) d) xpl image of a sheared chlorite vein (Ch) surrounded by completely recrystallised quartz (Qz). All images in Fig 5-14 are from sample VF2.

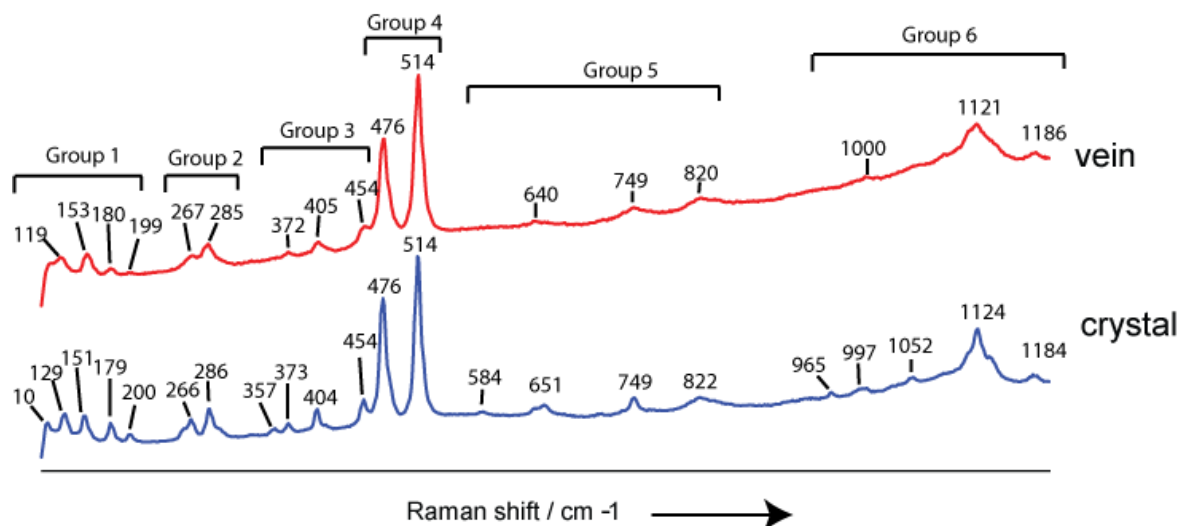


Figure 5-15: Raman spectrum from an original K-feldspar crystal and a non-luminescent K-feldspar microvein that cut the original crystal. Discussed in text (Sample VF2).

5.4.2.3.2 *Thick fault core band*

Where the fault core is 10cm up to 1m thick, the breccia and cataclasite can be easily distinguished. The breccia has a similar composition and appearance to that in the inner damage zone. The main compositional difference between the breccia and the inner damage zone, is a higher proportion of K-feldspar and chlorite, and a lower proportion of albite within the breccia. The characteristic features of the breccia are: dilated grain boundaries (which are accentuated by an orange/brown staining); sub-grains in quartz; and sheared chlorite veins. Quartz has higher proportions of BLG compared to the inner damage zone and abundant sub-grains which are oriented NW-SE. Throughout the breccia the two different varieties of chlorite occur (brown/gold interference colour and purple/blue interference colour) and in some locations they co-exist in the same sample (e.g. VF3). Both types of chlorite occur in sheared and unsheared veins.

The cataclasite is composed of quartz, K-feldspar, albite, chlorite and epidote, there are no host rock characteristics recognisable, and the matrix is made up of clasts of variable sizes (μm to mm; Figure 5-16). The finest grained material (ultracataclasite) is dark grey and is entirely composed of clasts of $<50 \mu\text{m}$ within a finely comminuted matrix (Figure 5-17a). The clasts are quartz, albite and K-feldspar, and the comminuted matrix is primarily K-feldspar and epidote. Throughout the ultracataclasite there are numerous thin ($20 \mu\text{m}$) sheared chlorite veins which anastomose along strike (Figure 5-17a).

The majority of the cataclasite matrix has a bimodal grain size (Figure 5-16). There quartz- and feldspar- (albite and K-feldspar) rich zones and pods made of fragments $200\text{-}1000 \mu\text{m}$ in size within areas dominated by clasts less than $200 \mu\text{m}$. The finer grained areas are dominated by feldspar whereas the coarser areas are dominated by quartz. In both areas the feldspars are either anhedral and fractured or have a granoblastic texture. Larger fragments of feldspar are strongly fractured and cross-cut by microveins of K-feldspar. Albite is also strongly fractured and fractures are filled with K-feldspar.

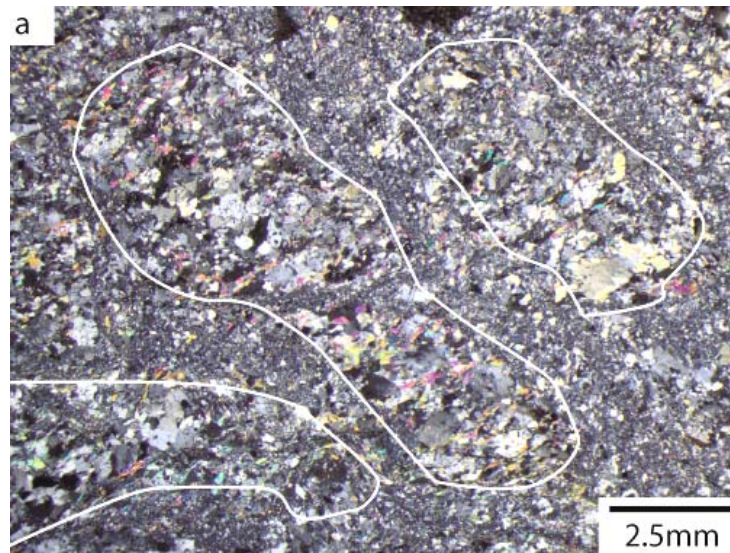


Figure 5-16: xpl image of cataclasite from the thick core within the VF
 Image shows a bimodal grain size distribution with the areas of coarser grained material highlighted in white. Sample VF14.

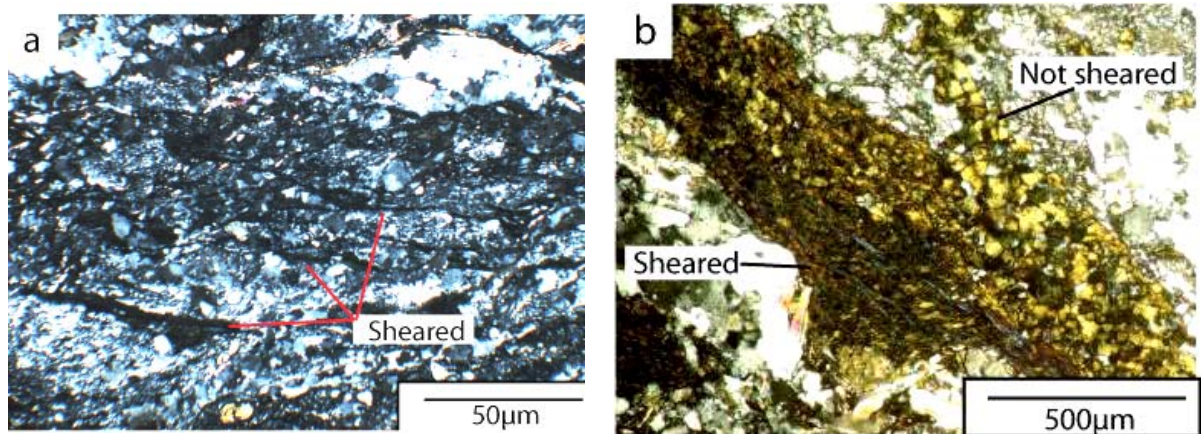


Figure 5-17: Characteristic features of the cataclasite within the VF.
 a) xpl image of the ultracataclasite in the thick fault core. Sheared chlorite veins within the ultracataclasite are arrowed. b) xpl image of a chlorite vein with sheared and unshattered crystals. Both images are from VF14

Quartz shows a range of textures throughout the cataclasite. The fine grained quartz is almost completely recrystallised by BLG; pods of quartz (~200-1000 μm) show BLG mainly on the grain boundaries; and large clasts have undulose extinction, and are strongly fractured, BLG is common throughout the larger quartz clasts and it contains a high density of fluid inclusions. The largest fragments of quartz in the cataclasite are also cross-cut by chlorite veins and the edges of the fragments can be off-set by up to 2.5 mm (Figure 5-18).

Chlorite veins are abundant throughout the cataclasite and are dominantly oriented NW-SE. They range from 10 μm to 1mm thick and from 500 μm to several centimetres long and can be sheared or unshattered (Figure 5-17b). Within

some veins, quartz and chlorite co-exist and the boundary between them is cusped.

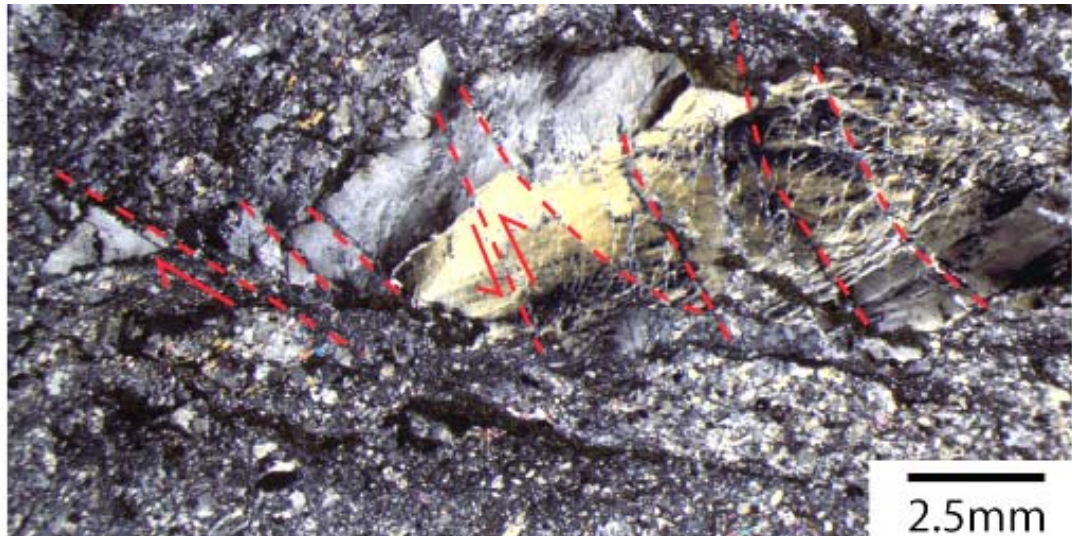


Figure 5-18: xpl image of a large quartz fragment within the cataclasite in the VF. that has been fractured, and some displacement has occurred along the fracture planes (highlighted in red). Sample VF14.

5.5 Virgin Fault Interpretation

5.5.1 Outer Damage Zone

The outer damage zone is characterised by a poorly defined foliation and quartz microveins. Throughout the rock biotite is partially chloritized; quartz has undulose extinction, BLG, fractures and fluid inclusions; and feldspars with a variety of textures. These features may result from fluid-rock interactions and this is discussed below.

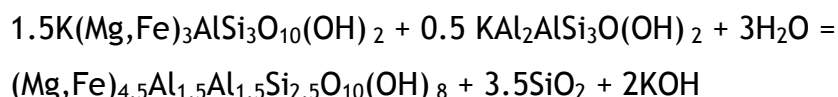
Chloritization of biotite is common in retrogressive conditions and it can occur by direct replacement of biotite by chlorite (Parry & Downey, 1982; Equation 3), or by dissolution-precipitation involving the consumption of either muscovite or K-feldspar (McNamara, 1966; Equation 4; Equation 5). Throughout the outer damage zone the foliation is not as clearly defined as in the host rock suggesting that muscovite and biotite have both been dissolved. However, where biotite is in the matrix, there is only evidence for direct replacement of biotite by chlorite (Figure 5-7d). Therefore the lack of a well defined foliation and partial replacement of matrix biotite implies that Equation 3 and Equation 4 could have been occurring. These reactions release K^+ , Mg^{2+} and quartz into the system and

thus this material may be available for other processes that may be occurring throughout the outer damage zone.

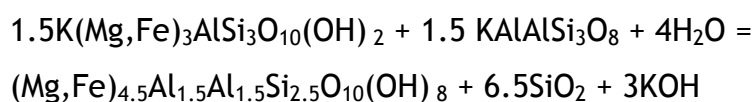
Equation 3: Biotite + H⁺ = Chlorite + K⁺ + Mg²⁺ + Quartz (Parry & Downey, 1982)



Equation 4: Biotite + Muscovite + Water = Chlorite + Quartz + KOH (McNamara, 1966)



Equation 5: Biotite + K-feldspar + Water = Chlorite + Quartz + KOH (McNamara, 1966)



The proportion of quartz does not change across strike of the fault zone (Figure 5-5), thus little or no quartz appears to have been added or removed from the system. The concentration of quartz in microveins requires dissolution of the quartz in the matrix and re-precipitation into veins. Therefore a fluid was present during deformation and vein formation. All quartz has undulose extinction and shows BLG along grain boundaries indicating deformation occurred after precipitation and that temperatures were ~300°C. In comparison to the host rock, more of the grain boundaries of quartz in the damage zone are effected by BLG. Differences in the amount and type of recrystallization that occurs in quartz can be a result of high temperature and low strain rates or low temperature and high strain rates (Hirth and Tullis, 1992). If temperature was the cause then the temperature did not exceed 350°C as sub-grain rotation does not occur within the fault rocks. However, within the outer damage zone there is not enough evidence to rule out either of these possibilities and so deformation could have occurred at an increased strain rate or slightly higher temperatures.

Fracturing and primary and secondary fluid inclusions all occur in quartz but the sizes of the primary inclusions differ between the host and vein quartz. Primary inclusions in the host are <20 µm while those in the veins are 20-60 µm. The

difference in size of the primary fluid inclusions indicates that they may represent two separate populations and therefore the quartz may have precipitated in different events. The primary inclusions in the quartz microveins are likely to record information on the fault zone fluids that were responsible for the redistribution of quartz. The secondary inclusion trails in both the host and vein quartz are of similar size and therefore could have formed in response to the same deformation event. Fracturing in a N-S orientation occurs in both the host and vein quartz meaning that the fracture event occurred after precipitation and plastic deformation of the veins.

Dissolution of the quartz from the matrix and reprecipitation into veins would create a transient porosity throughout the rock as a result of where the quartz was dissolved from in the fault rock matrix. Throughout the fault rock some of the matrix feldspars have a granoblastic texture (Figure 5-7b). Granoblastic textures can occur due to high temperature recrystallization in a fluid absent environment ($>500^{\circ}\text{C}$) (Passchier & Trouw, 2005), recrystallization in low temperature environments in the presence of a fluid, or by direct precipitation from a fluid. BLG in quartz indicates that temperatures were approximately 300°C and the local distribution of the granoblastic texture indicates that the conditions were not widespread throughout the rock. Quartz has been dissolved and reprecipitated indicating the presence of a fluid, therefore combined with temperature estimates being $\sim 300\text{C}$; this points towards the granoblastic feldspars forming in association with a fluid phase and that the feldspar precipitated as the quartz was being dissolved and re-precipitated into veins. The fact that the K-feldspar is interstitial to the albite in the granoblastic areas (Figure 5-7c) indicates that the albite precipitated first and that the K-feldspar grew around it perhaps during precipitation from a fluid.

The change of the shape and size of the albite from being large and euhedral in the host gneisses, to subhedral in the outer damage zone indicates that the albites have been dissolving and reprecipitating or recrystallizing in the presence of a fluid. The decrease in size of the feldspars (primarily albite) in the outer damage zone is therefore a result of interaction with a fluid phase.

The main differences in mineralogy between the outer damage zone and host rock are higher and lower proportions in K-feldspar and albite respectively.

However, microstructures show that both albite and K-feldspar were precipitating and that K-feldspar formed after albite. A comparison of the mineral proportions in the host rock gneiss compared to the outer damage zone show that 7% of albite is lost from the host and this is balanced by an increase in K-feldspar abundance by 6%. Equation 2 shows that albite can react to form K-feldspar in the presence of a fluid and vice versa and therefore replacement of one feldspar by another would satisfy the mineralogical observations. Feldspathization can take place in a closed system but changes in temperature and pressure will only bring about very small amounts of reaction (Wintsch, 1975). The replacement of albite by K-feldspar requires the addition of potassium (Equation 2). Chloritization of biotite releases K^+ into the fluid-rock system (Equation 3 and Equation 4) and this may be sufficient to drive the feldspathization reactions. However, the proportion of biotite in the host rock and outer damage zone are comparable. Hence, the amount of K^+ released during chloritization is unlikely to have enabled a 6% increase in the K-feldspar proportions in the outer damage zone. In an open system introduction of K^+ or loss of H^+ may enable larger volumes of K-feldspar to precipitate and only small amounts of deformation required to drive this reaction. Therefore, deformation in the VF was probably associated with an open fluid system.

The rock of the outer damage zone has been described as being weakly bleached and refers to the rock being whiter than the host rock. Bleaching within granitic rocks is typically due to fluid-rock interactions effecting the mineralogy of the rock (Chester et al., 1993; Di Toro and Pennacchioni, 2005; Hövelmann et al., 2010). The main reaction occurring in the outer damage zone is chloritization of biotite and K-feldspathization. Both of these reactions have been associated with colour changes in fault rocks (Chester et al., 1993; DiToro & Pennacchioni, 2005), and therefore are likely to be the cause of bleaching in the outer damage zone.

5.5.1.1 Inner Damage Zone

The inner damage zone is very similar to the outer damage zone in many respects and hence is characterised by quartz microveins, subhedral albite, and areas of granoblastic feldspar. However, there are also chlorite and epidote veins; K-feldspar, chlorite and epidote proportions increase towards the fault

core; and albite, muscovite, biotite and garnet proportions are corresponding lower.

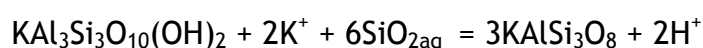
Chlorite and epidote veins indicate that brittle deformation and fluid flow occurred. The mineral fill can be used to estimate fluid temperature and chlorite and epidote typically signify temperatures <350°C (Bird et al., 1984; Bird and Spieler, 2004). The chlorite veins are composed of two different kinds of chlorite which are distinguished by their interference colours (brown/gold and purple/blue varieties). Quantitative analysis⁵ of the different chlorites shows that the chlorite with brown interference colours has approximately 16% Fe and 10% Mg, while the chlorite with purple interference colours has approximately 23% Fe and 6% Mg. The presence of these two chlorite compositions implies that there were at least two chlorite forming events or the chlorites represent two end member compositions and that the fluid composition varied through time. Within section 5a one of the veins is composed of quartz and chlorite (purple/blue interference). The boundary between the two minerals is cusped (Figure 5-11e) and indicates that the quartz is being replaced by an Fe-rich chlorite. The Mg-rich chlorite veins cross-cut the quartz veins and so they also formed after quartz precipitation, however age of relative growth of the Fe-rich and Mg-rich chlorites is unknown.

BLG recrystallization in the quartz microveins is more pervasive in the inner damage zone compared to the outer damage zone, but no sub-grain rotation occurs. The type and distribution of fluid inclusions is the same as in the outer damage zone and the quartz crystals have been cross-cut by fractures. The textures therefore indicate dissolution-reprecipitation of quartz followed by plastic deformation and then brittle deformation. The increased volume of BLG within the inner damage zone implies that deformation occurred at slightly higher temperatures or increased strain rates compared to the outer damage zone or host rock but the temperature did not exceed 350°C. The presence of BLG in both the inner and outer damage zone implies that there is no great temperature gradient between the two locations. Therefore, an increase in strain rate is likely to be the mechanism for causing the increased amount of BLG.

⁵ Table of results shown in Appendix 2.

The feldspars from the inner damage zone matrix contain many of the same textures that occur in the feldspars in the outer damage zone indicating that dissolution of albites and precipitation of K-feldspar and albite occurred. K-feldspar proportions are 19% higher and albite proportions 13% lower in the inner damage zone compared to the host rock. The change in K-feldspar and albite proportions compared to host implies that a large amount of reaction took place. This change in mineral proportions therefore implies that feldspathization was associated with an open system (Wintsch, 1975). Albite can be replaced directly by K-feldspar, however K-feldspar proportions are 19% higher whereas albite proportions are 13% lower, indicating a 6% unexplained difference in K-feldspar proportions. Biotite and muscovite proportions are lower in the inner damage zone compared to the host rock and outer damage zone indicating that they have been dissolved. Chloritization of biotite can consume muscovite and release K^+ (Equation 4) providing a source of K^+ for K-feldspar production. Muscovite can also react with quartz to form K-feldspar (Equation 6) and thus provides another mechanism for K-feldspathization to occur. Both of the feldspathization reactions (Equation 4 and Equation 6) require near neutral pH conditions (McNamara, 1966; Wintsch et al., 1995) indicating that although the system may have been open to fluids, the amount of H^+ supplied did not create acidic fluid-rock conditions.

Equation 6: Muscovite + Quartz = K-feldspar (Wintsch et al., 1995)



The replacement of one feldspar by another has been frequently observed (Labotka et al., 2004; Niedermeier et al., 2009; Putnis, 2002) and the relationships between albite and K-feldspar in the inner damage zone (e.g. Figure 5-11b and c) are similar to those reported in such studies. The albite-K-feldspar textures, such as pitting and small inclusions of albite within K-feldspar, suggest that replacement occurred by interface-coupled dissolution-precipitation (Cole et al., 2004; Hövelmann et al., 2010; Labotka et al., 2004; Niedermeier et al., 2009; Putnis, 2002). This process requires a fluid-film at the mineral-mineral interface (O'Neil and Taylor, 1967), and for the fluid to be supersaturated with respect to the product (Hövelmann et al., 2010). The production of K-feldspar by dissolution-precipitation therefore implies that a

K-rich fluid would have been present during fault evolution. Grain size of the feldspars is reduced compared to the outer damage zone and the anhedral shapes signify that dissolution was occurring and therefore grain size reduction involved mineral reactions.

Bleaching of the inner damage zone rock is more noticeable than in the outer damage zone rock. The main bleaching reactions, chloritization and K-feldspathization, have produced more chlorite and K-feldspar within the inner damage zone compared to the outer damage zone. This suggests that more reaction was able to take place in the inner damage zone and hence, the bleaching that occurs is more noticeable than in the outer damage zone.

5.5.1.2 Fault core - Narrow core

The narrow fault core is composed of co-existing breccia and cataclasite (Figure 5-12). Cataclasis is a result of fracturing and rotation of particles causing a decrease in grain size of the rock (Blenkinsop, 1991). The cataclasite is composed of clasts of quartz, albite, K-feldspar and epidote within a K-feldspar-rich cement (Figure 5-13a). For the K-feldspar to form around the fragments indicates that it came in after cataclasis and was precipitated from a fluid. K-feldspar results in hardening of the fault rock (Wintsch et al., 1995) and so its precipitation may have influenced the evolution of the fault. Chlorite veins do cut the cataclasite indicating that cementation of the cataclasite prevented cataclastic flow and promoted brittle fracturing. Fracturing enhances permeability and chlorite precipitation shows that the fractures temporarily transmitted fluids. The chlorite veins throughout the narrow core are magnesium rich while the iron rich chlorite occurs along the PSS. There are no cross cutting relationships between the different chlorite compositions.

The breccia is composed of fragments with the boundaries highlighted by an Fe staining (Figure 5-13b). This staining indicates that an Fe-rich fluid was able to infiltrate around the fragments, therefore dilation must have occurred to create the additional space. The porphyroclasts within the breccia are primarily composed of quartz, K-feldspar and albite and veins of Mg rich chlorite cross-cut the rock. The large K-feldspar fragments are fractured and veined with a non-luminescent variety of K-feldspar while the smaller fragments show anhedral

crystals or a granoblastic texture. The textures indicate dissolution of albite and reprecipitation of K-feldspar. Raman spectroscopy indicates that the non-luminescent K-feldspar is structurally different (Freeman et al., 2008) and therefore represents a different type/generation of K-feldspar. A low temperature, non-luminescent K-feldspar that is common in low temperature hydrothermal settings is Adularia. Given the similarities between the K-feldspar veins and adularia, it is likely that the non-luminescent K-feldspar veins are composed of adularia. Adularia has a maximum formation temperature of 265°C (Steiner, 1970) and is known to have formed in fluids with temperatures as low as 100-200°C (Glodny and Grauert, 2009). Co-existence of chlorite and K-feldspar occur in epithermal, adularia-sericite type alteration (Hemley and Jones, 1964), which is characterised by near neutral pH conditions and most likely an open system (Wintsch, 1975; Glodny & Grauert, 2009).

Close to the cataclasite bands and adjacent to sheared chlorite bands the quartz can be almost completely recrystallised by BLG while in the larger fragments sub-grains occur within the crystals. The increased level of BLG indicates that either the temperatures in the fault are approaching 350°C or that high strain rates occurred during deformation. The variable quartz microstructures throughout the narrow core samples infer that the conditions were not stable over distances of a few centimetres. If the microstructures were in response to temperature it is unlikely that it would be variable over such a short distance and thus the microstructures would be more consistent. In fault zones, shear strain rates increase towards the centre of a fault, which in turn promotes brittle deformation (Patterson, 1978). In the narrow core the quartz closer to the PSS has increased amounts of BLG and also suggests that shear strain rates increase towards the core.

5.5.1.3 Fault core - Thick core

In the areas where the breccia and cataclasite are easy to distinguish the former is very similar to the inner damage zone rock. However, in the breccia in the thick core the chlorite veins are sheared, grain boundaries are dilated and Fe stained, and both the Fe- and Mg-rich chlorites are present. These features indicate a minimum of three fracturing events associated with fluid flow: quartz microveins; Mg-rich chlorite veins; and dilation of breccia associated with an Fe-

rich fluid and chlorite precipitation. The large volumes of K-feldspar precipitation imply that the system was open to fluids. Quartz preserves evidence of plastic deformation which probably occurred due to increased shear strain rates and shearing of the chlorite veins shows that some localised slip occurred after chlorite precipitation.

Bands of ultracataclasite occur in the cataclasite in the thick core and the former are characterised by having sheared chlorite bands throughout. The cataclasite was therefore fractured, fractures filled with chlorite, and the veins subsequently sheared, thus the ultracataclasite bands record multiple deformation events. The matrix of the cataclasite is bimodal with finer grained areas being dominated by feldspar and the coarser areas by quartz. Feldspar shapes indicate that dissolution-reprecipitation is prevalent within the cataclasite and that grain size reduction for feldspars is primarily by reaction. In the finer grained areas quartz crystals have mainly been recrystallised by BLG (sub-rounded crystals) but were also deformed by cataclasis. In the coarser areas the quartz is similar to that which occurs in microveins with pods oriented NW-SE, BLG and lots of primary and secondary fluid inclusions. The quartz is also fractured with some offset recorded along the fractures (Figure 5-18). The main grain size reducing mechanism in quartz is BLG and fracturing whereas in K-feldspar it is by fluid-rock interaction processes. The average grain size of quartz is greater than that of feldspar in the cataclasite and thus grain size reduction by fluid-rock interaction is widespread. The coarser areas of quartz are similar in form to the quartz microveins and this may explain why the quartz is coarser grained. Quartz microveins resulted in the creation of feldspar and quartz rich patches within the fault. The feldspar rich areas being finer grained are therefore going to be weaker and more likely to deform by cataclastic flow than quartz (Fitz Gerald and Stünitz, 1993; Tullis and Yund, 1985; White, 1979). Within the finer grained areas the quartz is recrystallised by BLG or fragmented and angular which is characteristic of cataclasis. The microstructures imply that due to segregation of the primary components and the different grain size reducing mechanisms that operate in quartz and feldspar; cataclasis was initiated within the feldspar rich areas.

The coarse and fine grained areas of the cataclasite are crosscut by numerous chlorite veins and both sheared and unsheared veins occur. Veining of the

cataclasite indicates the cataclastic material was periodically strong enough to yield by brittle fracturing rather than cataclastic flow. K-feldspar proportions increase in the cataclasite and could have resulted in hardening of the cataclasite, promoting fracturing. Many of the chlorite veins are sheared and this indicates that after vein formation slip was localized onto the veins.

5.5.1.3.1 Comparison of the narrow and thick core

The main differences between the two fault cores are the volume of cataclasite and breccia present and that in the narrow core the cataclasite and breccia coexist while in the thick core they are separate. Differences between the two cores indicate that within the narrow core the deformation is distributed between the cataclasite and breccia, whereas in the thick core the majority of deformation is localised within the cataclasite or on chlorite veins in the breccia. The narrow core is probably a precursor to the thick core as all of the microstructures found in the narrow core (breccia and cataclasite) can be identified in the cataclasite in the thick core.

The cataclasite in the narrow core is very similar in nature to the ultracataclasite in the thick core with the only differences being smaller clast size and sheared chlorite veins in the ultracataclasite. The process of cataclasis results in grain size reduction and therefore if more deformation was focussed onto the cataclasite in the narrow core, it is likely that it would evolve towards a similar grain size as the ultracataclasite. The breccia in the narrow core has large fragments which are strongly fractured and veined, there are sheared chlorite veins, recrystallised feldspars and the quartz crystals show different intensities of BLG throughout. All of these microstructures occur in the cataclasite in the thick core with the only difference being that the size of the fragments and the average grain size in the thick core is smaller. Therefore with continued deformation and fluid-rock reactions the fragment size of the narrow breccia would decrease and a similar texture to cataclasite in the thick core would evolve. The breccia in the thick core is effected by fracturing and dilation and slip is localised onto veins. This indicates that as the fault core became thicker the deformation was concentrated onto the finer grained material. Based on these observations a model for fault core evolution in the VF is shown in Figure 5-19. The model shows four main steps in core formation. Step 1 is

reactivation of pre-existing joints. This enables fluid infiltration and fluid-rock interactions causing grain size reduction (step 2) which weakens the rock (White, 1979; Tullis & Yund, 1985; Fitz Gerald & Stünitz, 1993). Movement on the PSS causes cataclasis along the PSS and brecciation of the adjacent altered rock. The movement results in cataclasite along the PSS and around the breccia fragments (step 3). Continued movement associated with fracturing and brecciation breaks down the breccia forming cataclasite and causes brecciation of the adjacent altered rock (step 4). In relation to the model the narrow core is representative of step 3 while the thick core is more akin to step 4 (Figure 5-19).

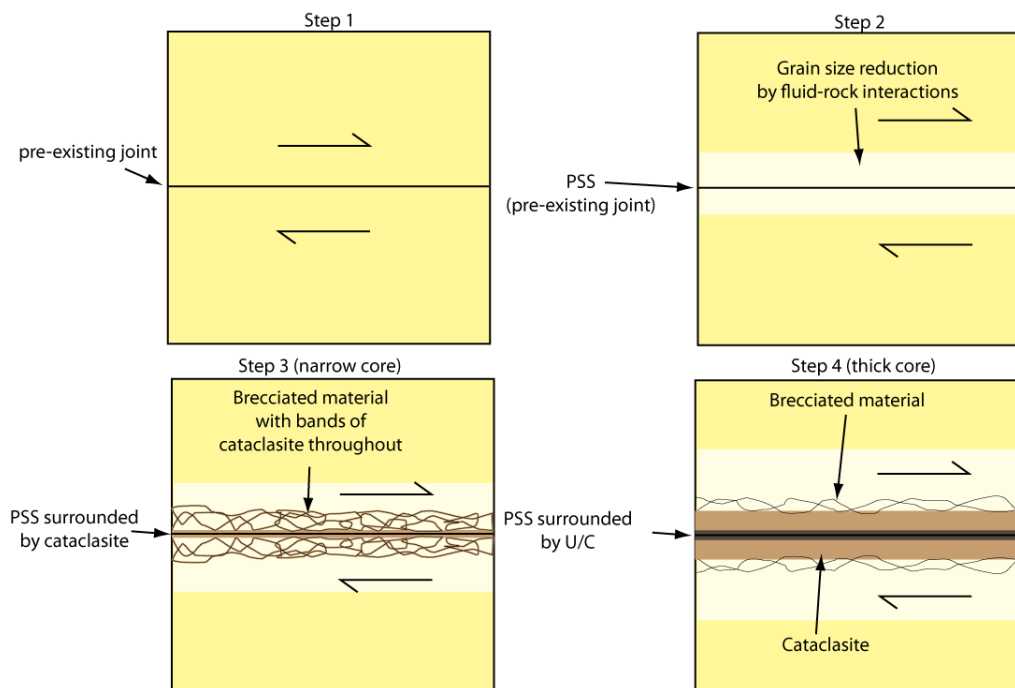


Figure 5-19: Evolution model for the fault core within the VF.

Step 3 is representative of the narrow core while step 4 is representative of the thick core in the VF. PSS = principal slip surface. Cartoon not to scale.

5.5.1.4 Virgin Fault Summary

The main reactions taking place within the VF are the retrogression of garnet and biotite, dissolution-precipitation of quartz, replacement of albite by K-feldspar, breakdown of muscovite to K-feldspar and chlorite precipitation. The majority of the reactions take place throughout the entire fault zone with only muscovite breakdown being localised to the inner damage zone and fault core. K-feldspar precipitation is common throughout the fault and the amount of K-feldspar precipitating increases towards the fault core, in part linked to muscovite breakdown.

Reactions and textures indicate the presence of fluid within the fault zone and the precipitation of K-feldspar indicates that the fluid was likely supersaturated in K^+ and at near neutral pH conditions (Wintsch, 1975). The Fe and Mg rich chlorites also indicate that there were at least two fluids of different compositions within the fault. Biotite and muscovite are stable above $\sim 380^\circ\text{C}$ (Bucher and Frey, 2002) and epidote can form at temperatures as low as $150\text{--}200^\circ\text{C}$ (Bird et al, 1984; Bird & Spieler, 2004). The presence of epidote and the retrogression of biotite therefore indicate that temperatures were in the region of $150\text{--}380^\circ\text{C}$. However, BLG in quartz occurs from $300\text{--}350^\circ\text{C}$ and brittle deformation is typically associated with conditions below 300°C . Therefore the maximum temperature for deformation was $300\text{--}350^\circ\text{C}$ and this decreased over time giving way to brittle deformation conditions.

The dominant processes occurring within the damage zone are fluid-rock reactions. The reactions result in grain size reduction of feldspar and removal of garnet, biotite, muscovite and albite from the rock. In the fault core, the reactions are coupled with cataclasis and therefore grain size reduction is by reaction and brittle deformation. BLG in quartz forms in response to temperature conditions and/or increased strain rates. In the damage zone, BLG is fairly consistent throughout the rock and imply that the BLG was primarily in response to temperature. However, in the core the intensity of recrystallization by BLG is variable over distances of millimetres to centimetres but the most recrystallised quartz is commonly within 3mm of the PSS. The variable nature of the BLG microstructures indicates that temperature was not the control but that BLG increased towards the PSS in response to increased strain rates towards the centre of the fault.

5.6 Ciao Ciao fault (CCF)

The CCF was mapped for 800m along strike and due to limited exposure the petrological study is based on a few good exposures. Within the CCF, the fault zone is composed of a fault core and damage zone. There are no variations in bleaching intensity within the damage zone and so it will simply be referred to as the damage zone throughout the description. The following results are based on across strike variations only as exposures of cataclasite and foliated

cataclasite only occur at locality 5. Samples analysed are shown in Table 5-2 and a map showing the location of the samples within the field area can be found in Appendix 1.

5.6.1 Grain size and mineralogy

Grain size measurements were recorded for quartz and feldspar (K-feldspar and albite) within the fault rock. The grain size is similar within the host rock and damage zone (Figure 5-20). However, the grain size decreases across strike from ~1200 to ~30 μm from the damage zone rock to the cataclasite (Figure 5-20), and within the damage zone and breccia the feldspars are always smaller than the quartz. From the cataclasite to the foliated cataclasite, the grain size of feldspar does not change but the grain size of quartz increases from ~30 μm to ~300 μm (Figure 5-20).

Across strike of the CCF muscovite, chlorite and calcite modal proportions are higher compared to the host rock; albite, epidote, biotite and garnet proportions are lower; and K-feldspar and quartz proportions are constant across the fault (Figure 5-21). Biotite, epidote and garnet do not occur in any of the fault rocks. The greatest changes in proportion from host to core are in albite and muscovite with albite decreasing by ~ca 16% and muscovite increasing by ca 23% (Figure 5-22).

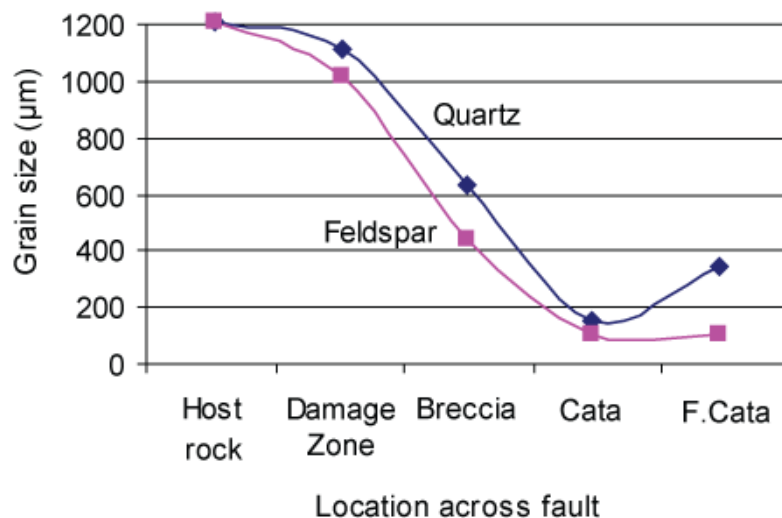


Figure 5-20: Grain size variation across strike for the main matrix minerals in the CCF. Feldspar = K-feldspar and albite, Cata = cataclasite and F.Cata = foliated cataclasite.

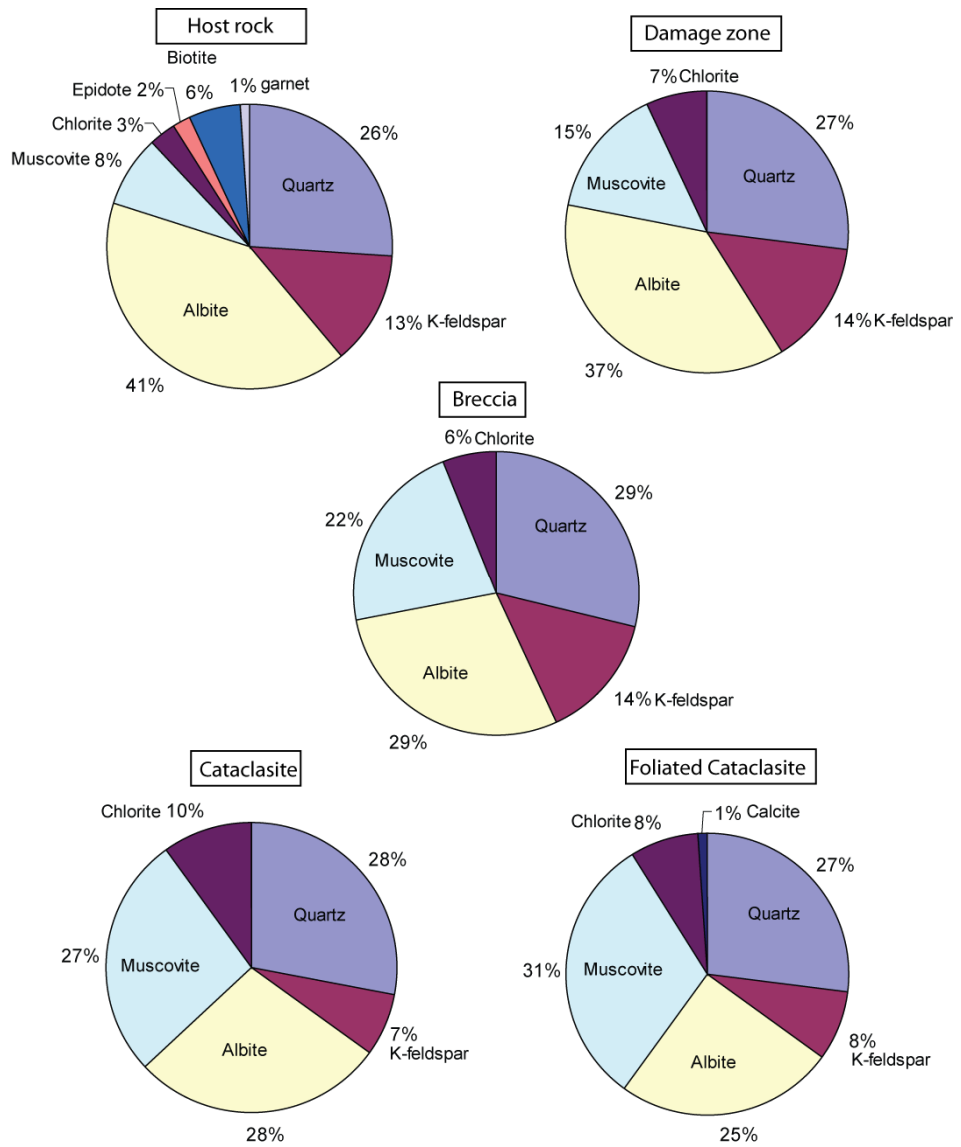


Figure 5-21: Across strike variations of the minerals within the Ciao Ciao Fault.

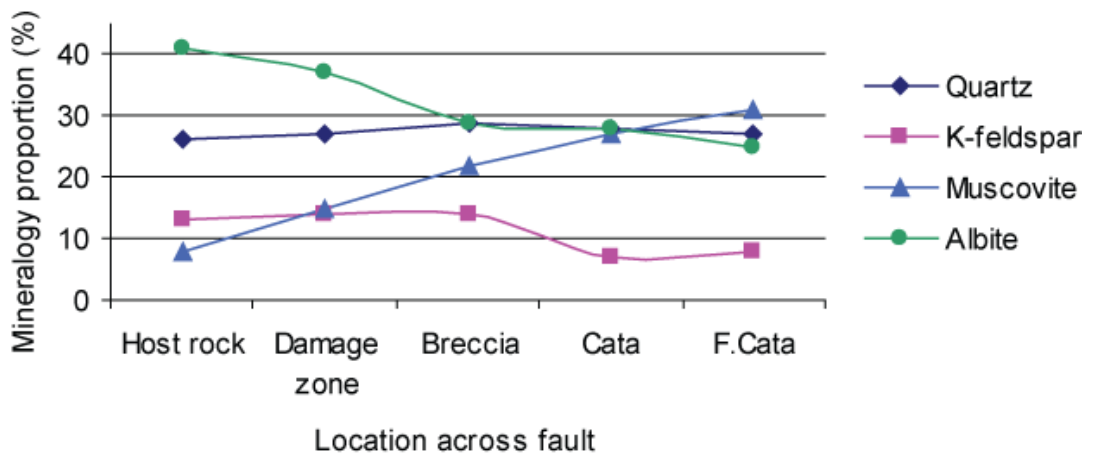


Figure 5-22: Across strike variations of the main minerals in the Ciao Ciao Fault. Cata = cataclasite; F.Cata = foliated cataclasite.

5.6.2 Micro-structures and -textures

5.6.2.1 Damage zone

Host rock characteristics are prevalent within the damage zone. There are augen, a biotite (red/brown) and muscovite defined foliation, undulose extinction and minor BLG of quartz, and the dominant feldspar in the matrix is albite (Figure 5-23). The characteristic features within the damage zone are large open fractures, chlorite veins and minor sericitization of feldspars.

Fractures vary from being open, ~1 mm wide, several centimetres long and lined with muscovite to intra-crystalline fractures with negligible apertures and no fill. The large open fractures are typically oriented E-W and/or NE-SW and spaced 1-5 cm apart (Figure 5-23) while the intra-crystalline fractures typically occur in quartz, are oriented N-S and are sparse.

Chlorite veins are ~100 μm thick, several millimetres long and the trace of the vein gently undulates along strike. Veins are spaced several centimetres apart and only observed in thin section. In xpl the chlorite has blue/grey interference colours.

The majority of feldspars (albite and K-feldspar) in the damage zone are large and euhedral but have also been effected by sericitization. The, sericitization is associated with the grain boundaries (outer 20-50 μm effected) and does not effect the feldspar cores.

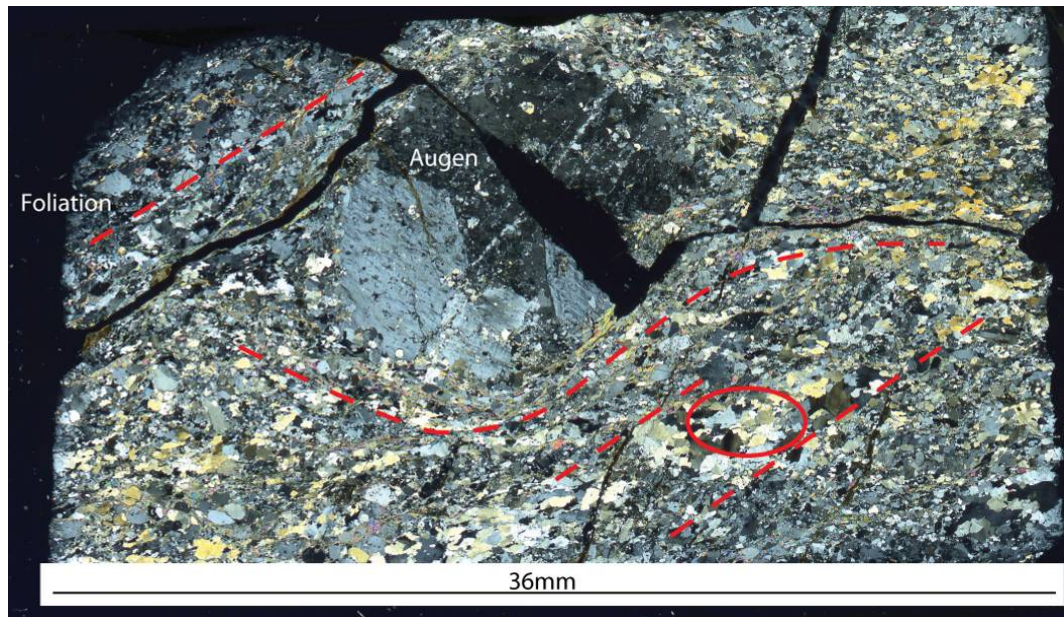


Figure 5-23: Damage zone rock from the CCF. The foliation within the rock is highlighted by red dashed lines. An area of quartz with undulose extinction is circled (xpl, Sample CC1).

5.6.2.2 Breccia

The breccia occurs between the damage zone and cataclasite (Figure 4-18) and the boundaries between the different rock types are sharp (Figure 5-24). The mineralogy of the breccia is characterised by quartz, albite, muscovite and K-feldspar. The average grain size is 500 μm , however quartz tends to be slightly larger (600-800 μm) while feldspars tend to be smaller (200-400 μm). The breccia is dominated by fractures extending for up to several centimetres through the rock. These are oriented NW-SE and NE-SW with the former being more pervasive. Along the NW-SE oriented fractures there are often small offsets (up to 100 μm) and/or bands of recrystallization and/or brittle fragmentation of the surrounding crystals.

Quartz is subhedral and occurs as large pods which are approximately 1 mm in diameter, or as random crystals distributed throughout the matrix. Quartz has undulose extinction, is fractured, and has been recrystallised by BLG. In the pods of quartz, BLG tends to be restricted to the grain boundaries, however in the matrix the entire crystal can be recrystallised.

Feldspars are subhedral with lobate to gently curving grain boundaries. Feldspars are often associated with muscovite which occurs around and within the outer rim of the feldspars.

Muscovite forms in thin bands which anastomose and interconnect with other bands. Muscovite may also be present in large strongly sheared clumps. Chlorite is randomly distributed throughout the breccia.

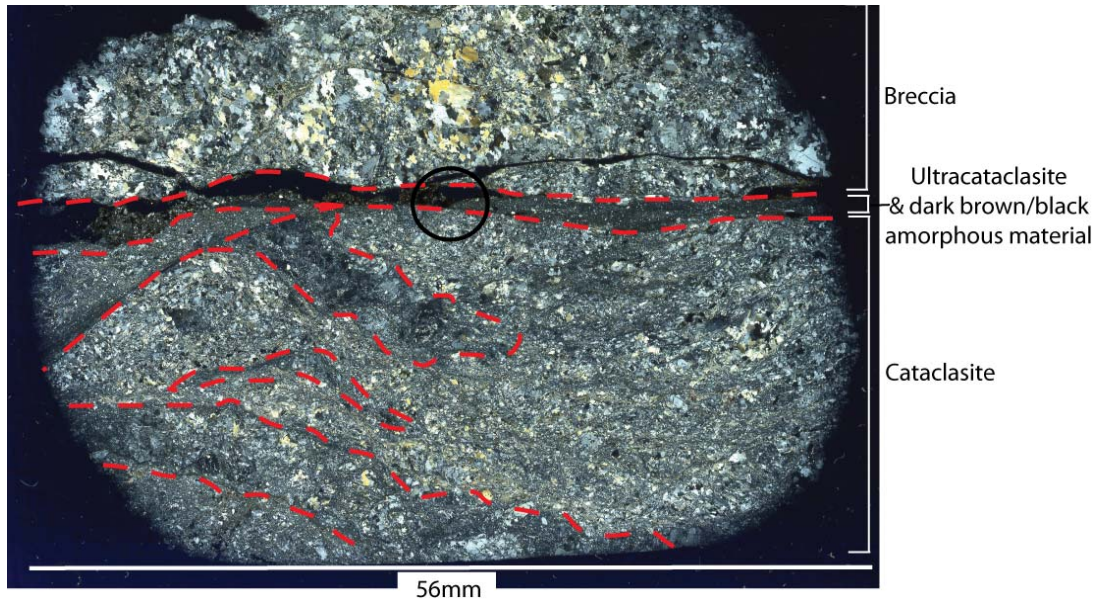


Figure 5-24: xpl image of the boundary between the breccia and cataclasite within the CCF. Central ultracataclasite band marks the boundary between the breccia and cataclasite. Different generations of cataclasite are identified by colour and have been indicated by the red dashed lines. Dark brown/black amorphous material occurs at the boundary and the area circled is enlarged in Figure 5-26. Sample = CC2.

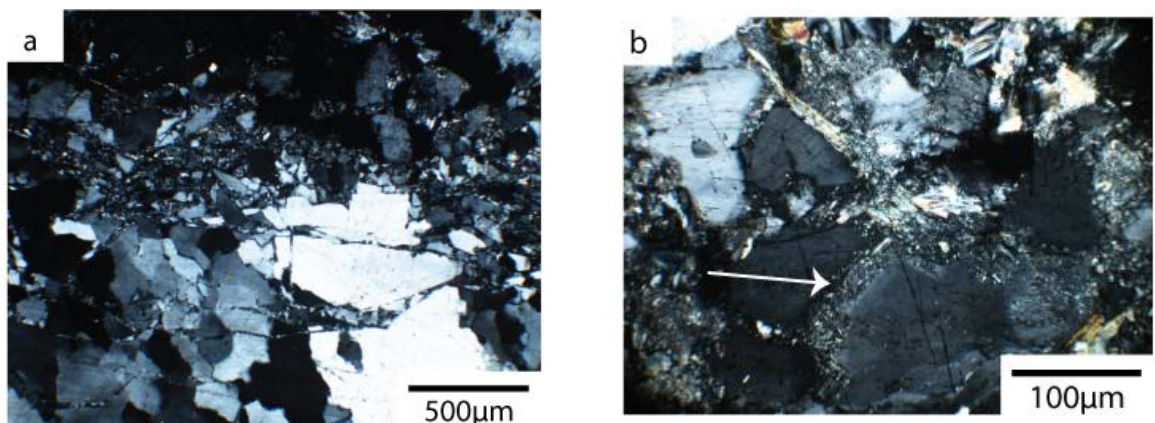


Figure 5-25: Microstructures within the breccia from the CCF. a) xpl image showing brittle fracturing and fragmentation of quartz. b) xpl image of feldspars that have been effected by sericitization (arrowed). Both images are from sample CC2.

5.6.2.3 Cataclasite

The cataclasite within the CCF is texturally similar to that observed in the VF. However, in the CCF no chlorite veins cut the cataclasite and there is a much higher proportion of muscovite (25% more); the average grain size is smaller; and different generations of ultracataclasite are present.

Ultracataclasite is composed of angular and sub-rounded clasts of quartz, K-feldspar and albite which are $\leq 30 \mu\text{m}$. Different generations of ultracataclasite are distinguished in the CCF primarily by colour (Figure 5-24). The boundary between the different generations is sharp and compositional variations can be distinguished based on the proportion of clasts to comminuted material.

At the boundary between the breccia and the cataclasite there is a thin vein of brown/black amorphous material. There are no clasts within the amorphous material and it appears glassy in plane polarised light (Figure 5-26a). The amorphous material occurs as either injection veins into the wall rock or where it cuts the ultracataclasite the latter is enveloped by the amorphous material (Figure 5-26a). SEM imaging reveals that the amorphous material is composed of ultrafine clasts ($< 20 \mu\text{m}$) (Figure 5-26b). There are no crystallites within the dark material and so indicates that it is not pseudotachylyte.

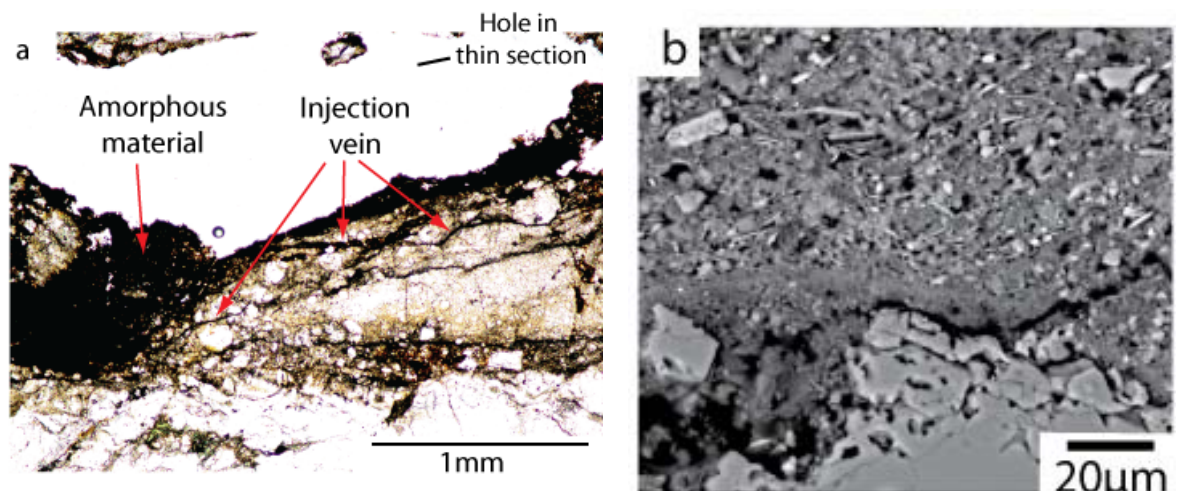


Figure 5-26: Amorphous material at the boundary between the breccia and cataclasite
 a) enlarged ppl image of the amorphous material that is circled in Figure 5-24. Image highlights injection veins of the dark material into the wall rock
 b) SEM-BSE image of the amorphous material showing that it is composed of ultrafine clasts. Both images are from sample CC2.

Muscovite and chlorite have very similar textures throughout the cataclasite. Both minerals are fine grained (~50-200 μm) and disseminated throughout the cataclasite. The phyllosilicates often align in thin bands oriented NW-SE, the bands undulate along strike and are often associated with fracture planes.

Quartz and feldspar both have similar textures to those in the cataclasite from the VF. Within the CCF quartz and feldspar are both finer grained than in the VF cataclasites (by ~20-40 μm). The majority of feldspar crystals have disintegrated into small clasts. There are very few large intact feldspars but where they do occur they are strongly sericitised. Quartz clasts are angular, larger than feldspar fragments (by ~40 μm), and where larger pods of quartz do occur they are strongly fractured and BLG is common.

5.6.2.4 Foliated cataclasite

The foliated cataclasite is very similar to the cataclasite in terms of mineralogy and general textures. However in the foliated cataclasite muscovite proportions are higher, albite proportions are lower and there are no cross cutting bands of ultracataclasite. Chlorite veins, microveins of quartz (1-3 mm long), and a foliation defined by muscovite is present (Figure 5-27).

Chlorite veins are laterally continuous, they vary in thickness along their trace (10s of μm to 100s of μm) and the orientation of a single vein can change from NW-SE to E-W (Figure 5-27). The foliation is defined by muscovite bands which are several micrometres thick and anastomose along the trace of the foliation.

The quartz microveins within the foliated cataclasite are oriented approximately NW-SE, sub-parallel to the foliation (Figure 5-27), and contain large crystals of quartz (200-500 μm). Throughout the cataclasite the quartz within the microveins has variable textures. Some microveins have euhedral crystals with minor BLG and undulose extinction, whereas other microveins contain crystals that are strongly fractured and BLG is common (Figure 5-28).

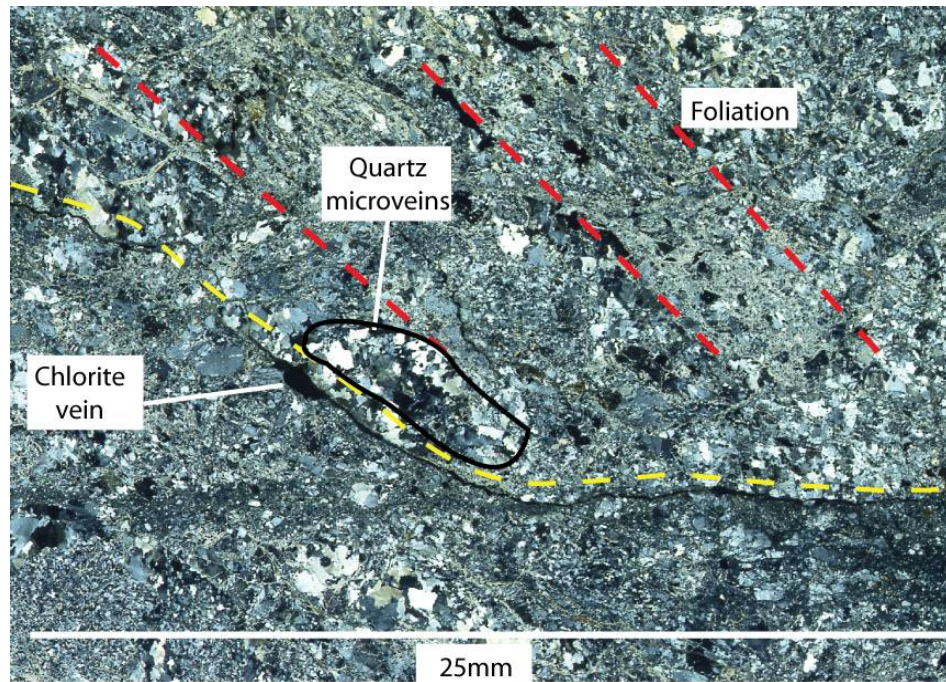


Figure 5-27: xpl image of the foliated cataclasite within the CCF. The foliation is highlighted by red lines, a chlorite vein which changes orientation along its trace is highlighted by a yellow line adjacent to the vein and a quartz microvein oriented NW-SE is circled. Sample = CC3.

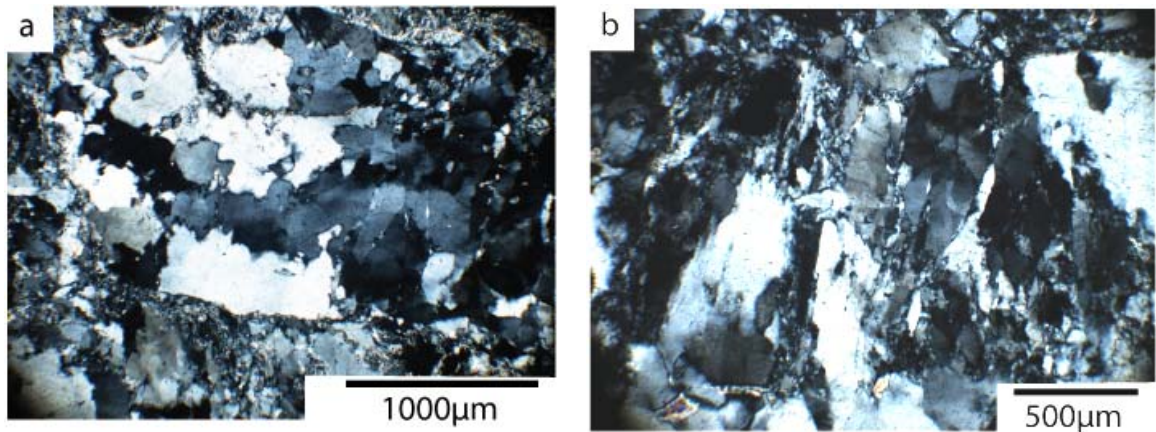


Figure 5-28: xpl images of the quartz microstructures in foliated cataclasite. a) Quartz with only minor BLG on grain boundaries. b) Quartz that has been strongly effected by BLG. Both samples are from CC3.

5.7 Interpretation – Mineralogy and micro-structures

5.7.1 Damage zone

Host rock characteristics are prevalent within the damage zone with only minor evidence of deformation. BLG in quartz is restricted to the grain boundaries. There is no obvious increase in the proportions of BLG from host to damage zone and therefore the BLG indicates ambient temperatures of approximately 300°C. Open fractures and chlorite veins imply brittle conditions (<300°C) associated with fluid flow and mineral precipitation. The reactions occurring in the matrix of the damage zone include the alteration of garnet (Equation 1), biotite and feldspars (Equation 7 and/or Equation 8). The lack of biotite throughout the damage zone indicates that it has dissolved however, the muscovite proportions have not decreased compared to the host rock. Therefore the most likely reaction for biotite dissolution would be Equation 5. This reaction consumes biotite and K-feldspar and produces chlorite and quartz of which the former does occur in veins within the damage zone. Feldspar alteration/sericitization affects albite in the damage zone (Figure 5-22) and the alteration is concentrated at the grain boundaries of the feldspars. The outer rims (20-40 µm) of the crystals are affected by sericitization (muscovite) but the alteration has had no clear effect on the size and/or shape of the feldspars.

Sericitization is common during hydrothermal alteration of granitic rocks (Sandstrom et al., 2010) and indicates the presence of a fluid and highly acidity conditions (Hemley & Jones, 1964; Wintsch et al., 1995). To create such conditions fluids must have been abundant, as small amounts of fluid result in K-feldspar precipitation (Wintsch, 1975). Sericitization releases quartz in solution (Equation 7), however there is no evidence for quartz precipitation in the cataclasite. Therefore the quartz must have been removed from the system in solution and implies that the cataclasite was open to fluids (O'Hara, 2007; O'Hara, 1994). Quartz within the matrix does not have dissolution textures and therefore combined with the incipient nature of the sericitization reaction indicates that the fluid-rock conditions promoting sericitization and quartz dissolution were short lived.

Equation 7: K-feldspar = Sericite (muscovite) + quartz (Wintsch et al., 1995)



Equation 8: Albite = Sericite (muscovite) + quartz (Wintsch et al., 1995)



5.7.2 Breccia

There is a change in mineralogy and an increase in the amount of deformation that occurs in the breccia compared to the damage zone. The dominant processes taking place include the breakdown of feldspars by sericitization and a combination of brittle and ductile deformation of quartz.

The proportion of muscovite increases by 14% and albite decreases by 12% in the breccia compared to the host rock (Figure 5-22). All feldspars have been partially sericitised and therefore the high abundance of muscovite must include the alteration of K-feldspar even though compared to the host rock, no significant change in K-feldspar proportion was recorded. Sericitization is pervasive throughout the feldspar crystals (Figure 5-25b) and causes grain size reduction via fluid-rock interactions throughout the breccia. Sericitization of feldspars releases quartz in solution (Equation 8) however there is no significant increase in quartz proportions in the breccia compared to the host rock (Figure 5-22). Open system behaviour promotes quartz dissolution and feldspar alteration creating porosity (Janssen et al., 1998; O'Hara, 2007; O'Hara, 1994), therefore if open system behaviour was active in the brecciated zone any excess quartz would be kept in solution and removed from the fault rock. Also, within the breccia the amount of potassium needed for sericitization of albite, can not be balanced by the amount of K released by the alteration of biotite, garnet and K-feldspar (Figure 5-21), suggesting an external source of K was required.

The matrix quartz has been strongly effected by fracturing and BLG. In areas where the quartz crystals are large the fragments are strongly fractured with small offsets on the fractures whereas in finer grained areas quartz is almost completely recrystallised by BLG. The variability of quartz micro-structures within the brecciated rock indicates that the most likely cause for higher

proportions of BLG compared to the host rock, was increased strain rates. Grain size reduction has therefore occurred by mechanical breakdown and recrystallization.

5.7.3 Cataclasite

At the boundary between the breccia and cataclasite there is a dark brown/black amorphous material. The dark material engulfs numerous fragments and forms injection veins into the wall rock. When observed using SEM-BSE the material has no crystallites and is not comparable to pseudotachylyte found in other seismogenic faults (DiToro & Pennacchioni, 2005; Kirkpatrick et al, 2008; Mitterpergher et al., 2009). However, the colour and nature of the material is more akin to crush-pseudotachylyte (Janssen et al., 2010) or fluidised ultracataclasite which may indicate a seismic event along the CCF (Lin, 2011) that initiated at the boundary between the breccia and cataclasite.

The cataclasite has a relatively uniform grain size (<150 µm) and is dominantly composed of quartz, albite, K-feldspar and muscovite. Compared to host rock, the muscovite proportions are higher, albite proportions are lower, and quartz and K-feldspar proportions are similar to the host. All feldspars are strongly sericitised but there is no evidence of quartz precipitation indicating adequate permeability existed to enable fluid flow. Hence acidic conditions and open system behaviour prevailed.

Throughout the matrix, feldspar clasts are angular to sub-angular and are intimately associated with muscovite. Quartz fragments are either angular or completely recrystallised by BLG indicating brittle deformation and/or increased strain rates. Grain size reduction has therefore been primarily by reaction in feldspars and by fracturing and/or cataclasis in quartz.

5.7.4 Foliated cataclasite

There are two defining characteristics of the foliated cataclasite; a strong foliation and a larger average grain size of quartz compared to the cataclasite. The foliation is defined by muscovite which precipitated in response to the alteration of feldspars within the fault rock. There is no clear foliation in any of

the other fault rocks. However, the matrix of the foliated cataclasite is quartz and feldspar-rich and the majority of the microstructures, except for foliation and quartz microveins, are the same as those observed in the cataclasite and likely formed by the same mechanisms i.e. grain size reduction by reaction and/or fracturing and cataclasis.

The dominant processes of creating a foliation within the cataclasite are solution transfer, mechanical rotation, and growth of new minerals in the preferred orientation (Passchier & Trouw, 2005). In the foliated cataclasite there is no evidence for dissolution-reprecipitation of the muscovites, however the proportion of muscovite is higher compared to the other fault rocks (Figure 5-22). Within the cataclasite, muscovites can be aligned but the network of muscovites is not pervasive through the rock and thus there is no clear foliation. Assuming that cataclasite is the precursor to foliated cataclasite (Jefferies et al., 2006a) and that one of the active deformation mechanisms is cataclasis; it seems likely that the foliation formed due increased proportions of muscovite enabling an interconnected network (Jefferies et al., 2006a) and the rotation of the existing particles into the preferred orientation.

Quartz microveins occur within the foliated cataclasite and are oriented approximately sub-parallel to the muscovite defined foliation (Figure 5-27). Quartz proportions are not higher within the foliated cataclasite compared to other fault rocks. The cataclasite contains clasts of approximately the same grain size, indicating that all of the fault rock minerals have been broken down. If cataclasite evolves into foliated cataclasite, for the grain size of quartz to increase in the foliated cataclasite requires periodic precipitation of quartz during faulting. Variation in microstructures shows that some quartz is completely recrystallised by BLG while other crystals show minor amounts of deformation, signifying that some quartz is almost unaffected by the faulting process. This suggests that quartz precipitate periodically during faulting and is subsequently deformed during later events.

Quartz is released during sericitization, indicating acidic conditions, however quartz precipitation indicates that the foliated cataclasite is periodically closed with respect to fluids (Janssen et al., 1998). The other fault rocks show no evidence of quartz precipitation and therefore the microveins in the foliated

cataclasite signify that this is the only fault rock within the CCF that is closed to fluids. Within foliated cataclasite the foliation can act as a fluid seal (Jefferies et al., 2006b), thus the foliated zone may have lower permeability and this promotes quartz precipitation (Janssen et al., 1998). Therefore as the fault core evolves it ceases to be an open system with respect to fluids. The main difference between the other core rocks and the foliated cataclasite is the presence of the foliation and this implies that in response to continued fluid-rock alteration and muscovite formation the foliation reduces the permeability of the fault rock.

5.7.5 Summary CCF

The CCF is composed of a damage zone and fault core of which the fault core can be divided into breccia, cataclasite and foliated cataclasite (Figure 5-29). Fractures are well defined within the damage zone and breccia but the cataclasite and foliated cataclasite the rock is granular (Figure 5-29). The amount of sericitization increases from damage zone to fault core, and a foliation and quartz microveins occur in the foliated cataclasite. The boundaries between the different rock types are typically sharp, however the boundary between the cataclasite and foliated cataclasite is transitional (Figure 5-29).

The main reactions occurring within the CCF are the retrogression of garnet and biotite and sericitization of feldspars. These reactions occur in all parts of the fault, but the extent of sericitization increases from the damage zone through to the foliated cataclasite. The reactions and textures indicate that a fluid was present within the fault, that the fluid system was open, except in foliated cataclasite, and that the fluid was acidic. Increased proportions of muscovite within the core enabled an interconnected network of muscovites to form which allowed a foliation to develop within the cataclasite.

Sericitization is considered as low grade hydrothermal alteration and combined with BLG in quartz indicates temperatures $<350^{\circ}\text{C}$. Sericitization and plastic deformation has been overprinted by cataclasis indicating that conditions were subsequently in the brittle regime ($<300^{\circ}\text{C}$) and thus temperatures decreased with time.

In the damage zone the fracturing and reactions have little to no effect on the mineral properties (shape & size), however in the fault core grain size reduction is primarily by reaction in feldspars and by fracturing and cataclasis in quartz. The increase in brittle deformation from the damage zone to fault core may indicate an increase in strain rate across the fault (Patterson, 1978) and the presence of fluidized ultracataclasite shows that some of the slip on the fault may have been seismic.

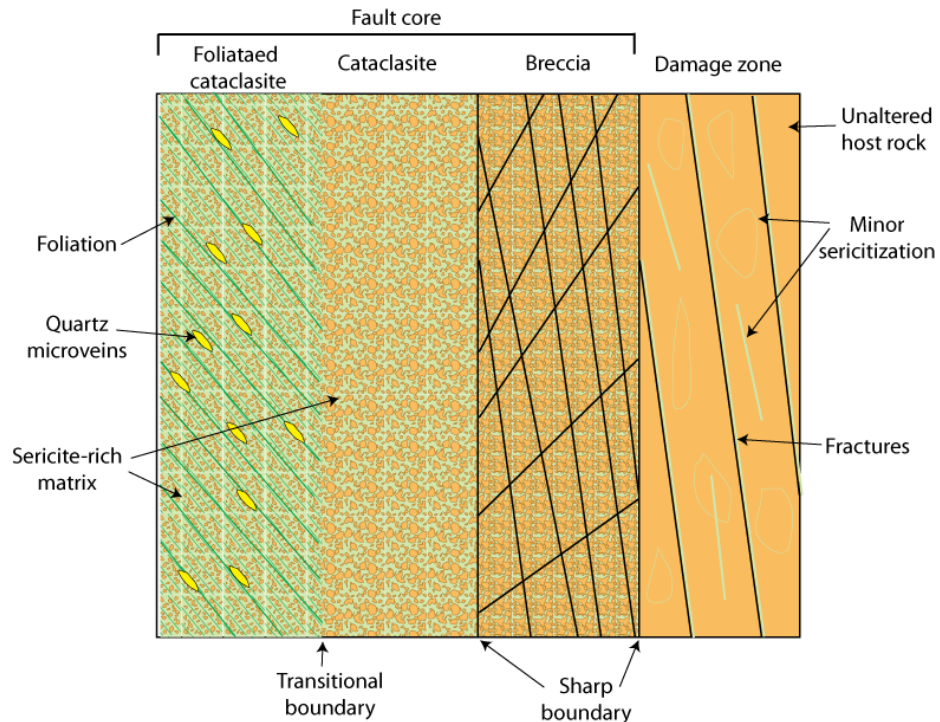


Figure 5-29: Schematic representation of the different components of the Ciao Ciao Fault. CCF is composed of a damage zone and fault core of which the fault core can be divided into breccia, cataclasite and foliated cataclasite.

5.8 Comparing the microstructural evolution of the Virgin and Ciao Ciao Faults

The VF is approximately 70 m long with ~10 cm of offset while the CCF is ~10 km long and has 250 m of displacement. Both fault zones are composed of a damage zone and fault core. The damage zone of the VF is sub-divided into an inner and outer damage zone, with intense and minor bleaching respectively, and the core is composed of breccia and cataclasite. In the CCF, there is no sub-division of the damage zone and the core is composed of breccia, cataclasite and foliated cataclasite. Across strike of both fault zones there are many microstructural similarities. In both fault zones the greatest change in mineralogy compared to

the host rock occurs in the fault core, grain size is reduced from host rock through to fault core, the damage zone and breccia are dominated by fluid-rock reactions and the fault core is dominated by brittle deformation. However, between the faults the main differences are the fluid-rock reactions that occur and the microstructural nature of quartz within the cataclasite.

5.8.1 Grain size reduction

Throughout both fault zones the dominant textural change across is in the average grain size, with grain size decreasing from the host rock through to the cataclasite, and foliated cataclasite in the CCF. The main mechanism for causing grain size reduction in the damage zone and breccia is by fluid-rock interactions. In the VF, albite is replaced by finer grained K-feldspar, whereas in the CCF, albite is replaced by fine grained muscovite. In the fault core, fracturing and cataclasis are the dominant deformation mechanisms and they too result in grain size reduction. Fine grained material is weaker than the coarse grained counterpart (White, 1979; Tullis & Yund, 1985; Fitz Gerald & Stünitz, 1993) and subsequently, it can be deformed more easily by granular flow/cataclasis (Stünitz and Gerald, 1993). If finer grained material is weaker, then this implies that with regards to strength, the fault core is the weakest part of the fault zone.

Throughout both faults the amount of reaction that occurs across strike increases towards the fault core and this is associated with a continual decrease in grain size. Therefore, increased fluid-rock reactions result in a finer grain size within the fault rock and thus a weaker rock. Since a weaker rock is more likely to deform by cataclasis (Stünitz & Fitz Gerald, 1993) this will in turn expose fresh unreacted surfaces and create fluid pathways (Jefferies et al., 2006b). This indicates that there is a feedback mechanism between deformation, fluid flow, fluid-rock reactions, and fault weakening (Figure 5-30). Deformation enables fluids to infiltrate; fluids cause reactions; reactions cause grain size reduction; grain size reduction causes weakening; weakening promotes deformation; deformation enables fluid flow. This means that once deformation has initiated, providing there is ample amounts of fluid to cause reactions to occur, then fault

weakening should result and continue to become weaker as fluid-rock reactions and deformation continues.

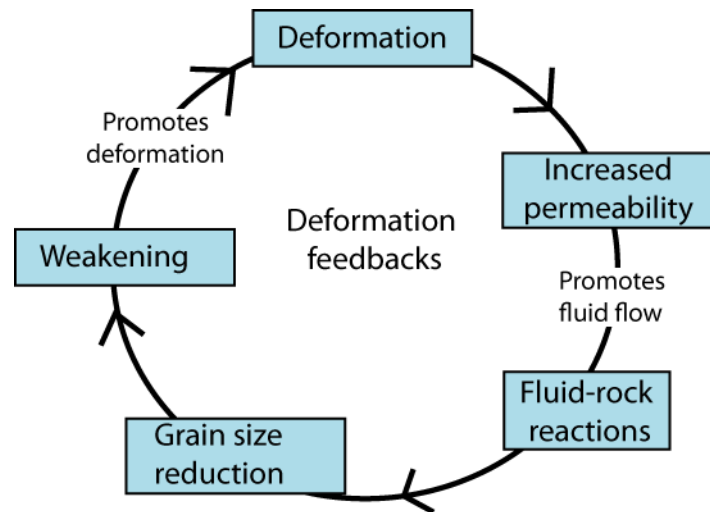


Figure 5-30: Flow chart showing the various feedbacks that occur in response to deformation. The cycle is likely to continue providing there is ample fluid promoting weakening reactions.

5.8.2 Reactions

The main reactions occurring within the VF are the replacement of albite by K-feldspar (Equation 2) and the breakdown of muscovite to K-feldspar (Equation 6). In the CCF, the dominant reaction is the replacement of albite by muscovite (Equation 8). In both fault zones, additional potassium is required. However, the VF also required near neutral conditions for K-feldspar precipitation whereas the CCF required acidic conditions for muscovite precipitation.

The minerals precipitated within a fault will also affect the rheology of the fault rock. K-feldspar is known to cause fault rock hardening whereas muscovite results in fault weakening (Wintsch et al., 1995; Wibberley, 1999; O'Hara, 2007). Grain size reduction will cause weakening of the fault rock, as even a small proportion of fine grains are capable of causing significant weakening (Tullis & Yund, 1985; Fitz Gerald & Stünitz, 1993). However, cementation by K-feldspar can result in the fault rock being stronger than the original (Wintsch, 1998) and thus, there is a delicate balance between weakening and hardening as a result of fluid-rock interactions. The reactions that have occurred within the faults therefore indicate the VF has been weakened by grain size reduction and

hardened by K-feldspar precipitation while the CCF has been weakened by grain size reduction and also precipitation of muscovite.

The fluid-rock reactions and resulting mineralogy of the fault rock therefore has an effect on the strength of the fault and how it will subsequently deform. Reactions can be controlled by various factors such as pressure, temperature, chemical composition, and fluid-rock ratios. Assuming that the VF and CCF are at a similar level in the crust and therefore similar pressure-temperature conditions; then the variation in reactions between the VF and CCF could be caused by:

1. The same fluid but different fluid-rock ratios. Fluid-rock ratio can change by: deformation increasing the surface area available for reactions (Wintsch, 1975), therefore increasing the amount of alkalis relative to the amount of H^+ ; or by increasing the volume of fluid present relative to the surface area of reacting rock (Wintsch et al., 1995) thus increasing the amount of H^+ relative to the amount of alkalis. This mechanism requires neither a change in temperature or pressure (Wintsch, 1975).
2. Introduction of a different fluid. The reactions that occur will be controlled by the composition of the host rock and the composition of the fluid. Different fluids will supply different chemical components and thus promote different reactions.

The most common mechanism that has been suggested within fault zones to explain differences in reactions is option 2, whereby deformation changes the ratio of alkalis to hydrogen ions (e.g. Wintsch et al., 1995; Wibberley, 1999; O'Hara, 2007). Deformation typically raises the K^+/H^+ activity ratio and drives the reaction to precipitate K-feldspar whereas muscovite precipitation is promoted by an abundance of water i.e. reduced K^+/H^+ activity ratio (Hemley & Jones, 1964; Wintsch, 1975; Wintsch et al., 1995). Since deformation is common to both the VF and CCF, the production of muscovite is more likely related to greater volumes of fluid within the CCF. Information on the fluids within the fault zones can be assessed by carrying out fluid inclusion and stable isotope studies, oxygen and hydrogen. Fluid inclusions can be used to gauge the temperature and compositions of the fluids. Stable isotopes can be used to show

what the sources of the fluids (e.g. meteoric or metamorphic) and to model if the fluids evolved in terms of changing fluid-rock ratios.

5.8.3 *Microstructural differences in cataclasite*

The cataclasite within the VF is primarily composed of quartz and K-feldspar whereas in the CCF, the cataclasite is composed of quartz, K-feldspar and muscovite. The addition of muscovite within the CCF can be explained by the different reactions occurring but the microstructural textures of quartz and feldspar also differ and these can be used to infer how conditions changed between the fault zones. In the VF, the cataclasite is dominantly composed of feldspar clasts in a matrix of quartz which has been completely recrystallised by BLG and/or cemented by K-feldspar. However, in the CCF the cataclasite is dominated by angular clasts of quartz in a matrix of feldspar and mica.

Experimental work by Hirth & Tullis (1992) has shown that the rates of the different dislocation creep regimes, such as BLG and sub-grain rotation, are in part dependent upon temperature and strain rate. Similar microstructures can therefore be produced at higher temperatures and lower strain rates or lower temperatures and higher strain rates (Hirth & Tullis, 1992). However, this study did not assess the microstructures that occur at the brittle-ductile transition, and thus comparing brittle microstructures (CCF) to brittle-plastic microstructure (VF) can not be assessed. Hirth & Tullis (1994) investigated the various microstructural regimes that occur across the brittle-ductile transition in quartz. They showed that as temperature and/or pressure increased there was a transition from cataclastic faulting to semi-brittle faulting to semi-brittle flow to dislocation creep. Semi-brittle flow involves cataclasis and crystal plastic behaviour whereas cataclastic faulting has limited to no plastic deformation. Compared with the VF and CCF the microstructures indicate that the VF deformed predominantly by semi-brittle flow while the CCF deformed by cataclastic flow. The differences in the observed microstructures therefore indicate that the CCF deformed under brittle conditions while the VF deformed at slightly higher temperatures which coincided approximately with the brittle-ductile transition. Sibson (1977) states that a quartz-feldspar rock will deform by cataclasis at $\sim 250^{\circ}\text{C}$. Therefore the CCF is likely to have been deforming at

approximately 250°C while the VF deformed at temperatures approaching 300°C (the brittle-ductile transition).

5.9 Summary

The VF and CCF have been exhumed from seismogenic depths (approximately the brittle-ductile transition (250-350°C = ~10-15 km at normal geothermal gradient (Sibson, 1977)). Across strike of both faults the processes occurring are similar. There is grain size reduction by fluid-rock reactions, brittle deformation is concentrated in the fault core, and the largest change in mineralogy proportions and grain size compared with the host rock, is associated with the fault core. Microstructures show that the VF deformed at approximately the brittle-ductile transition while deformation in the CCF occurred within the brittle regime. The main difference between the two fault zones is the mineralogy. In the VF, fluid-rock reactions have resulted in K-feldspar precipitation whereas in the CCF muscovite precipitation occurred. Fault rock composition influences how the fault will deform and therefore is of great importance in understanding fluid-rock interactions and fault evolution. To understand why the different reactions have taken place and therefore why the faults evolved by different fluid-rock reactions fluid inclusion and stable isotope (oxygen and hydrogen) studies have been carried out.

6 Fluid inclusions and isotope studies

6.1 Introduction

Fault zones are renowned for being sites of fluid infiltration. Permeability and thus potential fluid flux, is known to vary substantially across fault zones (Evans et al., 1997; Wibberley and Shimamoto, 2005; Wintsch et al., 1995; Zhang and Tullis, 1998) and the water-rock reactions that occur can result in either fault weakening or hardening (Di Toro and Pennacchioni, 2005; O'Hara, 2007; Park et al., 2006; Wibberley, 1999). Mineral precipitation is believed to effect how slip is accommodated within fault zones (Moore and Rymer, 2007; O'Hara, 2007; Wibberley, 1999; Wibberley et al., 2007) with fault hardening being a possible precursor to seismic slip and pseudotachylyte production (DiToro & Pennacchioni, 2005). Although fluids are almost synonymous with fault zones, the relationship between the evolution of fluid flow and fault zone evolution is still unclear.

Fluids have played a key role in fault zone evolution at Passo Moro. Detailed macro- and micro-structural analyses have unravelled a complex deformation history which was associated with hydrothermal alteration of fault rocks and precipitation of new minerals. The influence of fluid within the faults includes the quartz and chlorite veins, the chloritization of biotite, the crystallization of the two varieties of chlorite, the recrystallization of K-feldspar, and the replacement of albite by K-feldspar.

The main differences between the VF and CCF fault zones are the formation of muscovite and presence of fluidized ultracataclasite in the CCF. This implies more acidic conditions in this fault and that some of the slip may have been accommodated seismically (Lin, 2011; Wibberley and McCaig, 2000; Wintsch et al., 1995). Three possible causes for these differences are the temperatures of deformation, the presence of different fluids, and/or different water-rock ratios in the fault zones.

Information about previous fluid(s) that a rock has interacted with is recorded in the textures, mineralogy and isotopic composition of the minerals. Water-rock

interactions lead to shifts in the original isotopic composition of minerals (Nabelek et al., 1992), which in turn can be used to identify the source of the fluid and if water-rock ratios vary (Criss and Taylor, 1986; Jenkin et al., 1994; Sheppard, 1986). The oxygen and hydrogen isotopic composition of a mineral is controlled by two main factors: the isotopic composition of the fluid and the temperature of interaction (C. W. Field., 1985; Field and Fifiarek, 1985). The latter is determined by fluid inclusion studies and this together with the measured composition of the mineral enables the isotopic composition of the fluid to be calculated using equations such as Equation 9.

$$\text{Quartz } \delta^{18} O_{(\text{mineral-water})} = 3.34 \frac{10^6}{T^2} - 3.31 \quad \text{Equation 9}$$

Fractionation equation for Quartz from Matsuhisa et al.,(1979).

Using the carefully deciphered microstructural evolution of the faults; fluid inclusion and stable isotope studies can be applied to unravel the fluid history and assess the role fluids played during fault zone evolution. In-situ mineral samples were collected via micro-drill for oxygen isotope analysis enabling a unique characterization of fault zone hydrology. The primary focus of this stable isotope (oxygen and hydrogen) and fluid inclusion study to answer the following questions:

1. What was the temperature of the fluids?
2. What was the source of the fluids within the host rock and the Virgin and Ciao Ciao Faults?
3. What was the equilibrium-disequilibrium character was of the mineral assemblages.
4. How do structural variations within and between faults affect the mineral signature recorded and why.
5. Were the fault zones open, closed or limiting open with respect to fluid flow?

6.2 Methods

6.2.1 Sample preparation

Rough crush samples. Approximately 1kg of each rock type was sampled for mineral separation and mineral concentrates were obtained by carrying out the following techniques.

1. All samples were crushed using a Retsch BB2/A crusher and Bico UA35 pulverisor with manganese jaws to produce a rough crushed sample with chips of approximately 0.5-1 mm in diameter.
2. Density separation was carried out on a Gemini table and material separated into heavy, medium, light and extra light portions.
3. Vertical and angled magnetic separation using Frantz L-1 magnetic barrier separators to extract the strongly magnetic portions.
4. Heavy liquids (LST Fastfloat - variable densities up to 2.82 ± 0.2 g/ml) and froth flotation were utilised to separate out quartz from K-feldspar.
5. Mineral picking was carried out when necessary to extract any rock fragments from the mineral split to ensure sample purity.

Mineral powders. In situ micro-sampling was carried out to produce powdered samples of approximately 1mg in size. Polished blocks were created from thin section off-cuts and imaged by incident light microscope, SEM-SE, BSE, CL and X-Ray analysis to confirm the mineral composition and distribution. All information was recorded on a map of the polished block and used to guide micro-sampling (Figure 6-1). Micro-sampling was carried out at the NERC Isotope Community Support Facility at the Scottish Universities Environmental Research Centre (SUERC) at East Kilbride. Polished blocks were fixed to the microscope base plate using Crystal Bond wax and samples obtained using the New Wave Micromilling system version 1.4.0 (Figure 6-2).

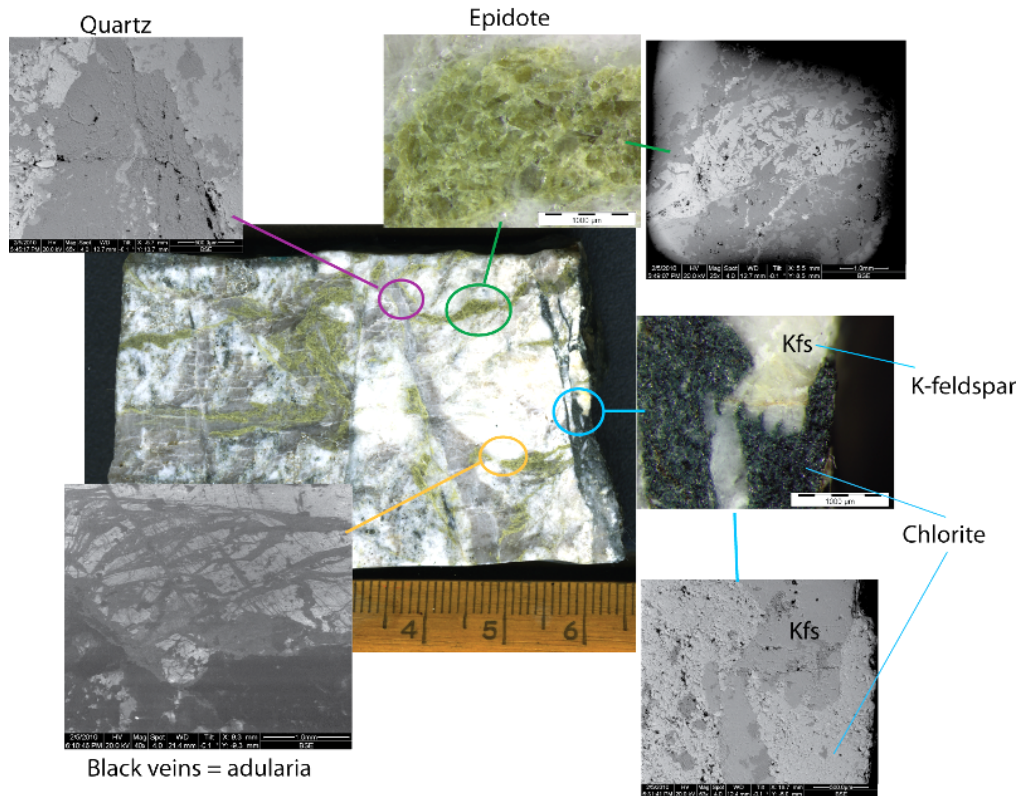


Figure 6-1: Polished block prepared for micro-drilling with associated images of drill sites.

Colour images are from an incident light microscope and grey scale images are SEM-BSE images.

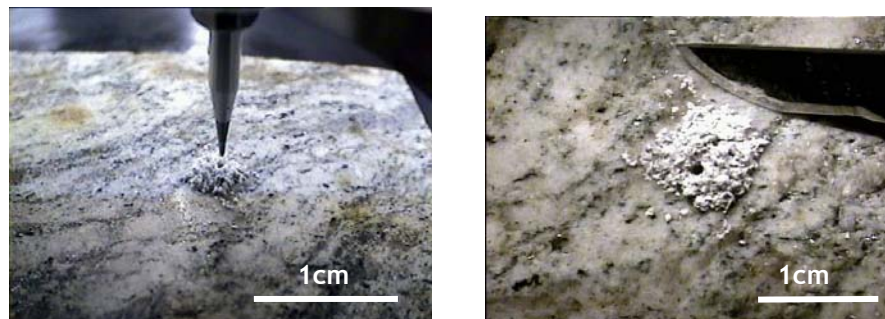


Figure 6-2: Drilling of polished blocks. Left = Drill bit used for micro-drilling. Right = birds eye view of powder produced. Scalpel for scale.

Fluid inclusion wafers. After micro-sampling the polished blocks were used to make the double polished wafers. Each fluid inclusion wafer was analysed at room temperature by light microscope to characterise the fluid inclusions in terms of size, shape, number of phases present, abundance and whether the inclusions are primary, secondary etc. The sample was then broken into small chips (~2 mm in diameter) and analysed on a Linkham THMSG600 heating-freezing stage mounted on a Zeiss Axioplan microscope. Calibration of the fluid inclusion stage was carried out using a calcite chip and analyses of inclusions of

CO₂ (freeze at -56.6 °C) and a precision of ±0.5 °C was calculated by repeat analyses of the calcite chip.

6.2.2 Analytical techniques

Fluid Inclusion Studies: Samples were cooled to -110 °C to ensure all phases present were frozen and then heated up until the homogenization temperatures were reached. On heating of the samples very few phase changes were observed e.g. CO₂ melting and first melting of the aqueous phase (T_{fm}). The majority of data collected was related to the temperature when the aqueous fluid became ice free (T_{mlce}) and the homogenization temperature (T_H). The T_{mlce} is the depression of freezing point (pure water freezes at 0 °C) and is used to estimate the weight percentage of salt within the solution, whereas the T_H is the temperature when the vapour bubble homogenises with the liquid and represents the minimum trapping temperature of the fluid (Shepherd et al., 1985).

Stable Isotope Data. Oxygen and hydrogen analyses were carried out at the NERC Isotope Community Support Facility at SUERC, East Kilbride. Oxygen isotopic compositions were analysed by laser fluorination using a technique modified after that of Sharp (1990). Samples of ~1 mg were decomposed by laser ablation in an atmosphere of chlorine trifluoride; the resultant oxygen gas was reacted with graphite rods to produce carbon dioxide, the isotopic composition of which was determined using a VG SIRA 10 mass spectrometer.

Hydrogen analysis was done by *in vacuo* bulk heating. Approximately 1g of silicate minerals were analysed whereas for the phyllosilicates only 0.5g was required due to the higher proportion of hydrogen present within the minerals. The prepared samples were dried overnight in a vacuum at 200 °C to remove any adsorbed water on grain surfaces before being analysed for δD. The hydrogen vacuum line was calibrated using glass capillaries containing international (v-SMOW and GISP) and internal lab water standards (Lt Std). Decrepitation of the minerals was done in a degassed platinum crucible by induction heating up to 1500 °C for 45 minutes. The released water was then reduced to H₂ in a chromium furnace at 800 °C using the method of Donnelly et al. (2001). The amount of H₂ produced was quantitatively measured in an Hg-manometer before

being collected. The H₂ gas was analysed using a VG-Micromass 602D Mass spectrometer.

To assess the uncertainty associated with oxygen and hydrogen analyses, several standards were repeatedly analysed in between fault rock mineral analysis. For oxygen analyses the standards used were NBS-28 (quartz sand), SES (quartz), UWG-2 (garnet) with results having an average uncertainty of $\pm 0.1\%$ and standard deviation of 0.3⁶. The standards used during hydrogen analyses were V-SMOW, GISP and Lt Std with results having an average uncertainty of $\pm 3\%$ and standard deviation of 1.1. It is assumed that the uncertainty associated with the standards is the same as for the mineral samples. Therefore, all oxygen and hydrogen results will have an associated uncertainty of $\pm 0.3\%$ and $\pm 3\%$ respectively. All stable isotope data will be presented in the delta per mil format ($\delta\%$) relative to Vienna-Standard Mean Ocean Water (V-SMOW).

6.2.2.1 Stable isotope quality control

Fifty four samples were analysed from Passo Moro which included host rock, Virgin & Ciao Ciao Fault, local vein material and repeats. From each rock (if present) quartz, K-feldspar, chlorite and epidote were analysed for their oxygen isotopic composition. During laser fluorination the volume of gas (or yield) released by reaction is measured and calculated into yield percentage. Mineral formulas were used to calculate the amount of oxygen that would be released for a given mass (1 μ g) of a particular mineral and subsequently used to work out yield percentages. Before detailed analyses could be carried out the data was filtered by yield (Figure 6-3). A yield of less than 60% is considered unsatisfactory (A. Boyce, pers com) and may indicate that a sample had reacted in the chamber prior to fluorination or because all of the sample may not have reacted during fluorination. Therefore samples with yields less than 60% will not be included in the data interpretation⁷. Over-yields are typically due to more than 1 μ g being analysed (weight of sample known prior to analysis) or as a result of re-opening the chamber in between each analysis combined with no pre-fluorination. If the yields are high and the reason why is unknown, then the data will also be discarded.

⁶ All standard results are shown in Appendix 3.

⁷ List of all samples analysed and results can be found in Appendix 3

A total of thirty nine samples of quartz, K-feldspar, chlorite, epidote and muscovite were analysed for hydrogen by *in-vacuo* bulk heating. The amount of hydrogen released was measured and converted into a yield which was measured in micromoles per mg ($\mu\text{mol}/\text{mg}$). Studies of quartz have revealed that the δD value may be affected by release of water from various reservoirs which were previously unexplained (Baatartsogt et al., 2007; Gleason et al., 1999; Gleason et al., 2008; Polyá et al., 2000). Gleason et al., (2008) found that quartz results with yields of $<0.025\mu\text{mol}/\text{mg}$ tends to represent those samples that were most affected by fluid reservoirs of an unknown source. Therefore, within in this study a yield of $0.025\mu\text{mol}/\text{mg}$ will be used as the cut off limit for analysed results in this study (Figure 6-4). δD results for quartz and K-feldspar are from fluid inclusions and so directly represent the circulating fluid, while the water released from chlorite, epidote and muscovite is structural and so requires a fractionation equation to be used to calculate the δD value of the fluid⁸.

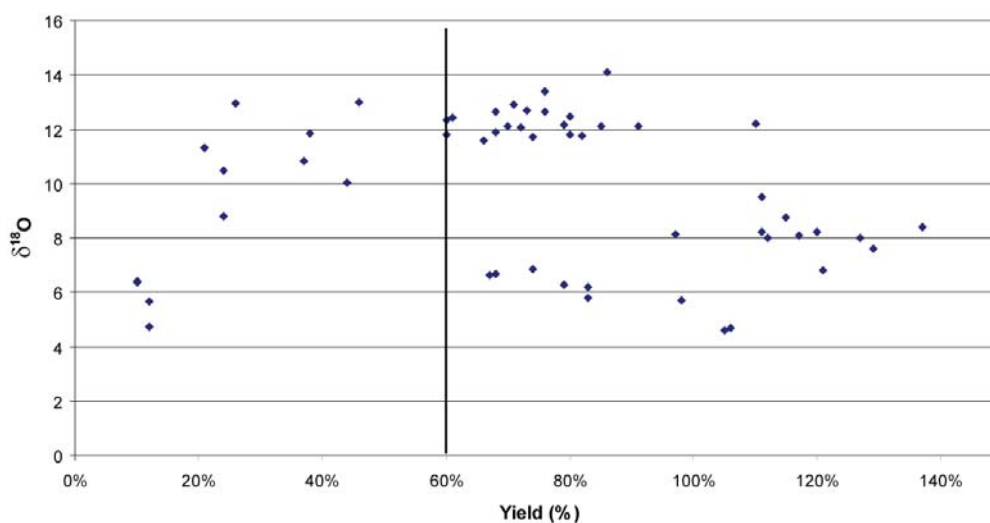


Figure 6-3: $\delta^{18}\text{O}$ Vs Yield percentage for all samples. Samples with a yield less than 60% are considered unreliable. Line shows cut-off point and all samples to the left will be disregarded in subsequent analyses and interpretations.

δD measurements of fluid inclusions has primarily been carried out on quartz samples and thus the validity of measuring δD in K-feldspar is untested (G.Jenkins, pers comm.). The method of trapping fluid inclusions in K-feldspar is the same as for quartz, however alteration of feldspars to phyllosilicates could affect the results. Due to the uncertainties with analyses of δD fluid inclusions in K-feldspar, the results should be viewed with caution.

⁸ All hydrogen fractionation equations used can be found in Appendix 4.

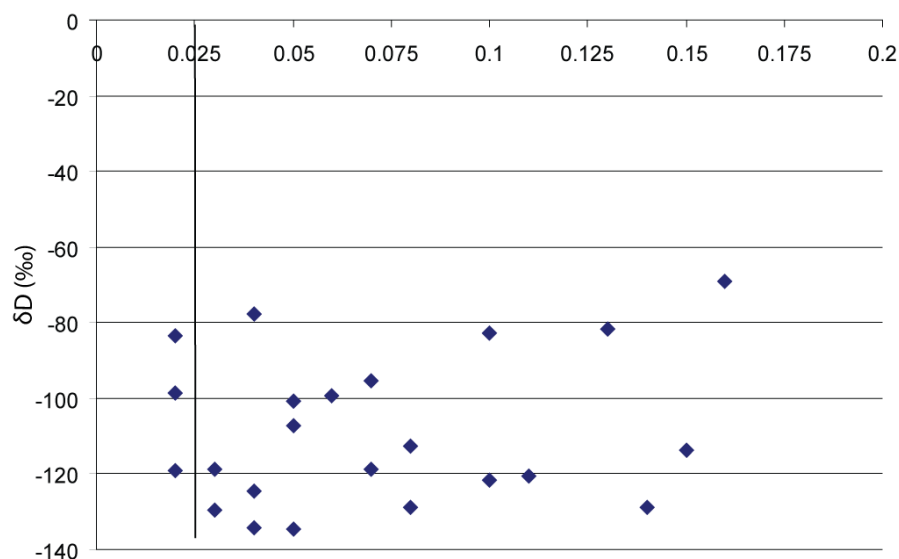


Figure 6-4: Yield v δD for samples from both fault zones. Line at $0.025\mu\text{mol/mg}$ indicates cut off point for sample analyses. Anything less than $0.025\mu\text{mol/mg}$ may give results not entirely related to the circulating fluid.

6.2.2.2 Chips or powders

The possibility that incomplete fluorination, and thus experimentally induced isotopic fractionation, might result from the preparation of powdered samples (A. Boyce, pers comm) was tested. Oxygen isotopic analysis was carried out on both rough crushed (chips) and powdered samples to compare results but no significant differences were recorded (Table 6-1). Mineral powders are from precise locations within the sample while mineral chips are representative of the entire sample. These results show that the $\delta^{18}\text{O}$ values were not affected by the various sample preparation techniques. Furthermore they imply that for a specific mineral, the isotopic values are consistent throughout the sample i.e. isotopic communication was pervasive for the mineral system.

Sample	Mineral	Yield (%)	Measured $\delta^{18}\text{O}$ (‰)
Host 1 – powder	Quartz	73	12.6
Host 1 – chips	Quartz	76	12.7
VF2 – powder	Quartz	110	12.2
VF2 – chips	Quartz	91	12.1

Table 6-1: Comparison of results between powdered and chipped samples.

6.3 Fluid inclusion study

6.3.1 Introduction

Many minerals grow in the presence of a fluid or melt and subsequently may be fractured one or more times. Such fractures may then heal in the presence of a fluid (Roedder, 1984). During these processes small quantities of the surrounding fluid are commonly trapped as fluid inclusions and consequently represent a fluid that existed at some time in the rocks geological history (Roedder, 1984). Fluid inclusions can be classified as primary, pseudosecondary or secondary inclusions; a classification that relates to how the inclusion was trapped (Roedder, 1984; Shepherd et al., 1985). Trapping during crystallization/recrystallization of minerals yields primary inclusions; healing of fractures during crystal growth produces pseudosecondary inclusions; and healing of fractures at a later time yields secondary inclusions (Shepherd et al., 1985). Inclusions in any sample are rarely from a single generation. In hydrothermal deposits, primary inclusions are often randomly distributed and relatively large, but secondary inclusions are often small, numerous and form in planar arrays (Roedder, 1984; Shepherd et al., 1985). The distinction in size does not always hold true however, separation of primary and secondary is critical as fluids may be of very different compositions and be trapped at different temperatures.

Fluid inclusions preserve information about the composition of the fluid and the homogenization temperature (minimum trapping temperature of fluid). By carrying out petrographic analysis and heating and cooling the sample much of the 'trapped' information can be extracted and integrated with fault and fluid evolution.

6.3.2 Previous work

Curti (1987) and Lattanzi et al (1989) studied the gold deposits at Pestarena in the Upper Anzasca Valley (5 Km southeast of Passo Moro). The ore bodies in the meta-granites occupy fractures and shear zones that are discordant with foliation. $\delta^{18}\text{O}$ results suggest gold bearing fluids were dominantly of metamorphic origin, or at least isotopically equilibrated with the surrounding

metamorphic rocks at temperatures greater than 400°C. Fluid inclusions indicate the gold precipitated from a CO₂-bearing moderately saline brine. Total homogenization temperatures were dominantly between 300-330°C, however there was also a less common presumably later, suite of CO₂ poor inclusions. These homogenised at 170-250°C and were interpreted as a late influx of cooler less saline fluids. Samples from Passo Moro can be compared to those from Pestarena to assess whether the fluids had similar composition and homogenization temperatures.

6.3.3 Samples

Nine samples were prepared from the VF and CCF for thermometric fluid inclusion analysis. Three samples were chosen from the host rock, one from each section of the VF and two samples from the CCF (Table 6-2). Samples have been taken from different parts of the faults such as the damage zone and fault core to enable characterization of different fault rock types.

6.3.4 Petrography

The studied fluid inclusions occur in quartz crystals. Primary and secondary fluid inclusions are observed in most samples and range in size from 5-40 µm and 5-30 µm respectively (Figure 6-5 & Table 6-2). In general primary inclusions are larger but there is an overlap in sizes (Table 6-2) and thus size can not be used to distinguish between them. Secondary inclusions are found in trails and, based on descriptions from Schmatz & Urai (2010), the observed trails represent healed microcracks and ghost grain boundaries (Figure 6-5a). The majority of fluid inclusions are two phase, liquid-vapour with degree of liquid fill being 90-95%. The remainder of the inclusions are purely liquid (no vapour bubble), purely vapour, or liquid-vapour + CO₂ (dark rim observed around vapour bubble) (Figure 6-5b) but these two types only make up a small proportion (<5%) of the inclusions observed.

The host rock sample has fewest fluid inclusions relative to the other samples. Host rock fluid inclusions are generally primary and associated with grain boundaries but a few secondary trails are observed throughout the sample. Within the faults, the quartz microveins have a greater amount of large (>25 µm)

primary inclusions, while dynamically recrystallised quartz has very small, barely visible inclusions. The CCF has higher proportions of fluid inclusions than the VF. However, inclusions tend to smaller in the CCF and are so small that it is difficult to collect any data from them other than their size (Figure 6-6).

Location*	Sample	Rock type	Feature / texture	Inc type	Size (µm)	Phases present
3	Host-3	host	clean crystal	P	~10	L+V
				S	~10	L+V
15	Qz-Epi	vein	vein	P	~10	L+V
				S	~10	L+V
16	Qz1	Qz Vein	vein	P	5-40	L+V
				S	5-30	L+V
Virgin Fault	VF1	ODZ	clean crystal	P	~10	L+V
				S	~10	?
Virgin Fault	VF2	IDZ/Core	microvein	P	5-20	L+V
				S	<10	?
Virgin Fault	VF3	Core	microvein			
				S	~10	?
Virgin Fault	VF7	Core	microvein	?	<10	?
				?	<10	?
Virgin Fault	VF12	IDZ	vein	P	10-35	L+V
				S	10-30	L+V
Virgin Fault	VF14	Cataclasite	microvein	P	10-40	L+V
				S	10-30	L+V
5	CC2	Cataclasite	fragments	?	<10	?
				S	<10	?
5	CC1	DZ	microvein	P?		?
				S	<20	?

Table 6-2: Samples and fluid inclusion description.

* Numbers indicate the locality number for where the sample was collected – for location see Appendix 1; For the Virgin Fault the locality of the sample within the fault is shown on Figure 4-4. ODZ = Outer damage zone, IDZ = Inner damage zone, DZ = Damage zone, Qz = quartz, P = primary inclusions, S = secondary inclusions, L+V = Liquid + Vapour, ? = inclusions which were too small to collect data from.

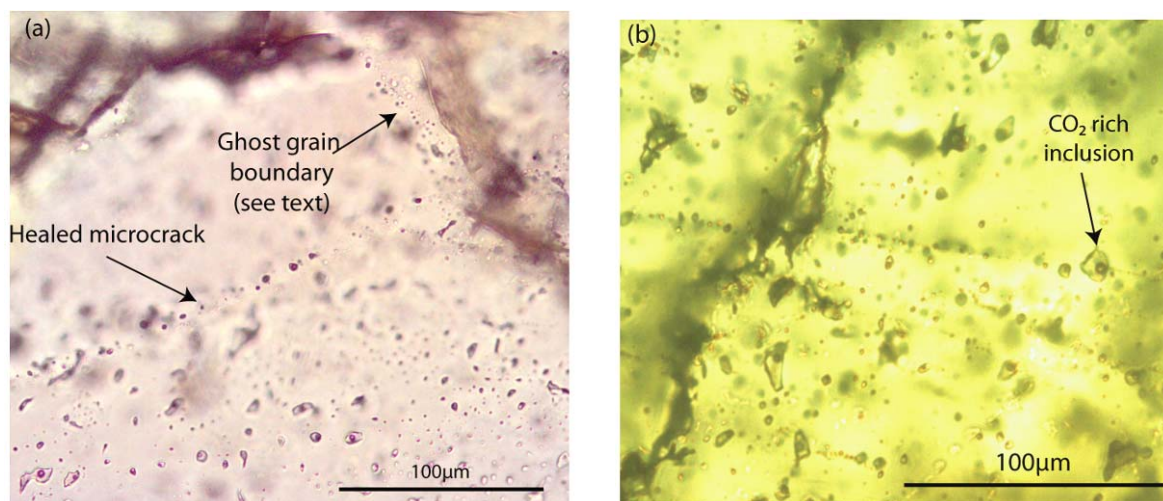


Figure 6-5: Typical size of fluid inclusions within the VF
(a) Fluid inclusions formed from a healed microcrack and ghost grain boundary (b) Example of a CO₂ rich inclusion.

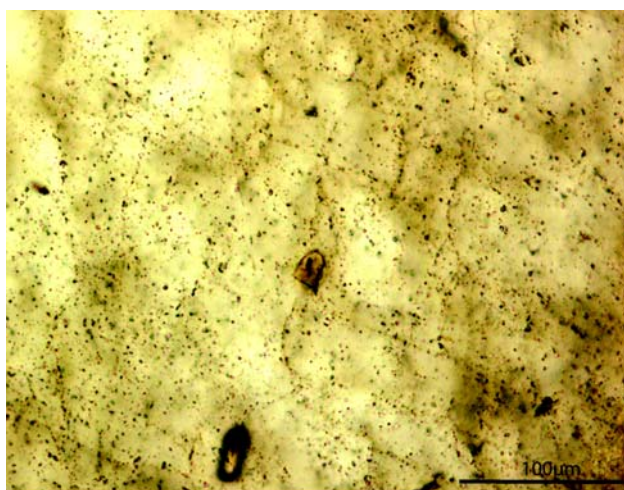


Figure 6-6: Fluid inclusions within the CCF fault rock.
Inclusions are so small that the internal composition of the inclusion can not be differentiated i.e. liquid-vapour proportions.

6.3.5 Heating and cooling results

Due to the small size of many of the fluid inclusions only three of the samples had inclusions which were large enough to carry out heating and cooling analysis on. All data collected is shown in Table 6-3.

Homogenization temperatures range from 180 °C to 296 °C at Passo Moro (Figure 6-7). In the VF only primary inclusions could be analysed as secondary inclusions were too small to see, whereas in the quartz vein both primary and secondary inclusions were analysed (Table 6-3).

The homogenization temperatures for primary and secondary inclusions in the quartz vein are 296 °C and ~187 °C respectively. Microscopic observations of the quartz vein showed that some primary fluid inclusions had dark boundaries, indicating that CO₂ may be present within the fluids. However, on heating the wafer, no phase transitions were observed in the primary inclusions (Table 6-3) and hence, there is no detectable evidence for CO₂ in the fluids.

Homogenization temperatures for primary inclusions in the VF range from 180 to 230 °C (Figure 6-7 and Table 6-3). Within the fault the T_{fm} varies from -28 to -10 °C and the T_{mlce} from -4 to 0 °C. -4 °C is a small depression in freezing point and implies that the fluid was of low salinity (Shepherd et al., 1985) i.e. it was essentially aqueous. The T_{fm} combined with the T_{mlce} can be used to estimate what the composition/salt system was of the fluid, and results point towards a NaCl-H₂O fluid system with 0-6 Wt % equivalent NaCl (Shepherd et al., 1985).

Sample*	Inc. No	Liquid fill (%)	P or S	T _{fm} (°C)	T _{mlce} (°C)	T _H (°C)	Trapping temp 2 (°C) ⁺	Trapping temp 3 (°C) ⁺⁺	Size (µm)
VF14	1	90	P	-28	-4	230	270	380	45
	2	95	P						25
	3	95	P						35
	4	95	P		0				40
	5	95	P		-0.1	180	210	310	25
	6	90	P	-10	-1.8	180	210	310	40
VF12	1	90	P	-27.9	-3.6	200	230	320	25
	2	95	P			210			20
Qz1	1	95	P		-5.3	296	370	470	25
	2	95	S			185			20
	3	95	S			188			25
Average**						196°C			

Table 6-3: Heating/freezing data from fluid inclusions which were large enough to collect data from.

P = primary inclusion; S = secondary inclusion. ** excluding the primary fluid inclusion temperature from the 090° quartz vein as it is likely to be from a different fluid inclusion population (see text). * locality of samples as indicated in Table 6-2. ⁺ Trapping temperature calculated using the homogenization temperature (this study), estimated minimum hydrostatic pressure for gold vein emplacement in the Anzasca valley (Curti, 1987), and isochores constructed by Bodnar & Vityk (1994). ⁺⁺ Trapping temperature calculated using the homogenization temperature (this study), estimated maximum lithostatic pressure for gold vein emplacement in the Anzasca valley (Curti, 1987), and isochores constructed by Bodnar & Vityk (1994). For discussion on the different trapping temperatures calculated see text.

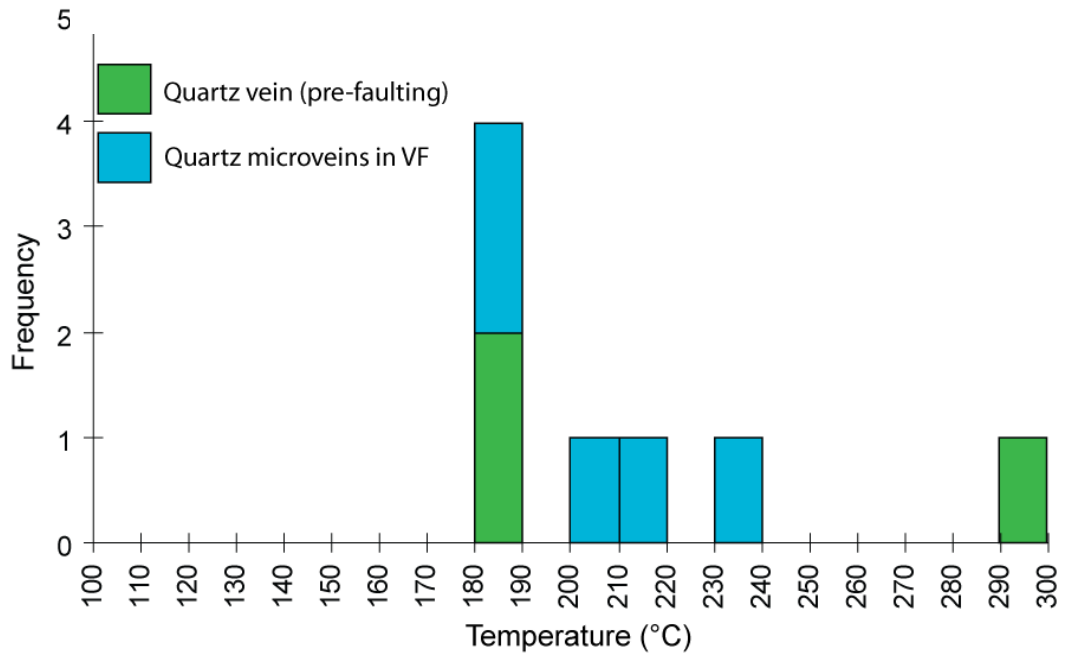


Figure 6-7: Frequency plot of homogenization temperatures at Passo Moro

6.3.6 Interpretation

6.3.6.1 Trapping temperatures

The homogenization temperatures recorded (Table 6-3) are based on lab analyses i.e. they were measured under no confining pressure. Mineral precipitation is assumed to have occurred at depth and therefore the load pressure at the depth of mineralization is likely to have been made up of a component of lithostatic and/or hydrostatic pressure. The homogenization temperature recorded is therefore the *absolute* minimum trapping temperature of the fluid within the fault zone and assumes no applied load pressure. It is therefore critical to correct the homogenization temperature for trapping of the fluid at depth.

The precise depth of fault activity has not been tightly constrained for the faults at Passo Moro. However, information is available on the conditions that prevailed during formation of the gold veins in the Anzasca Valley, which coincides with the maximum age of faulting at Passo Moro (Section 2.3.1). Within the Anzasca Valley a study by Curti (1987) estimated that the lithostatic pressure during gold precipitation was 1.7-2.2 kb and fluid pressure was 0.8-1.4 kb indicating that a component of the pressure acting on the fluid was of hydrostatic nature (see Curti (1987) for discussion of pressure estimates).

Depending on whether the faults were affected by hydrostatic pressure and/or lithostatic pressure the pressure correction required will vary. In Table 6-3 the trapping temperature was calculated for the minimum fluid pressure and maximum lithostatic pressure estimate provided by Curti (1987) (trapping temp 2 & 3 respectively). This provides the minimum and maximum trapping temperature of fault zone fluids *if* the faults were active at the same time as gold mineralization. If the faults formed after gold mineralization then trapping temperature 2 (Table 6-3) would be the maximum trapping temperature for the fault zone fluids.

6.3.6.2 Interpretation of results

The majority of inclusions from Passo Moro homogenise between 180-230°C with only one primary inclusion from the quartz vein that formed pre-faulting, homogenising at 296°C (Table 6-3 and Figure 6-7). Since the quartz vein formed prior to faulting it is likely that the precipitating fluids were hotter, and thus this trapping temperature probably indicates a different fluid event than that associated with the quartz microveins in the VF.

The microveins in the Virgin Fault formed in response to fault related activity and were one of the earliest formed structures (Ch 5). The primary inclusions are therefore representative of a fault zone fluid, and this fluid could be the first fluid that intruded the VF. Results from the primary fluid inclusions indicate that the fluid which precipitated the quartz microveins was of low salinity and the minimum trapping temperature was between 180-230°C (Figure 6-7). Secondary fluid inclusion trails in the microveins in the VF point towards multiple deformation and fluid flow events. However, all inclusions studied from the VF were primary and thus no information is known about the later fluids.

Studies of fluid inclusions from gold bearing veins in the Anasca Valley found two dominant types of fluid inclusions; a CO₂ rich fluid and a later aqueous fluid (Curti, 1987; Lattanzi et al., 1989). The homogenization temperatures for the CO₂ rich inclusions were between 300-340°C while the aqueous inclusions homogenise between 170-260°C (Curti, 1987; Lattanzi et al., 1989). This means that the two types of fluid inclusions (CO₂ rich and aqueous) represent two fluid populations, and thus, two different fluids.

Comparison of the fluid inclusion data from Passo Moro, to those from the gold veins shows several similarities. Within both data sets there are two populations of fluid inclusions; a high temperature (possibly) CO₂-rich fluid (~300-340°C), and a low temperature aqueous fluid (180-230°C). At both localities, the high temperature fluid is early with respect to the low temperature fluid. These similarities suggest that the two populations at Passo Moro correlate with the two populations at Pestarena. Therefore, the pre-faulting quartz veins are likely to have formed at a similar time to the gold veins and hence, suggests they formed at ~29-20 Ma (Pettke et al., 2000; Pettke et al., 1999). Based on the precipitation of gold veins, apatite fission track data, and fluid inclusion results, faulting at Passo Moro likely occurred between 29 Ma and 10 Ma (Hurford et al., 1991; Lattanzi et al., 1989; Pettke et al., 2000), and was associated with an essentially aqueous fluid.

6.3.7 Summary

At Passo Moro both primary and secondary fluid inclusions are found within the fault zones. Heating and cooling analysis shows that all fault related inclusions are aqueous and homogenise between 160-230°C. Therefore during deformation of the VF the infiltrating fluids were of similar composition and temperature.

6.4 Stable Isotope Data

Stable isotope analyses of co-existing minerals can be used in determining 1) the equilibrium-disequilibrium character of the mineral assemblages, 2) temperatures of formation, and 3) the source of fluids. If water-rock interactions have caused shifts in the original isotopic composition of the fault rock then by comparing host and fault rock results the fluids that interacted with the host and fault rocks can be characterised.

6.4.1 Host Rock Results

6.4.1.1 Frey's results

The main host rock at Passo Moro is granite gneiss and is composed of quartz, albite, K-feldspar, biotite, muscovite, garnet, chlorite and accessory minerals

(Ch 4). Frey et al (1976) carried out several types of analyses on the host rock and recorded evidence for Alpine resetting of the minerals. $\delta^{18}\text{O}$ results from Frey et al (1976) show a high degree of uniformity and the majority of δD values fall into the approximate range of -40 to -80‰ which is considered as ‘normal’ for igneous rocks (Frey et al., 1976) (Table 6-4). With regards to the metamorphic fluids there was no evidence for any significant input of oxygen from external sources and thus Monte Rosa effectively ‘stewed in its own juices’ (Frey et al., 1976). However, two δD values are outside the ‘normal’ range for igneous rocks (-134 and -157‰; Table 6-4). To attain such light values implies interaction with a meteoric fluid despite a lack of field or micro-scale evidence, thus some later water-rock interactions took place (Frey et al., 1976).

Sample	$\delta^{18}\text{O}$ values of mineral separates and water (‰)				δD values of hydrous minerals (‰)	
	Quartz	K-feldspar	Muscovite	Water	Muscovite	Biotite
86	12.6	10.8	9.8	9.8	-39	-70
92	14		11.1	11.3	-38	-70
366	12.8	10	10.2	8.4	-56	-134
369	11.6	10		8.6		-67
376	10.3			5.5		-157
377	12.5	10.2		8.4		-68
405	12.4			8.9		-77
411	12.9		10	9.6	-39	-69
416	12.9	11.3	10	9.7	-47	-72
Av. $\delta^{18}\text{O}^a$	12.5	10.4	10			
Av. Error (\pm)	0.3	0.4	0.1			

Table 6-4: Stable isotope results from Frey et al (1976).

^a Excluding samples 92 and 376 (for explanation of why these samples were excluded see Frey et al., 1976).

6.4.1.2 Host rock – this study

Host rock from Passo Moro was collected for analysis of $\delta^{18}\text{O}$ and δD (Table 6-5). Quartz, K-feldspar and muscovite (muscovite only analysed for δD) were separated, analysed and compared to that of Frey (1976).

Oxygen signature. Host rock quartz has an average $\delta^{18}\text{O}$ value of $12.3 \pm 0.3\text{‰}$ and 9.5‰ for K-feldspar (Table 6-5). $\delta^{18}\text{O}_{\text{Fluid}}$ values in equilibrium with the minerals

were calculated using the appropriate fractionation equations⁹, and the $\delta^{18}\text{O}_{\text{Fluid}}$ range from $\delta^{18}\text{O} +8.4$ to $+9.8\%$ for quartz and is 7.3% for K-feldspar.

Quartz $\delta^{18}\text{O}$ and fluid values are almost identical to those of Frey et al (1976) (Table 6-4). The K-feldspar has a lower $\delta^{18}\text{O}$ value than that recorded by Frey et al (1976) which in turn implies a lighter fluid interacting with the host rock. K-feldspar is known to re-equilibrate with later fluids down to temperatures as low as 50°C (Wenner and Taylor, 1971). Frey et al., (1976) also found evidence of a lighter, meteoric fluid interacting with the host rocks ($\delta\text{D} -134$ to -157% ; Table 6-4) and so it is possible that the K-feldspar partially re-equilibrated and so no longer retains information on Alpine fluids.

Hydrogen signature. The $\delta\text{D}_{\text{Fluid}}$ value of muscovite is -46% and a range of -99 to -129% was measured for quartz and K-feldspar (Table 6-5). Utilising the fractionation equation of Suzuoki & Epstein (1976) Frey's host rock data converts to a $\delta\text{D}_{\text{Fluid}}$ range of -15 to -35% . Muscovite from this study falls just outside Frey's range while quartz and K-feldspar are completely different and indicate interaction with more meteoric-like fluids. Frey did find evidence of such fluids interacting with the host in two samples which when converted have $\delta\text{D}_{\text{Fluid}}$ values of -90 and -113% . Results from quartz and K-feldspar in this study therefore agree with Frey's findings of a meteoric fluid interacting with the host rock.

δD values in quartz and K-feldspar reflect the composition of fluid inclusions in these minerals. The fluid inclusion study did reveal the presence of secondary trails within quartz (Table 6-2) confirming the infiltration of a later fluid in the host rock. This later fluid must dominate the fluid inclusion populations in the host rock and can explain the light δD values recorded. Results from Frey et al (1976) were from muscovite and biotite and so show that in some samples hydrogen exchange took place with hydrous minerals.

⁹ See Appendix 4 for all the fractionation equations used during oxygen and hydrogen stable isotope analyses.

Sample ¹	Rock type	Mineral	$\delta^{18}\text{O}$ (‰)	T_{H} (°C)	Estimated Temp (°C)*	$\delta^{18}\text{O}_{\text{Fluid}}$ (‰)**	δD_{Fluid} (‰)***
Host 1 (8)	UG	Qz	12.7		450	9.6	-99
Host 1 (8)	UG	Kfs	9.5		450	7.3	-101
Host 3 (10)	LG	Qz	11.7		450	8.7	-125
Host 3 (10)	LG	Kfs			450		-129
Host 3 (10)	LG	Musc			450		-46
Host 4 (11)	VUG	Qz	12.7		450	9.6	
Average Quartz value			12.3			9.3	
Standard Deviation			0.6			0.5	
VF1	ODZ	Qz			196		-119
VF2	FC	Qz	12.1		196	0.5	-83
VF2	FC	Qz	12.2		196	0.6	-83
VF3	FC	Qz	12.5		196	0.8	-119
VF4	FC	Qz	11.8		196	0.2	
VF5	OCZ	Qz	12.1		196	0.5	
VF6	IDZ	Qz	11.6		196	0.0	
VF7	FC	Qz	12.4		196	0.7	-107
VF8	ODZ	Qz	11.7		196	0.1	-119
VF12	IDZ	Qz	12.4	200		0.7	-78
VF14	FC	Qz	12.2	230		2.3	-82
Average value			12.1			0.7	-99
Standard Deviation			0.3			0.7	18.9
CC1 (5)	DZ	Qz	11.9		196	0.3	
CC2 (5)	FC	Qz	12.1		196	0.5	
CC3 (5)	FC	Qz	14.1		196	2.5	-120
CC3 (5)(repeat)	FC	Qz	13.4		196	1.8	-120
CC4 (24)	DZ	Qz	12.9		196	1.3	-122
Average value			12.9			1.3	-121
Standard Deviation			0.9			0.9	1.4
VF1	ODZ	Kfs			196		-135
VF2	FC	kfs	8.0		196	-1.6	-99
VF3	FC	Kfs	8.4		196	-1.2	-95
VF5	ODZ	kfs	8.0		196	-1.6	
VF7	FC	Kfs	7.6		196	-2.0	-113
VF8	ODZ	Kfs	8.8		196	-0.8	-134
VF14	FC	Kfs	8.1	230		-0.1	-69
Average value			8.1			-1.2	108
Standard Deviation			0.4			0.7	25.3
CC3 (5)	FC	Kfs	6.8		196	-2.8	-129
CC4 (24)	DZ	Kfs	8.2		196	-1.4	-114
Average value			7.5			-2.1	-122
Standard Deviation			1.0			1.0	10.6

Table 6-5 - continued on next page.

Sample ¹	Rock type	Mineral	$\delta^{18}\text{O}$ (‰)	T_{H} (°C)	Estimated Temp (°C)*	$\delta^{18}\text{O}_{\text{Fluid}}$ (‰)**	$\delta\text{D}_{\text{Fluid}}$ (‰)***
VF2	FC	Chl	6.9		196	3.5	-32
VF3	FC	Chl	6.7		196	3.3	-18
VF5	ODZ	Chl	5.8		196	2.5	
VF7	FC	Chl	5.7		196	2.3	-19
VF8	ODZ	Chl	6.6		196	3.3	-29
VF12	IDZ	Chl	4.6	200		1.2	-17
VF14	FC	Chl	6.2	180		0.1	-30
Average value			6.1			2.3	-24
Standard Deviation			0.8			1.3	6.9
CC3 (5)	FC	Chl			196		-79
CC4 (24)	DZ	Chl	4.7		196	1.3	-65
Average value							-72
Standard Deviation							9.9
VF1	ODZ	Musc			196		-86
VF3	FC	Musc			196		-72
VF14	FC	Musc		180			-109
CC (18)	Amp	Musc			196		-46
Modern day water							-152

Table 6-5: Oxygen and hydrogen stable isotope data for all samples at Passo Moro. ¹= number in brackets indicates the locality number for the sample, location map in Appendix 1; for the VF the sample location can be found in Figure 4-4. * = fluid temperature estimated from the average fluid inclusion value recorded – see Table 6-3. For host rock the estimated temperature is based on host rock studies by Frey et al (1976) ** = $\delta^{18}\text{O}_{\text{Fluid}}$ value calculated using the appropriate fractionation equation for the mineral, see Appendix 4. *** = δD for muscovite and chlorite calculated using the appropriate fractionation equation – see Appendix 4. FC = fault core, ODZ = outer damage zone, IDZ = inner damage zone, DZ = damage zone, Amp = amphibolite.

6.4.2 Fault rock results

6.4.2.1 Oxygen Isotope Compositions

Oxygen compositions. $\delta^{18}\text{O}$ values within both fault zones are tightly clustered for quartz, K-feldspar and chlorite (Figure 6-8). Standard deviations are typically small and range between 0.3-1.0 for all minerals from both faults (Table 6-5). Such homogeneity of results typically means there was a common hydrologic regime which enabled isotopic communication between the mineral in different samples (Baker, 1990; Dworkin, 1999).

Mineral and fault variations. Quartz $\delta^{18}\text{O}$ values from the VF are almost identical to the host but in the CCF they are typically higher than the host (Figure 6-8). In

both faults K-feldspar is depleted in ^{18}O , but K-feldspar from the CCF records the most depleted value (Figure 6-8). Chlorite from both fault zones consistently records the lightest $\delta^{18}\text{O}$ values of all the minerals (Figure 6-8).

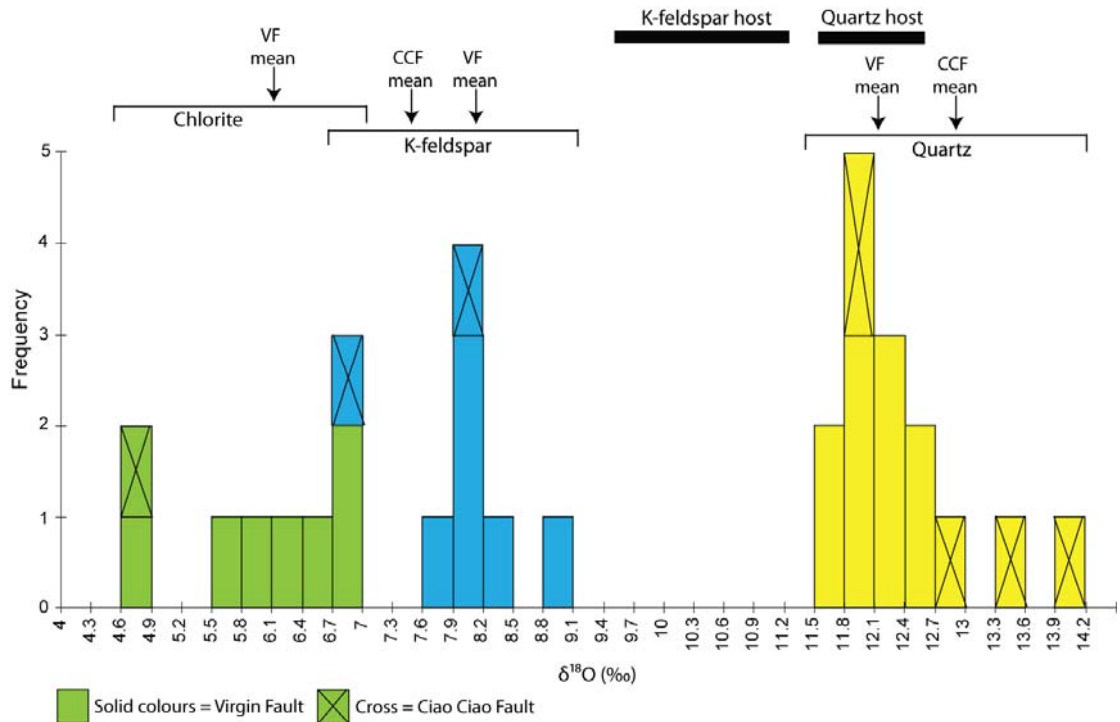


Figure 6-8: $\delta^{18}\text{O}$ values of fault rock minerals from the Virgin and Cio Cio Faults. The range of host rock values for quartz and K-feldspar are shown and the mean $\delta^{18}\text{O}$ value for each mineral in each fault. No mean is shown for chlorite in the CCF as only one measurement was recorded.

6.4.2.2 Co-existing minerals

6.4.2.2.1 Fractionation plots

$\delta^{18}\text{O}_{\text{mineral-mineral}}$ plots were used to estimate the degree of equilibrium between co-existing quartz and K-feldspar from the VF and CCF (Figure 6-9). *Assuming equilibrium* between co-existing minerals¹⁰, samples that fall along the same equilibrium line are thought to have formed under similar conditions (Gregory and Criss, 1986).

The majority of results from the VF and CCF lie between $\Delta = 3$ to $\Delta = 4$ (Figure 6-9). *Assuming equilibrium* between quartz and K-feldspar; this consistency in Δ values implies that similar conditions could have prevailed during mineral

¹⁰ Isotopic equilibrium between minerals means that the minerals interacted with the same fluid at the same time and that the minerals were able to freely exchange oxygen with the fluid.

precipitation. However, all of the mineral pairs have a calculated equilibrium temperature between -23 to 110°C (Figure 6-9) which is much lower than that measured from fluid inclusions (180 - 230°C , Section 6.3.6). Temperatures of -23 to 110°C are considered unrealistic at 7 - 12km , the estimated depth of fault activity (Ch 2 & 4) and the large fractionation values indicate disequilibrium between quartz and K-feldspar in both fault zones and possibly open system behaviour (Jenkin et al., 1992). The largest fractionation value was recorded in the fault core of the CCF (Figure 6-9), thus it records a greater degree of disequilibrium between quartz and K-feldspar compared to the rest of the VF and CCF.

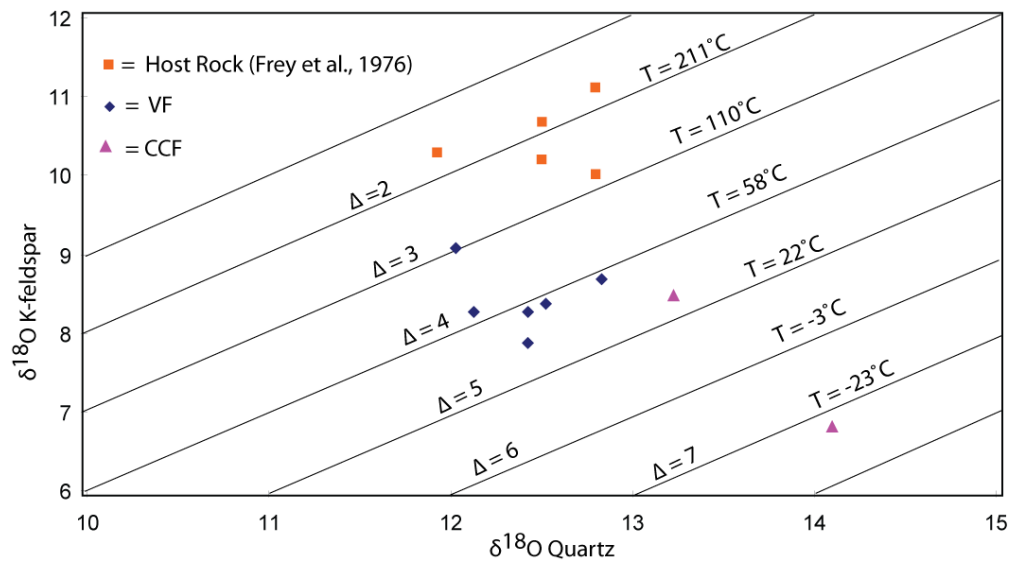


Figure 6-9: $\delta^{18}\text{O}_{\text{Quartz}}$ Vs $\delta^{18}\text{O}_{\text{K-feldspar}}$ for the host gneisses (from Frey et al., 1976) and fault rock samples from the VF and CCF. $\Delta = \delta^{18}\text{O}_{\text{Quartz}} - \delta^{18}\text{O}_{\text{K-feldspar}}$. Temperatures corresponding to $\Delta = \text{Quartz-K-feldspar}$ are calculated using fractionation equations from Matsuhisa et al., (1979) and O'Neil & Taylor, (1967) respectively.

6.4.2.3 Equilibrium fluid plots

For a measured $\delta^{18}\text{O}$ value the fluid $\delta^{18}\text{O}$ can be calculated for a range of temperatures (Bottinga and Javoy, 1975; Suzuoki and Epstein, 1976). Each line on a fluid equilibrium plot, represents all of the possible fluid $\delta^{18}\text{O}$ - temperature combinations that could precipitate a mineral with a specific measured $\delta^{18}\text{O}$ value (Figure 6-10). By plotting co-existing minerals on one graph, the plot can be used as a test for equilibrium or to estimate how the fluid $\delta^{18}\text{O}$ - temperature conditions evolved with time. If two or more mineral curves intersect, the point of intersection is known as the equilibrium point; and this point indicates what

the equilibrium fluid $\delta^{18}\text{O}$ - temperature was during precipitation of the minerals. However, if the mineral curves do not intersect, this implies disequilibrium between the minerals, and means they did not precipitate from the same fluid at the same time. If the temperature of precipitation is known, for example by fluid inclusions, then the change in fluid $\delta^{18}\text{O}$ required to precipitate the minerals at different times can be estimated (e.g. Figure 6-10).

6.4.2.3.1 *Virgin Fault*

Textural evidence suggests that the first phase of K-feldspar precipitation could be co-genetic with quartz but isotope fractionation data points towards disequilibrium (Figure 6-9). By using the mean fluid inclusion temperature (200°C Figure 6-7) an equilibrium-fluid plot shows that K-feldspar would have precipitated from a lighter fluid than quartz (Figure 6-10). Therefore, unless temperatures were significantly different during quartz and K-feldspar precipitation (by $\sim 30^\circ\text{C}$) K-feldspar precipitated from a lighter fluid.

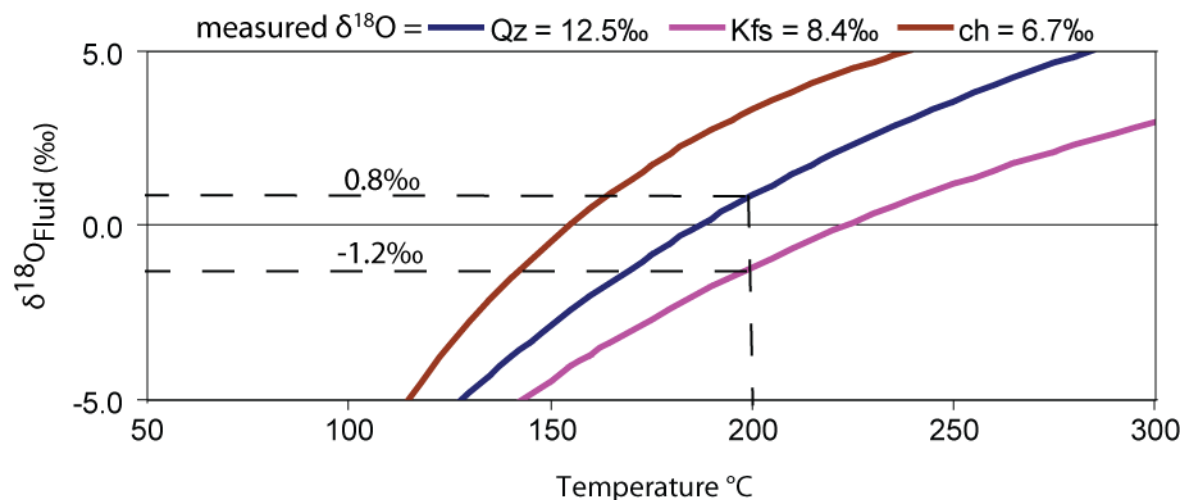


Figure 6-10: Equilibrium fluid diagram for co-existing minerals from VF3 in section 3 of the VF.

All fluid equilibrium mineral curves calculated using the appropriate fractionation equation for the mineral (see Appendix 4). Possible fluid compositions are highlighted for quartz and K-feldspar at 200°C .

Variations in fluid $\delta^{18}\text{O}$ can be due to different fluids of different compositions or different water-rock ratios. Given that these minerals are within the same fault rock sample and are of similar grain size (Ch 5); it is unlikely that the water-rock ratios were radically different. Therefore, the change in fluid $\delta^{18}\text{O}$ is likely to have been due to interaction with different fluids and hence that K-feldspar precipitated from a lighter fluid. Fluids with a lower $\delta^{18}\text{O}$ value are considered

to be more meteoric-like (Sheppard, 1986), therefore it is likely that K-feldspar interacted with a more meteoric-like fluid.

Cross-cutting relationships show that chlorite precipitated after quartz and K-feldspar. Using the fluid inclusion temperatures (160 to 230°C) chlorite could have precipitated from a fluid with $\delta^{18}\text{O}$ between +4.7 to +0.5‰ (Figure 6-11). Given that the VF was being exhumed (thus probably interacting with lighter, more meteoric-like fluids with time) and quartz formed prior to chlorite; chlorite must have precipitated from a fluid with a lighter $\delta^{18}\text{O}$ value than the fluid in equilibrium with quartz or it could have precipitated from a fluid of similar composition but at a lower temperature. If 230°C is the maximum temperature that quartz could have precipitated at (based on fluid inclusion results from this study), then if chlorite precipitated from a lighter fluid, then the chlorite would have precipitated from a fluid with a $\delta^{18}\text{O}$ value between +0.5 and +2.6‰ (Figure 6-11).

If K-feldspar did interact with a fluid at approximately 200°C then it would have been in equilibrium with a fluid of $\delta^{18}\text{O}$ -1.2‰ (Figure 6-10). This is representative of a more meteoric fluid (i.e. later) than that which precipitated chlorite (+0.5 to +2.6‰). Chlorite precipitated after K-feldspar and therefore chlorite is more likely to have interacted with a lighter fluid, thus results do not concur with microstructural observations. Both quartz and chlorite are unlikely to exchange oxygen with another fluid below temperatures of ~500°C (Criss et al., 1987; Giletti, 1986; Matthews et al., 1983); therefore the measured value reflects the isotopic composition of the fluid from which it precipitates. However, K-feldspar can re-equilibrate with fluids down to 50°C (Wenner & Taylor, 1976). This means that if K-feldspar interacted with a later fluid it could be isotopically reset and would not record information on the original fluid from which it grew. For K-feldspar to record a lighter fluid than chlorite suggest that after precipitation of the chlorite veins the K-feldspar was isotopically reset in the presence of another pervasive fluid in the fault zone. Hence, there was a minimum of three fluids within the fault zone, the first precipitated quartz and possibly K-feldspar; the second precipitated the chlorite veins, and the third reset the K-feldspar.

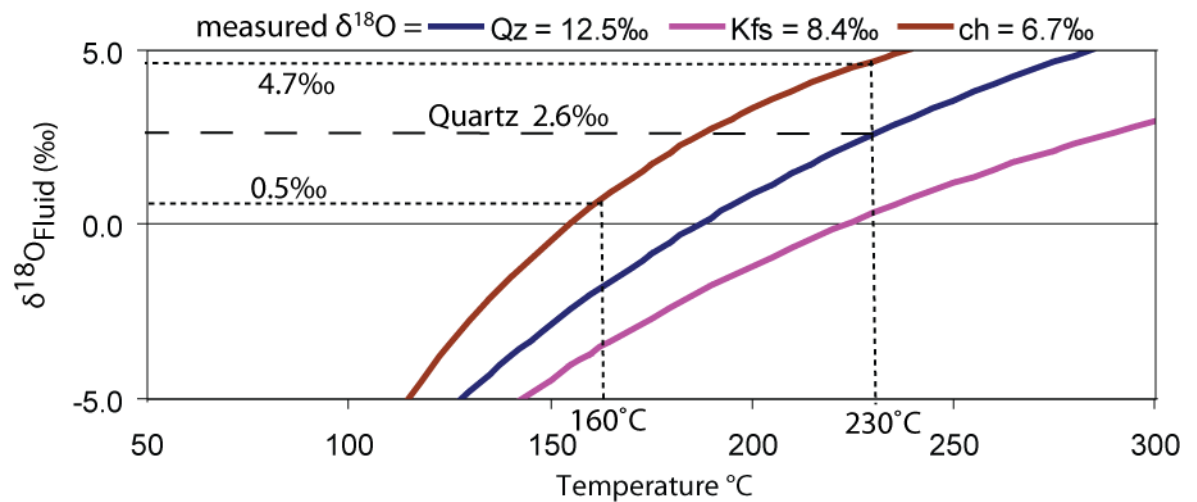


Figure 6-11: Equilibrium fluid diagram for co-existing minerals from VF03 in section 3 of the VF.

The maximum and minimum fluid compositions are highlighted by the dotted lines for chlorite between 160 to 230°C.

6.4.2.3.2 *Ciao Ciao Fault*

Within the CCF disequilibrium was inferred between quartz and K-feldspar from the fractionation plot (Figure 6-9). Microstructures from sample CC4 show chlorite cross-cutting the matrix but in some places evidence indicates that chlorite and quartz could be co-genetic (Ch 5). The equilibrium fluid plot for the CCF shows that quartz and chlorite could be in equilibrium with the same fluid for the entire temperature range recorded by fluid inclusions (160-230°C) (Figure 6-12). Therefore based on observations and the equilibrium plot it is likely that at some point in the evolution of the CCF quartz and chlorite were both precipitating.

The equilibrium plot also shows that between 160-230°C K-feldspar continually records a lighter $\delta^{18}\text{O}$ fluid value than quartz or chlorite. K-feldspar therefore records interaction with, more meteoric-like fluid. K-feldspar has been cross-cut by chlorite veins in sample CC4. This means that K-feldspar probably interacted with fluids similar to that which precipitated quartz, but that K-feldspar must have re-equilibrated with a later fluid for it to record equilibrium with a lighter fluid than that with chlorite.

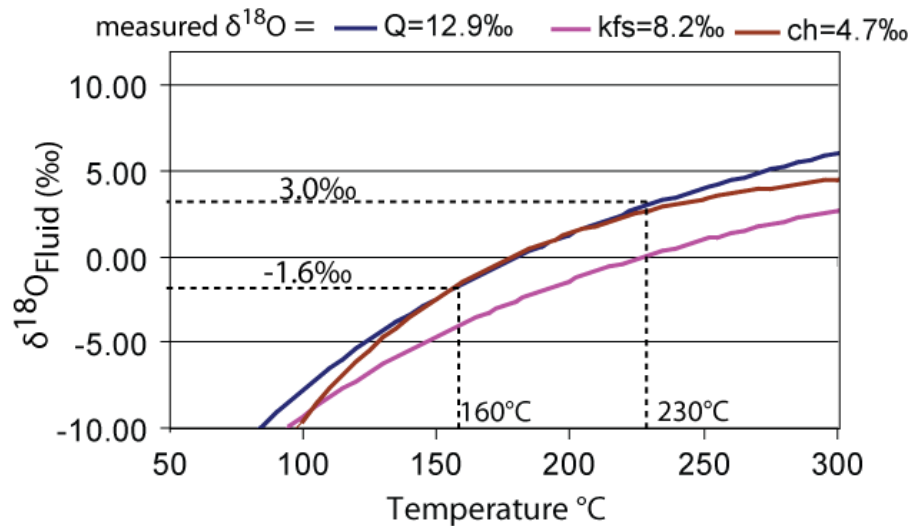


Figure 6-12: Equilibrium fluid plot for co-existing minerals from CC4 in the CCF. The dotted lines highlight the range in temperature and $\delta^{18}\text{O}$ fluid compositions over which quartz and chlorite could have been in equilibrium.

6.4.2.4 Structural Variations

6.4.2.4.1 *Virgin Fault - Variation in fault rock type.*

Investigations were carried out on four samples of quartz from different fault rocks within Section 3 of the VF. By comparing the isotopic composition with different fault rocks it will be possible to assess how fluids evolve during fault development. Quartz has been chosen for this analysis as it closes to oxygen exchange below $\sim 500^{\circ}\text{C}$ (Criss et al., 1987; Gilletti, 1986; Jenkin et al., 1991), therefore it will not re-equilibrate with later fluids after crystallization. Consequently, any variation in $\delta^{18}\text{O}$ composition will reflect conditions during the growth of quartz. The samples analysed are from the fault core (VF3), bleached outer damage zone (VF5), strongly bleached inner damage zone (VF6), and a second less developed fault core (VF4) (Fig 4-4).

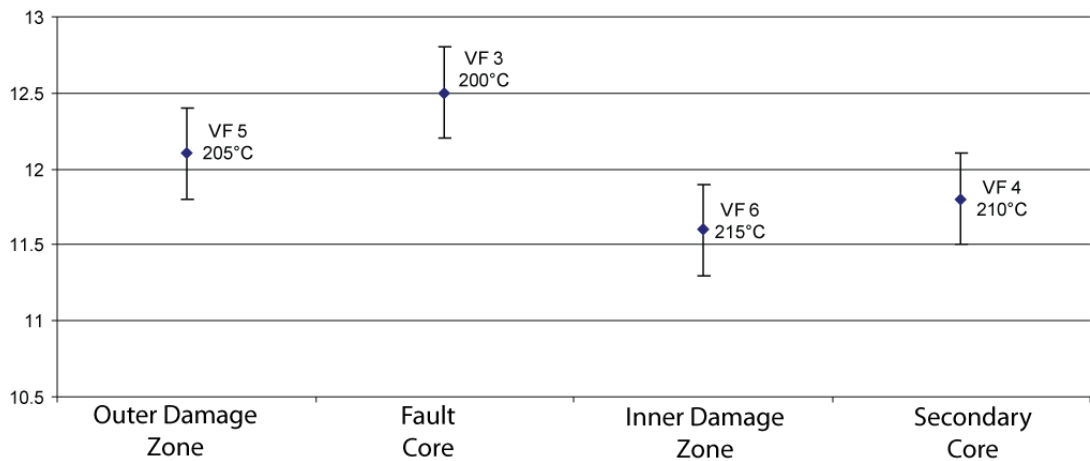


Figure 6-13: $\delta^{18}\text{O}_{\text{Quartz}}$ and calculated temperatures across strike of the VF based on $\delta^{18}\text{O}_{\text{Fluid}}$ being +1‰.

Temperatures calculated using fractionation equation of Matsuhisa et al., (1979).

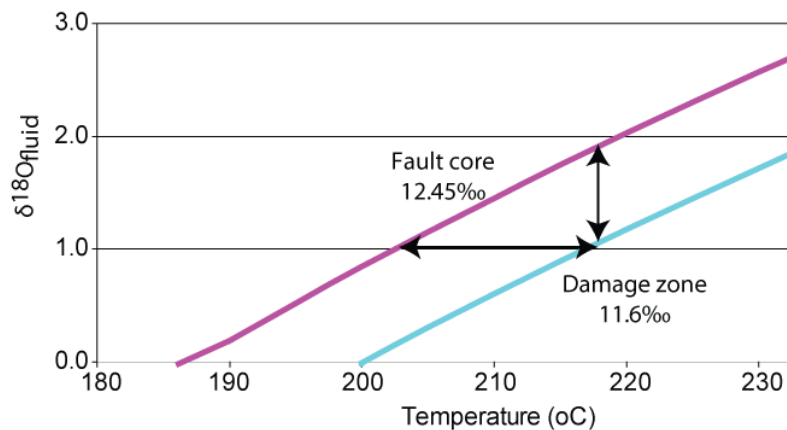


Figure 6-14: Fluid equilibrium diagram for quartz samples across strike of Section 3. For the same fluid to have precipitated quartz with a value of 12.45‰ and 11.6‰ would require either the temperature or $\delta^{18}\text{O}_{\text{Fluid}}$ to change (highlighted by the two arrows).

Variations in $\delta^{18}\text{O}_{\text{Quartz}}$ between the fault rocks show that $\delta^{18}\text{O}$ is highest in the fault core (VF3 - 12.5‰) and lowest in the strongly bleached inner damage zone (VF6 - 11.6‰) and are statistically significant (Figure 6-13). The differences between other samples VF5 -VF3 and between VF6-VF4 are within error ($\pm 0.3\%$; Figure 6-13). For a fluid to be able to precipitate quartz with a $\delta^{18}\text{O}$ of +12.45‰ and +11.6‰ would require: changing the $\delta^{18}\text{O}$ of the fluid; or changing temperature (Figure 6-14).

If temperature was the dominant control on the $\delta^{18}\text{O}_{\text{Quartz}}$ values then results imply that the temperature decreased by approximately 15°C within the core (Figure 6-14). Samples VF3 and VF6 were approximately 50cm apart within the fault and so the temperature change indicates a thermal gradient of 30°C/m.

Morrison & Anderson (1998) used stable isotope results to imply a negative thermal gradient across a thrust fault and calculated a gradient of 2.2°C/m. They described this as an 'extreme thermal gradient' and so a gradient of 30°C/m is more than excessive, especially for such a small fault.

Increases in $\delta^{18}\text{O}_{\text{Fluid}}$ in the fault core can be caused by either a different heavier fluid or by having lower water-rock ratios. The consistent isotopic composition of quartz results within the VF (Table 6-5) implies a common hydrologic system i.e. a single fluid. Therefore changes in water-rock ratio are likely to be the cause of elevated $\delta^{18}\text{O}_{\text{Fluid}}$ recorded in the fault core.

The water-rock ratio is a measure of the mass or volume of water to rock, within a given volume of rock, and is controlled by the permeability of the rock (Ohmoto, 1986). In rocks with a low permeability, the water-rock ratio is low and consequently the effects of water-rock interaction on the rock are small (Taylor, 1977); Figure 6-15). However, in a rock with a high permeability and high water/rock ratio, the effects of water-rock interactions on the rock are more pronounced (Figure 6-15). This means that if a fluid started with the same composition and then evolved at different water-rock ratios, the minerals precipitated would record different water-rock ratios. The mineral precipitated in the low permeability rock would record a heavier $\delta^{18}\text{O}$ signature (location A in Figure 6-15) than the mineral in the high permeability rock (location B in Figure 6-15).

Studies of faults in granitic rock have shown that the damage zone typically has enhanced permeability compared to the fault core (Balsamo et al., 2010; Evans et al., 1997; Wibberley and Shimamoto, 2003) which is due to increased fracturing in the damage zone compared to a fine grained, comminuted cataclasite in the core. A difference in permeability effects the water/rock ratio (Ohmoto, 1986; Roselle et al., 1999; Taylor, 1977) which in turn influences the $\delta^{18}\text{O}_{\text{Fluid}}$ signature recorded by the mineral (Figure 6-15). Cataclasite does occur in the fault core of the VF, and therefore would result in the fault core having a lower permeability and compared to the damage zone. Lower permeabilities and water/rock ratios result in a heavier $\delta^{18}\text{O}_{\text{Fluid}}$ signature being recorded by a mineral (Figure 6-15) providing all other parameters are equal. Therefore, the variation in quartz $\delta^{18}\text{O}_{\text{Fluid}}$ recorded across strike in the VF, is probably due to

reduced permeability in the fault core compared to the damage zone as a result of cataclasis in the fault core (Balsamo et al., 2010; Zhang and Tullis, 1998).

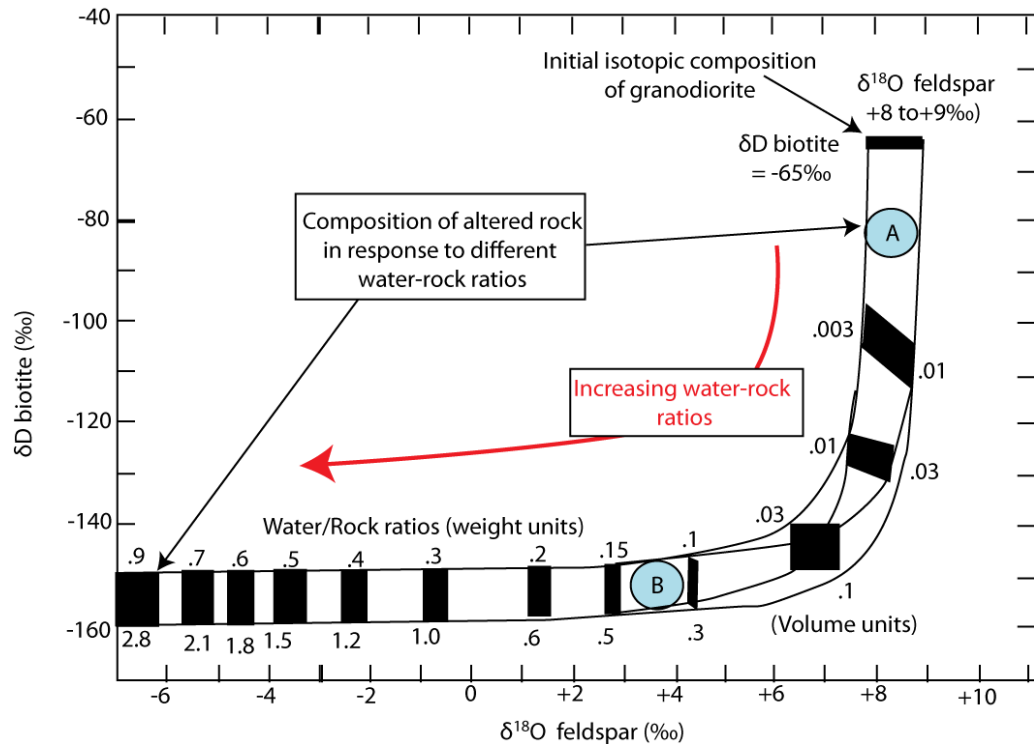


Figure 6-15: Calculated water-rock ratio curve.

Calculated values of biotite δD and feldspar $\delta^{18}O$ that would be produced at various W/R ratios by alteration of a typical granodiorite by meteoric-hydrothermal fluid at moderate temperatures. Locations A and B on the plot represent minerals precipitated from the same composition of fluid, but in rocks with lower and higher permeabilities respectively. Modified from Taylor (1977).

6.4.2.4.2 *Virgin Fault - Variation along strike*

Differences in the character of the fault along its length can provide evidence for localization of deformation and/or fluids.

The isotopic signature of quartz, K-feldspar and chlorite were measured from the outer damage zone and fault core in both section 3 (VF5 & VF3) and section 4 (VF7 & VF8) of the VF (Figure 4-4) (Table 6-6). The $\delta^{18}O$ values in section 3 are higher within the fault core than the damage zone, whereas in section 4 K-feldspar and chlorite record lower $\delta^{18}O$ values in the fault core (Table 6-6).

Mineral	S3 DZ (‰)	S3 Core (‰)	S4 DZ (‰)	S4 Core (‰)
Quartz	12.1	12.5	11.7	12.4
K-feldspar	8.0	8.4	8.8	7.6
Chlorite	5.8	6.7	6.6	5.7

Table 6-6: $\delta^{18}\text{O}$ values from outer damage zone and fault core in section 3 (S3) & 4 (S4) of the Virgin Fault.

Higher quartz $\delta^{18}\text{O}$ across strike of the fault in section 3 was explained by lower water-rock ratios in the fault core due to cataclasis reducing the permeability. Cataclasite does occur in the fault core of section 4, therefore the decreased permeability will effect the water-rock ratio and result in a heavier $\delta^{18}\text{O}$ being recorded (Figure 6-15), and thus can explain the higher quartz $\delta^{18}\text{O}$ in the core (Table 6-6). Since cataclasite does occur in section 4, the same pattern should occur in other minerals providing the mineral precipitated from the same fluid at the same temperature in the damage zone and fault core. K-feldspar and chlorite show the opposite behaviour in section 4 and so this means that they were either precipitated from one fluid at different temperatures in the core and damage zone or from different fluids in the core and dame zone.

The difference in K-feldspar and chlorite $\delta^{18}\text{O}$ could be explained by $\sim 30^\circ\text{C}$ and $\sim 15^\circ\text{C}$ change in fluid temperature respectively (Figure 6-16). Such a large temperature change over a short distance ($<1\text{m}$) is considered as an extreme temperature gradient (section 6.4.2.4.1; Morrison & Anderson, 1998). Therefore a temperature change is unlikely to have caused the fractionation pattern in section 4 of the VF. This means that the fractionation pattern in section 4 of the VF is probably caused by the fault core and damage zone minerals being precipitated from different fluids.

For both K-feldspar and chlorite in section 4 of the VF, the lightest $\delta^{18}\text{O}$ value is recorded in the fault core. This implies that a lighter fluid infiltrated the fault core in section 4 and thus indicates multiple fluids within the fault zone. The fact that the fluid was not recorded in the outer damage zone or in section 3 infers that some deformation and fault zone fluids were localized/restricted to certain parts of the fault zone, and specifically the fault core.

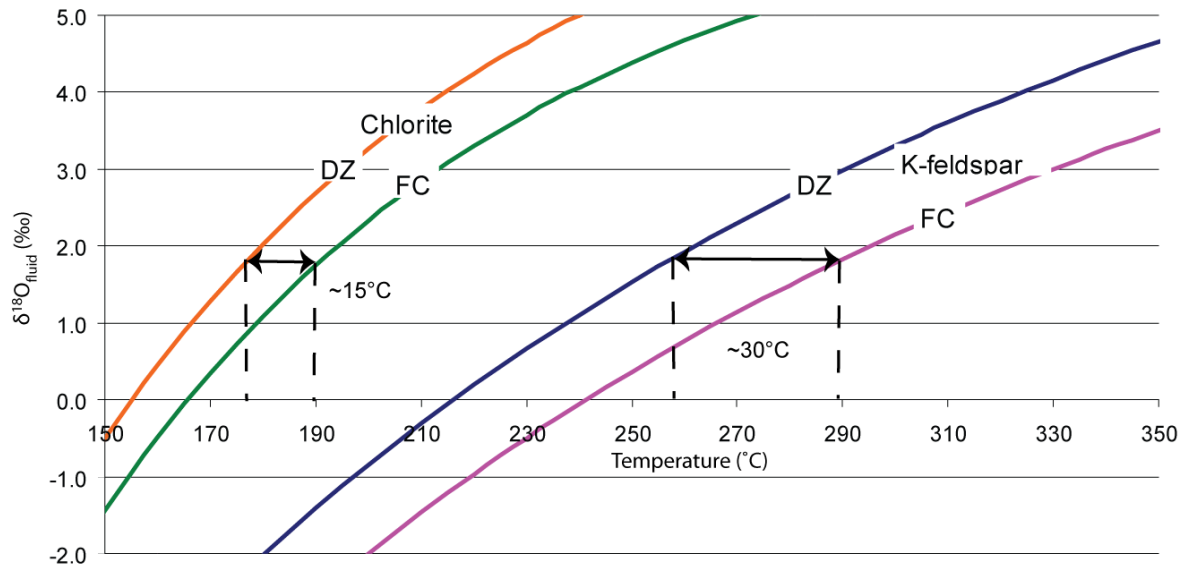


Figure 6-16: Fluid-equilibrium plot for chlorite and K-feldspar in the damage zone and fault core at section 4 of the VF.

Arrows between the damage zone (DZ) and fault core (FC) in both faults highlight the temperature change required to cause the change in $\delta^{18}\text{O}$ recorded.

6.4.2.4.3 *Ciao Ciao Fault - Variation in fault rock type*

The transition from host rock through to fault core can be observed at grid 641875, 094165 on the CCF. Quartz $\delta^{18}\text{O}$ composition increases from the outer damage zone through to the fault core (Figure 6-17). The damage zone and breccia have almost identical $\delta^{18}\text{O}$ signatures but the $\delta^{18}\text{O}$ is ~2‰ higher in the foliated cataclasite compared to host. Quartz has been precipitated within the foliated cataclasite whereas in the damage and breccia quartz only shows evidence of fracturing and no evidence of newly precipitated quartz. Quartz is unlikely to re-equilibrate at low temperatures (Giletti, 1986) and studies show that micro-fracturing alone is unable to cause isotopic homogenization (O'Hara et al., 1997); thus the $\delta^{18}\text{O}$ value of the damage zone quartz should record host rock conditions.

Since quartz within the damage zone of the CCF records host rock conditions, this indicates that the foliated cataclasite records an increase in $\delta^{18}\text{O}$ compared to host. Fluid-rock interactions typically result in a significant reduction in the $\delta^{18}\text{O}$ signature of the rock (Sheppard, 1986; Criss & Taylor, 1986), thus an increase in $\delta^{18}\text{O}$ of the foliated cataclasite in the CCF seems out of place. Criss & Taylor (1986) state that because of very large mineral-water fractionation factors at low temperatures, the $\delta^{18}\text{O}$ of rocks can actually be increased by low temperature interactions with meteoric waters. Therefore, if permeability and

temperature was sufficiently low within the foliated cataclasite, quartz could record an increase in $\delta^{18}\text{O}$. Cataclasite evolution due to repeated slip events and foliation development are known to significantly reduce the permeability of a rock (Jefferies et al., 2006a; Zhang and Tullis, 1998) and thus will radically decrease the water-rock ratios. As well as this, sericitization associated with quartz precipitation *only* occurs in the foliated cataclasite in the CCF. This implies that the foliated cataclasite ceased to be an open system (Section 5.7.4) and indicates that the permeability became so low that the foliated cataclasite was no longer being refreshed by external fluids. The textures within the CCF therefore indicate that an increase in quartz $\delta^{18}\text{O}$ in the foliated cataclasite is probably due to very low permeabilities reducing the water-rock ratio, and possibly the presence of a low temperature meteoric fluid as well.

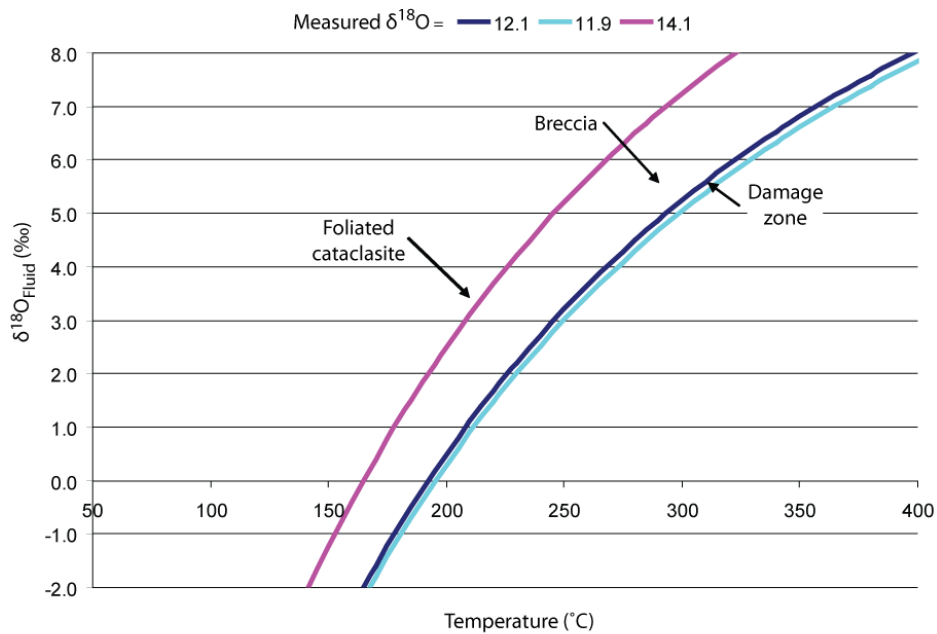


Figure 6-17: Equilibrium fluid diagram for across strike variations of Quartz on the CCF. Samples taken from location B. IDZ & ODZ = outer and inner damage zone respectively.

6.4.2.4.4 Variation along strike of the CCF

Quartz and K-feldspar were analysed from the foliated cataclasite (CC3) and the central fractured zone (CC4). Both the central fractured zone and the foliated cataclasite are fractionated compared to host (Figure 6-8) indicating that they have been effected by fluid-rock interactions. This means that fluid was able to infiltrate into the central fractured part of the CCF zone. A fluid-equilibrium plot shows that quartz $\delta^{18}\text{O}$ is higher in the foliated cataclasite whereas K-

feldspar $\delta^{18}\text{O}$ is lower in the foliated cataclasite compared to the central fractured zone (Figure 6-18).

The higher $\delta^{18}\text{O}$ in the foliated cataclasite has been interpreted as a result of decreased permeability due to cataclasis and foliation development (6.4.2.4.3). The central fractured zone is more akin to damage zone material (fractured and bleached) and so is likely to have higher permeability than the foliated cataclasite. This means the included block would have higher water-rock ratios, and thus corroborates an increase in $\delta^{18}\text{O}$ in the foliated cataclasite due to lower permeability and water-rock ratios.

K-feldspar records the opposite $\delta^{18}\text{O}$ fractionation pattern between the foliated cataclasite and central fractured zone to quartz (Figure 6-18). Since water-rock ratios are lower in the foliated cataclasite and this would cause the $\delta^{18}\text{O}$ to increase; to achieve such a fractionation pattern would therefore require a lighter fluid to have interacted with the foliated cataclasite. Multiple deformation and fluid flow events have been recorded in the fault core (Ch 5). It has also been suggested that if K-feldspar was previously exposed to a hydrothermal fluid then such 'pre-treatment' would make it more susceptible to low temperature resetting (Wenner & Taylor, 1976). Thus it is thought that the K-feldspar within the cataclasite was isotopically reset explaining the reversal in the fractionation pattern.

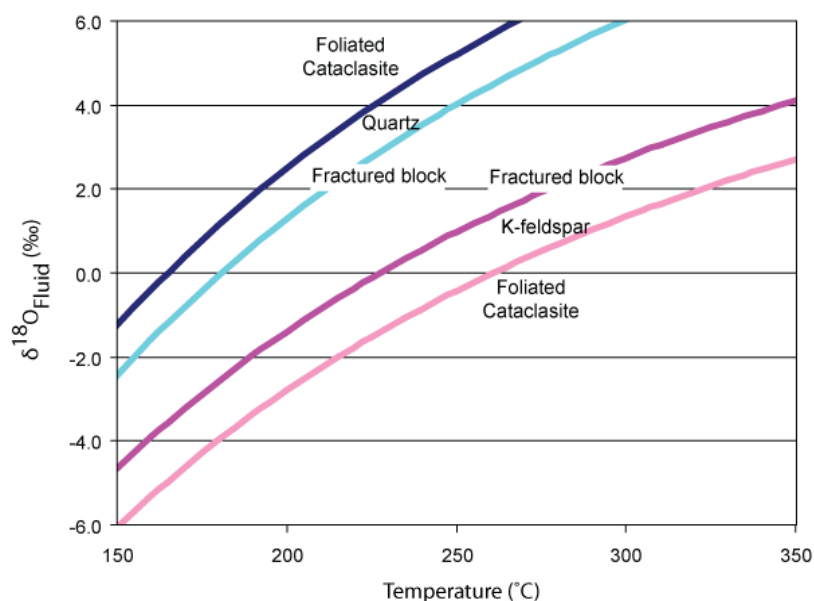


Figure 6-18: Fluid equilibrium diagram comparing the fractionation pattern for quartz and K-feldspar between the foliated cataclasite and the fractured central block in the CCF.

6.4.2.5 Hydrogen isotope compositions

The δD_{Fluid} compositions for the VF and CCF range from -15 to -135‰ (Figure 6-19). There are two distinct groups of data: -15 to -35‰ and -65 to -135‰ (Figure 6-19). The heavier group is comprised solely of chlorite from the VF and is within the range of fluid compositions estimated for the unmodified host rock. All other minerals including chlorite from the CCF are part of the lighter group which is significantly different from the fluids in equilibrium with the host rock. In general there is a spread of the δD_{Fluid} results, with each mineral recording a range of δD_{Fluid} values (Figure 6-19). Within Passo Moro the host rock fluid ranged from -15 to -45‰ (Figure 6-19) whereas the lightest value recorded in the faults is -135‰. To attain such light values requires interaction with a fluid from a deuterium depleted source. Meteoric waters are the only abundant natural source of fluid that is depleted in deuterium (Frey et al., 1976). This means that the VF and CCF must have interacted with meteoric derived fluids during their evolution.

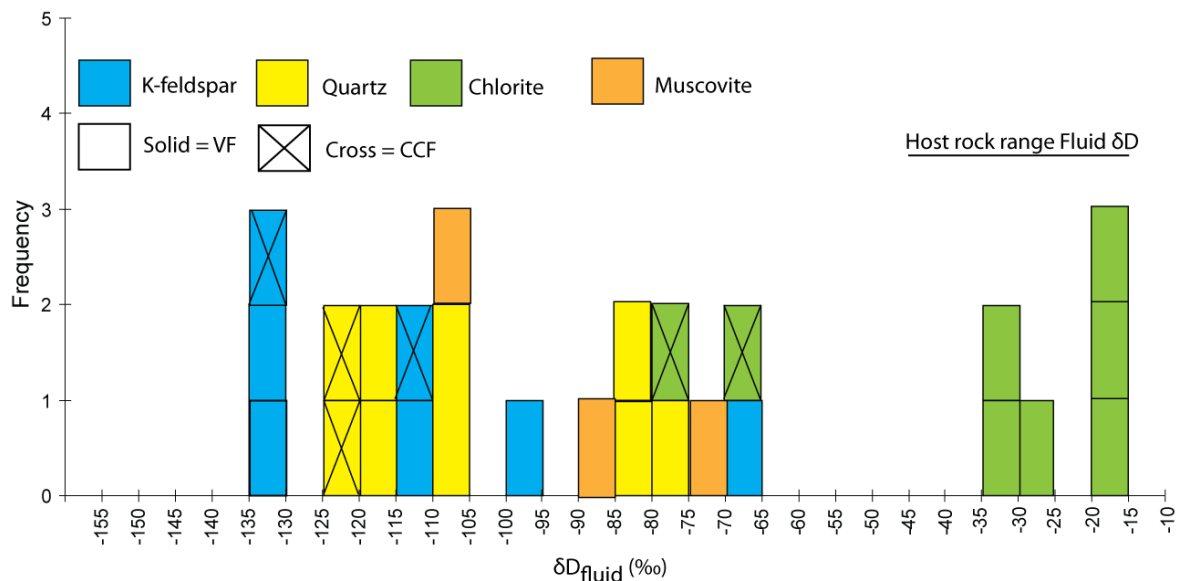


Figure 6-19: Hydrogen results for both fault zones at Passo Moro.

δD_{fluid} values for quartz and K-feldspar and δD values for hydrous minerals. Host rock range is calculated from muscovite and biotite and is based on a compilation of results from Frey et al., (1976) and this study. Fractionation equations for calculating δD_{Fluid} muscovite and chlorite can be found in Appendix 4.

6.4.2.5.1 The Virgin Fault

δD_{Fluid} values range from -15 to -135‰ within the VF. Chlorite is the only mineral that records a host-rock like isotopic signature whereas all other minerals record

isotopically lighter compositions (Figure 6-19). Hydrogen exchange is slow below 500 °C in chlorite (Graham et al., 1987) and consequently chlorite is unlikely to be isotopically reset. However, hydrogen exchange rates are rapid for muscovite between 150-400 °C (Vennemann and O'Neil, 1996). Fluid inclusions dominate the δD fluid signature of quartz and K-feldspar and consequently these are easily reset and are unlikely to record the original or primary fluid composition.

Due to the low temperatures (180 to 260 °C) and the minerals isotope composition being reset in the VF, chlorite is the only mineral that will preserve information on the fluids from which it precipitated. Chlorite shows that the hydrothermal fluids must have had a δD_{Fluid} value between -15 to -35‰ which is comparable to the metamorphic host fluid (6.4.1.2). Microstructural observations reveal that quartz and K-feldspar precipitated prior to chlorite, and so regardless of the δD_{Fluid} value they record as a result of resetting; they must have originally formed from a fluid of similar δD_{Fluid} composition than that which precipitated chlorite. This means that the majority of mineralization within the VF is likely to have been a result of fluids with a δD_{Fluid} between -15 to -35‰.

Two generations of chlorite are recognised in the VF of which one is sheared and the other is unsheared (Fig 5-11a & 5-14d respectively). The pristine nature of some of the chlorite veins (and lack of deformation in the associated quartz (Fig 5-11e), suggests that there was very little deformation after the second generation of chlorite was precipitated. The fact that the rest of the minerals record lighter fluids is probably due to the ease that they are isotopically reset. Undeformed chlorite associated with isotopically reset quartz, implies the periodic influx of lighter fluids into the VF without accompanying deformation. Fluid events as a result of an earthquake along another fault have been previously recorded (Eichhubl and Boles, 2000) and so confirms the possibility of fluid influx without significant deformation accumulating on the VF.

A δD_{Fluid} of -135‰ is typical of meteoric whereas -15 to -35‰ is more akin to a metamorphic fluid; hence the VF interacted with fluids from different sources. As faults exhume the rocks move towards meteoric fluids, thus their exhumation can be read. Results from the VF therefore indicate that during exhumation it equilibrated to an increasing extent with meteoric fluids. However,

microstructures and isotopic composition of chlorite show that the majority of mineralization and accumulated deformation in the fault zone was associated with deeper more metamorphic like fluids.

6.4.2.5.2 *The Ciao Ciao Fault*

Chlorite records δD_{Fluid} values of -65 to -80‰ within the CCF whereas quartz and K-feldspar record values between -110 to -130‰. These values are outwith host rock values and mean the CCF only recorded interaction with lighter fluids. Since chlorite is unlikely to be isotopically reset these relatively heavy fluids may represent the first that infiltrated the fault. Quartz and K-feldspar records fluid compositions as light as -130‰ within the fault core, indicating that lighter fluids that had a more meteoric isotopic composition were intersected during exhumation.

6.4.2.5.3 *Fault and fluid variations*

δD_{Fluid} values within the two fault zones show that the VF interacted with fluids with δD_{Fluid} from -15 to -135‰ whereas the CCF interacted with fluids with a δD_{Fluid} of -65 to -130‰ (Figure 6-19). Since faults intersect progressively lighter fluids during exhumation, these results imply that the VF was open to fluid infiltration for a rather longer than the CCF. Given that small faults evolve into larger more complex fault zones (Martel, 1990) it might be expected that the CCF (being a more mature fault zone) would record interaction with a greater variety of fluids than the VF.

Excluding chlorite, because it will not be isotopically reset, the δD_{Fluid} values range from -69 to -134‰ and -114 to -129‰ for the VF and CCF respectively (Table 6-5, Figure 6-19). Hence, the VF records a far greater range of δD_{Fluid} composition, than the CCF. Although the data set is limited within the CCF, analyses come from samples that are 800 m apart and so this might infer a pervasive fluid throughout the fault zone causing resetting. However, co-existing quartz and K-feldspar from the VF can have a difference in δD_{Fluid} values of up to 24‰ (Sample VF3, Table 6-5). Variation of δD_{Fluid} values within and between samples in the VF points to the lack of a common hydrologic system in the fault. The lack of interaction of the CCF with heavier fluids is therefore

likely to be related to fluids being pervasive and causing isotopic widespread resetting.

6.4.2.6 Water-rock ratio modelling

Isotopes of hydrogen and oxygen are used routinely to identify the source of aqueous fluids (Sheppard, 1986). However, the isotopic composition of a fluid can be affected by water-rock ratios, temperature, and composition of host rock (Gregory & Criss, 1986). Assuming the fluid is principally of meteoric origin its evolution with varying water-rock ratios and temperature can be modelled for a rock and meteoric fluid of known composition (Criss and Taylor, 1986; Field and Fifarek, 1985; Taylor, 1977) (Figure 6-15).

Water-rock calculations are used as a means of determining the final isotopic composition of a fluid after equilibration with a rock for different water-rock ratios and is a function of: initial (unexchanged) composition of the water and rock; the temperature of equilibration, which determines the fractionation factor between rock and water; and ratio of unexchanged oxygen and hydrogen atoms in the water to those in the rock (Field and Fifarek, 1985; Ohmoto and Rye, 1974). This relationship is after Ohmoto & Rhy (1974) and is expressed as:

$$\delta_w^f = \frac{\delta_r^i - \Delta_{r-w} + [(w/r)(\delta_w^i)]}{1 + (w/r)}$$

Equation 10

With respect to the faults, the initial $\delta^{18}\text{O}$ composition of the rocks that have been hydrothermally altered can be estimated by analysing the host rocks outside the altered area. The initial δD of the hydrothermal H_2O can be estimated from D/H analyses of the alteration mineral assemblages, and in this case chlorite will be used as the δD is inherited at the time of formation (Jenkin et al., 1992). By applying the meteoric water equation ($\delta\text{D}\text{‰} = 8 \delta^{18}\text{O}\text{‰} + 10$;

Craig, 1966) we can then calculate the initial $\delta^{18}\text{O}$ of the meteoric fluid (Taylor, 1977). By utilising Equation 10 the δD and $\delta^{18}\text{O}$ is calculated for varying water-rock ratios. Results are then compared to these curves and dependant on whether they lie along the curve or not will indicate if they formed in a fluid-rock system which evolved in terms of water-rock ratio or from different fluids.

For modelling water-rock ratio evolution the isotopic composition of the host rock at Passo Moro was defined as $\delta^{18}\text{O}$ 12.3‰ δD -60‰. These values were based on the average isotopic compositions of quartz (this study) and biotite (from Frey et al., 1976) from the host rock for $\delta^{18}\text{O}$ and δD respectively (Table 6-4 and Table 6-5). Three possible compositions of infiltrating fluids were modelled and the initial fluid compositions selected were based upon the $\delta\text{D}_{\text{Fluid}}$ composition of chlorite in the VF ($\sim\delta\text{D}$ - 25‰) and the CCF (δD - 65‰), and from the lowest δD value recorded in the CCF (δD -135‰). A fluid temperature of 260°C was chosen for the two heavier fluids and 200°C for the lighter fluid (Figure 6-20) as these temperatures produced modelled evolution paths that intersected with the greatest number of analyses. The fluid results from fault rock minerals were then compared to the water-rock ratio evolution curves (Figure 6-20).

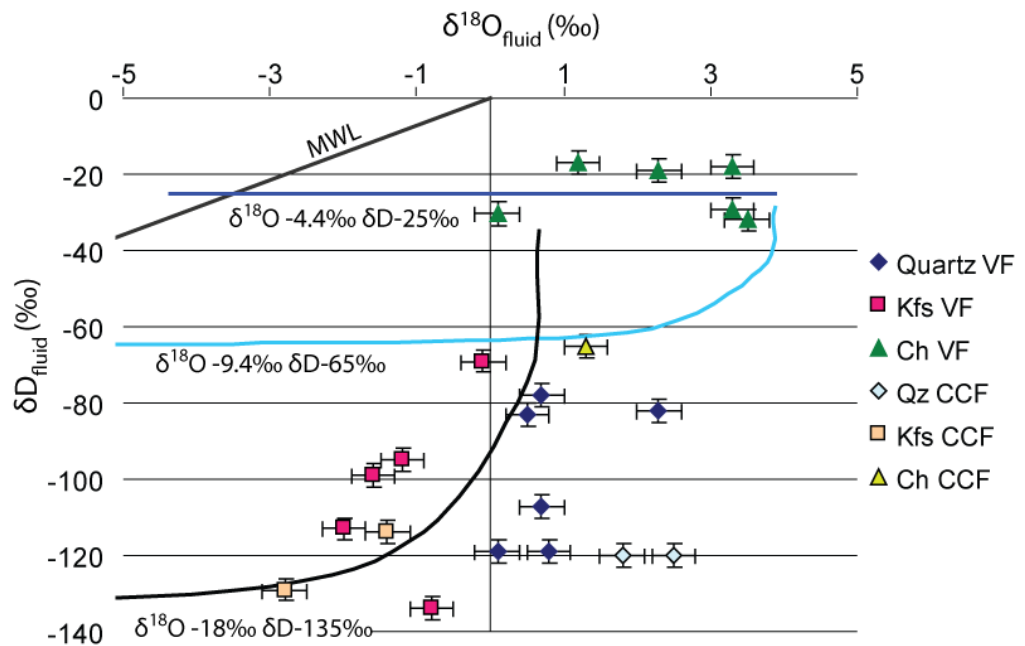


Figure 6-20: $\delta^{18}\text{O}_{\text{fluid}} / \delta\text{D}_{\text{fluid}}$ plot plus modelled fluid evolution profiles for three possible meteoric derived fluids.

Temperature of modelled systems is 260°C for fluids with $\delta\text{D}_{\text{fluid}}$ -25 and -65‰ and 200°C for $\delta\text{D}_{\text{fluid}}$ -135‰. Qz = quartz, Kfs = K-feldspar, Ch = chlorite, MWL = Meteoric water line.

The $\delta^{18}\text{O}_{\text{fluid}} / \delta\text{D}_{\text{fluid}}$ plot shows that the data points are scattered over a variety of $\delta^{18}\text{O}_{\text{fluid}}$ and $\delta\text{D}_{\text{fluid}}$ values and do not fit the modelled curves well (Figure 6-20). Quartz always plots to higher $\delta^{18}\text{O}_{\text{fluid}}$ values than modelling predicts while K-feldspar typically plots to lower $\delta^{18}\text{O}_{\text{fluid}}$ values (Figure 6-20).

In terms of isotopic resetting chlorite will not be reset; quartz $\delta\text{D}_{\text{fluid}}$ value can be reset; and both $\delta^{18}\text{O}$ and $\delta\text{D}_{\text{fluid}}$ can be reset in K-feldspar. This means that quartz and K-feldspar are unlikely to record the composition of the fluid from which they precipitated and so will not plot at the predicted position on a fluid evolution curve. If quartz and K-feldspar originally formed from, or interacted with, a similar fluid to that which precipitated chlorite, which is suggested by the fault rock microstructures (Chapter 5); by adjusting the $\delta\text{D}_{\text{fluid}}$ value of quartz and K-feldspar to that of co-existing chlorite it may be more representative of the δD of the precipitating fluid. Such δD adjustments were done for quartz and K-feldspar from the VF and quartz from the CCF and the revised plot is shown in Figure 6-21. K-feldspar was not adjusted from the CCF as the two data points do fall along the calculated fluid evolution path for the fluid with δD -135‰. This is also the lightest fluid recorded within the faults and so if

it was the last fluid that precipitated/reset the K-feldspar then the data points should be representative of the fluid.

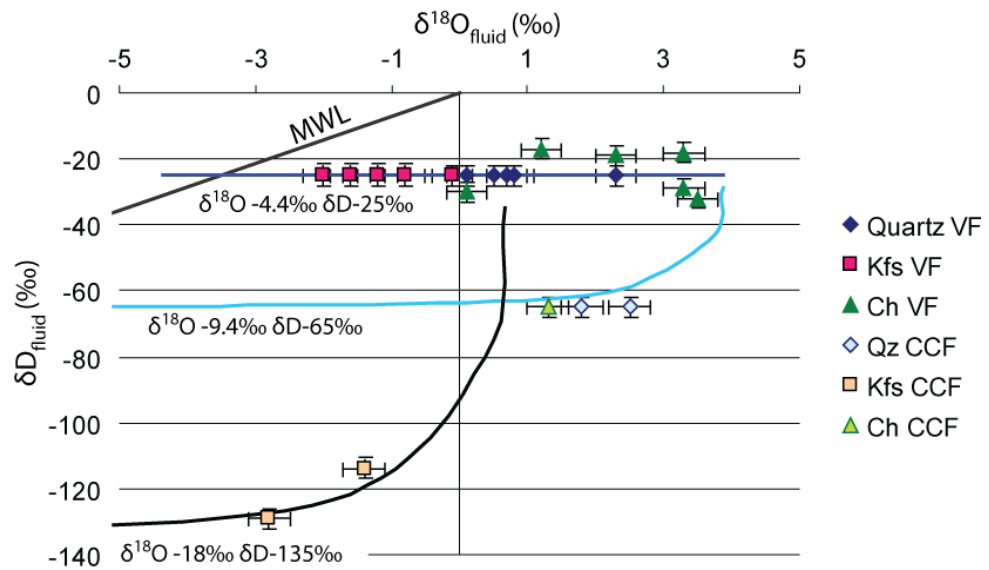


Figure 6-21: $\delta^{18}\text{O}_{\text{Fluid}} / \delta\text{D}_{\text{Fluid}}$ plot with modified data from the VF and CCF. Quartz and K-feldspar $\delta\text{D}_{\text{Fluid}}$ values modified to that of the co-existing chlorite in VF and only quartz modified in the CCF.

With quartz and K-feldspar adjusted to the fluid values of chlorite, all data points fall close to the modelled fluid evolution curves (Figure 6-21). Multiple curves are needed to fit the data (dictated by variable chlorite results) and this reflects the presence of multiple fluids within the fault zones (Figure 6-21). However, the close proximity of the data points to the modelled fluid evolution indicates that the fault zone fluids can be assessed in terms of water-rock ratios.

The location of the K-feldspar points along the x-axis for the fluid of $\delta\text{D} -25\text{‰}$ are unlikely to be representative of the water-rock ratio associated with the precipitation of K-feldspar. For the models K-feldspar has only been adjusted in terms of fluid δD , but due to the continual fractionation of oxygen between K-feldspar and water down to low temperatures (Wenner and Taylor, 1971), there is no clear evidence of the original fluid $\delta^{18}\text{O}$ composition that interacted with the feldspar. However, modelled interaction with more meteoric-like fluids drives the measured $\delta^{18}\text{O}$ to lower $\delta^{18}\text{O}$ values and therefore the original fluid must have had a higher $\delta^{18}\text{O}$. This would shift the K-feldspar data points towards a similar composition as quartz on the $\delta^{18}\text{O}_{\text{Fluid}} / \delta\text{D}_{\text{Fluid}}$ plot and so would

corroborate with microstructural observations suggesting a similar time of formation.

6.4.2.6.1 *Water-rock ratios*

The calculated water-rock ratio curves are constructed by utilising Equation 10 and the δD and $\delta^{18}O$ is calculated for water-rock ratios that vary from 1:1000 to 100:1. The location of the different water-rock ratios curves can be plotted onto the modelled curves, and the analyses assessed in terms of evolving water-rock ratios (Figure 6-22).

Based on the adjusted results from the VF and CCF; the VF records water-rock ratios from 1:1 to 1:100 whereas the CCF fluids record a water-rock ratio of approximately 1:10 (Figure 6-22). This indicates that both fault zones were rock dominated i.e. greater proportion of rock to water.

Virgin Fault. Within the VF the high degree of homogeneity of individual mineral $\delta^{18}O$ values (Table 6-5) indicates a common hydrological system, but disequilibrium between minerals implies the system was open to fluids. Within the VF a variety of water-rock ratios are recorded varying from strongly rock dominated (1:100) to a regime with more water present (towards 1:1) (Figure 6-22). An open system is described as one where fluids are progressively infiltrating and the water-rock ratios increase with time (Gregory and Criss, 1986). Chlorite veins in the VF formed after quartz and K-feldspar however, on the water-rock ratio plot the majority of the chlorite data are linked to lower water-rock ratios than quartz or K-feldspar (Figure 6-22). If the VF was open and water-rock ratios increased with time, then the timing of microstructures would imply that chlorite should precipitate at higher water-rock ratios, not lower. Lower water-rock ratios infer that water-rock ratios decreased with time, and thus the system became progressively more rock dominated. This means that during evolution of the VF fluids were infiltrating but also being used up and likely resulted in sealing of the fault rock.

Quartz and K-feldspar record lighter fluids within the fault zone than predicted by the modelled curves (Figure 6-20 & Figure 6-22). For quartz and K-feldspar to be isotopically reset they must have interacted with later fluids and so the VF must have been breached at a later stage. Such behaviour in faults may

represent a combined conduit-barrier type system (Goddard and Evans, 1995; Logan and Decker, 1994) where brittle failure allows the infiltration of fluid and cementation seals the fault off again (closed system) (Janssen et al., 1998). The variable δD composition of fluid in equilibrium with quartz and K-feldspar in the VF (Table 6-5) indicates multiple fluids and the lack of a pervasive fluid. This points towards the VF being a limited open system (Gregory & Criss, 1986) whereby finite volumes of fluid would periodically infiltrate the fault zone.

Ciao Ciao Fault. The data points from the CCF plot at a water-rock ratio of approximately 1:10 (Figure 6-22). Therefore, in general the minerals within the CCF do not record information on an evolving water-rock system, but rather changing fluid compositions with almost constant water-rock ratios. This type of behaviour is not considered as representing an open system (Gregory and Criss, 1986), but rather is more indicative of cycles of high and low permeability whereby there are periodic influxes of fluid.

Within the CCF quartz records the lowest water-rock ratio (Figure 6-22). This suggests that the fault was not an open system. The continued influx of fluid tends to cause silica dissolution and feldspar alteration creating porosity (Janssen et al., 1998) as opposed to silica precipitation. Quartz microveins *only* occur within the foliated cataclasite of the CCF and these were subsequently been deformed by brittle fracturing. Microstructural and isotopic evidence therefore points towards the foliated cataclasite of the CCF being deformed, sealed and deformed again. Thus the foliated cataclasite of the CCF is subject to cycles of higher and lower permeability and hence is a limited open system for fluids.

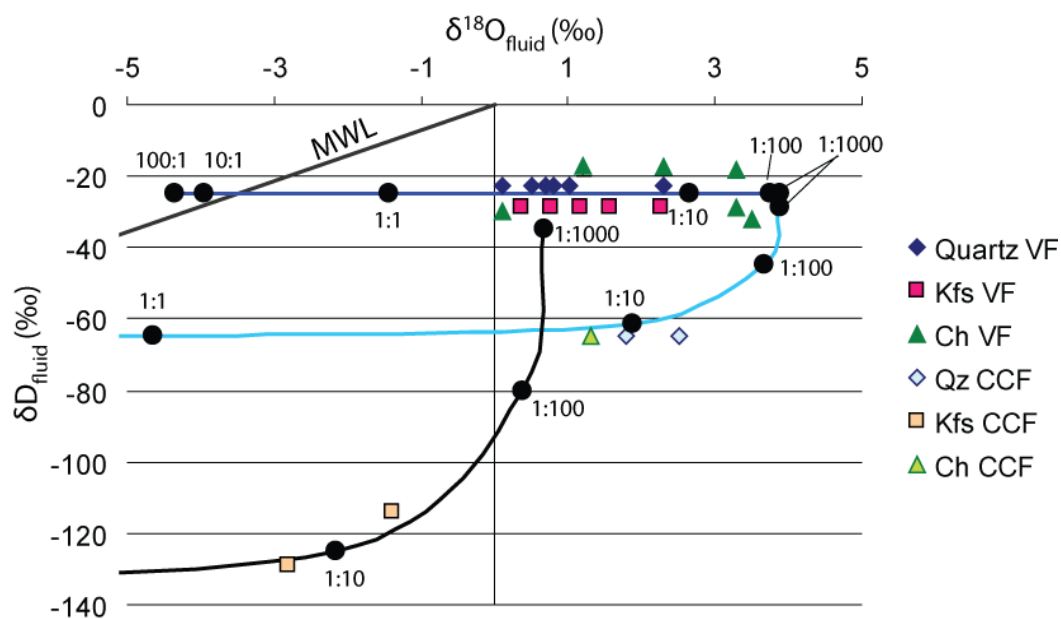


Figure 6-22: $\delta^{18}\text{O}_{\text{Fluid}} / \delta\text{D}_{\text{Fluid}}$ plot with modelled fluid evolution curves and associated water-rock ratios.

K-feldspar in the VF has been adjusted in terms of $\delta^{18}\text{O}_{\text{Fluid}}$ and $\delta\text{D}_{\text{Fluid}}$.

6.4.2.6.2 Fluid source

The compositions of the three chosen fluids for water-rock ratio modelling have a $\delta^{18}\text{O}_{\text{Fluid}}$ and $\delta\text{D}_{\text{Fluid}}$ of: -4.4‰ , -25‰ ; -9.4‰ , -65‰ ; and -18‰ , -135‰ . The majority of mineralization in the VF is thought to have occurred in response to a fluid with $\delta\text{D}_{\text{Fluid}}$ of -15 to -35‰ (6.4.2.5). A fluid of this composition is isotopically similar to the magmatic-like host fluids (Frey et al., 1976; Table 6-6). However, the $\delta^{18}\text{O}_{\text{Fluid}} / \delta\text{D}_{\text{Fluid}}$ plot shows that the $\delta^{18}\text{O}_{\text{Fluid}}$ signatures within the VF vary from approximately 0 to 3.5‰ (Figure 6-22). Frey et al (1976) only studied host rock samples and therefore implied that Monte Rosa ‘stewed in its own juices’. However, the variety in $\delta^{18}\text{O}_{\text{Fluid}}$ values in the VF can only be achieved by interaction with an oxygen depleted source. Evidence supports the progressive infiltration of meteoric-derived fluids, which are depleted in $\delta^{18}\text{O}$, into the fault zones. Meteoric fluids are known to infiltrate to depths of approximately 10 km (Nesbitt and Muehlenbachs, 1989); thus it is possible for meteoric derived fluids to have interacted with the VF and to have caused the depletion in $\delta^{18}\text{O}$ of the fault zone minerals.

Within the CCF the minerals record evidence of light fluids which are outwith the range of host rock fluid values. The depletion of δD of the fluids is indicative of interaction of meteoric like fluids and so the CCF interacted with meteoric

derived fluid. Values vary from δD -65 to -130‰ and so infer that the fluids became more meteoric-like during fault zone evolution.

6.4.3 Discussion

6.4.3.1 Fluid flow through faults

Fault zones are conduits for fluid flow throughout the crust with the size and distribution of the damage zone and fault core being the dominant control on what type of permeability structure/fluid flow system exists (Caine et al., 1996). Fault zones are known to act as conduits and or barriers in space and time (Logan & Decker, 1994; Goddard & Evans, 1995; Caine et al., 1996). Permeability and fluid flow are terms which are often interchanged however the existence of permeability does not mean that fluids flowed through the rock. Geochemical reactions within fault zones are generally fluid induced (Wibberley, 1999) and so hydrothermal alteration is usually taken as evidence for the presence of a fluid (Chester et al., 1993; Faulkner et al., 2008; Moore and Rymer, 2007; Wibberley et al., 2007). There are only a few studies that consider what volume of fluids was present in a fault zone, if fluids were always present, and what their presence tells us about faulting conditions (Goddard and Evans, 1995; Gudmundsson, 2001; Hashimoto et al., 2009). The presence, volume and chemistry of a fluid all have important implications for water-rock interactions and fault rock rheology (Wintsch et al., 1995). Thus, understanding the fluid history is critical to understanding fault evolution.

6.4.3.1.1 What stable isotopes tell us

The Virgin and Ciao Ciao Faults:

Timing of water-rock interactions: Disequilibrium between minerals suggests that minerals did not precipitate from or interact with, the same fluid at the same time. The variation in fluid $\delta^{18}O$ values also means that most minerals were precipitated from a fluid of different composition and so could not have interacted with the same fluid at the same time.

Temperature and pressure of fluids within the faults: Fluid inclusion temperatures provide a minimum trapping temperature of $\sim 200^\circ C$ (Table 6-3) for the fault zone fluids and are based on no load pressure during mineralization.

However, to get the best fit curves for the water-rock ratio modelling, a fluid temperature of 260°C for early mineralization in the VF and CCF was required (Figure 6-20). It was only K-feldspar precipitation from the CCF that recorded precipitation from a fluid of ~200°C. Due to fluid-rock interactions occurring after precipitation, quartz and K-feldspar from both faults were reset by a fluid which was at ~200°C, however mineralization is likely to have begun from a hotter fluid. Table 6-3 includes estimates for trapping temperatures depending on the pressure conditions within the fault zones. Trapping temperature 2 (Table 6-3) is based on a fluid pressure of 0.8 kbars; which is the estimated minimum hydrostatic pressure during gold precipitation (Curti, 1987). By using this pressure estimate a pressure corrected trapping temperature of 210-270°C within the VF is calculated (Table 6-3). The temperature used for water-rock modelling correlates with the calculated temperature range of trapping for a hydrostatically pressurised fluid. Therefore these results indicate that during the initial phases of mineralization within the VF and CCF, the fluids are likely to have been hydrostatically pressurised with the maximum hydrostatic pressure being 0.8 kbar. As faulting and exhumation continued the hydrostatic pressure gradually decreased until there was effectively no load pressure acting on the fluids (K-feldspar precipitation) within the fault zones.

Multiple fluids: Along the strike of the faults, differences in fractionation patterns were observed. These differences were in response to localised water-rock interactions with different fluids (Section 6.4.2.4.2 and 6.4.2.4.4) and so is evidence of multiple fluids. Variable chlorite δD signatures in both faults indicate changing fluid sources (Figure 6-19). Lighter δD values imply more meteoric like fluids (Sheppard, 1986) and such light isotopic fluids are typically intersected during exhumation (Jenkin et al., 1994; Uysal et al., 2006).

Fluid volumes:

The Virgin Fault: Microstructures indicate that the order of precipitation was quartz with K-feldspar then chlorite. By assessing the location of calculated fluid composition in equilibrium with these minerals relative to modelled water-rock ratio curves, results imply that water-rock ratios evolved from approximately 1:1 to 1:100. This means that fluids were equilibrating with the rock with time, thus the system became progressively more rock dominated. This is the opposite of

what occurs in an open system (progressively increasing water-rock ratios (Gregory & Criss, 1986). However, the fact that new fluids are being introduced means the system is not completely closed. Therefore the VF is a limited open system whereby only a finite volume of fluid was infiltrated during a deformation event.

The Ciao Ciao Fault: Calculated isotopic compositions of fluids within the foliated cataclasite and central fractured zone of the CCF suggest water-rock ratios of approximately 1:10 i.e. rock dominated conditions. These results are from quartz, K-feldspar and chlorite, which are all associated with rock dominated conditions (Wintsch et al., 1995). Muscovite also exists in the foliated cataclasite of the CCF which is evidence of fluid dominated conditions (Wintsch et al., 1995). The mineralogy of the foliated cataclasite therefore implies switching of conditions between fluid- and rock-dominated. If the system was evolving towards higher water-rock ratios (open system) quartz dissolution would be expected (providing the initial fluid is quartz undersaturated e.g. a meteoric fluid). This is not the case in the foliated cataclasite; therefore the foliated cataclasite was evolving to lower water-rock ratios and so became more rock dominated with time. Fluids of different compositions were being infiltrated and so the evidence indicates that the foliated cataclasite was a limited open system with finite volumes of fluid being infiltrated periodically. The data points on the $\delta^{18}\text{O}_{\text{Fluid}} / \delta\text{D}_{\text{Fluid}}$ plot only come from the foliated cataclasite and the central fractured block for the CCF and so can not be used to assess what the water-rock condition were in the damage zone, breccia or cataclasite. In these rocks no quartz precipitation has occurred and feldspars are altered (Ch 5) suggesting open system behaviour (Janssen et al., 1998). Therefore microstructures combined with oxygen and hydrogen isotopic analyses of the fault zone fluids imply that the damage zone, breccia and cataclasite were open to fluids, whereas the foliated cataclasite was limited open.

6.4.4 Conclusions

- Fluid inclusion studies reveal the former presence of fluids at 180 to 260 °C within both fault zones.
- The initial phase of deformation and mineralization is likely to have occurred at hydrostatic pressures of ≤ 0.8 kbar. This pressure would have gradually decreased during exhumation till there was effectively no load pressure acting on the fluids.
- Hydrothermal alteration in both fault zones has effected the $\delta^{18}\text{O}$ and δD values of quartz, K-feldspar, chlorite and muscovite.
- Isotopic disequilibrium occurs between all minerals in the VF. In the CCF quartz and chlorite may be co-genetic but both minerals are in disequilibrium with K-feldspar. The extent to which each mineral is fractionated from the host is larger in the CCF than VF, indicating a greater degree of disequilibrium between the fluid and minerals in the CCF.
- The faults intersected multiple fluids of different compositions. Both fault zones have interacted with meteoric-derived waters and the CCF records progressively more interaction with meteoric-like fluids than in the VF.
- Isotopic resetting of H in quartz and K-feldspar indicates that after deformation had ceased along the VF it remained open to later influxes of meteoric-derived fluids.
- Across the strike of both faults the quartz $\delta^{18}\text{O}$ value increases within the fault core. The changes in quartz $\delta^{18}\text{O}$ are a result of low permeability within the fault core compared to the host rock and damage zone. Decreased permeability causes the water-rock ratio to decrease which in turn causes the quartz $\delta^{18}\text{O}$ to increase.
- Only finite volumes of fluid intersected the VF and the foliated cataclasite of the CCF during a given deformation event

- The VF and the foliated cataclasite in the CCF evolved towards rock dominated conditions
- The VF and the foliated cataclasite in the CCF may be considered as limited open and experienced cycles of high and low permeability.

7 Discussion

7.1 Fault growth and fluid flow

Fault zones are commonly long lived zones of weakness in the Earth's crust and how they form is relevant to studies in earthquake mechanics and subsurface fluid flow (Martel, 1990). Fault zones can grow by propagation in an intact body of rock or by linkage of pre-existing structures (Crider and Peacock, 2004; Martel, 1990; Martel et al., 1988) and, as a fault evolves, its architecture and hydraulic properties may vary over space and time (Caine et al., 1996; Evans et al., 1997). Fault growth has been studied in relation to individual faults and populations of faults (Ackermann and Schlische, 1997; Granier, 1985; Martel, 1990; Martel et al., 1988; Peacock, 1991; Reches and Lockner, 1994; Segall and Pollard, 1983) and similar studies exist with respect to fluid flow and permeability of a fault zone/population (Cox, 1999; Evans et al., 1997; Evans, 2005; Miller and Nur, 2000; Rojstaczer and Wolf, 1992; Townend and Zoback, 2000). However, there are few studies that have investigated how the hydraulic properties of a fault zone vary during growth and the differences in hydraulic properties that occur depending on whether the fault is active or not. Studies on fault growth have shown that small faults evolve into large ones and studies on fault populations show that small and large faults often coexist and may or may not be active at the same time (Martel et al., 1988; Martel, 1990; Ackermann & Schlische, 1997). Locations where fault populations are exposed, e.g. Passo Moro, are therefore ideal for understanding how the hydraulic properties vary between faults of different sizes and also how the hydrology changes during fault zone/population evolution.

7.1.1 Evolution of fault populations

There are two main hypotheses on how faults evolve within a fault population; these include nucleation and growth through intact rock (e.g. Ackermann & Schlische., 1997) or growth by reactivation and linkage of pre-existing structures (e.g. Martel et al., 1988; Martel, 1990).

Ackermann & Schlische (1997) describe a scenario whereby a large master fault cross cuts the host rock and it is surrounded by an abundance of small faults.

However, adjacent to the master fault there is an elliptical area that contains no small faults. The distribution has been interpreted as resulting from the master fault forming early relative to the other faults. Growth of the large fault was associated with a stress-reduction shadow (which scales with length) in the adjacent rock, preventing nucleation of faults in this area. Outwith the stress-reduction shadow it is thought that the small faults nucleated en masse whenever the critical strain threshold was reached. Within other studies stress shielding has been suggested (Cowie et al., 2000) and this phenomenon has also been illustrated in numerical models (Willemse, 1997).

The model by Martel et al., (1988) and Martel (1990) is based on growth by reactivation and linkage of pre-existing joints. In this model there is a supposedly random distribution of joints of various lengths and joint spacing. In the formation of a compound fault zone Martel (1990) outlined four main stages of development: 1) Opening of joints 2) development of small faults 3) development of simple faults 4) formation of compound fault zones (Fig 4-24). During the growth process the number of active fault zones decreases with deactivation of small faults in the vicinity of the larger faults. In this model it is also believed that a stress shadow developed as the faults got longer and subsequently the small faults within the stress shadow became inactive. Fault growth by this mechanism is widely accepted and has been used to explain fault population patterns in numerous studies (Lahren and Schweickert, 1991; Mollema and Antonellini, 1999; Pachell and Evans, 2002).

In both models for fault growth and population evolution the larger faults are associated with a stress shadow, however the timing of the formation of the small faults differs. Given that fault movement is commonly associated with fluid flow, therefore by providing the relative timing of fluid flow, the timing and growth of faults can be constrained. The timing and sources of fluids can be determined by applying microstructural and stable isotopic analyses to the hydrothermal assemblage; the fluids therefore offer the unique opportunity to date the formation of the small faults, hence distinguishing which mechanism of fault growth was active in an area. This would enable timing of the faults

relative to each other to be confirmed and a hypotheses to be suggested for the hydraulic evolution of an area.

7.1.2 Hydraulic properties of fault zones/populations

The architecture of fluid migration in the Earth's crust is influenced by the spatial and temporal variations in rock permeability, and the evolution of permeability is controlled by the competition between porosity creation and destruction processes (Cox, 1999). Within an individual fault the permeability is heterogeneous (Evans et al., 1997; Wibberley & Shimamoto, 2003). In general the damage zone has an increased permeability compared to the fault core (Caine et al., 1996; Evans et al., 1997); however the permeability of the fault core and the fault zone will vary with consecutive deformation events, as deformation can create new fractures or re-open existing fractures (Cox, 1999) (Balsamo et al., 2010; Caine et al., 1996; Zhang and Tullis, 1998).

In a fault population one or two major flowing structures are usually present, surrounded by a swarm of smaller structures, which support minor amounts of flow (Evans, 2005). Based on a bore-hole study, Evans (2005) showed that approximately 95% of flow was within a single fault zone. Permeable faults are critically stressed; however critical stressing is not sufficient enough to maintain high permeability (Townend & Zoback, 2000; Evans, 2005). Within large faults high permeability is believed to be maintained by semi-continuous incremental slip, whereas in small faults deformation is more episodic (Townend & Zoback, 2000). Within fault zones fluid flow can be highly dynamic over short time scales (< tens to hundreds of years) (Oliver, 2001) and earthquakes can temporarily increase flow rates (Rojstaczer & Wolf, 1992). The earthquakes cause cyclic changes in permeability (Cox, 1999) and result in the flow rates varying from $<10^{-8}$ m/s (average flow rate) to $\geq 10^{-2}$ m/s (co-seismic flow rate) (Oliver, 2001). Some changes are short lived and related to dilational waves generated by the earthquake (Cooper et al., 1965; Eaton and Takasaki, 1959; Liu et al., 1989; Rojstaczer and Wolf, 1992), while others are long term and the reason why is not well understood (Rojstaczer & Wolf, 1992).

7.1.3 Fault growth and fluid flow at Passo Moro

At Passo Moro it has been shown in chapter 4 that the studied faults initiated on pre-existing joints and that they grew by linkage of joints in a similar manner as described by Martel (1990) (Ch 4). In relation to the different stages in fault evolution outlined by Martel (1990), the VF and SF resemble a small fault whereas the CCF are similar to a compound fault zone. I have suggested that neither the VF nor SF could have evolved into the CCF; and this was due to the distribution of pre-existing joints. Within the rock surrounding the VF the joint density was so low that there were no available joints to enable linkage and growth. Conversely, around the SF the joint density is so high that the strain across an individual fault strand would have been so low that building up enough stress to cause failure would have been impossible. Both the VF and SF therefore represent deactivated small faults; their different length and fault-rock types are a result of the original joint density.

Hydrothermal minerals within the VF and CCF were analysed for stable isotopes of hydrogen and oxygen to gain information about the fluid(s) that were flowing through the fault zones. The main minerals analysed were quartz, K-feldspar and chlorite because they were abundant in both fault zones. For each mineral the oxygen and hydrogen signature of the fluid is trapped within the crystal structure during precipitation of the mineral. The closure temperature to oxygen/hydrogen exchange are different for each mineral and so are the mechanisms through which fluids can be trapped within the crystal lattice, the minerals can record information on one or more of the infiltrated fluids. Results from the fault zones indicate that the VF records mineral precipitation from a metamorphic-like fluid (δD -20 and -40‰), followed by later micro-fracturing events with fluids that have δD -65 to -135‰. However, the CCF records mineral precipitation from a fluid with δD -65 to -75‰ and later micro-fracturing events with fluids that varied from -110‰ to -135‰. These results can be interpreted as indicating that soon after chlorite precipitation in the VF, the fault became deactivated. Within the CCF the mineralization associated with the δD -65‰ fluid (and associated micro-fracturing in the VF) is believed to indicate the point when the CCF was able to tap into fluids which were more meteoric. This change in fluid source is possibly associated with evolution from a small fault into a

simple or compound fault zone. As the CCF continued to evolve and be exhumed it continued to intersect isotopically lighter fluids which were recorded by mineralization of chlorite and micro-fracturing in quartz and K-feldspar.

With respect to Martel's model of fault evolution the results from this study would imply that small faults (similar to the VF) can periodically transmit fluids, resulting in mineral precipitation during the period when they are active. However, once deactivated they can still periodically transmit fluids, but it is primarily via micro-fracture networks. Periodic fluid flow by micro-fractures can be explained by the off-fault damage produced from the passing of a dynamic rupture pulse on another fault e.g. the CCF (Faulkner et al., 2011). Mitchell & Faulkner (2009) found that fluid inclusion planes decreased in number with perpendicular distance from the fault and for a fault with ~220 m of displacement, the width of micro-fracturing was approximately 115 m. The VF is within ~100 m of the CCF and thus could preserve micro-fracturing in response to ruptures on the CCF. Earthquakes enhance fluid flow in the vicinity of a rupture (Rojstaczer & Wolf, 1992) and micro-cracking can enable pervasive penetration of fluids into a rock (Brantley et al., 1990). Thus small faults could record fluid pulses associated with deformation on adjacent faults even when the small fault is deactivated. Host rock quartz and K-feldspar from Passo Moro has also been reset in terms of the δD signature (Table 6-5) and implies that the micro-fracturing related to large ruptures

The CCF records no evidence of a metamorphic-like fluid. However since large faults have evolved from small ones, which should have a similar history to the small deactivated faults, it is likely that due to isotopic resetting, a compound fault does not preserve the early fluid flow. The majority of lighter fluids are recorded via micro-fracturing but the extensive feldspar alteration and lack of quartz precipitation (in the damage zone, breccia and cataclasite) indicate that the CCF was open to fluids (Janssen et al., 1998). The fact that the lighter fluids are primarily recorded by micro-fractures therefore indicates that there was a continual supply of fluids (causing alteration of feldspars) but there was periodic fracturing events enabling the lighter fluids to be recorded. The fluids recorded by fluid inclusions in the CCF have a signature of δD -110 to -135‰ and are therefore essentially meteoric (local meteoric waters today are δD -151‰).

Results from the CCF and VF therefore indicate that both fault zones have recorded fluid flow events. The δD signatures recorded by the VF are heterogeneous, whereas those recorded by the CCF are homogenous. This has been interpreted as being a result of numerous fracturing and fluid flow events in the VF associated with small volumes of fluid which results in partial isotopic resetting of quartz and K-feldspar. However, in the CCF there are numerous fracturing and fluid flow events but the volume of fluid flowing through the system is large, and causes complete isotopic resetting of quartz and K-feldspar.

7.1.4 A model for fluid flow associated with faults that grow by linkage of pre-existing joints

The proposed model for fault and fluid evolution (Figure 7-1) is based on results from this study. The model assesses how the fluid signature and fluid flux change with time during fault and fault population evolution. It is assumed that an entire fault population is exhumed together. Therefore the crustal block that the faults are within will intersect fluids of a similar composition at the same time, but whether the fluid is recorded or not by the fault will differ. The different steps within the model represent fault deactivation after formation of (1) a small-, (2) simple-, (3) and compound fault zone. With respect to the model the y-axis is fluid flux and the x-axis is time. An increase in flux signifies an intrusion of a finite volume of fluid into a fault, but with no implication for what volume of fluid was intruded. Where the flux lines are connected by a horizontal line, the horizontal line represents continual fluid flow i.e. an open system. While the fault is active the fluid may be recorded by precipitation or recrystallization of minerals and/or fluid inclusions; however, when the faults are deactivated, the main mechanism of recording the fluid signature is by micro-fracturing and healing.

Stage 1 and 2 of the model shows that although a simple fault zone has accumulated more slip than a small fault; hydraulically the small and simple fault zones behave in a similar way (Figure 7-1). Within small and simple faults fracturing is associated with the intrusion of finite volumes of fluid into the fault and thus, the fluid related with each of these events is likely to be recorded. However, the array of fluid compositions that occur in between fracturing events

will not be recorded as a result of fault- and fracture sealing (Brantley et al., 1990; Claesson et al., 2007; Eichhubl and Boles, 2000; Sibson, 1986; Wintsch, 1998). For continuous flow to occur high permeability must be maintained, which in turns implies continual faulting/incremental slip (Townend & Zoback, 2000). Within a fault population, the faults which are oriented optimally within the stress field grow more rapidly and thus the majority of deformation is concentrated onto a few faults (Martel, 1990; Martel et al., 1988; Walsh et al., 2003). Some of the smaller faults may be critically stressed, however this is not a sufficient condition for permeability to develop (Evans, 2005) and permit continual fluid flow and mineral precipitation. Large faults are also associated with an abundance of weak minerals, enabling slip to occur more easily (Jefferies et al., 2006a; Tembe et al., 2010; Wintsch et al., 1995). It is therefore unlikely that a small or simple fault zone in the vicinity of a weak compound fault would be experiencing continual faulting and fluid flow.

Stage 3 in the model shows how fluid flow changes as a fault evolves from a small fault into a compound fault zone. Initially when the fault is small only periodic pulses of fluid are associated with deformation occur and thus only fluids linked with the fracturing will be recorded. As the fault grows, deformation and weakening continue and once a compound fault is formed, it becomes a site of localised deformation (Ackermann and Schlische, 1997). This results in the fault being active semi-continually and thus the fault would be semi-permanently open to fluids (Evans, 2005). This would also be associated with periodic earthquakes enhancing fluid flow and these events are represented by spikes in fluid flux during the period of continual flow (Figure 7-1). Due to the pervasive and continual flow of fluids, the minerals will to variable extents (dependent on individual mineral) be isotopically re-equilibrating with the fluid. Therefore, due to isotopic resetting, the minerals are more likely to record the most recent fluid. This means that small and simple faults may record an array of fluid compositions that the faults intersected during exhumation, whereas compound faults will only record the last pervasive event.

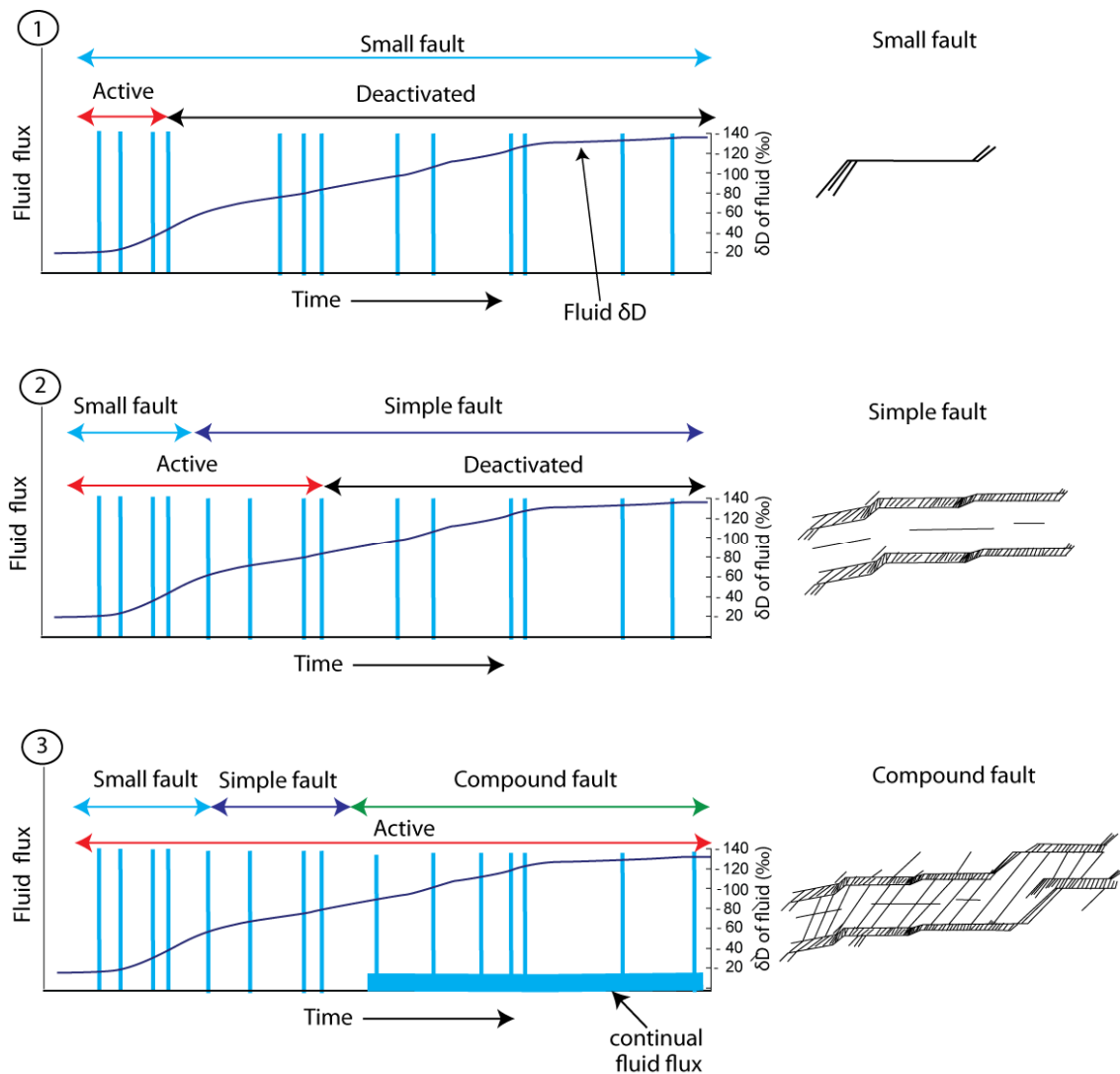


Figure 7-1: A conceptual model for fault population and fluid evolution. The three scenarios highlighted represent the three types of fault that can occur in a fault population. The graph associated with each fault shows the period of fault activity, if or when the fault evolved into a larger fault, when the fault deactivated, and the associated fluid regime that prevails throughout the lifetime of the fault population. Fault image modified from Martel (1990).

7.2 Effects of core development on fault strength

As fault zones evolve in space and time they accumulate deformation and the faults evolve in terms of their architecture, mineralogy, deformation mechanisms and fluid content. The two main types of deformation mechanisms are mechanical and chemical breakdown. Mechanical deformation (fracturing and cataclasis) typically increases permeability, whereas chemical breakdown (dissolution-precipitation or recrystallization) affects the grain size and the bulk fault rock composition. Changing the grain size and composition of a rock has knock-on effects to the rock strength and rheology (Fitz Gerald and Stünitz, 1993; Tullis and Yund, 1985; White, 1979; Wintsch et al., 1995) and thus affects

how a fault will deform and evolve. As well as grain size and composition the fabric within a rock has a significant control on rock strength (Boulton et al., 2009; Ikari et al., 2011; O'Hara, 1994), therefore the destruction or formation of fabrics will also affect the fault strength and the subsequent evolution of the fault.

7.2.1 Mechanical deformation processes

The mechanical deformation processes occurring within a fault zone are fracturing and cataclasis. The main fault properties that are affected by mechanical deformation are grain size and permeability. Fracturing and cataclasis break the rock up into smaller pieces, causing the grain size to reduce (Blenkinsop, 1991). Fine grained material is weaker and can be deformed more easily by granular flow/cataclasis (White, 1979; Tullis & Yund, 1985; FitzGerald & Stunitz, 1993). Therefore as deformation proceeds and grain size decreases, there is likely to be a switch in deformation mechanism from fracturing to cataclasis (FitzGerald & Stunitz, 1993).

Fracturing within fault zones result in an increase in permeability (Mitchell and Faulkner, 2008). Compared to host rock it is often found that the damage zone has increased permeability while the fault core has decreased permeability (Evans et al., 1997; Faulkner et al., 2010) (Figure 7-2). The latter is due to the decreased grain size of the core material compared to the host-rock, enabling closer packing of the particles, thus decreasing the permeability (Crawford et al., 2008). However, although the bulk permeability of the core is reduced, the process of cataclasis causes fracturing and dilation and thus could create temporary permeable pathways for the ingress of fluids (Wibberley, 1999; Jefferies et al., 2006a). Increased permeability within a fault zone promotes fluid flow and fluid-rock interactions (Wintsch et al., 1995), thus mechanical deformation is intimately linked with chemical processes (Figure 5-30). Mechanical deformation exposes fresh surfaces and therefore the amount of mechanical breakdown that occurs can affect the fluid-rock ratio within the fluid-rock environment.

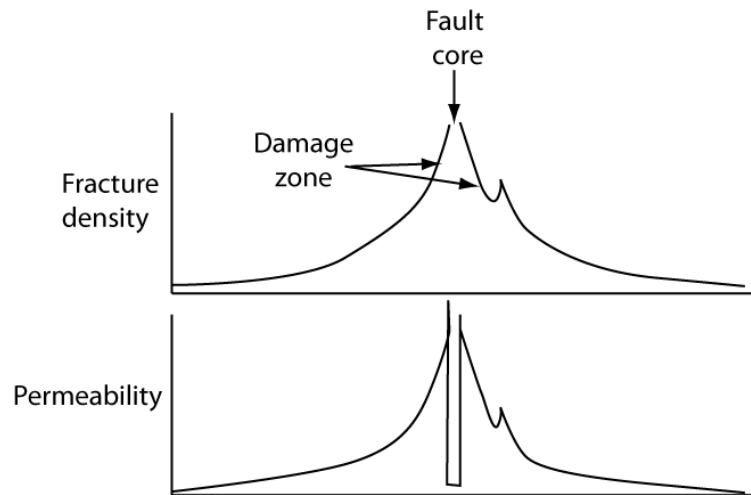


Figure 7-2: The effect of fracturing on permeability within a fault zone. Damage zone has enhanced permeability relative to the host while the fault core has decreased permeability. From Faulkner et al., (2010).

7.2.2 Chemical processes

Fluid-rock reactions have been extensively studied in granitic rock exhumed from seismogenic depths, with the most commonly reported hydrothermal minerals being K-feldspar, quartz, chlorite and muscovite (Evans & Chester., 1995; Wibberley, 1999; DiToro & Pennacchioni, 2005; Faulkner et al., 2008; Kirkpatrick et al., 2008; Mittempergher et al., 2009). K-feldspar and quartz are framework silicates, while chlorite and muscovite are sheet silicates; and these two types of mineral have opposing effects on fault strength. K-feldspar and quartz result in fault strengthening, whereas chlorite and muscovite cause fault weakening (Wintsch et al., 1995; Wibberley, 1999). The proportion of these minerals within the host rock and fault rock and whether a fabric is present or not will therefore govern the bulk strength of the fault rock (Crawford et al., 2008; Ikari et al., 2011; Moore and Lockner, 2011; Takahashi et al., 2007; Tembe et al., 2010).

Fluid-rock reactions can occur by direct replacement of one mineral by another, by dissolution-reprecipitation or by nucleation and growth of a new phase. Dissolution-reprecipitation and nucleation of new minerals result in a change in the average grain size and shape, thus affecting the strength of the rock (White, 1979; Tullis & Yund, 1985; FitzGerald & Stunitz, 1993).

The reaction of greatest significance within granitic fault zones is the transformation of K-feldspar and or albite to muscovite (Equation 11; Equation

12). These reactions are reversible and so depending on the conditions feldspar can be replaced by muscovite or vice versa. In general muscovite will precipitate in acidic fluid conditions, while K-feldspar will form in near neutral conditions (Hemley & Jones, 1964; Wintsch, 1975; Wintsch et al., 1995).

Equation 11: K-feldspar = Sericite (muscovite) + quartz



Equation 12: Albite = Sericite (muscovite) + quartz



The stability fields of feldspar and muscovite have been studied by a number of authors (Hemley, 1959; Hemley and Jones, 1964; Wibberley, 1999; Wintsch et al., 1995) (Figure 7-3). The results show that as the ratio of alkalis to hydrogen ions vary, either muscovite or feldspar will precipitate. The ratios can be changed by either deformation, which increases the amount of reactive surfaces, and/or by the intrusion of meteoric water, which increases the amount of H^+ within the system (Wintsch, 1975; Wintsch et al., 1995). Depending on the amount of new surfaces exposed and the volume of fluid intruded there are three main paths by which the fluid could evolve through time (Figure 7-3).

1. Deformation associated with a small volume of fluid. The availability of alkalis is greater than H^+ , indicating a rock dominated system which promotes K-feldspar precipitation.
2. Deformation and large volume of fluid. The increased volume of fluid results in the system being fluid dominated (H^+ rich) causing muscovite precipitation. As the fluid is used up, the system evolves to be rock dominated causing K-feldspar precipitation.
3. Permanent supply of fresh unreacted fluid. This enables a fluid dominated system to prevail causing a prolonged period of muscovite precipitation.

This shows that depending on the fluid-rock conditions within a fault, different minerals can precipitate and thus have varying effects on fault rock strength and

rheology. Therefore as a fault evolves, the fluid-rock conditions can also evolve, resulting in changing mineralogy and fault strength with time.

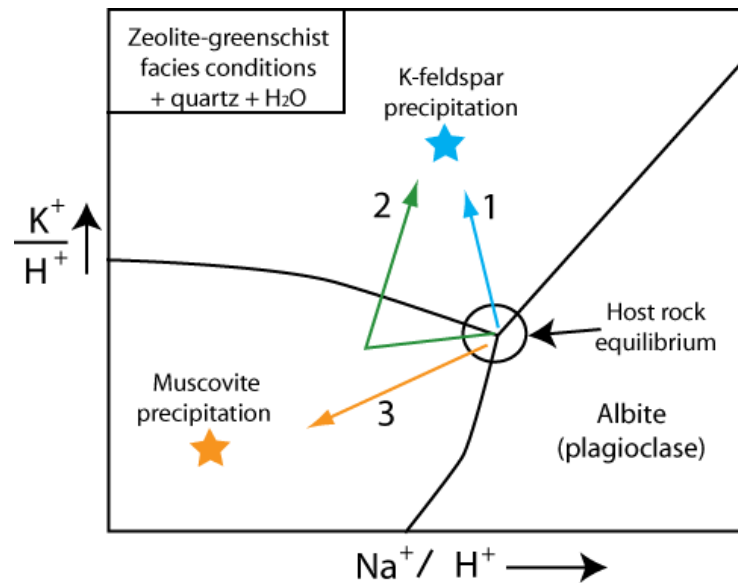


Figure 7-3: Fluid activity diagram showing mineral stability of muscovite and feldspar. Paths 1, 2 and 3 represent different fluid-rock ratio conditions. 1) Rock dominated conditions = K-feldspar precipitation 2) Fluid dominated conditions that evolve to rock dominated conditions = muscovite precipitation followed by K-feldspar precipitation 3) Fluid dominated conditions = muscovite precipitation. Fluid activity diagram modified from Wintsch et al., (1995).

7.2.3 Fault core evolution at Passo Moro

At Passo Moro the VF and CCF are both affected by fracturing and cataclasis, but the chemical reactions that took place are different. K-feldspar, quartz and chlorite are common within the VF, while muscovite is prevalent in the CCF. Microstructural observations show that in the VF and CCF, core formation occurs by several steps, which have either weakening or strengthening effects (Figure 7-4). Strengthening of the fault core tends to result in fracturing (Wintsch, 1998) while weakening processes promote cataclasis.

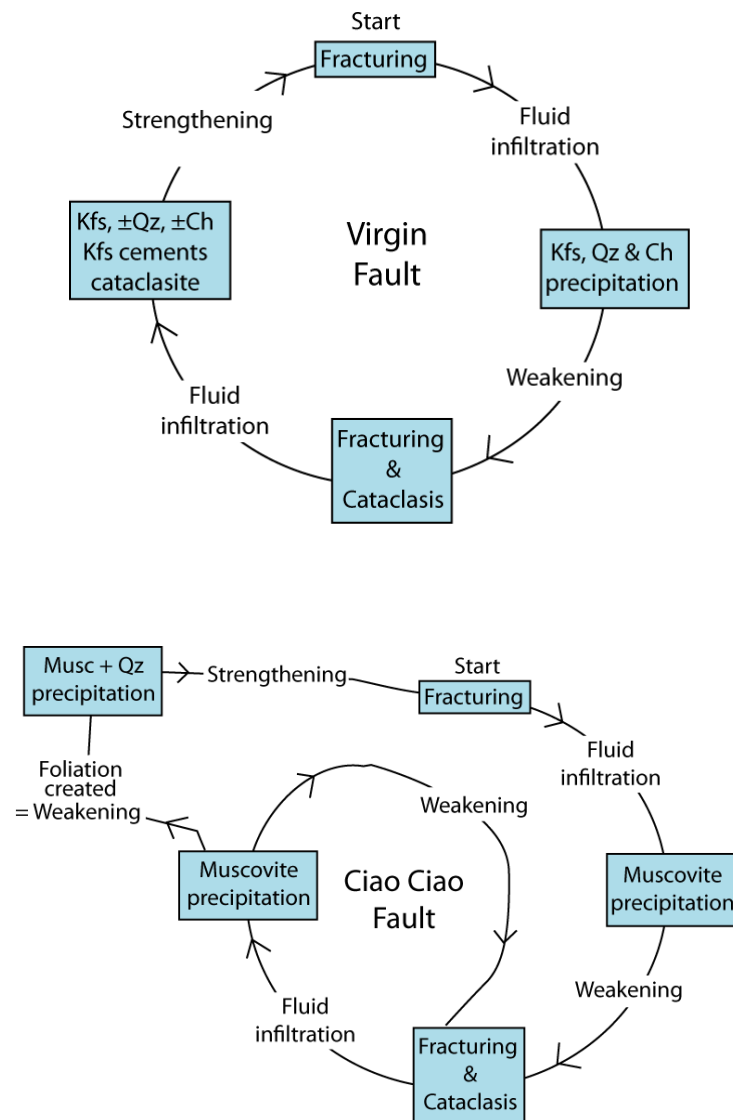


Figure 7-4: Illustration of the steps that occur during core formation within the VF and CCF. In the VF the process is cyclical while in the CCF weakening by muscovite precipitation continues until proportions are high enough to form an interconnected network. The processes are likely to continue in both faults until deactivation or the fault evolves. Kfs = K-feldspar, Qz = quartz, musc = muscovite, ch = chlorite.

Mechanical deformation within the VF increases permeability and promotes fluid-rock interactions. Due to low permeability and/or a small volume of fluid intruded, the system is rock dominated promoting K-feldspar, quartz and chlorite precipitation (e.g. option 1, Figure 7-3). The proportion of phyllosilicates to feldspar and quartz is not affected greatly by these reactions (Figure 5-4) and therefore in terms of mineralogy the strength is not affected significantly. However, reactions cause a reduction in grain size, causing weakening of the rock. This promotes cataclasis, which enables more fluids to intrude and more reactions to occur. K-feldspar proportions increase and the

cataclasite is cemented causing the rock to acquire a strength similar to that of the host rock (Wintsch, 1998), which in turn promotes fracturing (Figure 7-4).

Fracturing increases permeability in the CCF and a large fluid intrusion creates a fluid dominated regime and precipitation of muscovite (e.g. option 3, Figure 7-3). Due to the high volumes of fluid, feldspar alteration and quartz dissolution are also promoted (Janssen et al., 1998). Alteration causes grain size reduction and combined with muscovitization, both processes cause weakening. Weakening promotes cataclasis which increases permeability and continued fluid dominated conditions cause muscovitization to continue. This process will continue until enough muscovite has been precipitated to enable an interconnected network of phyllosilicates/ a foliation to develop (Figure 7-4). On short timescales the foliated cataclasite can act as a fluid barrier (Jefferies et al., 2006b) preventing refreshment of the fluids within the foliated zone. Closing of the area to fluids promotes quartz precipitation, which strengthens the fault rock and may lead to fluid over pressuring and failure (Jefferies et al., 2006b).

7.2.4 Implications for fault strength during evolution

The mineral reactions observed in the VF and CCF are completely different and consequently the two faults must have been characterised by different strength and evolution. The strength of a rock is primarily related to composition. The weaker minerals can withstand less stress resulting in failure whereas a rock composed of stronger minerals will remain intact. A rock that has been cemented with K-feldspar can have a strength similar to that of the host (Wintsch, 1998) while sericitized rock is significantly weaker. Therefore a sericitized rock will fail at a lower applied stress than a K-feldspar cemented rock (Figure 7-5a) and so, small faults similar to the VF are going to be stronger and less likely to fail compared to a large weak fault like the CCF.

Fluid-rock ratios have a strong control over what the fluid activity of a system is and subsequently what minerals will be precipitated (Figure 7-3). As a fault grows it accumulates damage and increased fracturing results in increased permeability (Figure 7-2). This enables more fluids to be intruded into the fault zone and thus changes the fluid-rock ratio and mineral stability. Based on Martel's model of fault growth (Martel., 1990), the three fluid activity options in

Figure 7-3, could represent the fluid conditions associated with each stage of growth in Martel's model. In this case the 3 options described above would correlate to a small, simple and compound fault zone. This implies that as a fault evolves, permeability increase, causing a larger volume of fluids to be intruded, causing the mineralogy to change and weakening to occur (Figure 7-5a).

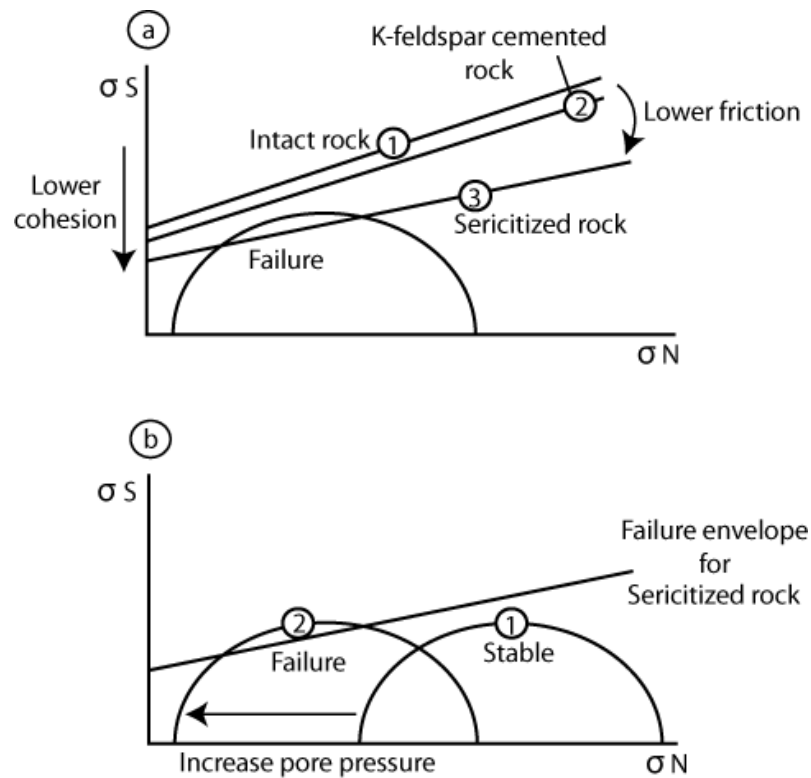


Figure 7-5: Mohr diagrams showing changes that occur as a result of fluid-rock reactions. a) Sericitization of the rock results in replacement of strong K-feldspar and albite being replaced by weaker muscovite. b) The foliation created within the fault rock acts as a seal to migrating fluids. The fluid-rock conditions continue to cause mineral precipitation which results in an increase in pore pressure and eventually failure of the rock.

In studies of fault populations, the faults which are optimally oriented for growth within the applied stress field, will grow faster than faults with a less favourable orientation (Ackermann & Schlische, 1996; Walsh et al., 2003). With continued growth, deformation is localised onto fewer faults causing the deactivation of smaller faults (Martel et al., 1988; Martel., 1990; Walsh et al., 2003). The faults that are optimally oriented for growth will therefore evolve more rapidly in terms of fluid-rock conditions; hence they will become weaker quicker. The death of smaller faults is therefore likely to be in part controlled by the strength of the faults within the population, as a large weak fault will be more likely to fail than a small strong fault (Figure 7-5).

7.2.4.1 Fault core evolution in the CCF and implications for the strength of mature faults

Evolution of the fault core in the CCF occurs by continual fracturing, cataclasis and fluid flow promoting muscovitization (Figure 7-4). As alteration of feldspars progresses the proportion of muscovite (sericite) within the rock increases until an interconnected network of muscovite (i.e. a foliation) is formed. Within the CCF, the foliated area is the only location where quartz microveins have been precipitated and indicates that conditions changed in this area. On short timescales the foliation planes can act as a fluid barrier (Jefferies et al., 2006b) preventing refreshment of the fluids within the foliated zone. Closing of the area to fluids promotes quartz precipitation, and may lead to fluid overpressuring and failure (Jefferies et al., 2006b) (Figure 7-5b). This means that although the creation of a foliation will significantly lower the strength of the fault rock (O'Hara, 1994; Wibberley, 1999; Ikari et al., 2011); the foliation also prevents fluid refreshment and thus may promote overpressuring and failure (Figure 7-5b).

The strength of a rock is in part controlled by fabric and the composition of the rock, with mineral alignment and high proportions of clay and or phyllosilicates being associated with weak fault rocks (Takahashi et al., 2007; Crawford et al., 2008; Boulton et al., 2009; Tembe et al., 2010; Ikari et al., 2011; Lockner et al., 2011). Failure of the rock in response to foliation creation therefore disrupts the foliation and increases the quartz content of the cataclasite (Boulton et al., 2009). Both effects will therefore increase the strength of the cataclasite (Ikari et al., 2011) and thus increase the strength of the fault compared to the pre-failure conditions. Failure and cataclasis will create new permeable pathways into the foliated cataclasite enabling the ingress of chemically active fluids (Jefferies et al., 2006a). Therefore, muscovitization can progress again leading to the foliation being reformed. Processes of foliation creation and destruction in the core will therefore be cyclic and thus the core strength will periodically increase and decrease with time.

7.2.4.2 A model for evolution of fault strength with time and during evolution

The results from this study show that small faults record different fluid-rock reactions to large faults and consequently the strength of the faults are significantly different (Figure 7-5a). As faults within a population grow, smaller faults will be deactivated while larger faults will continue to grow. The evolution of fault strength during the lifetime of a fault population will therefore differ for a small, simple or compound fault. After a fault has deactivated, movement on the fault ceases, but if the fault is within the damage zone of a larger fault, it may transmit fluids in response to deformation on a larger adjacent fault.

The proposed model for fault strength evolution is shown in Figure 7-6 and it is separated into three stages, which represent different periods of fault evolution in Martel's model (1990). The model not only shows how fault strength changes during growth from a small fault to a compound fault but also how the strength of a fault varies after deactivation.

The fault strength during activity is indicated by the red line (Figure 7-6). Faults are known to have initiated on pre-existing joints and so the initial strength is reduced compared to host rock. Fracturing and/or cataclasis will cause the strength of the rock to decrease and so the initial phase in faulting is weakening. The associated K-feldspar precipitation causes strengthening of the rock to a similar value as the host (Wintsch, 1998) and then fracturing will decrease strength again. Small faults do not evolve past this stage and so the final strength of the fault is high due to feldspar precipitation. Evolution to a simple fault zone increases permeability and consequently both muscovite and k-feldspar precipitate (option 2 Figure 7-3). The increased proportions of muscovite causes gradual weakening of the fault zone, however K-feldspar precipitation results in the rock strength being increased to a similar value as the host. Only when a compound fault is formed does significant weakening occur. The large volumes of fluid enable continual muscovitization and weakening of the fault and when a foliation is developed there is another drop in fault strength. However, foliation development results in quartz precipitation and failure. Quartz precipitation and disruption of the foliation increase the

fault strength but also enable the ingress of fresh reactive fluids promoting muscovitization. The fault will then experience cycles of increased and decreased strength as muscovite is precipitated, a foliation develops, failure and quartz precipitation occurs, and the foliation is reformed.

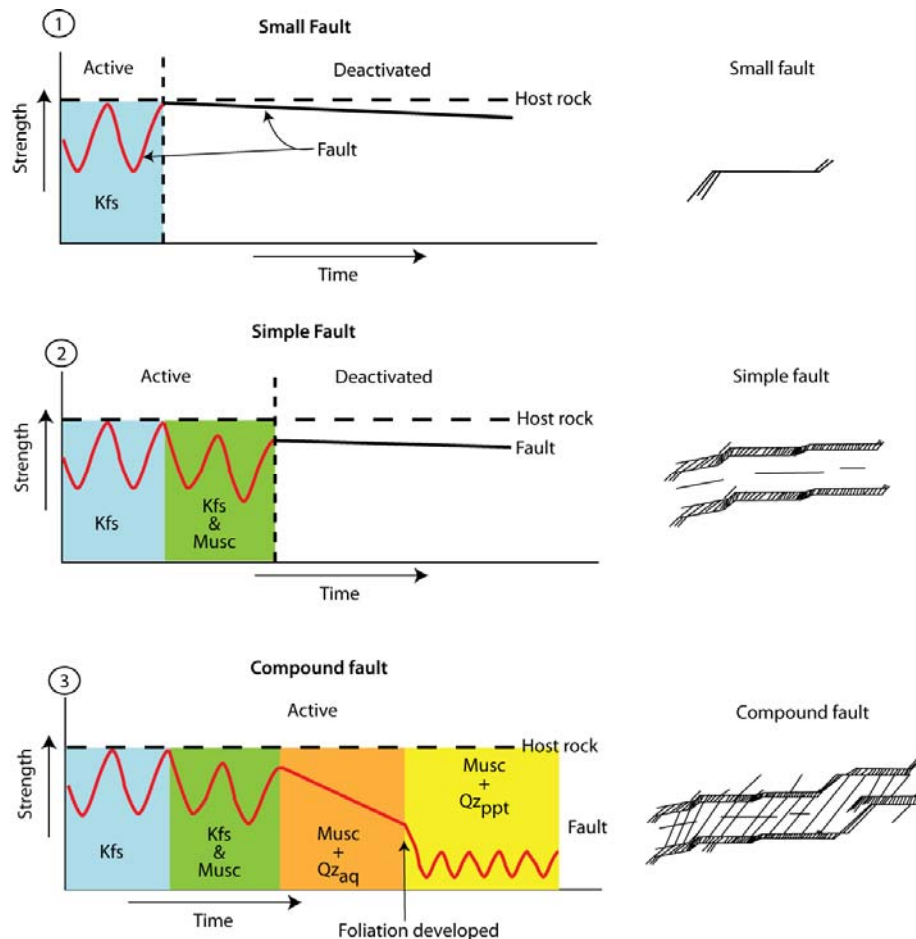


Figure 7-6: Fault core strength changes during fault growth and fault population evolution. The main strength fluctuations occur during fault activity. Kfs = K-feldspar, Musc = muscovite, Qz_{aq} = Quartz in solution, Qz_{ppt} = Quartz precipitation.

Such changes in fault strength as a fault grows will have implications for the nucleation of earthquakes. Rock composition and fluid pressurization can affect earthquake ruptures (Cappa, 2011; Crawford et al., 2008; Ikari et al., 2011; Tembe et al., 2010). Fluid pressurization can act as a weakening mechanism, which exerts a critical control on earthquake rupture (Cappa, 2011), while the fabric and composition of cataclastic rock can determine whether a rupture will be seismic or aseismic (Ikari et al., 2011 and references therein). It is therefore critical to combine the stage of fault evolution with fluid conditions and microstructural evolution to understand what processes are occurring and how the changes may ultimately affect earthquake dynamics.

8 Conclusions and further work

The main aim of this study was to understand the nature of fluid-rock interactions at seismogenic depths in order to provide an insight on the effects of fluids on faults. My objectives were to provide constraints on the temperature, source and volumes of the fluids that interacted with the fault-rock; the nature of the rock-fluid reactions and their dependence on fault architecture and size; and on the effect/s of the products of fluid-rock interactions on fault zone evolution. These constraints were determined employing a series of methods including a detailed field mapping of Passo Moro, a careful study of the geology of the area, a field description of three newly identified faults (Virgin, Spaghetti and Ciao Ciao Fault), a microstructural description of the VF and CCF, and a fluid inclusion and isotopic study of the host rock, VF and CCF. A summary of the main conclusions are as follows:

- Field mapping at Passo Moro has provided a detailed description of the host rock and distribution of joints and faults within the field area. Logging of the host rock has shown that there are three main rock types, granite gneiss, metasedimentary rocks and amphibolite, and the host rock has variable grain size, texture, structure and contains minor intrusions.
- The granite gneiss has been divided into three units based upon location and internal variability: Upper Gneiss, Variable Upper Gneiss and Lower Gneiss.
- The variations in host rock properties affect the mechanical properties of the rock and consequently affect the density of the early formed 010° joints.
- The early formed joints acted as mechanical boundaries for later forming joints and faults, and faults acted as a mechanical boundary for later forming joints.
- Field and microscopic analysis has confirmed the main characteristics of the three studied fault zones. All faults cut granite gneiss, are right

- lateral strike-slip faults, and fluid-rock alteration occurs throughout the faults. The VF is 70m long and has several centimetres of displacement; the SF is ~220 m long and has several centimetres of displacement; and The CCF is at least 10 km long and has 200 m of displacement.
- Microstructural and stable isotopic analyses indicate that the fault zones were exhumed to the Earth's surface from the seismogenic zone.
- The faults at Passo Moro formed by reactivation of pre-existing joints and grew in a similar way as described by Martel (1990) whereby small faults link to form simple fault zones, which connect to form compound fault zones. The VF and SF have not grown beyond a small fault and so are therefore considered as a deactivated small fault while the CCF would be akin to a compound fault zone.
- The VF is isolated in two dimensions and is composed of a damage zone and fault core, whereas the SF contains several closely spaced fault strands which are primarily composed of damage zone rock. The differences in their fault architectures are due to the distribution of pre-existing structures throughout the field area, created by host rock variations.
- Fluidised ultracataclasite in the CCF indicates that at least part of the slip may have been accommodated seismically.
- Hydrothermal minerals are indication of fluid flow through all fault zones during fault activity. Hydrothermal alteration occurs to the greatest extent within the fault core of the VF and CCF.
- K-feldspar precipitation is common throughout the VF and indicates rock-dominated conditions, low permeability and fault rock hardening. These conclusions are based on the fact that in order to precipitate K-feldspar, a fluid needs to be supersaturated in K^+ and at near neutral pH conditions.
- Fe- and Mg-rich chlorites in the VF indicate that there were at least two fluids of different compositions within the fault.

- The dominant reaction in the CCF is sericitization of feldspars, which indicates a fluid-dominated system, acidic conditions, and weakening of the fault rock.
- Grain size reduction within the VF and CCF occurs by mechanical and chemical breakdown.
- The different fluid-rock geochemical reactions in the VF and CCF are controlled by the evolutionary stage at which the two faults were at when they interacted with the fluids, the permeability of the rock and the volume of fluid infiltrating the fault zone.
- Fluid inclusions show that the fluids were between 170-260°C and had a very low salt content, hence they were essentially meteoric.
- Mineralizing fluids within the VF are metamorphic-like while mineralizing fluids in the CCF are more meteoric-like.
- Stable isotopes indicate that 1) fluid-rock interactions occurred at different times for different minerals within the VF and CCF 2) the faults intersected multiple fluids of different compositions 3) fluids became more meteoric-like with time 4) only finite volumes of fluid entered the fault zone during a given deformation event 5) the faults evolved towards rock dominated conditions 6) the VF would be considered as a limited open system while the CCF was open 7) the faults experienced cycles of high and low permeability.
- When compared with Martel's model (1990), field and isotope results indicate that small faults do become inactive while other faults continue to grow. However, small faults will continue to transmit fluid via micro-fracture networks that form in response to deformation on a large fault, enhancing fluid flow throughout the surrounding rocks.
- Fluid-rock conditions ultimately control the type of fluid-rock reactions and therefore whether hardening or weakening of the fault zone will occur.

- Changes in fluid-rock conditions are strongly affected by deformation and hence growth of a fault zone. Therefore as a fault evolves, fluid-rock interactions change and the mineralogy of the fault rock changes.
- Evolution of a small fault to a compound fault is associated with cyclic weakening and strengthening events. Once fluid flow is semi-continuous, muscovitization can proceed uninterrupted causing continual weakening of the fault rock. When mica proportions are high enough a foliation will form causing significant fault weakening. However, foliation development promotes quartz precipitation and overpressurising of the pore fluid which results in failure and temporary strengthening of the core.
- Results from this study have implications for earthquake rupturing, the evolution of faults and fault populations and the hydrology of a fault zone and a fault population. These results should be of interest for mining and mineralization studies, fault population studies for oil migration, and studies on the storage of nuclear waste in crystalline rock.

8.1 Further work

After carrying out this investigation of fluid-rock interactions in fault zones from seismogenic depths a number of questions have been answered but a number of questions/queries have also been raised.

This work leaves unanswered the evolution of faults as the exhumation of rocks now exposed at Passo Moro proceeded. The time of exhumation could be constrained by using a combination of thermochronological techniques, such as fission track and (U-Th)/He methods in zircon and apatite which would provide time-Temperature paths from ~200 to 70 °C (Ehlers and Farley, 2003) . The metamorphic history of the area is well understood, however timing of exhumation of these rocks through the shallow crust is poorly known (Amato et al., 1999).

The CCF has only been mapped for 800 m along strike, yet it is estimated to be approximately 10 km long. To gain a better understanding of how this fault evolved, more information are needed about variability of the fault along strike,

the rocks that intersects, the fault architecture and its displacement. The observations carried out during this study indicate that faults at Passo Moro initiated on pre-existing joints; if the CCF cuts different mechanical rock units, however, it may have evolved by different mechanisms or different fluid-rock reactions in different areas. A better knowledge of the characteristics of the CCF would provide insights on possible along strike variations of fault-fluid-rock relationship and on the evolution of fault populations.

At Passo Moro the faults have initiated on joints, and evolved in a manner similar to that described by Martel (1990). Within this study only small and compound fault zones were analysed. To get a clearer picture of how fluid-rock interactions vary during fault evolution it would be of use to return to Passo Moro and locate a simple fault zone. In this way all the three cases presented by Martel (1990) would be studied in the field, providing a complete test of the model.

Within the VF, K-feldspar precipitation is pervasive throughout the fault zone and it is related to the early phases of faulting and fluid flow within the fault system. By carrying out Ar-Ar dating on the K-feldspar veins the first fluid flow events associated with faulting could be dated. This would enable an estimation of the timing of fault initiation at Passo Moro. By combining this information with an analysis of the local and regional stresses, faulting in the area could be related to the large scale tectonic evolution of the western Alps.

Studies of the fault core in the VF indicate that quartz microveins were one of the earliest formed structures and that grain size reduction was by bulging recrystallization under low temperature and high strain conditions. In the CCF the reactions occurring are different, quartz is randomly distributed throughout the damage zone rock and breccia, and quartz deforms by cataclasis. Results from Hirth & Tullis (1994) imply that the differences in the cataclastic texture of quartz are a result of the transitions that occur across the brittle-ductile transition. However, if the pre-failure fault rock is of different strength this may also result in different textures. Therefore deformation experiments on a rock-dominated and fluid-dominated rock systems could better assess how the reactions influence deformation mechanisms within a fault zone.

The fluids within the fault zones have primarily been analysed using stable isotopes of oxygen and hydrogen and a limited amount of fluid inclusion data. To better constrain the fluid temperature, composition and evolution a larger number of samples from the CCF could be collected and more stable isotope and fluid inclusion studies carried out. As well as this, Raman microscopy would also enable the composition of the fluids to be analysed and thus the differences between host rock fluids and primary and secondary fluid inclusions within the precipitated quartz be determined.

Many of the differences in the fluid-rock interactions are a result of changing fluid-rock conditions of which permeability is one of the primary controls. By characterising permeability across strike in both fault zones the relationship between changes in mineralogy proportions with permeability could be assessed.

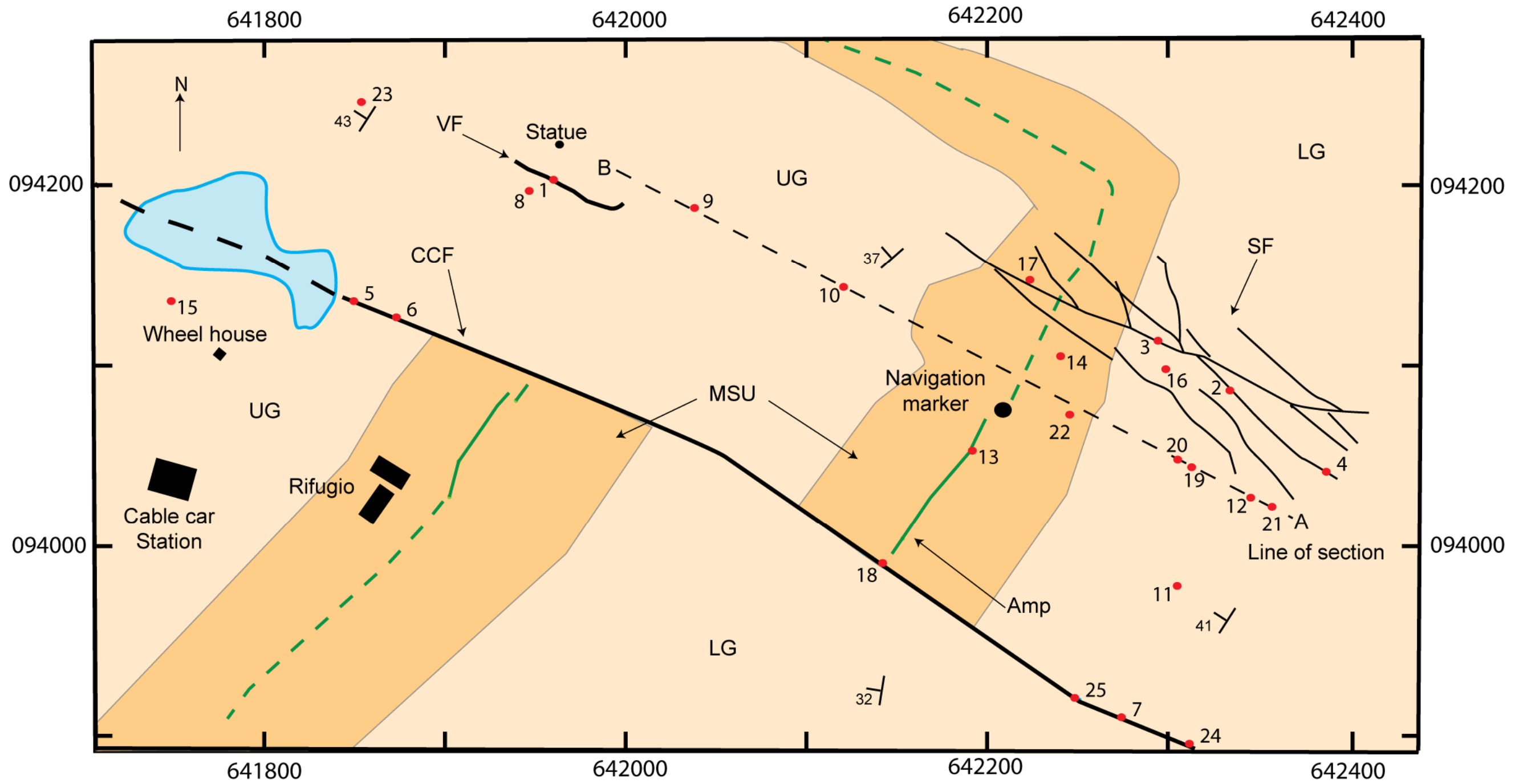
Within the fault core of the CCF there is a transition from cataclasite to foliated cataclasite. The proportion of muscovite is higher in the foliated cataclasite compared to the cataclasite and host rock, and quartz microveins occur in the foliated cataclasite. Although increased muscovite proportions and foliation creation cause weakening of the fault, quartz precipitation is likely to result in strengthening. To assess the effect of quartz precipitation, strength tests could be carried out on the fault rock. By sampling the quartz rich portions of the foliated cataclasite and comparing it to an area where the foliation is apparently unaffected by quartz precipitation, this would enable the effect of foliation disruption and quartz precipitation to be quantified in terms of fault strength.

Various hypotheses have been suggested within this study. To test them a similar study on fault-fluid-rock evolution could be carried out in the Sierra Nevada, California. This is the site where Martel (1990) developed the model on fault evolution and at this site there are small, simple and compound fault zones. The fluid-rock evolution could therefore be assessed for all stages of Martel's and the Passo Moro fault evolution model. The tectonic evolution of the Sierras is different to that of Passo Moro (subduction followed by strike-slip faulting as opposed to subduction followed by continental collision) and therefore results would also indicate if the fluid-rock evolution that occurs in Passo Moro is typical to other tectonic settings.

Appendices

Appendix 1

Locality map for all locations quoted throughout the thesis. Localities are the red dots and locality number is adjacent to the dot. Referencing system used is the CH 1903 co-ordinate system. For descriptions of the geological units see Figure 3-1b.



Appendix 2

Quantitative elemental analysis of samples was carried out by standardised analysis using a Sigma SEM with integrated Oxford Instruments and INCA microanalysis computer software.

Quantitative results for the two chlorites with different birefringence colours.

Purple chlorite	Element	Weight (%)
	O	48.91
	Mg	6.08
	Al	11.35
	Si	10.61
	Fe	23.03
Total		100

Brown chlorite	Element	Weight (%)
	O	51.32
	Mg	10.16
	Al	10.64
	Si	11.56
	Fe	16.32
Total		100

Appendix 3

Oxygen stable isotope data for all samples analysed.

Sample name	Mineral	Yield %	Raw $\delta^{18}\text{O}$	$\delta^{18}\text{O}_{\text{smow}}$ Mineral
Host 3	Kfs	26%	-9.02	12.93
Host 3	Qz	74%	-10.14	11.7
Host 1	Qz	73%	-9.29	12.7
Host 1	Qz	76%	-9.32	12.62
Host 1	Kfs	111%	-12.1	9.5
Host 1	Kfs	10%	-15.13	6.37
Host 4	Qz	68%	-9.3	12.65
VF1	Qz	46%	-8.88	12.98
VF2	Epi	97%	-13.62	8.14
VF2	Qz	91%	-9.54	12.1
VF2	Qz	110%	-9.42	12.2
VF2	Chl	74%	-14.82	6.87
VF2	kfs repeat	127%	-13.5	8
VF2	Kfs	12%	-15.98	5.67
VF3	Qz	80%	-9.48	12.45
VF3	Kfs	21%	-10.57	11.32
VF3	Kfs	137%	-13.09	8.4
VF3	Chl	68%	-15.03	6.67
VF6	Qz	66%	-10.30	11.6
VF4	Qz	60%	-10.1	11.81
VF7	vein Qz	60%	-9.58	12.35
VF7	Kfs	129%	-13.94	7.6
VF7	Chl	98%	-15.78	5.7
VF8	Qz	82%	-10.17	11.74
VF8	Kfs	115%	-12.78	8.76
VF8	Chl	67%	-15.05	6.64
VF5	Qz	72%	-9.55	12.07
VF5	Chl	83%	-15.79	5.8
VF5	Kfs	24%	-12.73	8.8
VF5	kfs	112%	-13.52	8.01
VF12	Qz	61%	-9.52	12.44
VF12	Chl	105%	-16.88	4.6
VF14	Qz	79%	-9.78	12.15
VF14	Chl	83%	-15.48	6.2
VF14	kfs	56	-8.19	13.5
VF14	Kfs	117%	-13.46	8.1
CC2-Br	Qz	85%	-9.55	12.1
CC2-Br	Kfs	10%	-15.29	6.39
CC2-Cc	Kfs	12%	-16.87	4.74
CC2-Cc	Qz	44%	-11.8	10.04
CC3	Qz	86%	-7.55	14.1
CC3	Qz	76%	-8.26	13.4
CC3	Kfs	121%	-14.73	6.8
CC1	Qz	68%	-9.7	11.9
CC1	Kfs	24%	-11.38	10.48
CC4	Qz	71%	-8.73	12.9
CC4	Kfs	120%	-13.38	8.2

Sample name	Mineral	Yield %	Raw $\delta^{18}\text{O}$	$\delta^{18}\text{O}_{\text{smow}}$ Mineral
CC4	Chl	106%	-16.74	4.7
Epi-001	Kfs	38%	-10.05	11.86
Epi-001	Qz	80%	-10.14	11.78
Epi-001	Epi	111%	-13.38	8.2
Epi-B	Chl	79%	-15.32	6.27
Epi-B	Qz	37%	-11.06	10.81
Qz vein	Qz	70%	-9.55	12.1

Standard data for oxygen analyses. Raw data was plotted against the known value for the standard and a trend line added to the plot. The equation for the line (shown) was subsequently used to calculate the minerals $\delta^{18}\text{O}_{\text{smow}}$ value from the raw value that was measured. The equation for the line differs due to it being recalculated during different analytical sessions. The difference noted is the analytical uncertainty for the standard and these values were used to calculate the average uncertainty for the samples analysed.

Sample	Raw $\delta^{18}\text{O}$	Calculated $\delta^{18}\text{O}$	Known value	Difference	Equation
SES	-11.415	10.44	10.15	0.3	$y = 1.0439x + 22.355$
SES	-11.538	10.31	10.15	0.2	$y = 1.0439x + 22.355$
uwg-2	-15.865	5.79	5.8	0.0	$y = 1.0439x + 22.355$
uwg-2	-15.682	5.98	5.8	0.2	$y = 1.0439x + 22.355$
NBS28	-12.733	9.06	9.58	-0.5	$y = 1.0439x + 22.355$
NBS28	-12.349	9.46	9.58	-0.1	$y = 1.0439x + 22.355$
SES	-11.3	10.56	10.15	0.4	$y = 1.0439x + 22.355$
SES	-11.509	10.34	10.15	0.2	$y = 1.0439x + 22.355$
SES	-11.138	10.73	10.15	0.6	$y = 1.0439x + 22.355$
UWG-2	-15.53	6.14	5.8	0.3	$y = 1.0439x + 22.355$
UWG-2	-15.61	6.06	5.8	0.3	$y = 1.0439x + 22.355$
NBS28	-12.55	9.25	9.58	-0.3	$y = 1.0439x + 22.355$
NBS28	-12.625	9.18	9.58	-0.4	$y = 1.0439x + 22.355$
SES	-11.244	10.62	10.15	0.5	$y = 1.0439x + 22.355$
SES	-11.57	10.28	10.15	0.1	$y = 1.0439x + 22.355$
SES	-11.693	10.15	10.15	0.0	$y = 1.0439x + 22.355$
SES	-11.495	10.36	10.15	0.2	$y = 1.0439x + 22.355$
SES	-11.586	10.26	10.15	0.1	$y = 1.0439x + 22.355$
SES	-11.946	9.88	10.15	-0.3	$y = 1.0439x + 22.355$
SES	-11.755	10.08	10.15	-0.1	$y = 1.0439x + 22.355$
SES	-11.396	10.46	10.15	0.3	$y = 1.0439x + 22.355$
SES	-11.319	10.54	10.15	0.4	$y = 1.0439x + 22.355$
SES	-11.435	10.42	10.15	0.3	$y = 1.0439x + 22.355$
SES	-11.321	10.54	10.15	0.4	$y = 1.0439x + 22.355$
SES	-11.521	10.33	10.15	0.2	$y = 1.0439x + 22.355$
SES	-11.132	10.73	10.15	0.6	$y = 1.0439x + 22.355$

Sample	Raw $\delta^{18}\text{O}$	Calculated $\delta^{18}\text{O}$	Should be	Difference	Equation
SES	-11.797	10.04	10.15	-0.1	$y = 1.0439x + 22.355$
SES	-11.812	10.02	10.15	-0.1	$y = 1.0439x + 22.355$
SES	-11.723	10.12	10.15	0.0	$y = 1.0439x + 22.355$
SES	-11.868	9.97	10.15	-0.2	$y = 1.0439x + 22.355$
SES	-11.963	9.87	10.15	-0.3	$y = 1.0439x + 22.355$
SES	-11.814	10.02	10.15	-0.1	$y = 1.0439x + 22.355$
SES	-11.65	10.19	10.15	0.0	$y = 1.0439x + 22.355$
SES	-12.048	9.78	10.15	-0.4	$y = 1.0439x + 22.355$
SES	-10.308	11.59	10.15	1.4	$y = 1.0439x + 22.355$
SES	-12.161	9.66	10.15	-0.5	$y = 1.0439x + 22.355$
SES	-12.077	9.75	10.15	-0.4	$y = 1.0439x + 22.355$
SES	-12.076	9.75	10.15	-0.4	$y = 1.0439x + 22.355$
UWG2	-18.22	3.20	5.8	-2.60	$y = 1.0234x + 21.845$
UWG2	-15.60	5.89	5.8	0.09	$y = 1.0234x + 21.845$
UWG2	-15.55	5.93	5.8	0.13	$y = 1.0234x + 21.845$
SES	-10.64	10.96	10.15	0.81	$y = 1.0234x + 21.845$
SES	-11.34	10.24	10.15	0.09	$y = 1.0234x + 21.845$
NBS28	-13.98	7.54	9.6	-2.06	$y = 1.0234x + 21.845$
UWG2	-14.89	6.61	5.8	0.81	$y = 1.0234x + 21.845$
UWG2	-15.38	6.10	5.8	0.30	$y = 1.0234x + 21.845$
UWG2	-11.59	9.98	5.8	4.18	$y = 1.0234x + 21.845$
SES	-9.58	12.04	10.15	1.89	$y = 1.0234x + 21.845$
SES	-11.56	10.01	10.15	-0.14	$y = 1.0234x + 21.845$
NBS28	-12.21	9.35	9.6	-0.25	$y = 1.0234x + 21.845$
UWG2	-14.86	6.64	5.8	0.84	$y = 1.0234x + 21.845$
UWG2	-14.48	7.02	5.8	1.22	$y = 1.0234x + 21.845$
SES	-11.47	10.10	10.15	-0.05	$y = 1.0234x + 21.845$
UWG2	-15.46	6.02	5.8	0.22	$y = 1.0234x + 21.845$
UWG2	-15.32	6.16	5.8	0.36	$y = 1.0234x + 21.845$
SES	-14.04	7.70	6.57	1.1	$y = 1.0439x + 22.398$
SES	-14.10	7.63	6.45	1.2	$y = 1.0439x + 22.398$
SES	-14.17	7.56	6.33	1.2	$y = 1.0439x + 22.398$
SES	-14.24	7.49	6.21	1.3	$y = 1.0439x + 22.398$
SES	-14.37	7.35	5.97	1.4	$y = 1.0439x + 22.398$
SES	-14.44	7.28	5.85	1.4	$y = 1.0439x + 22.398$
SES	-14.50	7.21	5.73	1.5	$y = 1.0439x + 22.398$
SES	-14.57	7.14	5.61	1.5	$y = 1.0439x + 22.398$
UWG2	-14.70	6.80	5.37	1.00	$y = 1.0234x + 21.845$
UWG2	-14.77	6.73	5.25	0.93	$y = 1.0234x + 21.845$

Hydrogen stable isotope data for all samples analysed

Sample name	mineral	δD_{smow}^*
VF2	epidote	-103.8
VF2	chlorite	-66.8
VF14	Muscovite	-98.6
VF14	Chlorite	-64.5
Host 3	Muscovite	-68.8
VF12	Chlorite	-52
VF3	chlorite	-52.7
Sample name	mineral	δD_{smow}^*
VF8	chlorite	-64.2
VF7	chlorite	-54.05
Epi-001	Muscovite	-63.7
Amp	Muscovite	-76.3
CC4	Chlorite	-100.5
CC3	Chlorite	-113.8
VF3	Muscovite	-62.2
CC3	Kfs	-128.7
Host 3	Kfs	-128.8
VF8	Kfs	-134.3
VF14	Kfs	-69.1
VF2	Kfs	-99.4
VF3	Kfs	-95.2
Host-3	quartz	-124.5
VF14	quartz	-81.7
VF2	quartz	-82.9
VF1	quartz	-119.2
VF8	quartz	-118.94
CC3	quartz	-120.4
VF3	quartz	-118.6
VF7	quartz	-107.1
VF7	Kfs	-112.8
Host - 1	quartz	-98.5
Host - 1	Kfs	-100.8
CC4	quartz	-121.5
CC4	Kfs	-113.8
VF12	quartz	-77.7

* = δD_{smow} is of the mineral for chlorite, muscovite and epidote, but for quartz and K-feldspar δD_{smow} is of the fluid.

Standard	δD_{smow}
Lt Std	-93.9
Lt Std	-95
GISP	-184.6
GISP	-186.1
Lt Std	-93.4
Lt Std	-94.2
Lt Std	-92.9
LtStd	-93.7
Sea Water	-6
GISP	-189.7
Lt Std	-95.9
GISP	-189
GISP	-189.9
GISP	-187.7
Ltd STd	-92.9
Lt Std	-94.7
Sea Water	-5.9
Sea Water	-5.7

Appendix 4

Host and fault rock minerals were analysed in terms of their oxygen and hydrogen stable isotopic composition. The isotopic composition of a mineral is controlled by the temperature of interaction and the composition of the fluid and the relationship between the different phases and temperature is typically described by a fractionation equation (e.g. Equation 13). The equation used to calculate the isotopic composition of the fluid is dependent on the mineral being analysed and the isotopic system being analysed (i.e. oxygen or hydrogen). Providing the appropriate fractionation equation is used and the temperature of interaction is known; the isotopic composition of the interacting fluid can be deciphered. Analyses of host and fault rock minerals will therefore enable the isotopic composition of the fluid(s) that have interacted with the host and/or fault rock minerals to be deciphered.

$$\text{Quartz } \delta^{18} O_{(\text{mineral-water})} = 3.34 \frac{10^6}{T^2} - 3.31 \quad \text{Equation 13}$$

Fractionation equation for Quartz from Matsuhisa et al.,(1979).

Different fractionation equations can be used for one particular mineral in an isotopic system e.g. oxygen fractionation between quartz and a fluid. For example, Zhang et al (1989) studied oxygen fractionation between quartz and water that accompanies hydrothermal crystallization of quartz from silica gel between 180-550°C and at different salinities; whereas Matsuhisa et al (1979) investigated oxygen isotopic fractionation between quartz-albite-anorthite and water between 300-825°C. Both of these fractionation equations are for oxygen fractionation between water and quartz however the prevailing conditions differ greatly. This means that several equations may exist to describe the isotopic relationship between a mineral and a fluid, however not all of the equations will be suitable for the isotopic system being analysed.

To select an appropriate fractionation equation to interpret the fluid-rock system at Passo Moro, the conditions related to a particular fractionation equation were compared to those that prevailed during fault-fluid-rock interaction at Passo Moro. In some cases there was no set of conditions which

matched exactly to those at Passo Moro e.g. for oxygen isotopic analysis of quartz the equation by Matsuhisa et al (1979) was utilised. The study by Matsuhisa et al (1979) indicates that the fractionation equation is applicable for temperatures between 300-825°C, however at Passo Moro temperatures were as low as 200°C. The relationship to lower temperatures can be predicted based on their results, but this may not represent the relationship that actually exists in nature. However, when no fractionation equation correlated precisely, the most appropriate equation was selected. Meteoric fluids are isotopically lighter than magmatic or metamorphic fluids (for oxygen and hydrogen stable isotopes) and so the effect of fluid-rock interaction with a meteoric fluid can be predicted. This means that the calculated results can be critically assessed to determine if they were plausible. If the results were unrealistic then a different equation was selected.

Due to the variety of fractionation equations available, this means that for all of the minerals assessed the fluid results I have presented in this thesis are only one possible interpretation of the measured data. Nevertheless, the choice of fractionation equation only affects the interpretation related to fluid-rock evolution and the precise fluid source. The shifts observed in the measured data infer a more meteoric-like input and hence back-up the various conclusions made from the isotopic study.

Fractionation equations used for oxygen results.

K-feldspar - O'Neil, J.R., and Taylor, H.P. Jr. (1967). The oxygen isotope and cation exchange chemistry of feldspars. *Amer. Mineral.* 52, pp. 1414-1437.

Equation: feldspar-K \rightleftharpoons H₂O

$$1000 \ln \alpha = D \frac{(10^6)}{T^2} + E \frac{(10^3)}{T} + F$$

D: 2.910; E: 0.00; F: -3.40

Quartz - Matsuhisa, Y., Goldsmith, J.R. and Clayton, R.N. (1979). Oxygen isotopic fractionation in the system quartz-albite-anorthite-water. *Geoch. Cosmochim. Acta* 43, pp. 1131-1140.

Equation: quartz \rightleftharpoons H₂O

$$1000 \ln \alpha = D \frac{(10^6)}{T^2} + E \frac{(10^3)}{T} + F$$

D: 3.340; E: 0.00; F: -3.31

Chlorite – Cole D.R. & Ripley E.M. (1998). Oxygen isotope fractionation between chlorite and water from 170-350C : A preliminary assessment based on partial exchange and fluid/rock experiments, *Geochimica et Cosmochimica Acta*, 63. P. 449-457.

Equation: chlorite \rightleftharpoons H₂O

$$1000 \ln \alpha = C \frac{(10^9)}{T^3} + D \frac{(10^6)}{T^2} + E \frac{(10^3)}{T} + F$$

C: 2.693; D: -6.342; E: 2.97; F: 0.00

Fractionation equations used for hydrogen results.

Biotite - Suzuoki, T. and Epstein, S. (1976). Hydrogen isotope fractionation between OH-bearing minerals and water. *Geochim. Cosmochim. Acta* 40, pp. 1229-1240.

Equation: biotite \rightleftharpoons H₂O

$$1000 \ln \alpha = D \frac{(10^6)}{T^2} + E \frac{(10^3)}{T} + F$$

D: -21.300; E: 0.00; F: -2.80

Chlorite - Graham, C.M., Viglino, J.A., and Harmon, R.S., 1987, Experimental-Study of Hydrogen-Isotope Exchange between Aluminous Chlorite and Water and of Hydrogen Diffusion in Chlorite: *American Mineralogist*, v. 72, p. 566-579.

200-500°C $1000 \ln \alpha = -30$ to -40

Muscovite - Vennemann, T.W., and O'Neil, J.R., 1996, Hydrogen isotope exchange reactions between hydrous minerals and molecular hydrogen: I. A new approach for the determination of hydrogen isotope fractionation at moderate temperatures: *Geochimica et Cosmochimica Acta*, v. 60, p. 2437-2451.

I utilised the fractionation factor for mineral-water utilising Bottinga (1969) (column C).

Temp. (°C)	$1000 \ln \alpha$, Min.-H,	$1000 \ln \alpha$, Mineral-Water (Vapor)				$1000 \ln \alpha$, Mineral-Water (Liquid)			
		A	B	C	D	A	B	C	D
		Muscovite							
200	697.4	12.4	10.4	13.4	23.4	9.0	7.0	10.0	20.0
250	547.9	-42.1	-51.1	-45.1	-36.1	-40.3	-49.3	-43.3	-34.3
300	465.0	-47.0	-61.0	-54.0	-45.0	-43.4	-57.4	-50.4	-41.4
400	338.5	-52.5	-74.5	-67.5	-59.5	-55.6	-77.6	-70.6	-62.6
Fractionation factors from: A - Suess (1949); B - Cerrai et al. (1958); C - Bottinga (1969); D - Richet et al. (1977). All are water vapor - hydrogen fractionation factors used to calculate the mineral - water fractionations from the experimental data. Fractionations between water liquid and vapor are after Horita and Wesolowski (1994).									

List of references

- Ackermann, R.V., and Schlische, R.W., 1997, Anticlustering of small normal faults around larger faults: *Geology*, v. 25, p. 1127-1130.
- Amato, J.M., Johnson, C.M., Baumgartner, L.P., and Beard, B.L., 1999, Rapid exhumation of the Zermatt-Saas ophiolite deduced from high-precision SmNd and RbSr geochronology: *Earth and Planetary Science Letters*, v. 171, p. 425-438.
- Baatartsogt, B., Wagner, T., Taubald, H., Mierdel, K., and Markl, G., 2007, Hydrogen isotope determination of fluid inclusion water from hydrothermal fluorite: Constraining the effect of the extraction technique: *Chemical Geology*, v. 244, p. 474-482.
- Baker, A.J., 1990, Stable Isotopic Evidence for Fluid-Rock Interactions in the Ivrea Zone, Italy: *J. Petrology*, v. 31, p. 243-260.
- Balsamo, F, Storti, and F, 2010, Grain size and permeability evolution of soft-sediment extensional sub-seismic and seismic fault zones in high-porosity sediments from the Crotone basin, southern Apennines, Italy: *Kidlington, ROYAUME-UNI, Elsevier*, 16 p.
- Bauer, P., Palm, S., and Handy, M.R., 2000, Strain localization and fluid pathways in mylonite: inferences from in situ deformation of a water-bearing quartz analogue (norcamphor): *Tectonophysics*, v. 320, p. 141-165.
- Bearth, P., 1952, *Geologie und Petrographie des Monte Rosa.: Beitr Geol Karte Schweiz*, v. NF96, p. 94.
- Bergbauer, S., and Martel, S.J., 1999, Formation of joints in cooling plutons: *Journal of Structural Geology*, v. 21, p. 821-835.
- Berger, A., and Bousquet, R., 2008, Subduction-related metamorphism in the Alps: review of isotopic ages based on petrology and their geodynamic consequences: *Geological Society, London, Special Publications*, v. 298, p. 117-144.
- Billi, A., Salvini, F., and Storti, F., 2003, The damage zone-fault core transition in carbonate rocks: implications for fault growth, structure and permeability: *Journal of Structural Geology*, v. 25, p. 1779-1794.
- Bird, D.K., Schiffman, P., Elders, P., Williams, W.A., and McDowell, S.D., 1984, Calc-silicate mineralization in active geothermal systems: *Economic Geology*, v. 79, p. 671-695.
- Bird, D.K., and Spieler, A.R., 2004, Epidote in Geothermal Systems: *Reviews in Mineralogy and Geochemistry*, v. 56, p. 235-300.
- Bistacchi, Bistacchi, A., Dal, P., Piazz, G.D., Massironi, Massironi, M., Zattin, Zattin, M., Balestrieri, and Balestrieri, M., 2001, The Aosta-Ranzola extensional fault system and Oligocene-Present evolution of the Austroalpine-Penninic wedge in the northwestern Alps: *International Journal of Earth Sciences*, v. 90, p. 654-667.
- Bistacchi, A., Eva, E., Massironi, M., and Solarino, S., 2000, Miocene to Present kinematics of the NW-Alps: evidences from remote sensing, structural analysis, seismotectonics and thermochronology: *Journal of Geodynamics*, v. 30, p. 205-228.
- Blenkinsop, T.G., 1991, Cataclasis and processes of particle size reduction: *Pure and Applied Geophysics*, v. 136, p. 59-86.
- Bocquet, J., Delaloye, M., Hunziker, J.C., and Krummenacher, D., 1974, K-Ar and Rb-Sr Dating of blue amphiboles, micas, and associated minerals from

- the Western Alps: Contributions to Mineralogy and Petrology, v. 47, p. 7-26.
- Bottinga, Y., and Javoy, M., 1975, Oxygen isotope partitioning among the minerals in igneous and metamorphic rocks: *Rev. Geophys.*, v. 13, p. 401-418.
- Boulton, C., Davies, T., and McSaveney, M., 2009, The frictional strength of granular fault gouge: application of theory to the mechanics of low-angle normal faults: Geological Society, London, Special Publications, v. 321, p. 9-31.
- Bousquet, R., Goffé, B., Henry, P., Le Pichon, X., and Chopin, C., 1997, Kinematic, thermal and petrological model of the Central Alps: Lepontine metamorphism in the upper crust and eclogitisation of the lower crust: *Tectonophysics*, v. 273, p. 105-127.
- Bousquet, R., Oberhänsli, R., Goffe, B., Wiederkehr, M., Koller, F., Schmid, S.M., Schuster, R., Engi, M., Berger, A., and Martinotti, G., 2008, Metamorphism of metasediments at the scale of an orogen: a key to the Tertiary geodynamic evolution of the Alps: Geological Society, London, Special Publications, v. 298, p. 393-411.
- Brantley, S.L., Evans, B., Hickman, S.H., and Crerar, D.A., 1990, Healing of Microcracks in Quartz - Implications for Fluid-Flow: *Geology*, v. 18, p. 136-139.
- Brogi, A., 2008, Fault zone architecture and permeability features in siliceous sedimentary rocks: Insights from the Rapolano geothermal area (Northern Apennines, Italy): *Journal of Structural Geology*, v. 30, p. 237-256.
- , 2011, Variation in fracture patterns in damage zones related to strike-slip faults interfering with pre-existing fractures in sandstone (Calcione area, southern Tuscany, Italy): *Journal of Structural Geology*, v. 33, p. 644-661.
- Brown, E.H., 1969, Some Zoned Garnets from Greenschist Facies: *American Mineralogist*, v. 54, p. 1662-6.
- Bucher, K., and Frey, M., 2002, Petrogenesis of metamorphic rocks: Heidelberg, Springer.
- Bürgi, C., Parriaux, A., and Franciosi, G., 2001, Geological characterization of weak cataclastic fault rocks with regards to the assessment of their geomechanical properties: *Quarterly Journal of Engineering Geology and Hydrogeology*, v. 34, p. 225-232.
- C. W. Field., R.H.F., 1985, Light stable isotope systematics in the epithermal environment, *in* Berger, B.R., and Bethke, P.M., eds., *Geology and geochemistry of epithermal systems, Volume 2: Reviews in Economic Geology*, p. 99-128.
- Caine, J.S., Evans, J.P., and Forster, C.B., 1996, Fault zone architecture and permeability structure: *Geology*, v. 24, p. 1025-1028.
- Cappa, F., 2011, Influence of hydromechanical heterogeneities of fault zones on earthquake ruptures: *Geophysical Journal International*, v. 185, p. 1049-1058.
- Casas, A.M., Oliva, B., Román-Berdiel, T., and Pueyo, E., 2003, Basement deformation: tertiary folding and fracturing of the Variscan Bielsa granite (Axial zone, central Pyrenees): *Geodinamica Acta*, v. 16, p. 99-117.
- Ceriani, S., and Schmid, S.M., 2004, From N-S collision to WNW-directed post-collisional thrusting and folding: Structural study of the Frontal Penninic Units in Savoie (Western Alps, France): *Eclogae Geologicae Helvetiae*, v. 97, p. 347-369.

- Chester, F.M., Evans, J.P., and Biegel, R.L., 1993, Internal Structure and Weakening Mechanisms of the San Andreas Fault: *J. Geophys. Res.*, v. 98, p. 771-786.
- Chester, F.M., and Logan, J.M., 1986, Implications for mechanical properties of brittle faults from observations of the Punchbowl fault zone, California: *Pure and Applied Geophysics*, v. 124, p. 79-106.
- Chopin, C., and Monié, P., 1984, A unique magnesiochloritoid-bearing, high-pressure assemblage from the Monte Rosa, Western Alps: petrologic and ⁴⁰Ar-³⁹Ar radiometric study: *Contributions to Mineralogy and Petrology*, v. 87, p. 388-398.
- Claesson, L., Skelton, A., Graham, C., and MÖRth, C.M., 2007, The timescale and mechanisms of fault sealing and water-rock interaction after an earthquake: *Geofluids*, v. 7, p. 427-440.
- Cole, D.R., Larson, P.B., Riciputi, L.R., and Mora, C.I., 2004, Oxygen isotope zoning profiles in hydrothermally altered feldspars: Estimating the duration of water-rock interaction: *Geology*, v. 32, p. 29-32.
- Cooper, H.H., Jr., Bredehoeft, J.D., Papadopoulos, I.S., and Bennett, R.R., 1965, The Response of Well-Aquifer Systems to Seismic Waves: *J. Geophys. Res.*, v. 70, p. 3915-3926.
- Coward, M., and Dietrich, D., 1989, Alpine tectonics – an overview: Geological Society, London, Special Publications, v. 45, p. 1-29.
- Cowie, P.A., Gupta, S., and Dawers, N.H., 2000, Implications of fault array evolution for synrift depocentre development: insights from a numerical fault growth model: *Basin Research*, v. 12, p. 241-261.
- Cox, S.F., 1999, Deformational controls on the dynamics of fluid flow in mesothermal gold systems: Geological Society, London, Special Publications, v. 155, p. 123-140.
- Crawford, B.R., Faulkner, D.R., and Rutter, E.H., 2008, Strength, porosity, and permeability development during hydrostatic and shear loading of synthetic quartz-clay fault gouge: *J. Geophys. Res.*, v. 113, p. B03207.
- Crider, J.G., and Peacock, D.C.P., 2004, Initiation of brittle faults in the upper crust: a review of field observations: *Journal of Structural Geology*, v. 26, p. 691-707.
- Criss, R., and Taylor, H.J., 1986, Meteoric hydrothermal systems, *in* J. Valley, H.T.J., J. O'Neil, ed., Stable isotopes in high temperature geological processes, Volume 16: Reviews in mineralogy, Mineralogical society, p. 373-424.
- Criss, R.E., Gregory, R.T., and Taylor Jr, H.P., 1987, Kinetic theory of oxygen isotopic exchange between minerals and water: *Geochimica et Cosmochimica Acta*, v. 51, p. 1099-1108.
- Curti, E., 1987, Lead and oxygen isotope evidence for the origin of the Monte Rosa gold lode deposits (Western Alps, Italy); a comparison with Archean lode deposits: *Economic Geology*, v. 82, p. 2115-2140.
- Dal-Piaz, G.V., 2001, History of tectonic interpretations of the Alps: *Journal of Geodynamics*, v. 32, p. 99-114.
- Dal-Piaz, G.V., Bistacchi, A., and Massironi, M., 2003, Geological outline of the Alps: Episodes, v. 26, p. 175-180.
- Dal-Piaz, G.V., Hunziker, J.C., and Martinotti, G., 1972, La Zona Sesia-Lanzo e l'evoluzione tettonico-metamorfica delle Alpi nordoccidentali interne: *Memorie della Societa Geologica Italiana*, v. 11, p. 433-460.
- Di Toro, G., and Pennacchioni, G., 2005, Fault plane processes and mesoscopic structure of a strong-type seismogenic fault in tonalites (Adamello batholith, Southern Alps): *Tectonophysics*, v. 402, p. 55-80.

- Donnelly, T., Waldron, S., Tait, A., Dougans, J., and Bearhop, S., 2001, Hydrogen isotope analysis of natural abundance and deuterium-enriched waters by reduction over chromium on-line to a dynamic dual inlet isotope-ratio mass spectrometer: *Rapid Communications in Mass Spectrometry*, v. 15, p. 1297-1303.
- Dworkin, S.I., 1999, Geochemical constraints on the origin of thrust fault fluids: *Geophys. Res. Lett.*, v. 26, p. 3665-3668.
- Dyer, R., 1988, Using joint interactions to estimate paleostress ratios: *Journal of Structural Geology*, v. 10, p. 685-699.
- Eaton, J.P., and Takasaki, K.J., 1959, Seismological interpretation of earthquake-induced water-level fluctuations in wells: *BULLETIN OF THE SEISMOLOGICAL SOCIETY OF AMERICA*, v. 49, p. 227-245.
- Ehlers, T.A., and Farley, K.A., 2003, Apatite (U²³⁸Th)/He thermochronometry: methods and applications to problems in tectonic and surface processes: *Earth and Planetary Science Letters*, v. 206, p. 1-14.
- Eichhubl, P., and Boles, J., 2000, Rates of fluid flow in fault systems - evidence for episodic rapid fluid flow in the miocene Monterey Formation, Coastal California: *American Journal of Science*, v. 300, p. 571-600.
- Ellis, A.C., Barnicoat, A.C., and Fry, N., 1989, Structural and metamorphic constraints on the tectonic evolution of the upper Pennine Alps: Geological Society, London, Special Publications, v. 45, p. 173-188.
- Evans, J.P., and Chester, F.M., 1995, Fluid-rock interaction in faults of the San Andreas system: Inferences from San Gabriel fault rock geochemistry and microstructures: *J. Geophys. Res.*, v. 100, p. 13007-13020.
- Evans, J.P., Forster, C.B., and Goddard, J.V., 1997, Permeability of fault-related rocks, and implications for hydraulic structure of fault zones: *Journal of Structural Geology*, v. 19, p. 1393-1404.
- Evans, K.F., 2005, Permeability creation and damage due to massive fluid injections into granite at 3.5 km at Soultz: 2. Critical stress and fracture strength: *J. Geophys. Res.*, v. 110, p. B04204.
- Eyal, Y., Gross, M.R., Engelder, T., and Becker, A., 2001, Joint development during fluctuation of the regional stress field in southern Israel: *Journal of Structural Geology*, v. 23, p. 279-296.
- Faulkner, D.R., Jackson, C.A.L., Lunn, R.J., Schlische, R.W., Shipton, Z.K., Wibberley, C.A.J., and Withjack, M.O., 2010, A review of recent developments concerning the structure, mechanics and fluid flow properties of fault zones: *Journal of Structural Geology*, v. 32, p. 1557-1575.
- Faulkner, D.R., Mitchell, T.M., Jensen, E., and Cembrano, J., 2011, Scaling of fault damage zones with displacement and the implications for fault growth processes: *J. Geophys. Res.*, v. 116, p. B05403.
- Faulkner, D.R., Mitchell, T.M., Rutter, E.H., and Cembrano, J., 2008, On the structure and mechanical properties of large strike-slip faults: Geological Society, London, Special Publications, v. 299, p. 139-150.
- Field, C.W., and Fifarek, R., 1985, Light stable isotope systematics in the epithermal environment, *in* Berger, B.R., and Bethke, P.M., eds., *Geology and geochemistry of epithermal systems, Volume 2: Reviews in Economic Geology*, p. 99-128.
- Fitz Gerald, J.D., and Stünitz, H., 1993, Deformation of granitoids at low metamorphic grade. I: Reactions and grain size reduction: *Tectonophysics*, v. 221, p. 269-297.
- Freeman, J.J., Wang, A., Kuebler, K.E., Jolliff, B.L., and Haskin, L.A., 2008, CHARACTERIZATION OF NATURAL FELDSPARS BY RAMAN SPECTROSCOPY

- FOR FUTURE PLANETARY EXPLORATION: *The Canadian Mineralogist*, v. 46, p. 1477-1500.
- Frey, M., Hunziker, J.C., O'Neil, J.R., and Schwander, H.W., 1976, Equilibrium-disequilibrium relations in the Monte Rosa Granite, Western Alps: Petrological, Rb-Sr and stable isotope data: *Contributions to Mineralogy and Petrology*, v. 55, p. 147-179.
- Froitzheim, N., 2001, Origin of the Monte Rosa nappe in the Pennine Alps--A new working hypothesis: *Geological Society of America Bulletin*, v. 113, p. 604-614.
- Giletti, B., 1986, Diffusion effects on oxygen isotope temperatures of slowly cooled igneous and metamorphic rocks: *Earth and Planetary Science Letters*, v. 77, p. 218-228.
- Gleason, G.C., Tullis, J., and Heidelbach, F., 1999, The role of dynamic recrystallization in the development of lattice preferred orientations in experimentally deformed quartz aggregates: *Journal of Structural Geology*, v. 15, p. 1145-1168.
- Gleeson, S.A., Roberts, S., Fallick, A.E., and Boyce, A.J., 2008, Micro-Fourier Transform Infrared (FT-IR) and δD value investigation of hydrothermal vein quartz: Interpretation of fluid inclusion δD values in hydrothermal systems: *Geochimica et Cosmochimica Acta*, v. 72, p. 4595-4606.
- Glodny, J., and Grauert, B., 2009, Evolution of a hydrothermal fluid-rock interaction system as recorded by Sr isotopes: A case study from the Schwarzwald, SW Germany: *Mineralogy and Petrology*, v. 95, p. 163-178.
- Goddard, J.V., and Evans, J.P., 1995, Chemical changes and fluid-rock interaction in faults of crystalline thrust sheets, northwestern Wyoming, U.S.A: *Journal of Structural Geology*, v. 17, p. 533-547.
- Goffé, B., Bousquet, R., Henry, P., and Le Pichon, X., 2003, Effect of the chemical composition of the crust on the metamorphic evolution of orogenic wedges: *Journal of Metamorphic Geology*, v. 21, p. 123-141.
- Graham, C.M., Viglino, J.A., and Harmon, R.S., 1987, Experimental-Study of Hydrogen-Isotope Exchange between Aluminous Chlorite and Water and of Hydrogen Diffusion in Chlorite: *American Mineralogist*, v. 72, p. 566-579.
- Granier, T., 1985, Origin, damping, and pattern of development of faults in granite: *Tectonics*, v. 4, p. 721-737.
- Gregory, R., and Criss, R., 1986, Isotopic exchange in open and closed systems, *in* J. Valley, H.T.J., J. O'Neil, ed., *Stable isotopes in high temperature geological processes*, Volume 16: *Reviews in mineralogy*, Mineralogical Society, p. 91-128.
- Gross, M.R., 1993, The origin and spacing of cross joints: examples from the Monterey Formation, Santa Barbara Coastline, California: *Journal of Structural Geology*, v. 15, p. 737-751.
- Gross, M.R., Bahat, D., and Becker, A., 1997, Relations between jointing and faulting based on fracture-spacing ratios and fault-slip profiles: A new method to estimate strain in layered rocks: *Geology*, v. 25, p. 887-890.
- Gross, M.R., and Eyal, Y., 2007, Throughgoing fractures in layered carbonate rocks: *Geological Society of America Bulletin*, v. 119, p. 1387-1404.
- Gross, M.R., Fischer, M.P., Engelder, T., and Greenfield, R.J., 1995, Factors controlling joint spacing in interbedded sedimentary rocks: integrating numerical models with field observations from the Monterey Formation, USA: *Geological Society, London, Special Publications*, v. 92, p. 215-233.
- Gudmundsson, A., 2001, Fluid overpressure and flow in fault zones: field measurements and models: *Tectonophysics*, v. 336, p. 183-197.

- Hancock, P.L., 1985, Brittle microtectonics: principles and practice: *Journal of Structural Geology*, v. 7, p. 437-457.
- Hartley, A., 1974, A review of the geological factors influencing the mechanical properties of road surface aggregates: *Quarterly Journal of Engineering Geology and Hydrogeology*, v. 7, p. 69-100.
- Hashimoto, Y., Nikaizo, A., and Kimura, G., 2009, A geochemical estimation of fluid flux and permeability for a fault zone in Mugí mélangé, the Cretaceous Shimanto Belt, SW Japan: *Journal of Structural Geology*, v. 31, p. 208-214.
- Hemley, J.J., 1959, SOME MINERALOGICAL EQUILIBRIA IN THE SYSTEM K₂O-AL₂O₃-SiO₂-H₂O: *American Journal of Science*, v. 257, p. 241-270.
- Hemley, J.J., and Jones, W.R., 1964, Chemical aspects of hydrothermal alteration with emphasis on hydrogen metasomatism: *Economic Geology*, v. 59, p. 538-569.
- Hirth, G., and Tullis, J., 1992, Dislocation creep regimes in quartz aggregates: *Journal of Structural Geology*, v. 14, p. 145-159.
- , 1994, The brittle-plastic transition in experimentally deformed quartz aggregates: *J. Geophys. Res.*, v. 99, p. 11731-11747.
- Hodgson, R.A., 1961, Regional study of jointing in Comb Ridge-Navajo Mountain Area, Arizona & Utah: *American Association of Petroleum Geologists Bulletin*, v. 45, p. 1-38.
- Hövelmann, J., Putnis, A., Geisler, T., Schmidt, B., and Golla-Schindler, U., 2010, The replacement of plagioclase feldspars by albite: observations from hydrothermal experiments: *Contributions to Mineralogy and Petrology*, v. 159, p. 43-59.
- Hurford, A.J., Hunziker, J.C., and Stockhert, B., 1991, Constraints on the Late Thermotectonic Evolution of the Western Alps - Evidence for Episodic Rapid Uplift: *Tectonics*, v. 10, p. 758-769.
- Ikari, M.J., Niemeijer, A.R., and Marone, C., 2011, The role of fault zone fabric and lithification state on frictional strength, constitutive behavior, and deformation microstructure: *J. Geophys. Res.*, v. 116, p. B08404.
- J.D.Kirkpatrick, 2008, The structural architecture of seismogenic faults, Sierra Nevada, California : implications for earthquake rupture processes: unpublished Ph.D. thesis, Glasgow, UK.
- Janecke, S.U., and Evans, J.P., 1988, Feldspar-influenced rock rheologies: *Geology*, v. 16, p. 1064-1067.
- Janssen, C., Laube, N., Bau, M., and Gray, D.R., 1998, Fluid regime in faulting deformation of the Waratah Fault Zone, Australia, as inferred from major and minor element analyses and stable isotopic signatures: *Tectonophysics*, v. 294, p. 109-130.
- Janssen, C., Wirth, R., Rybacki, E., Naumann, R., Kemnitz, H., Wenk, H.R., and Dresen, G., 2010, Amorphous material in SAFOD core samples (San Andreas Fault): Evidence for crush-origin pseudotachylytes?: *Geophys. Res. Lett.*, v. 37, p. L01303.
- Jefferies, S.P., Holdsworth, R.E., Shimamoto, T., Takagi, H., Lloyd, G.E., and Spiers, C.J., 2006a, Origin and mechanical significance of foliated cataclastic rocks in the cores of crustal-scale faults: Examples from the Median Tectonic Line, Japan: *J. Geophys. Res.*, v. 111, p. B12303.
- Jefferies, S.P., Holdsworth, R.E., Wibberley, C.A.J., Shimamoto, T., Spiers, C.J., Niemeijer, A.R., and Lloyd, G.E., 2006b, The nature and importance of phyllonite development in crustal-scale fault cores: an example from the Median Tectonic Line, Japan: *Journal of Structural Geology*, v. 28, p. 220-235.

- Jenkin, G.R.T., Craw, D., and Fallick, A.E., 1994, Stable isotopic and fluid inclusion evidence for meteoric fluid penetration into an active mountain belt; Alpine Schist, New Zealand: *Journal of Metamorphic Geology*, v. 12, p. 429-444.
- Jenkin, G.R.T., Fallick, A.E., and Leake, B.E., 1992, A stable isotope study of retrograde alteration in SW Connemara, Ireland: *Contributions to Mineralogy and Petrology*, v. 110, p. 269-288.
- Jenkin, G.R.T., Linklater, C., and Fallick, A.E., 1991, Modeling of mineral $\delta^{18}\text{O}$ values in an igneous aureole: Closed-system model predicts apparent open-system $\delta^{18}\text{O}$ values: *Geology*, v. 19, p. 1185-1188.
- Keller, L.M., Abart, R., Stünitz, H., and De Capitani, C., 2004, Deformation, mass transfer and mineral reactions in an eclogite facies shear zone in a polymetamorphic metapelite (Monte Rosa nappe, western Alps): *Journal of Metamorphic Geology*, v. 22, p. 97-118.
- King, S.W., 1858, *The Italian Valleys of the Pennine Alps: A Tour Through All the Romantic and Less-frequented "vals" of Northern Piedmont, from the Tarentaise to the Gries*, London, Murray.
- Kirkpatrick, J.D., 2008, *The structural architecture of seismogenic faults, Sierra Nevada, California : implications for earthquake rupture processes*: unpublished Ph.D. thesis, Glasgow, UK.
- Kirkpatrick, J.D., and Shipton, Z.K., 2009, Geologic evidence for multiple slip weakening mechanisms during seismic slip in crystalline rock: *J. Geophys. Res.*, v. 114, p. B12401.
- Kronenberg, A.K., Kirby, S.H., and Pinkston, J., 1990, Basal Slip and Mechanical Anisotropy of Biotite: *J. Geophys. Res.*, v. 95, p. 19257-19278.
- Labotka, T.C., Cole, D.R., Fayek, M., Riciputi, L.R., and Stadermann, F.J., 2004, Coupled cation and oxygen-isotope exchange between alkali feldspar and aqueous chloride solution: *American Mineralogist*, v. 89, p. 1822-1825.
- Lahren, M.M., and Schweickert, R.A., 1991, TERTIARY BRITTLE DEFORMATION IN THE CENTRAL SIERRA-NEVADA, CALIFORNIA - EVIDENCE FOR LATE MIOCENE AND POSSIBLY YOUNGER FAULTING: *Geological Society of America Bulletin*, v. 103, p. 898-904.
- Lapen, T., Johnson, C., Baumgartner, L., Piaz, G., Skora, S., and Beard, B., 2007, Coupling of oceanic and continental crust during Eocene eclogite-facies metamorphism: evidence from the Monte Rosa nappe, western Alps: *Contributions to Mineralogy and Petrology*, v. 153, p. 139-157.
- Lattanzi, P., Curti, E., and Bastogi, M., 1989, Fluid inclusion studies on the gold deposits of the upper Anzasca Valley, northwestern Alps, Italy: *Economic Geology*, v. 84, p. 1382-1397.
- Lee, H.-K., and Kim, H.S., 2005, Comparison of structural features of the fault zone developed at different protoliths: crystalline rocks and mudrocks: *Journal of Structural Geology*, v. 27, p. 2099-2112.
- Lin, A., 2011, Seismic slip recorded by fluidized ultracataclastic veins formed in a coseismic shear zone during the 2008 Mw 7.9 Wenchuan earthquake: *Geology*, v. 39, p. 547-550.
- Liu, L.-B., Roeloffs, E., and Zheng, X.-Y., 1989, Seismically Induced Water Level Fluctuations in the Wali Well, Beijing, China: *J. Geophys. Res.*, v. 94, p. 9453-9462.
- Lockner, D.A., Morrow, C., Moore, D., and Hickman, S., 2011, Low strength of deep San Andreas fault gouge from SAFOD core: *Nature*, v. 472, p. 82-85.
- Logan, J.M., and Decker, C.L., 1994, Cyclic Fluid Flow Along Faults, *in* Survey, U.S.G., ed., Open File Report, p. 94-228.

- Mancktelow, N.S., 1992, NEOGENE LATERAL EXTENSION DURING CONVERGENCE IN THE CENTRAL ALPS - EVIDENCE FROM INTERRELATED FAULTING AND BACKFOLDING AROUND THE SIMPLONPASS (SWITZERLAND): *Tectonophysics*, v. 215, p. 295-317.
- Manda, A., and Mabee, S., 2010, Comparison of three fracture sampling methods for layered rocks: *International Journal of Rock Mechanics and Mining Sciences*, v. 47, p. 218-226.
- Maréchal, J.-C., and Perrochet, P., 2001, Theoretical relation between water flow rate in a vertical fracture and rock temperature in the surrounding massif: *Earth and Planetary Science Letters*, v. 194, p. 213-219.
- Martel, S.J., 1990, Formation of compound strike-slip fault zones, Mount Abbot quadrangle, California: *Journal of Structural Geology*, v. 12, p. 869-877, 879-882.
- , 1997, Effects of cohesive zones on small faults and implications for secondary fracturing and fault trace geometry: *Journal of Structural Geology*, v. 19, p. 835-847.
- , 1999, Mechanical controls on fault geometry: *Journal of Structural Geology*, v. 21, p. 585-596.
- Martel, S.J., Pollard, D.D., and Segall, P., 1988, Development of simple strike-slip fault zones, Mount Abbot quadrangle, Sierra Nevada, California: *Geological Society of America Bulletin*, v. 100, p. 1451-1465.
- Matsuhisa, Y., Goldsmith, J.R., and Clayton, R.N., 1979, Oxygen isotopic fractionation in the system quartz-albite-anorthite-water: *Geochimica et Cosmochimica Acta*, v. 43, p. 1131-1140.
- Matthews, A., Goldsmith, J.R., and Clayton, R.N., 1983, Oxygen isotope fractionation between zoisite and water: *Geochimica et Cosmochimica Acta*, v. 47, p. 645-654.
- Maxelon, M., and Mancktelow, N.S., 2005, Three-dimensional geometry and tectonostratigraphy of the Pennine zone, Central Alps, Switzerland and Northern Italy: *Earth-Science Reviews*, v. 71, p. 171-227.
- McNamara, M.J., 1966, Chlorite-Biotite Equilibrium Reactions in a Carbonate-Free System: *Journal of Petrology*, v. 7, p. 404-413.
- Micarelli, L., Benedicto, A., and Wibberley, C.A.J., 2006, Structural evolution and permeability of normal fault zones in highly porous carbonate rocks: *Journal of Structural Geology*, v. 28, p. 1214-1227.
- Miller, S.A., and Nur, A., 2000, Permeability as a toggle switch in fluid-controlled crustal processes: *Earth and Planetary Science Letters*, v. 183, p. 133-146.
- Milnes, A.G., Grellner, M., and Müller, R., 1981, Sequence and style of major post-nappe structures, Simplon–Pennine Alps: *Journal of Structural Geology*, v. 3, p. 411-420.
- Mitchell, T.M., and Faulkner, D.R., 2008, Experimental measurements of permeability evolution during triaxial compression of initially intact crystalline rocks and implications for fluid flow in fault zones: *J. Geophys. Res.*, v. 113, p. B11412.
- , 2009, The nature and origin of off-fault damage surrounding strike-slip fault zones with a wide range of displacements: A field study from the Atacama fault system, northern Chile: *Journal of Structural Geology*, v. 31, p. 802-816.
- Mitterpergher, S., Pennacchioni, G., and Di Toro, G., 2009, The effects of fault orientation and fluid infiltration on fault rock assemblages at seismogenic depths: *Journal of Structural Geology*, v. 31, p. 1511-1524.

- Mollema, P.N., and Antonellini, M., 1999, Development of strike-slip faults in the dolomites of the Sella Group, Northern Italy: *Journal of Structural Geology*, v. 21, p. 273-292.
- Moore, D.E., and Lockner, D.A., 2011, Frictional strengths of talc-serpentine and talc-quartz mixtures: *J. Geophys. Res.*, v. 116, p. B01403.
- Moore, D.E., and Rymer, M.J., 2007, Talc-bearing serpentinite and the creeping section of the San Andreas fault: *Nature*, v. 448, p. 795-797.
- Morrison, J., and Anderson, J.L., 1998, Footwall Refrigeration Along a Detachment Fault: Implications for the Thermal Evolution of Core Complexes: *Science*, v. 279, p. 63-66.
- Mulch, A., Teyssier, C., Cosca, M.A., Vanderhaeghe, O., and Vennemann, T.W., 2004, Reconstructing paleoelevation in eroded orogens: *Geology*, v. 32, p. 525-528.
- Nabelek, P., Labotka, T., and Russ-Nabelek, C., 1992, Stable Isotope Evidence for the Role of Diffusion, Infiltration, and Local Structure on Contact Metamorphism of Calc-Silicate Rocks at Noth Peak, Utah: *Journal of Petrology*, v. 33, p. 557-583.
- Narr, W., and Suppe, J., 1991, Joint spacing in sedimentary rocks: *Journal of Structural Geology*, v. 13, p. 1037-1048.
- Nesbitt, B., and Muehlenbachs, K., 1989, Origins and Movement of Fluids During Deformation and Metamorphism in the Canadian Cordillera: *Science*, v. 245, p. 733-736.
- Niedermeier, D., Putnis, A., Geisler, T., Golla-Schindler, U., and Putnis, C., 2009, The mechanism of cation and oxygen isotope exchange in alkali feldspars under hydrothermal conditions: *Contributions to Mineralogy and Petrology*, v. 157, p. 65-76.
- O'Hara, K., 2007, Reaction weakening and emplacement of crystalline thrusts: Diffusion control on reaction rate and strain rate: *Journal of Structural Geology*, v. 29, p. 1301-1314.
- O'Hara, K.D., 1994, Fluid-rock interaction in crustal shear zones: A directed percolation approach: *Geology*, v. 22, p. 843-846.
- O'Hara, K.D., Sharp, Z.D., Moecher, D.P., and Jenkin, G.R.T., 1997, The Effect of Deformation on Oxygen Isotope Exchange in Quartz and Feldspar and the Significance of Isotopic Temperatures in Mylonites: *The Journal of Geology*, v. 105, p. 193-204.
- O'Neil, J.R., and Taylor, H.P.J., 1967, The oxygen isotope cation exchange chemistry of feldspars: *American Mineralogist*, v. 52, p. 1414-1437.
- Ohmoto, H., 1986, Stable isotope geochemistry of ore deposits, *in* J. Valley, H.T.J., J. O'Neil, ed., *Stable isotopes in high temperature geological processes*, Volume 16: *Reviews in mineralogy*, Mineralogical society, p. 491-560.
- Ohmoto, H., and Rye, R.O., 1974, Hydrogen and Oxygen Isotopic Compositions of Fluid Inclusions in Kuroko Deposits, Japan: *Economic Geology*, v. 69, p. 947-953.
- Oliver, N.H.S., 2001, Linking of regional and local hydrothermal systems in the mid-crust by shearing and faulting: *Tectonophysics*, v. 335, p. 147-161.
- Pachell, M.A., and Evans, J.P., 2002, Growth, linkage, and termination processes of a 10-km-long strike-slip fault in jointed granite: the Gemini fault zone, Sierra Nevada, California: *Journal of Structural Geology*, v. 24, p. 1903-1924.
- Park, Y., Yoo, S.-H., and Ree, J.-H., 2006, Weakening of deforming granitic rocks with layer development at middle crust: *Journal of Structural Geology*, v. 28, p. 919-928.

- Parry, W.T., and Downey, L.M., 1982, Geochemistry of hydrothermal chlorite replacing igneous biotite: *Clays and Clay Minerals*, v. 30, p. 81-90.
- Passchier, C.W., and Trouw, R.A.J., 2005, *Micro-tectonics*: Berlin, Springer.
- Patterson, M., 1978, *Experimental rock deformation: the brittle field*: New York, Springer-Verlag.
- Peacock, D.C.P., 1991, Displacements and segment linkage in strike-slip fault zones: *Journal of Structural Geology*, v. 13, p. 1025-1035.
- , 2001, The temporal relationship between joints and faults: *Journal of Structural Geology*, v. 23, p. 329-341.
- Person M, Lukas P. Baumgartner, Bart Bos, James A.D. Connolly, Jean-Pierre Gratier, Frédéric Gueydan, Stephen A. Miller, Claudio L. Rosenberg, Janos Urai, and Yardley, B.W.D., 2007, Fluids, geochemical cycles, and mass transport in fault zones.: In “Tectonic Faults: Agents of Change on a Dynamic Earth”, MIT Press, p. 403-427
- Person, M., Baumgartner, L., Bos, B., Connolly, J., Gratier, J., Gueydan, F., Miller, S., Rosenberg, C., Urai, J., and Yardley, B., 2007, Group report: Fluids, Geochemical Cycles, and Mass Transport in Fault Zones, *in* Handy, M.R., Hirth, G., and Hovius, N., eds., *Tectonic Faults - Agents of Change on a Dynamic Earth: Dahlem Series*: Cambridge, MA, MIT Press.
- Pettke, T., and Diamond, L.W., 1997, Oligocene gold quartz veins at Brusson, NW Alps; Sr isotopes trace the source of ore-bearing fluid to ore a 10-km depth: *Economic Geology*, v. 92, p. 389-406.
- Pettke, T., Diamond, L.W., and Kramers, J.D., 2000, Mesothermal gold lodes in the north-western Alps: A review of genetic constraints from radiogenic isotopes: *Eur J Mineral*, v. 12, p. 213-230.
- Pettke, T., Diamond, L.W., and Villa, I.M., 1999, Mesothermal gold veins and metamorphic devolatilization in the northwestern Alps: The temporal link: *Geology*, v. 27, p. 641-644.
- Pollard, D.D., and Segall, P., 1987, Theoretical displacements and stresses near fractures in rocks: with applications to faults, joints, veins, dikes, and solution surfaces, *in* Atkinson, B.K., ed., *Fracture mechanics of rocks*: London, Academic Press, p. 277-349.
- Polya, D.A., Foxford, K.A., Stuart, F., Boyce, A., and Fallick, A.E., 2000, Evolution and paragenetic context of low δD hydrothermal fluids from the Panasqueira W-Sn deposit, Portugal: new evidence from microthermometric, stable isotope, noble gas and halogen analyses of primary fluid inclusions: *Geochimica et Cosmochimica Acta*, v. 64, p. 3357-3371.
- Putnis, A., 2002, Mineral replacement reactions: from macroscopic observations to microscopic mechanisms: *Mineralogical Magazine*, v. 66, p. 689-708.
- Rawnsley, K.D., Rives, T., Petti, J.P., Hencher, S.R., and Lumsden, A.C., 1992, Joint development in perturbed stress fields near faults: *Journal of Structural Geology*, v. 14, p. 939-951.
- Reches, Z.e., and Lockner, D.A., 1994, Nucleation and growth of faults in brittle rocks: *J. Geophys. Res.*, v. 99, p. 18159-18173.
- Ring, U., and Merle, O., 1992, Forethrusting, backfolding, and lateral gravitational escape in the northern part of the Western Alps (Monte Rosa region): *Geological Society of America Bulletin*, v. 104, p. 901-914.
- Roedder, E., 1984, *Fluid inclusions*, Mineralogical Society of America.
- Rojstaczer, S., and Wolf, S., 1992, Permeability changes associated with large earthquakes: An example from Loma Prieta, California: *Geology*, v. 20, p. 211-214.

- Roselle, G., Baumgartner, L., and Valley, J., 1999, Stable isotope evidence of heterogeneous fluid infiltration at the Ubehebe Peak contact aureole, Death Valley National Park, California: *American Journal of Science*, v. 299, p. 93-138.
- Ruf, J.C., Rust, K.A., and Engelder, T., 1998, Investigating the effect of mechanical discontinuities on joint spacing: *Tectonophysics*, v. 295, p. 245-257.
- Sandstrom, B., Annersten, H., and Tullborg, E.L., 2010, Fracture-related hydrothermal alteration of metagranitic rock and associated changes in mineralogy, geochemistry and degree of oxidation: a case study at Forsmark, central Sweden: *International Journal of Earth Sciences*, v. 99, p. 1-25.
- Schmatz, J., and Urai, J.L., 2010, The interaction of fluid inclusions and migrating grain boundaries in a rock analogue: deformation and annealing of polycrystalline camphor–ethanol mixtures: *Journal of Metamorphic Geology*, v. 28, p. 1-18.
- Schmid, S.M., Fügenschuh, B., Kissling, E., and Schuster, R., 2004, Tectonic map and overall architecture of the Alpine orogen: *Eclogae Geologicae Helvetiae*, v. 97, p. 93-117.
- Schulz, S.E., and Evans, J.P., 1998, Spatial variability in microscopic deformation and composition of the Punchbowl fault, southern California: implications for mechanisms, fluid-rock interaction, and fault morphology: *Tectonophysics*, v. 295, p. 223-244.
- Segall, P., and Pollard, D.D., 1983, Nucleation and Growth of Strike Slip Faults in Granite: *J. Geophys. Res.*, v. 88, p. 555-568.
- Sharp, Z.D., 1990, A laser-based microanalytical method for the in situ determination of oxygen isotope ratios of silicates and oxides: *Geochimica et Cosmochimica Acta*, v. 54, p. 1353-1357.
- Shea, W.T., and Kronenberg, A.K., 1992, Rheology and Deformation Mechanisms of an Isotropic Mica Schist: *J. Geophys. Res.*, v. 97, p. 15201-15237.
- Shepherd, T.J., Rankin, A.H., and Alderton, D.M.H., 1985, A practical guide to fluid inclusion studies: Glasgow, Blackie & Son Ltd.
- Sheppard, S., 1986, Characterization and isotopic variations in natural waters, *in* J. Valley, H.T.J., J. O'Neil, ed., *Stable isotopes in high temperature geological processes*, Volume 16: *Reviews in Mineralogy*, Mineralogical Society.
- Shipton, Z.K., and Cowie, P.A., 2001, Damage zone and slip-surface evolution over mu m to km scales in high-porosity Navajo sandstone, Utah: *Journal of Structural Geology*, v. 23, p. 1825-1844.
- Shipton, Z.K., Soden, A.M., Kirkpatrick, J.D., Bright, A.M., and Lunn, R.J., 2006, How thick is a fault? Fault displacement-thickness scaling revisited: *Earthquakes: Radiated Energy and the Physics of Faulting*, v. 170, p. 193-198.
- Sibson, R.H., 1977, Fault rocks and fault mechanisms: *Journal of the Geological Society*, v. 133, p. 191-213.
- , 1982, Fault zone models, heat flow, and the depth distribution of earthquakes in the continental crust of the United States: *BULLETIN OF THE SEISMOLOGICAL SOCIETY OF AMERICA*, v. 72, p. 151-163.
- , 1984, Roughness at the Base of the Seismogenic Zone: Contributing Factors: *J. Geophys. Res.*, v. 89, p. 5791-5799.
- , 1986, Earthquakes and Rock Deformation in Crustal Fault Zones: *Annual Review of Earth and Planetary Sciences*, v. 14, p. 149-175.

- Sibson, R.H., Robert, F., and Poulsen, K.H., 1988, High-angle reverse faults, fluid-pressure cycling, and mesothermal gold-quartz deposits: *Geology*, v. 16, p. 551-555.
- Steck, A., 2008, Tectonics of the Simplon massif and Lepontine gneiss dome: deformation structures due to collision between the underthrusting European plate and the Adriatic indenter: *Swiss Journal of Geosciences*, v. 101, p. 515-546.
- Steiner, A., 1970, Genesis of Hydrothermal K-Feldspar (Adularia) in an Active Geothermal Environment at Wairakei, New-Zealand: *Mineralogical Magazine*, v. 37, p. 916-924.
- Stipp, M., Stünitz, H., Heilbronner, R., and Schmid, S.M., 2002, The eastern Tonale fault zone: a 'natural laboratory' for crystal plastic deformation of quartz over a temperature range from 250 to 700 °C: *Journal of Structural Geology*, v. 24, p. 1861-1884.
- Stünitz, H., and Gerald, J.D.F., 1993, Deformation of granitoids at low metamorphic grade. II: Granular flow in albite-rich mylonites: *Tectonophysics*, v. 221, p. 299-324.
- Suzuoki, T., and Epstein, S., 1976, Hydrogen isotope fractionation between OH-bearing minerals and water: *Geochimica et Cosmochimica Acta*, v. 40, p. 1229-1240.
- Takahashi, M., Mizoguchi, K., Kitamura, K., and Masuda, K., 2007, Effects of clay content on the frictional strength and fluid transport property of faults: *J. Geophys. Res.*, v. 112, p. B08206.
- Taylor, H.P., 1977, Water/rock interactions and the origin of H₂O in granitic batholiths: *Journal of the Geological Society*, v. 133, p. 509-558.
- Tembe, S., Lockner, D.A., and Wong, T.-F., 2010, Effect of clay content and mineralogy on frictional sliding behavior of simulated gouges: Binary and ternary mixtures of quartz, illite, and montmorillonite: *J. Geophys. Res.*, v. 115, p. B03416.
- Tien, Y.M., Kuo, M.C., and Juang, C.H., 2006, An experimental investigation of the failure mechanism of simulated transversely isotropic rocks: *International Journal of Rock Mechanics and Mining Sciences*, v. 43, p. 1163-1181.
- Townend, J., and Zoback, M.D., 2000, How faulting keeps the crust strong: *Geology*, v. 28, p. 399-402.
- Trumpy, R., 2001, Why plate tectonics was not invented in the Alps: *International Journal of Earth Sciences*, v. 90, p. 477-483.
- Tullis, J., and Yund, R.A., 1985, Dynamic Recrystallization of Feldspar - a Mechanism for Ductile Shear Zone Formation: *Geology*, v. 13, p. 238-241.
- Uysal, I.T., Mutlu, H., Altunel, E., Karabacak, V., and Golding, S.D., 2006, Clay mineralogical and isotopic (K-Ar, $\delta^{18}\text{O}$, δD) constraints on the evolution of the North Anatolian Fault Zone, Turkey: *Earth and Planetary Science Letters*, v. 243, p. 181-194.
- Vennemann, T.W., and O'Neil, J.R., 1996, Hydrogen isotope exchange reactions between hydrous minerals and molecular hydrogen: I. A new approach for the determination of hydrogen isotope fractionation at moderate temperatures: *Geochimica et Cosmochimica Acta*, v. 60, p. 2437-2451.
- Wagner, G.A., Reimer, G.M., and Jager, E., 1977, Cooling ages derived by apatite fission track, mica Rb-Sr and K-Ar dating: The uplift and cooling history of the Central Alps: *Mem. 1st. Geol. Mineral. Univ. Padova*, v. 30, p. 27.
- Walsh, J.J., Childs, C., Imber, J., Manzocchi, T., Watterson, J., and Nell, P.A.R., 2003, Strain localisation and population changes during fault

- system growth within the Inner Moray Firth, Northern North Sea: *Journal of Structural Geology*, v. 25, p. 307-315.
- Walsh, J.J., Nicol, A., and Childs, C., 2002, An alternative model for the growth of faults: *Journal of Structural Geology*, v. 24, p. 1669-1675.
- Wenner, D.B., and Taylor, H.P., 1971, Temperatures of serpentinization of ultramafic rocks based on $\text{O}^{18}/\text{O}^{16}$ fractionation between coexisting serpentine and magnetite: *Contributions to Mineralogy and Petrology*, v. 32, p. 165-185.
- White, S., 1979, Grain and sub-grain size variations across a mylonite zone: *Contributions to Mineralogy and Petrology*, v. 70, p. 193-202.
- Wibberley, C., 1999, Are feldspar-to-mica reactions necessarily reaction-softening processes in fault zones?: *Journal of Structural Geology*, v. 21, p. 1219-1227.
- Wibberley, C.A.J., and McCaig, A.M., 2000, Quantifying orthoclase and albite muscovitisation sequences in fault zones: *Chemical Geology*, v. 165, p. 181-196.
- Wibberley, C.A.J., Petit, J.-P., and Rives, T., 2007, The effect of tilting on fault propagation and network development in sandstone-shale sequences: a case study from the Lodeve Basin, southern France: *Journal of the Geological Society*, v. 164, p. 599-608.
- Wibberley, C.A.J., and Shimamoto, T., 2003, Internal structure and permeability of major strike-slip fault zones: the Median Tectonic Line in Mie Prefecture, Southwest Japan: *Journal of Structural Geology*, v. 25, p. 59-78.
- , 2005, Earthquake slip weakening and asperities explained by thermal pressurization: *Nature*, v. 436, p. 689-692.
- Wilkins, S.J., and Gross, M.R., 2002, Normal fault growth in layered rocks at Split Mountain, Utah: influence of mechanical stratigraphy on dip linkage, fault restriction and fault scaling: *Journal of Structural Geology*, v. 24, p. 1413-1429.
- Willemsse, E.J.M., 1997, Segmented normal faults: Correspondence between three-dimensional mechanical models and field data: *J. Geophys. Res.*, v. 102, p. 675-692.
- Wintsch, R.P., 1975, Feldspathization as a Result of Deformation: *Geological Society of America Bulletin*, v. 86, p. 35-38.
- , 1978, A chemical approach to the preferred orientation of mica: *Geological Society of America Bulletin*, v. 89, p. 1715-1718.
- , 1998, Strengthening of fault breccia by K-feldspar cementation, *in* Snoke, A.W., Tullis, J., and Todd, V.R., eds., *Fault related rocks: A petrographic atlas*: Princeton, NJ, Princeton University Press, p. 42.
- Wintsch, R.P., Christoffersen, R., and Kronenberg, A.K., 1995, Fluid-Rock Reaction Weakening of Fault Zones: *Journal of Geophysical Research-Solid Earth*, v. 100, p. 13021-13032.
- Yardley, B.W.D., Banks, D.A., Bottrell, S.H., and Diamond, L.W., 1993, Post-metamorphic gold-quartz veins from N.W. Italy: the composition and origin of the ore fluid.: *Mineralogical Magazine*, v. 57, p. 407-422.
- Zhang, S., and Tullis, T.E., 1998, The effect of fault slip on permeability and permeability anisotropy in quartz gouge: *Tectonophysics*, v. 295, p. 41-52.